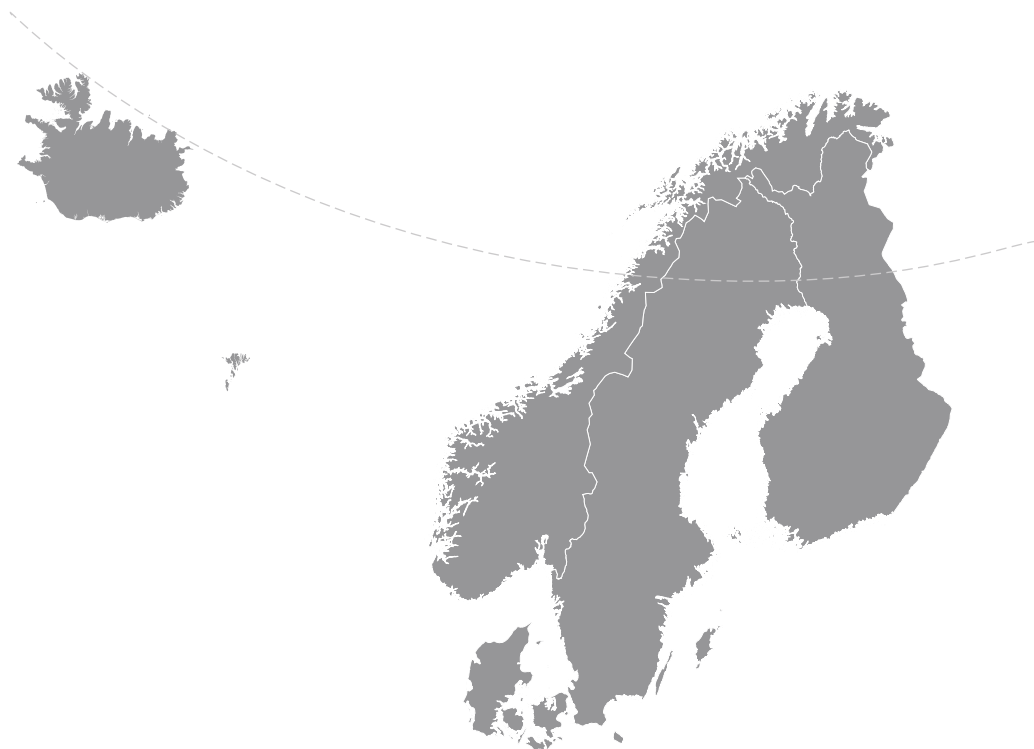


Nordic Concrete Research



Nordic
Concrete
Federation

NORDIC CONCRETE RESEARCH

**EDITED BY
THE NORDIC CONCRETE FEDERATION**

**CONCRETE ASSOCIATIONS OF: DENMARK
FINLAND
ICELAND
NORWAY
SWEDEN**

**PUBLISHER: NORSK BETONGFORENING
POSTBOKS 2312, SOLLI
N - 0201 OSLO
NORWAY**

STOCKHOLM/OSLO, JUNE 2018

Preface

Nordic Concrete Research (NCR) is since more than 35 years the only scientific journal devoted to concrete research in the Nordic countries, i.e., in Denmark, Finland, Iceland, Norway, and Sweden. It has a twofold aim; (i) to provide the Nordic concrete researchers a non-bureaucratic scientific journal with usually a rather rapid review process and (ii) to provide the readers a source of information on concrete news and novelties from the Nordic countries often highlighting items especially interesting for these countries concerning geography, geology, climate, and construction traditions.

The Nordic Concrete Federation and its Research Committee, that also constitutes the Editorial Board of NCR, have decided that NCR shall transfer from a paper journal to an electronic journal, where readers may read all papers free of charge. This system is called “Open Access” and is recommended by both universities and research councils to facilitate dissemination of new knowledge. Thereby, we are confident that NCR will attract both more authors and more readers. Due to highly appreciated financial support from the Nordic cement industry, also submitting papers will be free of charge. This volume of NCR will be published both electronically in Open Access and traditionally as on paper.

You are most welcome to submit research articles to the new, electronic Nordic Concrete Research. The second volume is scheduled for December 2018. For more information on the Nordic Concrete Federation and Nordic Concrete Research, see www.nordicconcrete.net. But for time being, I wish you an interesting reading of this volume’s ten papers covering both material aspects, e.g., Poisson’s ratio, thermal conductivity, and deterioration mechanisms, and structural aspects, e.g., meso-mechanics and an analysis of dome plug for the spent nuclear fuel repository.

Stockholm in June 2018

Johan Silfwerbrand
Editor of NCR

CONTENTS

| | | |
|----|--|-----|
| 1 | Tobias Danner & Mette Rica Geiker Long-term Influence of Concrete Surface and Crack Orientation on Self-healing and Ingress in Cracks – Field Observations | 1 |
| 2 | Magnus Döse & Johan Silfwerbrand Reduction of Radon Gas in Concrete Using Admixtures and Additives | 17 |
| 3 | Göran Fagerlund Frost Destruction of Concrete – A Study of the Validity of Different Mechanisms | 35 |
| 4 | Richard Malm Full-scale Test of an Unreinforced Concrete Dome Plug for the Spent Nuclear Fuel Repository | 55 |
| 5 | Nadia Al-Ayish, Otto During, Katarina Malaga, Nelson Silva & Kjartan Gudmundsson The Influence of Supplementary Cementitious Materials on Climate Impact of Concrete Structures Exposed to Chlorides | 77 |
| 6 | Lamis Ahmed Dynamic Measurements for Determining Poisson’s Ratio of Young Concrete | 95 |
| 7 | Ya Peng, Bård Pedersen, Serina Ng, Klaartje de Weerd & Stefan Jacobsen Filler and water reducer effects on sedimentation, bleeding and zeta-potential of cement paste | 107 |
| 8 | Louise Andersson, Johan Silfwerbrand, Anders Selander & Jan Trägårdh Continuous Preventive Bridge Maintenance of Swedish Municipalities – A Survey on Common Practice | 127 |
| 9 | Alisa Machner, Petter Hemstad & Klaartje De Weerd Towards the Understanding of the pH Dependency of the Chloride Binding of Portland Cement Pastes | 143 |
| 10 | Mohammad H. Baghban, Mahdi Kioumarsi & Sotirios Grammatikos Prediction Models for Thermal Conductivity of Cement-based Composites | 163 |
| | Research Council & Editorial Board of NCR | 173 |



DOI: 10.2478/ncr-2018-0001

ISSN online 2545-2819

ISSN print 0800-6377

© Article authors. This is an open access article distributed under the Creative Commons Attribution-NonCommercial-NoDerivs licens. (<http://creativecommons.org/licenses/by-nc-nd/3.0/>).

Received: March 12, 2018

Revision received: May 3, 2018

Accepted: May 3, 2018

Long-term Influence of Concrete Surface and Crack Orientation on Self-healing and Ingress in Cracks – Field Observations



Tobias Danner
MSc, PhD, Researcher
Norwegian University of Science and Technology
Department of Structural Engineering
Richard Birkelandsvei 1a, NO-7491 Trondheim
tobias.a.danner@ntnu.no



Mette Rica Geiker
MSc, PhD, Professor
Norwegian University of Science and Technology
Department of Structural Engineering
Richard Birkelandsvei 1a, NO-7491 Trondheim
mette.geiker@ntnu.no

ABSTRACT

This paper presents results from investigations on the long-term influence of concrete surface and crack orientation on ingress in cracks. Five reinforced concrete structures from Norway exposed to either de-icing salts or seawater have been investigated. Concrete cores were taken with and without cracks from surfaces with vertical and horizontal orientation. Carbonation in cracks was found on all de-iced structures, and a crack on a completely horizontal surface appeared to facilitate chloride ingress. Ingress of substances from seawater was found in all cracks from marine exposure. However, the impact of cracks on chloride ingress was unclear. Horizontal cracks on vertical surfaces appeared to facilitate self-healing.

Key words: Cracks, exposure, ingress, field observations, long-term

1. INTRODUCTION

The research presented in this paper is part of the ongoing research project “Ferry-free coastal route E39” initiated by the Norwegian Public Roads Administration. A main part of project WP 7.1.1 “Relevance of crack width and decompression requirements (limits) due to durability aspects of conventional reinforcement” is the collection of long-term field data on the influence of cracks on chloride ingress and reinforcement corrosion. Furthermore, the impact of exposure and orientation of concrete surface and cracks on self-healing and chloride ingress is investigated. This paper presents results from field studies performed in 2017.

Reinforcement corrosion due to chloride ingress or carbonation is one of the major deterioration mechanisms of steel reinforced concrete structures. There is evidence that cracks facilitate the ingress of chloride ions and shorten the time to initiate reinforcement corrosion [1].

According to Eurocode 2 [2] a limiting calculated crack width (w_{max}) should be established to maintain proper functioning or durability of reinforced concrete structures. For ordinary reinforcement and exposure classes XC, XD and XS the recommended value for w_{max} is 0.3 mm [2]. The *fib* model code for service life design (MC-SLD) [3] gives guidelines on the impact of cracks on service life. These guidelines for chloride and carbonation induced corrosion are summarized in Table 1 and Table 2. Horizontal surfaces with cracks and chloride exposure from top are regarded the most severe exposure condition. In this case special protective measures should be taken in the presence of cracks to ensure service life ≥ 10 years. For vertical or horizontal concrete surfaces with exposure from the bottom, service life ≥ 50 years is expected for surface crack width ($w_{k,cal}$) up to 0.3 mm given high quality concrete (cover ≥ 50 mm and $w/c \leq 0.5$). For carbonation induced corrosion, there is no differentiation made between horizontal and vertical surfaces. The concrete should be of “adequate quality” and $w_{k,cal} \leq 0.3$ mm to obtain a service life of at least 50 years [3].

Table 1 - Crack width guidelines for chloride induced corrosion on horizontal and vertical surfaces according to MC-SLD [3].

| Surface | Exposure | Crack | Crack width ($w_{k,cal}$) | Protective measure | Service life |
|------------|-------------|----------------------------------|-----------------------------|---|-----------------|
| Horizontal | From top | On top | No limit | Special measures | ≥ 10 years |
| Horizontal | From bottom | Water not leaking through cracks | ≤ 0.3 mm | High quality concrete (cover ≥ 50 mm; $w/c \leq 0.5$) | ≥ 50 years |
| Vertical | | | | | |

Table 2 - Crack width guidelines for carbonation induced corrosion according to MC-SLD (2006) [3].

| Surface | Exposure | Crack | Crack width ($w_{k,cal}$) | Protective measure | Service life |
|---------|----------|-------|-----------------------------|-------------------------|-----------------|
| - | - | - | ≤ 0.3 mm | Adequate concrete cover | ≥ 50 years |

Laboratory experiments of the influence of cracks on chloride ingress and corrosion are mainly performed on horizontal concrete surfaces with exposure from the top. A typical experimental set up is ponding of a crack with chloride solution from top [4]. When discussing the orientation of cracks, the orientation is only described with regard to the reinforcement, *i.e.* coincident cracks (parallel to reinforcement) and intersecting cracks (perpendicular to the reinforcement); but not with regard to the concrete surface [5].

Self-healing of cracks in concrete is highly dependent on the exposure condition and the presence of water is the most important factor [6]. The main mechanisms of self-healing seem to be of chemical nature. Chemical causes of self-healing of cracks exposed to water are *e.g.* further hydration of unhydrated cement grains or the formation of calcium carbonate crystals on the crack surface. The formation of calcium carbonate on crack surfaces is examined in detail and considered the most important mechanism of autogenic self-healing in the presence of fresh water [7]. Formation of C-S-H phases, portlandite and ettringite was observed in cracks after 3 month curing in water [8]. For cracked concrete exposed to seawater the formation of brucite ($\text{Mg}(\text{OH})_2$) or ettringite was also observed [9-11].

Only very few studies investigated the impact of surface and/or crack orientation on ingress. Most studies do not describe the exposure conditions in detail. Information on the surface orientation is typically lacking. According to the authors' knowledge there are no data available on the impact of crack and surface orientation on self-healing of cracks. This paper presents observations from field studies on chloride ingress and self-healing in cracks with regard to surface orientation and crack orientation.

2. MATERIALS AND METHODS

2.1 Materials

Investigated Structures

Table 3 gives an overview of the investigated field structures. Figure 1 shows the location of the investigated field structures. The investigations covered three structures exposed to de-icing salts (Cecilie Bridge, Tåsen Tunnel and Moholt Bridge) and two marine exposed structures (DNV column and Hafrsfjord Bridge). The investigations on Cecilie (16 years old) and Moholt Bridge (25 years old) concentrated on shrinkage cracks in the edge beams. The exact exposure of the edge beams is not well documented. The investigated edge beams were adjacent to the pedestrian path which was not salted. However, the driving lane was regularly salted as part of winter maintenance. Salt could have been transported to the edge beams by wind and salt spray due to frequent traffic. Additionally, the bridges are only 1 and 2 kilometres away from Trondheim fjord which could lead to some airborne chloride exposure. Similarly, it was not possible to define the exact exposure of the concrete core received from Tåsen Tunnel (20 years old). Inside the tunnel, no de-icing salts are used. However, the road where the tunnel is located is categorized in the highest priority class of winter maintenance in Norway, meaning regular use of de-icing salts. The distance between tunnel drive in and the location of the core was about 1 km. Both the DNV column and the foundations of Hafrsfjord Bridge are exposed to tidal seawater for 33 and 50 years, respectively. The DNV column was reinforced with three concentric reinforcement cages, parts of which was coupled to a sacrificial anode for an unknown period [12]. It is our expectation that the impact on ingress has been limited due to a very low current, as no corrosion of the reinforcement cages was observed after removing all the concrete.

Figure 2 illustrates the investigated structural parts showing the different orientation of the investigated concrete surfaces and the orientation of the investigated cracks. The red circles indicate locations of coring. Concrete cores were taken from horizontal and vertical surfaces. The edge beam from Cecilie Bridge was the only completely horizontal surface of all investigated structural parts. The edge beam from Moholt Bridge had a slope of about 4 %. From Tåsen Tunnel, the DNV column and the foundation of Hafrsfjord Bridge, cores were taken on vertical surfaces.

Table 3 - Overview over investigated structures [13]

| Structure | Cecilie Bridge | Tåsen Tunnel | Moholt Bridge | DNV column | Hafrsfjord Bridge |
|---------------------|--------------------------|---------------|---------------|-------------------------------------|----------------------|
| Type | Beam (Box-girder) bridge | Culvert | Slab bridge | Part time dynamically loaded column | Beam bridge (NIB) |
| Location | Trondheim | Oslo | Trondheim | Bergen | Stavanger |
| Structural part | Edge beam | Tunnel wall | Edge beam | Column | Foundation |
| Cracks | Shrinkage | Shrinkage | Shrinkage | Dynamic loading | Shrinkage, restraint |
| Cover (mm) | 70 | 50 | 50 | 50 | 90 |
| Concrete | C55 | N/A * | C45 | C60 | B35 |
| Cement | N/A | N/A | N/A | SP 30-4A | N/A |
| Cement Type | N/A | N/A | N/A | CEM I | N/A |
| Surface orientation | Horizontal | Vertical | Horizontal | Vertical | Vertical |
| Crack orientation | Vertical | Vertical | Vertical | Horizontal | Vertical |
| Age (years) | 16 | 20 | 25 | 33 | 50 |
| Exposure | De-icing salt | De-icing salt | De-icing salt | Tidal seawater | Tidal seawater |
| Climate | Inland | Inland | Inland | Marine | Marine |

* N/A: not available



Figure 1 – Map of Norway showing the location of the investigated bridges, after [14]

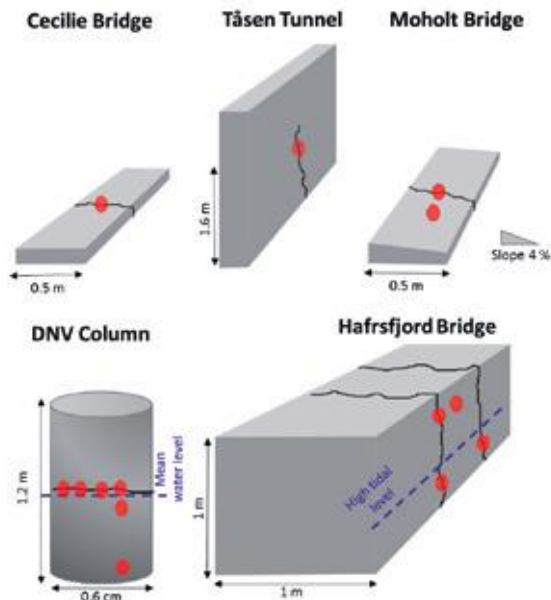


Figure 2 - Illustration of the investigated structural parts showing the concrete surface and crack orientation. Locations where cores were taken are illustrated in red.

While the Tåsen Tunnel and Hafrsfjord Bridge had vertical cracks, the DNV column had a crack with horizontal orientation. Except for the DNV column, it is expected that the investigated cracks are due to early drying shrinkage or thermal restraint. The investigated crack from the DNV column derives from dynamic loading [15]. None of the structures allowed cores to be taken from different surfaces or crack orientations.

Concrete Cores

For all structures it was tried to drill concrete cores through reinforcement with crack width above and below 0.3 mm [2]. Additionally, reference cores next to the cracks were taken when possible. Table 4 gives an overview of the drilled concrete cores from the investigated field structures. The approximate location of concrete cores is illustrated in Figure 2.

For Cecilie Bridge and Tåsen Tunnel it was only possible to retrieve one (1) core for the investigation. The concrete cores from both structures were drilled on a surface crack with crack width 0.45 mm. Three (3) cores were drilled from Moholt Bridge, with no crack and surface crack widths of 0.2 and 0.55 mm. The crack mouth of the investigated cracks from the de-iced structures appeared open.

From the DNV column six (6) concrete cores were drilled. Four (4) concrete cores were drilled on the horizontal crack in the tidal zone. Two (2) reference cores were drilled below the crack in the tidal zone. Core D_0aT was drilled only about 0.1 m below the crack while core D_0bT was drilled about 0.4 m below the crack. The crack was located close to the mean water level. The location of the mean water level at the DNV column is illustrated in Figure 2. The tidal changes in Bergen at the field station are about ± 0.8 m. The surface crack width on the cores varied between 0.15 to 0.50 mm. [16]

Six (6) concrete cores were taken from Hafrsfjord Bridge. Four (4) cores including a reference without crack were taken from the tidal zone. The mouth of the cracks in the tidal zone appeared sealed. The surface crack width was about 0.20 mm. Two (2) cores with cracks were taken in the splash zone. The surface crack width of these cores was 0.40 and 0.50 mm and the crack mouth appeared open.

Table 4 - Overview of the concrete cores taken from the different structures

| Structure | Core id. | Exposure | Height above mean water level (m) | Surface crack width (mm) | Crack depth (mm) | Concrete cover (mm) | Crack mouth open/sealed |
|--------------------|----------|----------|-----------------------------------|--------------------------|------------------|---------------------|-------------------------|
| Cecilie Bridge | C_0.45D* | De-iced | | 0.45 | 70 (wc)** | 70 | Open |
| Tåsen Tunnel | T_0.45D | De-iced | | 0.45 | 50 (wc) | 50 | Open |
| Moholt Bridge | M_0D | De-iced | | 0.00 | | 50 | |
| | M_0.2D | De-iced | | 0.20 | 40 | | Open |
| | M_0.55D | De-iced | | 0.55 | 70 (wc) | | Open |
| DNV column | D_0aT* | Tidal | -0.1 | 0.00 | | 50 | |
| | D_0bT | Tidal | -0.4 | 0.00 | 150 (wc) | | |
| | D_0.2aT | Tidal | +0.1 | 0.20 | 150 (wc) | | Sealed |
| | D_0.5T | Tidal | +0.1 | 0.50 | 150 (wc) | | Sealed |
| | D_0.15T | Tidal | +0.1 | 0.15 | 150 (wc) | | Sealed |
| | D_0.2bT | Tidal | +0.1 | 0.20 | 150 (wc) | | Sealed |
| Hafstrfjord Bridge | H_0T | Tidal | 0 | 0.00 | | 90 | |
| | H_0.2aT | Tidal | 0 | 0.20 | 100 (wc) | | Sealed |
| | H_0.2bT | Tidal | 0 | 0.20 | 110 (wc) | | Sealed |
| | H_0.2cT | Tidal | 0 | 0.20 | 120 (wc) | | Sealed |
| | H_0.4S* | Splash | +0.6 | 0.40 | 120 (wc) | | Open |
| | H_0.5S | Splash | +0.6 | 0.50 | 110 (wc) | | Open |

* D: de-icing salts; T: tidal zone; S: splash zone

** wc : whole core

Italic = extracted with reinforcement

2.2 Methods

Surface crack width measurements were performed manually with a crack width ruler (accuracy ± 0.05 mm) on the concrete surface before drilling of the concrete cores. The measurements were undertaken during spring or autumn at temperatures between 5 and 15°C.

Concrete cores were drilled with a water-cooled concrete saw and tapped dry. After a fast visual inspection in the field, the cores were tightly packed in several layers of plastic. Before analysis and in between experiments, the cores were stored in plastic in a room with a temperature of 5°C.

The concrete cores were used for chloride profile grinding and μ -XRF elemental mapping. The concrete cores were cut into two halves with a water-cooled concrete saw and tapped dry with a moist cloth. Quantitative chloride profiles were taken from one of the halves of concrete cores not containing cracks. Profile grinding was done in 5 mm steps for the first 30 mm and 10 mm steps from 30-100 mm. Thin layers were ground inwards from the exposed surface. The chloride content of these layers was determined with potentiometric titration method. About 5 g of the concrete powder of each section was dissolved in 50 ml 80°C (1:19) HNO₃ and filtrated after 1 h. The chloride content in the resulting filtrated solution was determined by potentiometric titration with a Titrando 905 titrator from Metrohm. 0.01 M AgNO₃ was used as titrant. [17]

Concrete cores taken with and without cracks were analysed with micro X-Ray fluorescence (μ -XRF) without further preparation [18]. Elemental maps were obtained on a M4 Tornado from Bruker. The instrument operates with a Ag X-Ray source and two silicon drift detectors simultaneously for fast analysis. A collimator focuses the X-ray beam to a spot size of about 25 μm . Elemental maps were acquired with 50 kV accelerating voltage and 600 μA tube current. A distance of 60 μm between each measuring point and a speed of 1 ms/pixel were chosen for qualitative maps. For each map, the signal detected as counts per second (cps) is normalized to 100 %. The brightest areas represent the highest measured cps. All maps are normalized individually and colour codes should not be compared directly.

Carbonation depth was characterized by spraying the freshly cut concrete surface with thymolphthalein indicator. After cutting, the concrete surface was dried with paper prior to spraying with the indicator solution. The thymolphthalein solution was prepared by dissolving 1 g of the indicator (powder, grade “ACS, Reag. Ph Eur” (VWR)) in a mix of 30 ml of deionized water and 70 ml of ethanol [19]. Thymolphthalein gives a colour change in the pH range of 9 to 10.5. Above this range, the colour of thymolphthalein gets bluish white, below it, thymolphthalein becomes colourless.

3. RESULTS AND DISCUSSION

In the results and discussion chapter the expression “self-healing of cracks” will be used in cases where a precipitation of new phases was observed inside the crack. However, neither mechanical nor ingress tests were performed to verify if the investigated cracks actually were self-healed or self-sealed, respectively.

3.1 De-iced Structures

Figure 3 shows the μ -XRF chlorine maps of concrete cores taken from Cecilie Bridge, Tåsen Tunnel and Moholt Bridge. The surface crack width of the cracks was 0.45 mm for Cecilie Bridge and Tåsen Tunnel and 0.55 mm for Moholt Bridge. Figure 3 (left) shows the chloride ingress in the cracked concrete core from Cecilie Bridge. An even chloride ingress over the whole width of the concrete core is visible within the first 10 mm. Besides that, chloride ingress is visible along the crack. Chloride ingress from the crack surface into the concrete was observed over the full length of the core, i.e. 100 mm. In contrast to this, the concrete cores from Tåsen Tunnel (Figure 3 middle) and Moholt Bridge (Figure 3 right) did not show an impact of the crack on the chloride ingress.

In the core from Tåsen Tunnel, somewhat higher chlorine intensities were observed around the steel-concrete interface compared to the bulk of the concrete. A possible explanation could be micro-cracking in the steel-concrete interface facilitating the accumulation of chloride. The surface crack width was similar in the core from Cecilie Bridge and Tåsen Tunnel. However, the core from Cecilie Bridge was taken from a horizontal surface, while a crack from a vertical surface was investigated in Tåsen Tunnel. The time of direct exposure is generally longer on a horizontal surface, which can explain the higher ingress into the crack observed in Cecilie Bridge.

In the core from the Moholt Bridge, there seems to be a very low level of chloride ingress in the concrete surface. The measured intensities in the surface near region are not much higher than in

the bulk of the concrete i.e. almost disappearing in the background noise. The investigated edge beam from Moholt Bridge is similar to the edge beam investigated on Cecilie Bridge, except for the slope. Both bridges are categorized in the same winter maintenance class and the wind exposure is similar. However, compared to Cecilie Bridge the edge beam of Moholt Bridge is not completely horizontal but had a slope of 4%.

In cores drilled above reinforcement from Moholt Bridge and Tåsen Tunnel general corrosion was found on the surface of the steel in contact with carbonated concrete. However, the extent of corrosion was limited. Carbonation in cracks was observed in all cores taken from de-iced structures regardless of the surface crack width. Figure 4 shows the corrosion imprint in the steel-concrete interface, general corrosion on the reinforcement and the carbonation of the crack surface from the concrete core taken from Moholt Bridge. The example shown is from the concrete core with limited chloride ingress presented in Figure 3 (right).

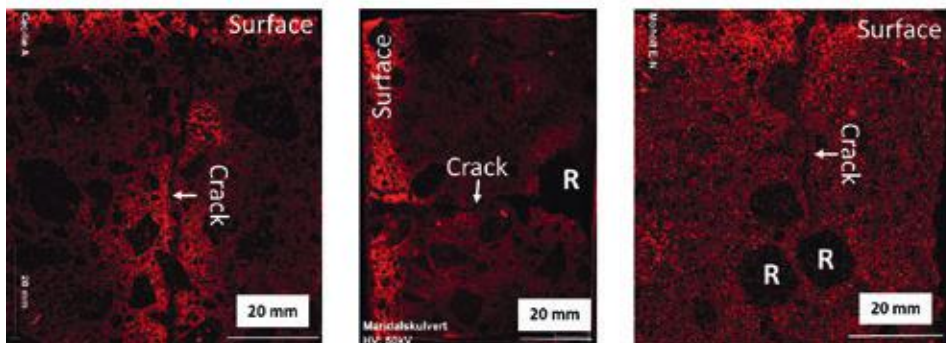


Figure 3 - μ -XRF chlorine maps of concrete cores from de-iced structures. Left: Core C_0.45D from the Cecilie Bridge; Middle: Core T_0.45D from the Tåsen Tunnel; Right: Core M_0.55D from the Moholt Bridge. The orientation of the cores represents the surface orientation in the field. R = reinforcement

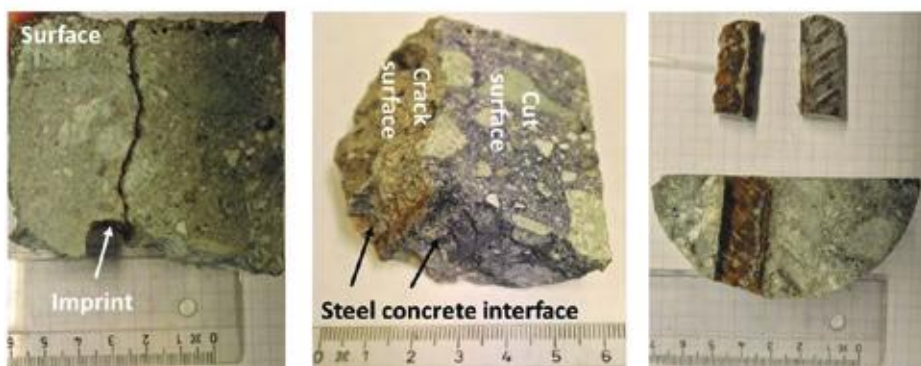


Figure 4 - Concrete core M_0.55D from the Moholt Bridge. Left: Cut concrete core; Middle: Carbonated crack surface and steel-concrete interface of the corroded rebar Right: General corrosion on the upper surface of the reinforcement and corrosion imprint in the steel-concrete interface for the reinforcement beneath the crack.

3.2 Marine Structures

For the marine exposed structures, quantitative chloride profiles of reference cores without crack were taken. μ -XRF mapping was performed on concrete cores with and without cracks. Figure 5 shows the chloride profiles of a core from the 33-year-old DNV column (D_0aT) and the 50-year-old Hafstrsfjord Bridge (H_0T). The chloride profiles look similar with about 0.6 % Cl by weight of concrete in the outer 10 mm of the concrete cores.

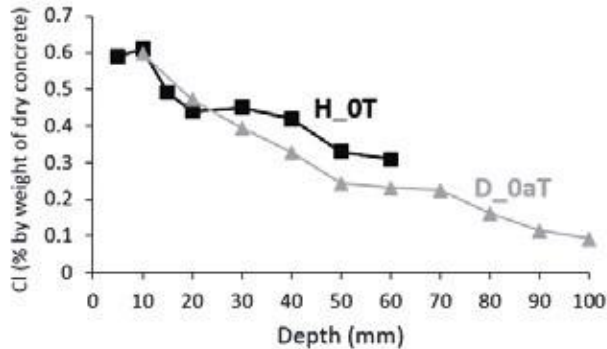


Figure 5 - Quantitative chloride profiles of cores H_0T and D_0aT from Hafstrsfjord Bridge and the DNV column, respectively. Both cores were without crack and from the tidal zone.

Figure 6 shows the chlorine, magnesium and sulphur maps of four concrete cores from the DNV column. The first core to the left is the reference core with no crack. All four concrete cores show an even chloride ingress from the concrete surfaces. Compared to the reference core there is no apparent deeper chloride ingress in the cracked cores. In the crack of core D_0.5T, magnesium is visible within the first 20 mm. In cores D_0.15T and D_0.2T, the cracks are difficult to see due their small size and the extensive self-healing observed in these cracks. Magnesium and calcium rich products were found in all cracks, which is typical for self-healing of concrete exposed to seawater [9, 11]. Right after cutting and after cleaning the reinforcement with acid, no corrosion was observed. During storage, corrosion developed on the cut steel surfaces in the concrete cores. Corrosion was especially observed on the outer reinforcement, which can be explained by a higher chloride content in this area. Further details on the investigations performed on the DNV column are given in [14].

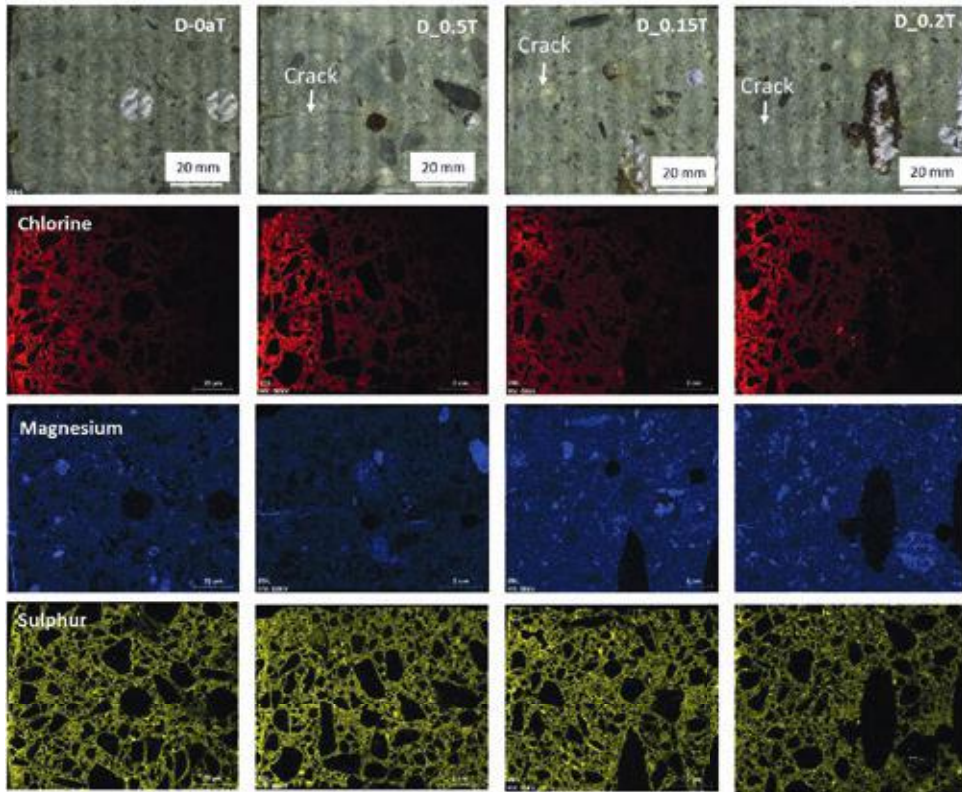


Figure 6 - Chlorine, magnesium and sulphur maps from cores from the DNV column. **Left:** Core D_0aT without crack from the tidal zone; **Middle left:** Core D_0.5T, surface crack width 0.5 mm; **Middle right:** Core D_0.15, surface crack width 0.15 mm; **Right:** Core D_0.2, surface crack width 0.2 mm. The cracked concrete cores were located about 0.2 m higher than the reference concrete core without crack. The indicated cracks are partly healed.

Figure 7 shows the chlorine, magnesium and sulphur maps of four concrete cores from Hafrsfjord Bridge from the tidal and splash zone. The first core to the left is the reference core with no crack. In the field, it was observed that the crack mouth was sealed in the tidal zone. The same cracks but higher up (splash zone) had an open crack mouth. When the concrete cores were extracted, the crack surfaces did not show signs of self-healing, independently of exposure. Most cores fell apart along the crack surface and had to be taped together for μ -XRF analysis. The cracks of the concrete cores shown in Figure 7 appear therefore larger than the original size. The sealing of the crack mouths in the tidal zone might be explained by leaching from the cement paste followed by precipitation. Although, no self-healing was observed, magnesium precipitation on the crack surfaces was detected with μ -XRF in all cores. Furthermore, ingress of sulphate through the cracks is clearly visible from the sulphate maps. While magnesium seems to precipitate on the crack surfaces, sulphur appears to diffuse into the concrete. Magnesium and sulphate were detected as deep as 100 mm in core H_0.4S. The very light spots in the sulphur maps are pores, and are also visible in the calcium mapping. This could be explained by potential precipitation of gypsum on the pore walls. Despite, the clear ingress of seawater in to the cracks, an impact of the cracks on chloride ingress was not detectable.

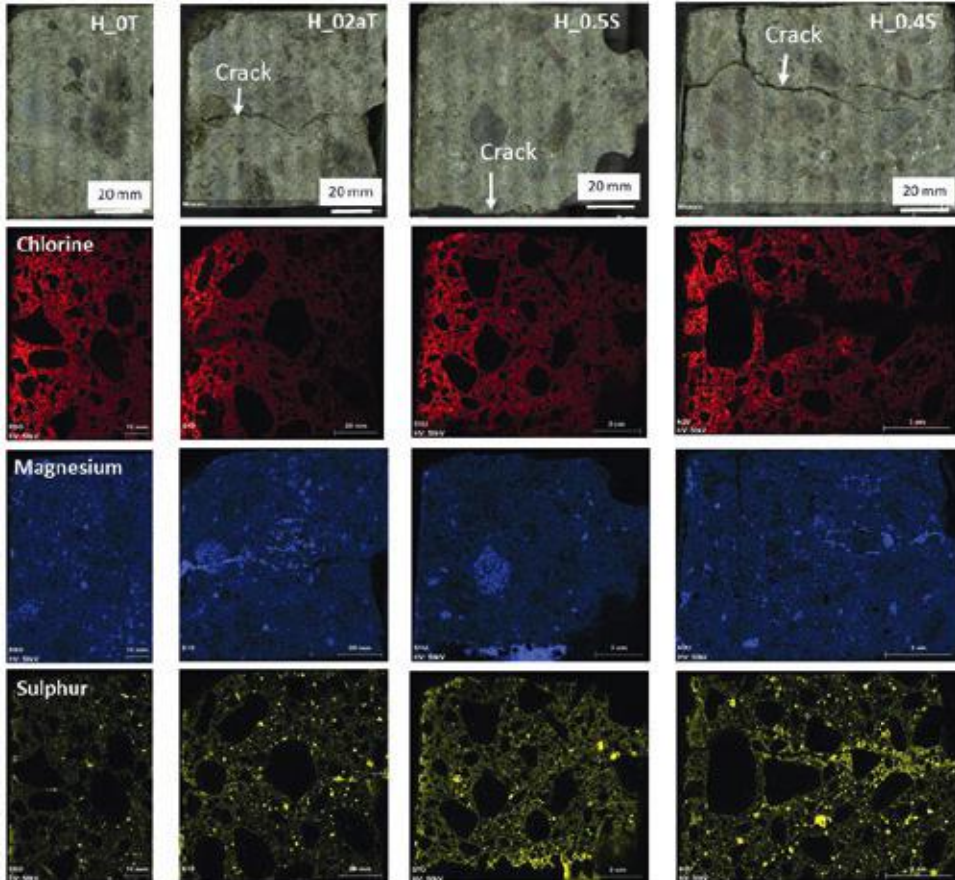


Figure 7 - Chlorine, magnesium and sulphur maps from cores from the Hafstrsford Bridge. **Left:** Core H_0T without crack from the tidal zone; **Middle left:** Core H_0.2aT, surface crack width 0.2 mm, from the tidal zone at the same height as core H_0T; **Middle right:** Core H_0.5S, surface crack width 0.5 mm from the splash zone; **Right:** Core H_0.4S, surface crack width 0.4 mm, from the splash zone.

Two cores from Hafstrsford Bridge (H_0T and H_0.5S) were drilled through reinforcement, one off crack and one on crack. Both the uncracked reference core (H_0T) and the cracked core (H_0.5S) did not show signs of reinforcement corrosion. Compared to the other investigated structures, the cover depth at the foundations of Hafstrsford Bridge was higher with about 90 mm.

As mentioned before, magnesium precipitation was observed inside cracks for both, the DNV column and Hafstrsford Bridge. However, self-healing was only observed in cores taken from the DNV column. Figure 8 shows a close up picture of the crack in core H_0.2aT from Hafstrsford Bridge and core D_0.5T from the DNV column. In core H_0.2aT we can see an open crack with some precipitation on the crack surface. In core D_0.5T we can see a layer of products closing the crack. In both cases, the phases were rich in calcium and magnesium.

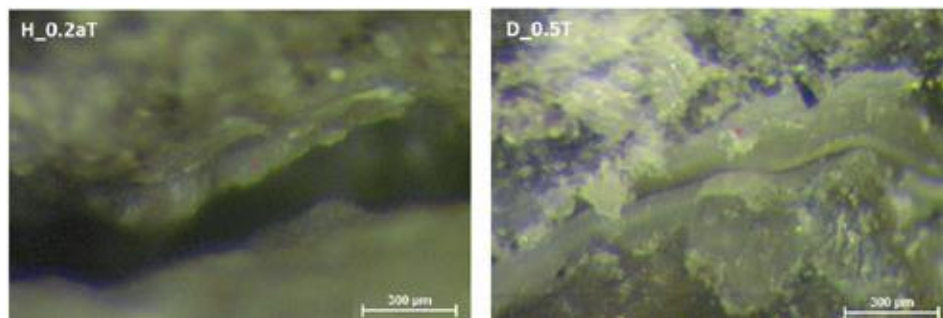


Figure 8 - Left: Open, not self-healed crack of core H_0.2aT from the Hafrsfjord Bridge; Right: Closed, self-healed crack of core D_0.5T from the DNV column.

3.3 Influence of concrete surface and crack orientation on ingress and self-healing

Table 5 gives a summary of the obtained results with regard to chloride ingress, carbonation, self-healing and corrosion.

Table 5 - Summary of results on chloride ingress and carbonation along cracks and self-healing of the analysed concrete cores from the different structures.

| Structure | Concrete surface | Surface crack width (mm) | Crack orientation | Impact of crack on chloride ingress | Carbonation in cracks | Self-healing | Impact of crack on corrosion |
|-------------------|------------------|--------------------------|-------------------|-------------------------------------|-----------------------|--------------|-------------------------------|
| Cecilie Bridge | Horiz. | 0.45 | Vertical | Yes | Yes | No | N/A |
| Tåsen Tunnel | Vert. | 0.45 | Vertical | No | Yes | No | N/A |
| Moholt Bridge | Horiz. | 0.0 0.2 0.45 | Vertical | No No | Yes Yes | No No | Yes No - CP |
| DNV Field Station | Vert. | 0.0 0.2 0.5 | Horizontal | No No No | No No No | Yes Yes | No - CP No - CP No - CP |
| Hafrsfjord Bridge | Vert. | 0.0 0.2 0.45 | vertical | No No | No No | No No | N/A No |

N/A = not available

CP = potentially cathodic protected via sacrificial anodes

Carbonation of cracks was observed on all the de-iced structures regardless of the surface orientation, and carbonation induced corrosion was observed on the reinforcement surface extracted with cores from the de-iced structures. A clear impact of a crack on chloride ingress was only observed for the completely horizontal surface (Cecilie Bridge).

Ingress of seawater in the cracks was observed in magnesium and sulphur mappings; however, a potential impact of cracks on chloride ingress was not detectable. The horizontal crack on the

marine exposed DNV column seem to favour self-healing, and complete self-healing of cracks was only observed in the cores taken from the DNV column. In contrast, the vertical crack on the Hafstrfjord Bridge was not self-healed. This might be explained by a horizontal crack being wet for longer time, as seawater might stay longer inside the crack after it is filled. In a vertical crack the water can move more freely out of the crack.

Figure 9 illustrates the observed long-term influence of concrete surface and crack orientation on ingress in cracks. A crack on a horizontal top surface (1) appears to represent the most severe condition with regard to ingress. This supports the guidelines given in the *fib* model code for service life design (MC-SLD) [3]. A crack on a vertical surface is less severe. The potential for self-healing of a crack in marine exposure seems to be facilitated with a horizontal crack, i.e. vertical cracks (2) appears more severe than horizontal cracks (3).

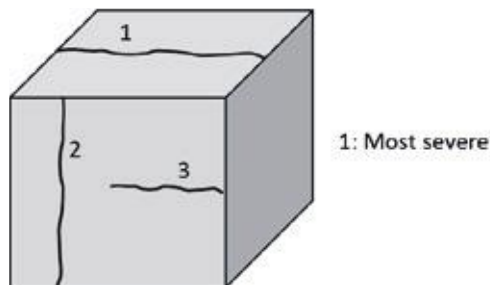


Figure 9 - Illustration of the observed long-term influence of concrete surface and crack orientation on ingress in cracks.

4. CONCLUSIONS

This research presents preliminary results from a limited amount of samples. However, there are some indications on the influence of exposure and orientation of surface and cracks on ingress and self-healing as listed below.

- On de-iced structures, chloride ingress in cracks was only observed on a completely horizontal surface. This supports the guidelines in MC-SLD describing horizontal surfaces with exposure from top as the most severe condition [3].
- Complete carbonation of crack surfaces was observed on all three structures exposed to de-icing salts regardless of surface crack width and surface orientation.
- On the two marine exposed structures, ingress of magnesium and sulphur from seawater was observed. Magnesium was precipitated inside the crack, while sulphur diffused from the crack surfaces into the concrete. The impact of cracks on chloride ingress was unclear.
- Complete self-healing of cracks was only observed for a horizontal crack on a vertical surface exposed to the marine tidal zone.

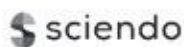
ACKNOWLEDGEMENTS

This research is part of the Norwegian Public Roads Administration (NPRA) Ferry-free coastal route project. NPRA and Trondheim municipality are acknowledged for providing access to Cecile-, Moholt-, Hafsråfjord Bridge and Tåsen Tunnel. DNV GL is acknowledged for providing concrete columns and NPRA is acknowledged for facilitating the collaboration. The financial sponsors of the project “Reinforcement Corrosion in Marine Concrete Structures Under Dynamic Loading” are acknowledged; the project made it possible to construct and expose the “DNV column”.

REFERENCES

1. Bertolini, L., B. Elsener, P. Pedferri, and R. Polder: “Corrosion of Steel in Concrete - Prevention, Diagnosis, Repair,” Wiley-VCH, Weinheim, Germany, 2004.
2. European Committee for Standardization (CEN): “EN 1992-1-1: Eurokode 2: Design of concrete structures – Part 1-1: General Rules and Rules for Buildings,” Brussels, Belgium 2004.
3. Fédération International du Béton (*fib*): “Model Code for Service Life Design,” *Bulletin* 34, Lausanne, Switzerland, 2006.
4. Michel, A., A.O.S. Solgaard, B.J. Pease, M.R. Geiker, H. Stang, and J.F. Olsen: “Experimental Investigation of the Relation between Damage at the Concrete-Steel Interface and Initiation of Reinforcement Corrosion in Plain and Fibre Reinforced Concrete,” *Cement and Concrete Research*, Vol. 77, December 2013, pp. 308-321.
5. The Concrete Society: “Relevance of Cracking in Concrete to Reinforcement Corrosion,” *Technical report* 44, 2nd edition. Hampshire, United Kingdom, December 2015.
6. De Rooij, M., K. Van Tittelboom, N. De Belie, and E. Schlangen: “Self healing Phenomena in Cement-based Materials,” *Rilem State of the Art Report*, Rilem Technical Committee 221-SHC, Springer, Heidelberg, Germany, 2013.
7. Edvardsen, C.: “Water Permeability and Autogenous Healing of Cracks in Concrete,” *Materials Journal*, Vol. 96(4), January 1999, pp. 448-454.
8. Jacobsen, S., J. Marchand, and H. Hornain: “Sem Observations of the Microstructure of Frost Deteriorated and Self-healed Concretes,” *Cement and Concrete Research*, Vol. 25(8), December 1995, pp. 1781-1790.
9. De Weerd, K., H. Justnes, and M.R. Geiker: “Changes in the Phase Assemblage of Concrete Exposed to Sea Water,” *Cement and Concrete Composites*, Vol. 47 (Supplement C), March 2014, pp. 53-63.
10. Fidjestøl, P. and N. Nilsen: “Field Test of Reinforcement Corrosion in Concrete, in Performance of Concrete in Marine Environment,” *SP-65*, American Concrete Institute, Detroit, United States of America, August 1980, pp.205-222.
11. Mohammed, T.U., N. Otsuki, and H. Hamada: “Corrosion of Steel Bars in Cracked Concrete under Marine Environment,” *Journal of Materials in Civil Engineering*, Vol. 15(5), October 2003, pp. 460-469.
12. Espelid, B., A. Kyte, S.O. Valdernesnes, and E. Handal: “Reinforcement Corrosion in Marine Concrete Structures under Dynamic Loading,” Det Norske Veritas, Bergen, Norway, 1987.
13. Norwegian Public Roads Administration: “Brutus - Bridge and Tunnel Archive”, Version 4.5.3, Oslo, Norway, March 2017.
14. www.railpass.com/plan-your-trip/maps/norway, assessed in April 2018

15. Andersen, J.H. and B. Espelid, Erfaringer fra FOU-Prosjektet "Dynamisk Belastning av Betongkonstruksjoner" in NIF-kurs: 34419020 Konstruksjoner i Lettbetong - Prosjektering og Produksjon, Det Norske Veritas, Storefjell, Norway 1993 (In Norwegian).
16. Danner, T. and M.R. Geiker: "Self-healing and Chloride Ingress in Cracked Concrete Exposed to Marine Environment for 33 Years", paper in preparation, NTNU, Trondheim, Norway, May 2018.
17. Nordtest – Nordic Innovation Centre, NT Build 443; Concrete, hardened: Accelerated Chloride Penetration, Oslo, Norway, November 1995.
18. Danner, T., De Weerd, K., Geiker, M.R.: "μ-XRF Characterisation of Chloride Ingress and Self-healing in Cracked Concrete", *Proceedings, XXIIIth Symposium on Nordic Concrete Research & Development*, Aalborg, Denmark, August 2017, pp. 119-122
19. Belda Revert, A., K. De Weerd, K. Hornbostel, and M.R. Geiker: "Carbonation-induced Corrosion: Investigation of the Corrosion Onset," *Construction and Building Materials*, Vol. 162, February 2018, pp. 847-856.



DOI: 10.2478/ncr-2018-0002

ISSN online 2545-2819

ISSN print 0800-6377

© Article authors. This is an open access article distributed under the Creative Commons Attribution-NonCommercial-NoDerivs licens. (<http://creativecommons.org/licenses/by-nc-nd/3.0/>).

Received: Feb. 6, 2018

Revision received: April 18, 2018

Accepted: April 18, 2018

Reduction of Radon Gas in Concrete Using Admixtures and Additives



Magnus Döse

Doctoral candidate, The Royal Institute of Technology (KTH)
Department of Civil and Architectural Engineering, Concrete Structures

The Swedish Cement and Concrete Research Institute (CBI)
Brinellgatan 4, SE-501 15 Borås
e-mail: magnus.dose@cbi.se



Johan Silfwerbrand

Professor, The Royal Institute of Technology (KTH)
Department of Civil and Architectural Engineering, Concrete Structures

Brinellvägen 23, SE-100 44 Stockholm
e-mail: jsilfwer@kth.se

ABSTRACT

The second largest cause of lung cancer is related to radon (^{222}Rn) and its progenies in our environment. Building materials, such as concrete, contribute to the production of radon gas through the natural decay of ^{238}U from its constituents. The Swedish Cement and Concrete Research Institute (CBI) has examined three concrete recipes where only an additive as well as fly ash were added as single constituents to a reference recipe and compared to a reference concrete. The inputs of an additive as well as a supplementary cementitious material (fly ash) were made as a mean to investigate their potential influence on the radon exhalation rates of the concrete. Measurements were performed with an ATMOS 33 ionizing pulsation chamber for at least five different occasions for each recipe during a 22 month period. The results indicate a reduction of the exhalation rate by approximately 30-35 % for each altered recipe. This means roughly 1.5-2 mSv per year decrease in effective dose to a human using an additive or a supplementary cementitious material such as fly ash in relation to the investigated standard concrete.

Key words: radon, effective dose, concrete, building materials, admixtures, additives, fly ash, health.

1. INTRODUCTION AND BACKGROUND

1.1 Ionizing radiation and health

The second largest cause of lung cancer is ionizing radiation generated by radon and its progenies [1]. The EU legislation, its Construction Products Regulations [2] and the EU's Basic Safety Standards (BSS) directive [3] currently put a strong focus on ionizing radiation of building materials and safety for the public. In 2018 the implementation of the current BSS should be fulfilled in the European countries' national legislation. From a national standpoint the increase in environmental awareness is noticed by adequate procurements involving legal certification documents in the building process relating to environmental issues for public health. The world health organization (WHO) also recommends a maximum radon level of 100 Bq/m³ due to large inter-pooling studies by Darby et al. [4] showing a clear link with increased mortality due to increase of radon in households.

Radon being a noble gas in the transformation chain of ²³⁸U was thoroughly monitored as an environmental risk to habitants in Swedish households in the 1980's [5]. A large part of the Swedish building stock is composed by concrete. However, in response to environmental goals by the national authorities the increased use of crushed bedrock instead of glaciofluvial sediments may in part increase the risks. The ²³⁸U and ²³²Th content in the crushed bedrock is higher than in natural glaciofluvial material. According to Jelinek and Eliasson [6] glaciofluvial materials, especially sands, have lower thorium and uranium levels compared to equivalent bedrock that has not been physically or chemically broken down. This is due to leaching through percolation of water and natural sorting processes that "flushes" the radioactive isotopes out from the coarser fractions, whilst they are enriched in the finer particle size fractions (clay and silt) [6].

Stranden [7] presented in experiments that the important parameters of radon exhalation of building materials primarily are; permeability, porosity, moisture, pressure gradient and temperature of the material. Since the temperature and pressure gradient are factors that have been set equal in this study, permeability of the material and its porosity and moisture content are the remaining key parameters.

The permeability is in part related to the porosity of the material [7, 8, 9, and 10]. Using Fick's first law of mass transfer, a diffuse flow through a material under a steady state condition of a radon source concentration, can be determined. The porosity could be related to diffusion through a material [9] according to

$$p = D/D_e \quad (1)$$

where, D is the diffusion coefficient (m²/s) and D_e , the effective diffusion coefficient (m²/s). The effective diffusion coefficient relates to the air voids in the system, while the diffusion coefficient relates to the areal cross section of the (bulk) material investigated.

The radon diffusion coefficients can be expressed as the diffusion length L (m) as to give a measure of how much radon that are exhaled before 50 % of the radon is decayed. Using the radon decay constant λ (s^{-1}), the diffusion relates to the radon diffusion length according to

$$L = \sqrt{D/\lambda} \quad (2)$$

The relative humidity (RH) or moisture content within the concrete is also a key ingredient in the transport mechanism of radon [7, 11]. Particularly, it is interesting how this impact reflects upon the exhalation rate of radon during hydration. The influence of relative humidity and moisture content of concrete on the radon exhalation rate was examined and modelled by Cozmuta et al. [11] for a concrete receipt with a w/c-ratio of 0.38. Figure 1 presents the modelled curve of exhalation of radon as a function of relative humidity within the concrete.

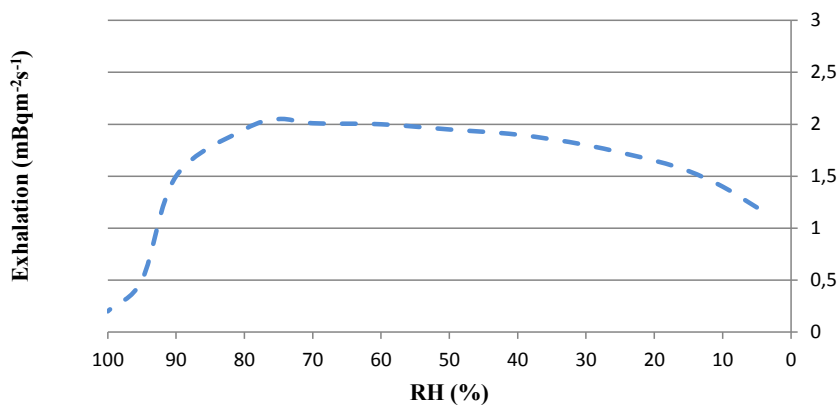


Figure 1 – The modelled curve demonstrates the very low radon exhalation rate at 100 to 90 % in relative humidity, meaning, very little radon escapes from the concrete surface, when the concrete is saturated (high moisture content). Based on [11].

Accordingly, an additive, that repels water droplets (hinders free transport –clogging the pores) from the concrete surface, may also have a direct effect of the permeability or diffusion rate within the concrete [8].

Measures to reduce radon in building materials have only been studied to a minor extent. Chauhan & Kumar [9] showed the potentials of reducing the radon gas exhalation rates from concrete using rice husk. Also Yu et al. [12] and Taylor-Lange et al. [13] demonstrated the possible measures of reducing the exhalation rate of radon gas from different concrete surfaces using supplementary cementitious materials, such as fly ash or metakaolin.

In this research a comparison of (i) a reference concrete, (ii) a reference concrete with an addition of a liquid additive (hydrophobant) as well as, (iii) a concrete with a supplementary cementitious material (SCM) added (fly ash) are made. The corrosion inhibitor and hydrophobant, X1002 Hycrete, is directly added to the water in the concrete recipe. The fly ash used is a class N – fly ash originating from E-mineral in Denmark.

2. METHODOLOGY

2.1 Radon exhalation rate and radon gas measurements

The principle makes use of a “closed system with a radon source enclosed”. As radon from the concrete product builds up within a sealed aluminum container a measure of the radon exhalation rate could be calculated for the first 24 hours. The codes adopted are defined in ISO Standard 11665-7 [14].

The radon gas exhalation rate E (Bq/m²h) is calculated knowing the initial conditions of the radon gas concentration in the “closed system” and within this project the linear regression model has been applied. The equation for the linear regression model [14] can be described as:

$$E = \frac{\{(C-C_0) \times V\}}{A \times t} \quad (3)$$

where: E = exhalation of radon gas (Bq/m²h), C = concentration of radon gas measured by the radon gas monitor (Bq/m³), C_0 = background concentration of radon gas at initiation (Bq/m³), t = time of duration (h), A = effective surface area of the sample (m²), V = volume of the container including hoses.

The Swedish Cement and Concrete Research Institute uses an ATMOS 33 (Figure 2), which is calibrated at a yearly basis at the Swedish Radiation and Safety Authority (in Swed. Strålsäkerhetsmyndigheten). The instrument is calibrated to a predefined level of 200 Bq/m³. A correction factor (F-factor) of 1.04 has been applied for all measurements.

The instrument uses an ionizing pulsation chamber, that measures the alpha decay of ²¹⁸Po. The decay of ²¹⁸Po has a distinct electric charge of 6 keV that could be counted and converted to ²²²Rn knowing the decay rates of ²²²Rn and ²¹⁸Po. Thus, the instrument displays the “radon level” in Bq/m³ in its display and numerical mean values are recorded and stored every 10 minutes. Consequently, a 24 hour recorded series always contains 144 mean values used for the regression analysis. The model neglects any back diffusion of the concrete [14]. To ensure good linearity during the first 24 hours of the measurement a large volume of air in relation to the exhalation area of the concrete is used.

Calculation of radon gas in indoor air within a room is according to guidelines in the Swedish legislation, Swedish National Board of Housing, Building and Planning [15] and their references to Åkerblom & Clavensjö [16]. Knowing the exhalation rate (E) of the construction material a finalized calculation of the radon gas level within a room can be completed. The calculated radon gas level (concentration in Bq/kg) within a room can be described as:

$$Cm = \frac{1}{(\lambda+n)} \times \frac{E \times A}{V} \quad (4)$$

where, Cm = radon level, concentration (Bq/m³) in the room, λ = radon decay constant, n = circulations of air/hour, E = exhalation rate of radon gas (Bq/m²h), A = surface of exhalation within the room (m²) and V = volume of the room (m³).



Figure 2 – The Atmos 33 (Atmos 12DPX) connected to the aluminum container. The hoses and connectors used are intended for high pressure gas flow (welding equipment). They are used as to ensure no leakage. The sealing of the containers is made with a butyl-aluminum tape that has been tested to ensure no leakage of radon.

2.2 Assessments

Concrete recipes

The concrete recipes contained identical constituents (aggregates, cement, water) where the only difference was (i) a contribution of an additive (Hycrete) to one recipe and, (ii) substitution of some Portland cement by fly ash (10 % wt. of binder content) to one of the concrete recipes.

Identical concrete cubes ($150 \times 150 \times 150$ mm) were cast and after demolding the cubes were cured in a water bath for one week. The cast cubes were thereafter stored in a conditioning room at 23°C and 50 % RH between all measurements. The measurements were conducted during a 22 month period encompassing five or six separate measurements for each concrete recipe.

A standard CEM II/A-LL 42.5 R (*Portland clinker cement with a portion of 6-20 % limestone and rapid hardening properties*) from the Skövde cement factory was used as binder. The component of air was set to approximately 1 %. A cement-content of 350 kg/m^3 was applied. The fly ash used originates from E-mineral (Denmark) and is categorized as B4 with fineness “N”. The efficiency factor, defined as k-value, was set to 1.

The recipe using an additive followed the recommendations of the manufacturer. The portion used was the recommended maximum dose of ~3 % (vol.) of the water content. Table 1 presents the recipes and proportions used.

Table 1 – Recipes and proportions (in kg/m³ and weight %) of the different constituents in the assessed concrete specimens.

| Constituents | Standard recipe | | Standard recipe + additive | | Standard recipe + fly ash | |
|---|-------------------|------------|----------------------------|------------|---------------------------|------------|
| | kg/m ³ | Weight (%) | kg/m ³ | Weight (%) | kg/m ³ | Weight (%) |
| Cement, CEM II | 350 | 15.4 | 350 | 15.3 | 315 | 11.8 |
| Crushed aggregate, 0/8 (75 wt %) | 1276.7 | 55.6 | 1277.7 | 56.0 | 1269.1 | 55.9 |
| Crushed aggregate 8/16 (25 wt %) | 425.6 | 18.7 | 425.9 | 18.7 | 423.0 | 15.8 |
| Water | 227.5 | 10.0 | 227.5 | 10.0 | 227.5 | 10.0 |
| Air | 0.01 (~1.5%) | 0.01 | 0.01 (~1.5%) | 0.01 | 0.01 (~1.5%) | 0.01 |
| Fly Ash - class N | | | | | 35 | 1.3 |
| Superplasticizer ¹ (sikament 56) | ~0.7 | 0.2 | ~0.7 | 0.2 | ~0.7 | 0.2 |
| Additive ¹ , Hycrete X1002 | - | | 10.5 | 2 | | - |
| Total | 2280.1 | | 2281.4 | | 2269.9 | |
| w/c ratio | 0.65 | | 0.65 | | 0.65 | |

¹ The additives sikament 56 and Hycrete X1002 are presented as “%” of cement binder weight.

Relative Humidity

Measurements were made using equipment from Vaisala Oy named Vaisala HM44. The equipment uses the variation in electric potential in the air due to the actual moisture content within the air (difference in conductivity) at a steady state temperature. A calibration kit, designed HMK 15 aided as to ensure limited drifting of the probes. The salts, LiCl and K₂SO₄, were chosen as to encompass the full span of relative humidity (11 to 98 % in RH at

approximately 20°C). Using calibration tables from Greenspan [17] an uncertainty less than 1.5 % was calculated for the probes before the first measurements were initiated.

The procedure to assess the relative humidity within the concrete could be defined as (i) a hole of 15 mm in diameter and 50 mm depth was drilled in each concrete cube 10 days after casting, (ii) black plastic tubes (hollow inside) were inserted into the drilled holes, (iii) a sealing epoxy were added between outside of plastic tubes and the concrete to ensure no leakage of air.

The measurements were conducted by inserting the probe inside the plastic tube and sealing it with a rubber gasket at the top (Figure 3). The probes were fixed in place for at least two days before the measurements were commenced according to recommendations [18]. The first measurements were made approximately two weeks after the concrete specimens were cast.

A supplementary control task was also conducted. The concrete specimens were also weighed within one day after measurement of their respective readings of the RH (Figures 4 and 5). This was conducted as to ensure that the measured relative humidity of the concrete specimens provided reasonably reliable values.



Figure 3 – Two of the three investigated concrete cubes (150 X 150 X 150 mm) sealed with aluminum tape on each side except the top. The figure also shows the plastic tubes on top as to measure the relative humidity. The current reading is 88.6 % in relative humidity using probe 7 at 23.9°C for the recipe containing an additive.



Figure 4 – The investigated concrete cubes resting on a carriage before measurement of their respective weight.

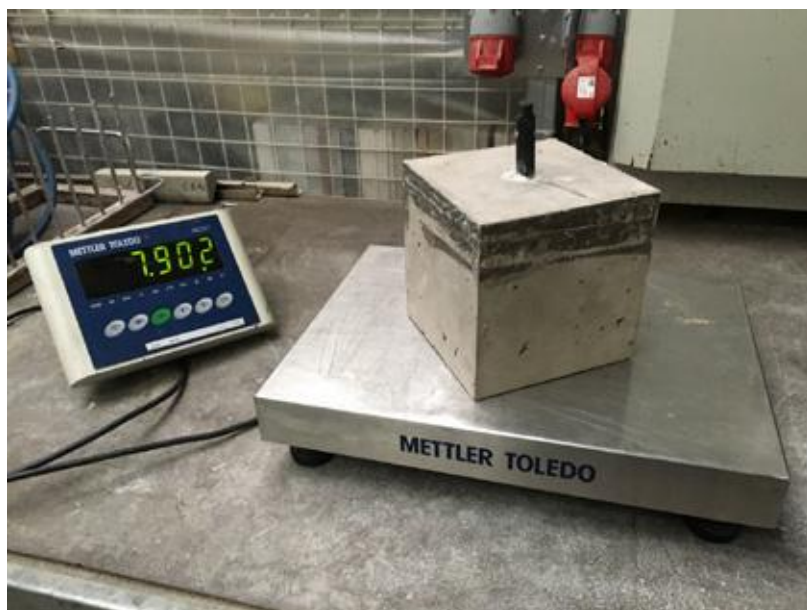


Figure 5 – Measurement of weight for one of the cast cubes. The same calibrated scalar from Mettler-Toledo was used for each weight measurement.

3. RESULTS

Figure 6 presents the measured radon exhalation rate of the three concrete recipes investigated as a function of time. The included error bars ($\pm 5\%$) originate from repetition measurements performed by Döse et al. [19] for similar recipes with the same w/c-ratio. The relative humidity as a function of time for each concrete cube investigated is also shown in Figure 7. A slight difference in their relative humidity could be observed after 22 months.

A distinct difference in exhalation rate between a standard recipe and a recipe using an additive or SCM is in general evident. An overall gross reduction of $\sim 30\text{-}35\%$ in the exhalation rate ($\text{Bq}/\text{m}^2\text{h}$) using an additive or SCM could be estimated for RH lower than $85\text{-}80\%$ (Figure 8)

But, the results of each concrete recipe are jittery and far from linear, particularly for readings where the relative humidity is high ($>80\text{-}85\%$ RH). However, in each measurement series a fairly low initial radon exhalation value is followed by a maximum. This is clearly evident in Figure 8 where the radon exhalation rate of the three concrete recipes investigated is presented as a function of the relative humidity.

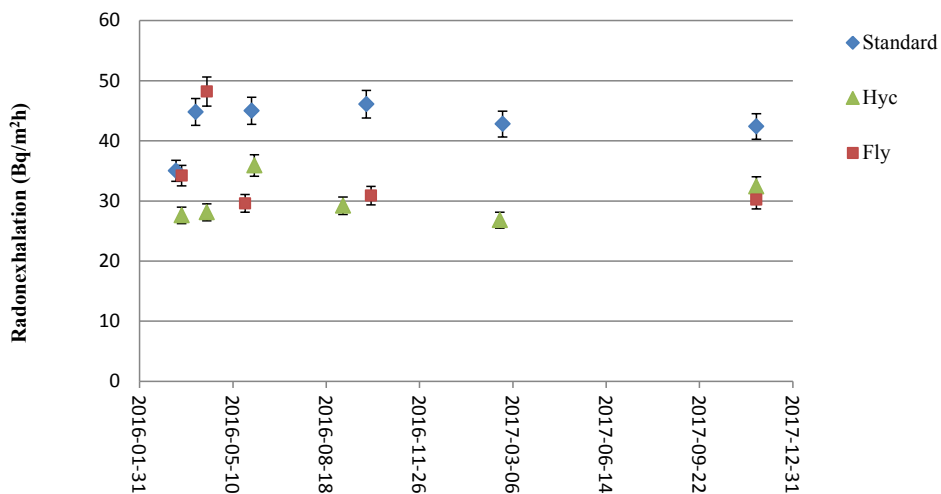


Figure 6 – The radon exhalation rate as a function of time (date) of the concrete recipe investigated. The error bars are $\pm 5\%$ [19].

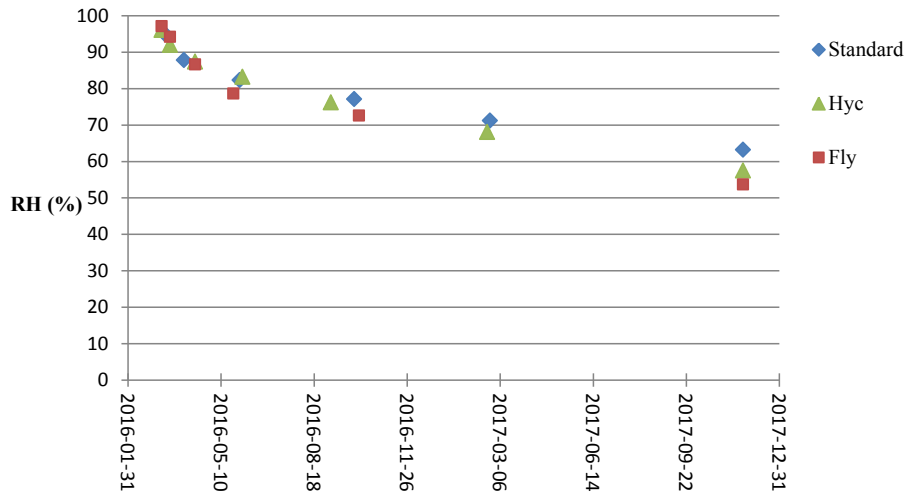


Figure 7 – The relative humidity as a function of time (date) for each concrete sample investigated.

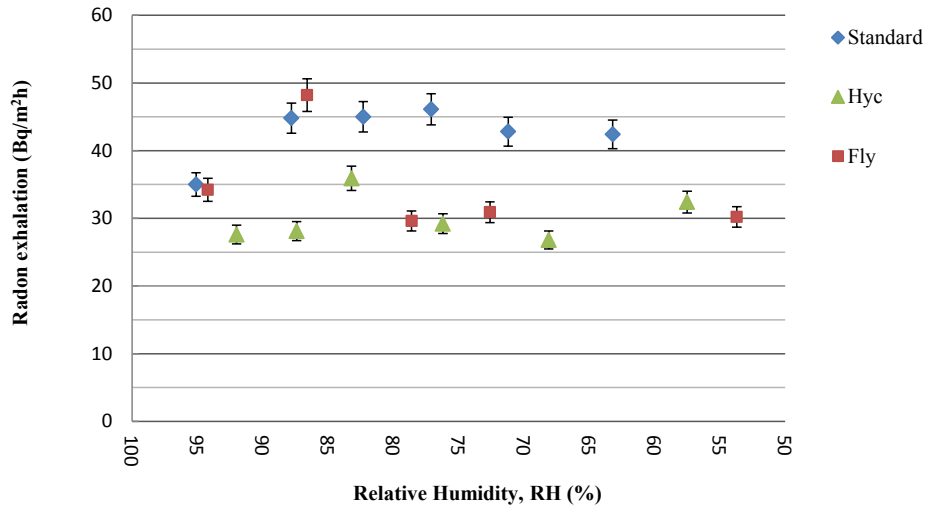


Figure 8 – The radon exhalation rate as a function of RH of the concrete samples investigated.

Control measurements of the concrete cubes’ masses were performed throughout the study. In Table 2, the measured initial length of the sides of the cubes, their initial and final masses and calculated volumes and densities are tabulated.

Table 2 – The initial and final mass, length of the cast cubes and their respective volume and density.

| Recipe | Mass, initial (kg) | Mass, final (kg) | Mass, loss (kg) | Length of sides of cubes | | | Volume (m ³) | Density (kg/m ³) |
|----------|-----------------------|---------------------|--------------------|--------------------------|-------|-------|-----------------------------|---------------------------------|
| | | | | A | B | C | | |
| Fly Ash | 7.368 | 7.238 | 0.130 | 0.150 | 0.150 | 0.149 | 0.0033 | 2201 |
| Standard | 8.016 | 7.911 | 0.105 | 0.149 | 0.151 | 0.151 | 0.0034 | 2378 |
| Hycrete | 8.010 | 7.902 | 0.108 | 0.150 | 0.151 | 0.151 | 0.0034 | 2340 |

Noticeably, the density of the concrete recipe containing fly ash is markedly lower than the densities of the other two recipes (Table 2). The other recipes also have slightly higher densities than designed. It is also apparent that the loss of water (mass) seemingly is greater for the recipe containing fly ash. In Figure 9 the density correction as the mass decrease during hydration for each recipe is shown. In Figure 10 the mass as a function of the relative humidity is presented. Using a polynomial function of 2nd order a strong r^2 -value can be demonstrated.

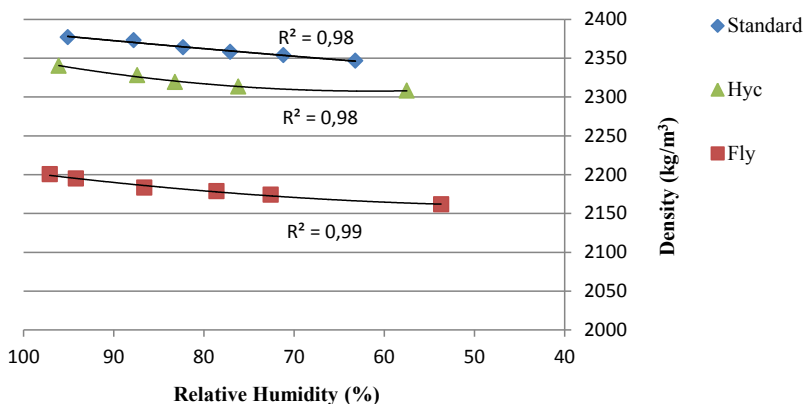


Figure 9 – The density of the concrete cubes as a function of the relative humidity for the three concrete cubes investigated.

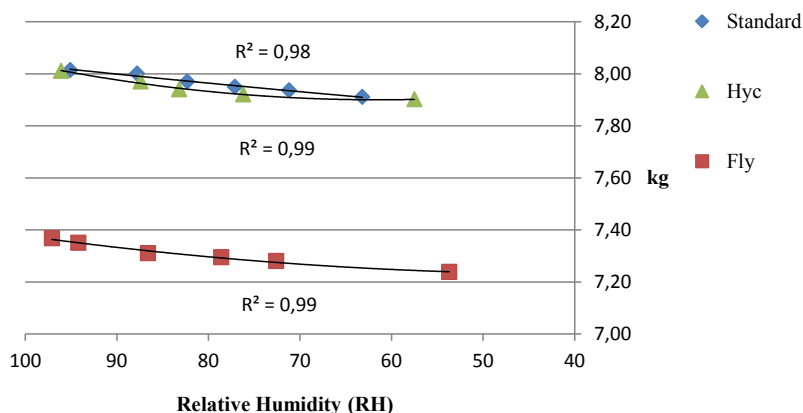


Figure 10 – The mass of the concrete cubes as a function of the relative humidity for the three concrete cubes investigated.

Figures 6 and 8 give an indication of a strong variation of the exhalation rate, especially the concrete recipe containing fly ash, at RH values > 85%. Seemingly a more reliable estimate of the mean radon exhalation rate could be achieved at RH values < 85-80 %. In Table 3, the exhalation rates for each concrete recipe and their ratios (difference) in percent (%) in relation to the standard recipe are presented.

Table 3 – The exhalation rates of the different concrete recipes and their ratios in relation to the standard recipe.

| Date | RH-Standard recipe (RH) | Radon exhalation - Standard (Bqh/m ²) | Radon exhalation - Fly ash (Bqh/m ²) | Radon exhalation - Hycrete (Bqh/m ²) | Difference in radon exhalation rate (%) - Fly ash/ Standard | Difference in radon exhalation rate (%) - Hycrete/ Standard |
|-------------------------|-------------------------|---|--|--|---|---|
| 2016-03-10 ¹ | 95.1 | 35 | 34 | 28 | 0.98 | 0.79 |
| 2016-04-06 ¹ | 87.8 | 45 | 48 | 28 | 1.08 | 0.63 |
| 2016-05-30 ¹ | 82.3 | 45 | 30 | 36 | 0.67 | 0.80 |
| 2016-09-20 ² | 77.1 | 46 | 31 | 29 | 0.67 | 0.63 |
| 2017-02-22 ¹ | 71.2 | 43 | - | 27 | - | 0.63 |
| 2017-11-22 ¹ | 63.2 | 42 | 30 | 32 | 0.71 | 0.76 |

¹Measurements of each recipe performed ± one week .²Measurements of each recipe performed ± two weeks.

4. DISCUSSION

The irregular pattern of radon exhalation rates displayed during the hydration process of in particular the recipe containing fly ash and in part the recipe containing a bulk additive (liquid) may have a sound explanation. For all recipes the initial (first) values measured had an RH in the interval 90-96 %. This is of interest in relation to the study made by Cozmuta et al. [11] where the exhalation rate for values in the range of 100-90 % in RH were modelled to be very low to moderate. This phenomenon is due to radon gas almost not being permeable in a water filled pore structure [11, 12] compared to air filled voids. The maximum levels of radon exhalation according to their study [11] were also in the range of an RH of 85-80 %. This seemingly corresponds satisfactorily to the current study. The reference concrete (Figure 7), in part, manifests their modelled behavior of the exhalation rate at different RH.

The difference in densities between the recipes could not be pleasingly explained. The standard recipe as well as the recipe containing fly ash deviates more than expected. The higher degree of evaporation of water (Table 2) of the fly ash recipe, however, may imply an added excess of water compared to the designed recipe that may in part explain the low w/c ratio. The difference in the measured densities between the standard recipe and the fly ash accounts for ~7 % wt. Radon exhalation is influenced by the density of a material and a material's density is proportional to the energy quantity "stopping power" [20], that could be defined as,

$$S = dE/dx \quad (5)$$

where S = stopping power (Mev/cm), dE is energy loss per traveled distance and dx is traveled distance

However, it is beyond the scope of this article to further elaborate on the density influence, but for concretes with a rather small difference between densities, the influence upon exhalation rate is considered negligible. For a deeper understanding the reader is advised to Isaksson & Rääf [21]. But, in short, an increased density yields a higher stopping power (MeV/cm) within a material (concrete), resulting in less radon being able to escape to the surface of a material. Consequently, if densities were set equal (as they were supposed to), the resulting radon exhalation difference between the investigated recipes would be even larger, than presented within this study. Significantly, and in view of the results, it could be seen that parameters, such as a materials permeability and porosity, hence have a much more substantial impact than the density difference observed between the concrete recipes.

The strong fluctuations of the radon exhalation rate at specifically, higher RH-values, are likely due to high initial porosities and loose pore structure of the concrete specimens in their initial stages of hydration. This favors a high transport rate [12]. This hypothesis is clearly demonstrated by Zhuqing & Guang [22], who through tests on cement pastes compared reference cement with admixtures containing fly ash during a two year period. This should be emphasized, especially for the binder mix containing fly ash (SCM), where the pozzolanic effect needs to initiate before a more consistent pore structure of the concrete is defined. This may explain the initial high values of the radon exhalation rate of the recipe containing fly ash.

De Jong [8] reported that an addition of fly ash in general reduces the general pore size, which is consistent with findings by Zhuqing & Guang [22], where the relative critical pore size of cement paste blended with fly ash is smaller than for reference cement paste after 90 days of curing and onwards. Setina et al. [23] reported similar conclusions where the use of micro silica

as a SCM reduced the total pore volume and also an overall smaller pore size compared to a reference concrete. Based on a series of experiments, also Keller et al. [24] reported that the use of fly ash gives a more dense concrete (better degree of compaction) and that the reduced pore size reduced the overall permeability of the concrete specimens. A decrease of the average pore size reduces the inter-connectivity between the pores and the permeability as a result. The current study seemingly supports this concept.

It is also the authors' belief that the rather small differences (in kg) in the input of aggregates between the concrete recipes should not have any remarkable influence upon the radon exhalation rate. Nor the substitutions of some fly ash instead of Portland cement. Even though the largest contribution of radium-226 and consequently radon resides from the aggregates, the minor difference between the recipes would not generate any significant change in the overall uranium (parent atom of radon production) content of the concrete cubes cast.

The liquid additive, Hycrete X1002, is a bulk additive that contains alkali-metal ions (sodium or potassium) in combination with carboxylic acid groups and polysiloxane constituents [25]. The product is protected by several US-patents [26-31]. Then general concept of bonding of a silane or polysiloxane to the concrete surface is in text and figures eminently explained by Selander in his doctoral thesis [32]. The initial key is to create a covalent bond of an inorganic substance to an organic. In brief, the hycrete bulk additive is added to the water, initiating a three stage process; (i) hydrolysis, followed by (ii) condensation and (iii) bonding [33]. In this process the alkoxy groups of the polysiloxanes generate a thin film (hydrophobic film) [33] that will swiftly bond to the cement, calcium-silicate hydrates (C-S-H) or aggregate surfaces. The carboxyl acid group (R-COOH) is strongly attracted to calcium at any surface, and the polymer (hydrophobic part) will subsequently position itself in close proximity to the surface [34]. This bonding with cement, or C-S-H or aggregate leads in turn to a reduced free transport of water and reduced breathability [33, 34] and hence also a reduced water absorption [34, 35]. The “hydrophobic film” acts in part as an impermeable layer [33]. This is caused by the large differences in surface tension of water and silicones ($72 \text{ mN} \times \text{m}^{-1}$ and $22 \text{ mN} \times \text{m}^{-1}$, respectively) and thus water cannot penetrate the film easily. However, as mentioned, the pore structure is still open, but with a lower diffusion coefficient [33].

V. Spaeth et al. [35] showed in experiments that this immediate contribution of a bulk additive as a result also delays the hydration of the C-S-H linkage. Selander et al. [34] demonstrated in a study with shotcrete the effect of adding a hydrophobic additive. The capillary absorption of the tested hydrophobic specimen with a w/c ratio of 0.55 was reduced by 85 % in relation to the reference concrete. Consequently, it is likely that the use of a hydrophobic product strongly reduces the diffusion length L of radon and less radon is able to reach the surface per unit time. As earlier described the diffusion length will consequently be much lower, indicating that only a part of the radon contained within the concrete cubes is able to reach the surface before it decays. In some recent experiments by Chauhan and Kumar [36], a concrete series using ordinary Portland cement with a w/c ratio of 0.45, and containing different additions of micro silica showed an interval of 0,02-0,13 m in radon diffusion length [36]. Meaning, most of the radon within the investigated cubes of this study would have been expected to contribute to the radon exhalation at the surface.

Though, the primary intent of the study was to investigate, whereas any differences could be observed in radon exhalation rate of three different concrete recipes, the study was not

thoroughly prepared. The lack of more study material (several concrete cubes of each recipe) in part hindered further examination of the diffusion rates of the concrete recipes or control measurements of the compressive strength of each material.

Secondly, since only one concrete cube of each recipe was studied, this statistically causes a relatively large uncertainty. Thus, further testing is emphasized and should be carried out before any definitive conclusions can be drawn. Nevertheless, a distinct trend in exhalation rate between the different recipes is noticeable for concrete specimens with a RH < 80-85 %.

Finally, the measurements depth for the RH may be addressed. The readings were made 50 mm into the concrete samples. This of course, does not reflect the relative humidity on the top surface, nor the core of the concrete cubes. The depth was chosen to be at least 50 mm into the concrete, to ensure reliable readings. Most certainly, the surface of the concrete will display slightly lower RH-values.

5. CONCLUDING REMARKS

In the current study it has been demonstrated a reduction of ~30-35 % of radon gas exhalation rate from concrete specimens using a liquid additive (Hycrete, X1002) or a SCM (fly ash) at relative humidity's <80-85 %. The use of SCM as a binder, also serves a mean to lower the overall use of Portland cement worldwide. This at the end generates a positive impact from an environmental aspect.

The effect of using a liquid additive or a SCM-material may have a strong impact on the radon gas exhalation rate of concrete and consequently the radon gas level within a room. Chauhan & Kumar [9, 36] demonstrated a similar effect using an alternative material such as rice husk and micro silica in different concrete recipes.

The reduction of radon exhalation rates also reduces the effective dose received by human beings. Using guidelines of ICRP [37], the reduction is equivalent to ~1.5-2 mSv per year. This is in relation to the reference value of the normal concrete specimen investigated and relates to the European reference room [38] where all walls, tile and floor are made of concrete.

The results demonstrate the significance and effectiveness of an additive and a supplementary cementitious material as an aid in reducing radon levels in building materials. Consequently, these material choices may be an optional way as to further limit the exhalation of radon. Further and more comprehensive studies are needed as to confirm and validate the initial assessments. Current studies are ongoing including several other liquid additives and supplementary cementitious materials in order to verify the initial results.

6. ACKNOWLEDGEMENTS

Special thanks to the Swedish Consortium for Financing Fundamental Research in the Concrete Area who has partly funded the research in the concrete area. Special thanks also to my colleagues at RISE CBI Betonginstitutet with guidance on the concrete castings produced.

REFERENCES

1. World Health Organization. “WHO Handbook on Indoor Radon: a Public Health Perspective,” World Health Organization, Geneva, Switzerland, 2009, 110 pp.
2. EC. “CPR - Regulation (EU) no 305/2011 of the European Parliament and of the Council Laying Down Harmonized Conditions for the Marketing of Construction Products and repealing,” Council Directive 89/106/EEC, *Official Journal European Union*, Vol. 88, 2011, pp. 5-43.
3. EC. “Council Directive 2013/59/Euroatom of 5 December 2013 Laying Down Basic Safety Standards for Protection against the Dangers Arising from Exposure to Ionizing Radiation, and repealing Directives 89/618/Euroatom, 90/641/Euroatom, 96/29/Euroatom, 97/43/Euroatom and 2003/122/Euroatom,” *Official Journal of the European Union*, Vol. 13, 2014, 73 pp.
4. Darby S, Hill D, Auvinen A, Barros-Dios JM, Baysson H, Bochicchio F, Deo H, Falk R, Forastiere F, Hakam M, Heid I, Kreienbrock L, Kreuzer M, Lagrade F, Mäkeläinen I, Muirhead C, Oberaigner W, Pershagen G, Ruano-Ravina A, Ruosteenoja E, Schaffrath Rosario A, Tirmarche M, Tomasek L, Whitley E, Wichmann H-E & Doll R: “Residential Radon and Lung Cancer: Detailed Results of a Collaborative Analysis of Individual Data on 7148 Persons with Lung Cancer, 14208 Persons without Lung Cancer from 13 Epidemiologic studies in Europe,” *Scandinavian Journal of Work, Environment and Health*, Vol. 32, 2006.
5. Mjönes L, Burén A, Swedjemark G A: “Radon Rates in Swedish Dwellings (Radonhalter i svenska bostäder),” *SSI-report-a 84-23*”, Stockholm, Sweden, 1984, 56 pp. (In Swedish).
6. Jelinek C & Eliasson T: “Radiation from Bedrock (Strålning från bergmaterial),” Geological Survey of Sweden, *SGU-report 2015:34*, Uppsala, Sweden, 2015, 26 pp. (In Swedish).
7. Stranden E, Kolstad A. K., Lind B: “The Influence of Moisture and Temperature on Radon Exhalation,” *Radiation Protection Dosimetry*, Vol. 7, No 1-4, 1984, pp. 55-58.
8. De Jong P & van Dijk W: “The Effect of the Composition and Production Process of Concrete on the ²²²Rn Exhalation Rate,” *Environmental International*, Vol. 22, 1996, pp. 287-293.
9. Chauhan R P & Kumar A: “Radon Resistant Potential of Concrete Manufactured Using Ordinary Portland Cement Blended with Rice Husk Ash,” *Atmospheric Environment*, Vol. 81, 2013, pp. 413–420.
10. Zhongnan S, Xiao X, Yanwen L, Jingna Y, Zhongyu H, Shizhao S, Lihong J, Weidong Z, Lijin X, Hongqiang Z, Jian Q, Wenzhan J, Tao Z, Liang H, Baohua W, Xiqiang L & Nan Z: “Experimental Exploration of the Waterproofing Mechanism of Inorganic Sodium Silicate-Based Concrete Sealers,” *Construction and Building Materials*, Vol. 104, 2016, pp. 276–283.
11. Cozmuta I, Van der Graaf E R & de Meijer R J: “Moisture Dependence of Radon Transport in Concrete: Measurements and Modeling,” *Health Physics*, Vol. 85, No. 4, 2003, Groningen, The Netherlands, pp. 438-456.
12. Yu K N, Young E C M, Stokes M J, Kwan M K & Balendran R V: “Radon Emanation from Concrete Surfaces and the Effect of the Curing Period, Pulverized Fuel Ash (PFA) Substitution and Age,” *Applied Radiation and Isotopes*, Vol. 48, No 7, 1997, pp. 1003-1007.
13. Taylor-Lange S C, Stewart J G, Juenger M C G & Siegel J A: “The Contribution of Fly Ash toward Indoor Radon Pollution from Concrete,” *Building and Environment*, Vol. 56, 2012, pp. 276-282.

14. ISO 11665-7. “Measurement of Radioactivity in the Environment — Air: Radon-222 — Part 7: Accumulation Method for Estimating Surface Exhalation Rate,” *International Standard* (ISO), First edition, Geneva, Switzerland, 2012, 23 pp.
15. Swedish National Board of Housing, Building and Planning: “The National Board of Housing, Building and Planning Regulatory Framework (Boverkets författningssamling),” BFS 2006:12 – BBR 12 (in Swedish), Karlskrona, Sweden, 2006, 44 pp. (In Swedish).
16. Åkerblom G & Clavensjö B: ”Book of Radon – Preventing Measures in New Buildings (Radonboken, förebyggande åtgärder i nya byggnader).” Formas, Stockholm, Sweden, 2004, 106 pp. (In Swedish).
17. Greenspan L: “Humidity Fixed Points of Binary Saturated Aqueous Solutions”. *Journal of Research of the National Bureau of Standards. A Physics and Chemistry*, Vol. 81a, No 1, 1977, pp. 89-95.
18. Åhs, M. ”Simulation of Moisture Measurements in Concrete with a Low w/c Ratio (Simulering av fuktmätning i betong med lågt vct),” TVBM; Div. of Building Materials, Faculty of Engineering, Lund University, Lund, Sweden, Vol. 3177, 2014, 46 pp. (In Swedish).
19. Döse M: “Ionizing Radiation in Concrete and Concrete Buildings – Empirical Assessment,” *Bulletin* 141, (*Licentiate Thesis*), Dept. of Civil and Architectural Engineering, School of Architecture and Built Environment, KTH Royal Institute of Technology, Stockholm, Sweden, 2016, 91 pp.
20. Isaksson M: “Basic Radiation Physics (Grundläggande strålningsfysik),” 2nd edition. Elanders, Studentlitteratur, Lund, Sweden, 2011, 330 pp.
21. Isaksson M & Råäf, C L: “Environmental Radioactivity and Emergency Preparedness,” CRC Press, Taylor & Francis Group, Florida, USA, 2016, 614 pp.
22. Zhuqing Y & Guang Y: “The Pore Structure of Cement Paste Blended with Fly Ash,” *Construction and Building Materials*, Vol. 45, 2013, pp. 30–35.
23. Setina J, Gabrene A & Juhnevicā I: “Effect of Pozzolanic Additives on Structure and Chemical Durability of Concrete,” *Procedia Engineering*, Vol. 57, 2013, pp. 1005-1012.
24. Keller G, Hoffmann B, & Feigenspan T: “Radon Permeability and Radon Exhalation of Building Materials,” *Science of the Total Environment*, Vol. 272, 2001, pp. 85-89.
25. Hycrete Inc.: “Material Safety data Sheet Hycrete X1002.” Hycrete Inc., p 3. www.hycrete.com
26. US-Patent 7261923. 2003. “Alkali Salt of Branched Dioic Acid and Defoamer; Post Surface Treating Construction Materials; Imparting Lasting, Effective Moisture Resistance”.
27. US-Patent 7381252. 2003. “Anti-Corrosion Admixture Composition for Concrete Compositions for Use in Reinforced Concrete Structures”.
28. US-Patent 7407535. 2006. “Compositions Containing a Disodium or Dipotassium C9-15 Branched Alken-1-Ylsuccinate for Treating Formed Concrete Structures; Despite Being Water Soluble the Treatments Deliver Improved Moisture Resistance”.
29. US-Patent 7498090. 2003. “A Material Such as Reinforced or Unreinforced Concrete Coated with a Disodium or Dipotassium Salt of an Unsaturated Dicarboxylic Acid, Such as Disodium Dodeceny succinate”.
30. US-Patent 7513948. 2006. “Autogenous Healing of Cracks in Concrete Structures”.
31. US-Patent 7670415. 2007. “Vapor Barrier for Porous Structures and System”.
32. Selander, A, “Hydrophobic Impregnation of Concrete Structures – Effects on Concrete Properties,” *Bulletin* 141 (*Doctoral Thesis*), Dept. of Civil and Architectural Engineering, School of Architecture and Built Environment, KTH Royal Institute of Technology, Stockholm, Sweden, 2010, 45 pp.

33. Roos M, König F, Stadtmüller S & Weyershausen B: “Evolution of Silicone Based Water Repellents for Modern Building Protection,” *Proceedings*, 5th International Conference on Water Repellent Treatment of Building Materials”, Brussels, Belgium, 2008, Aedificatio Publishers, pp. 3-16.
34. Selander A, Davant N & Malaga K: “Hydrophobic Shotcrete – a Method to Waterproof Tunnels,” *Proceedings*, Hydrophobe VII - 7th International Conference on Water Repellent Treatment and Protective Surface Technology for Building Materials, Lisbon, Portugal, 2014, pp. 67-75.
35. Spaeth V, Delplancke-Ogletree M P & Lecomte J P: “Hydration Process and Microstructure Development of Integral Water Repellent Cement Based Materials,” *Proceedings*, 5th International Conference on Water Repellent Treatment of Building Materials”, Brussels, Belgium, 2008, Aedificatio Publishers, pp. 245-254.
36. Chauhan R P & Kumar A: “Study of Radon Transport Modified with Silica Fume,” *Radiation Measurements*, Vol. 59, 2013, pp. 59-65.
37. ICRP. “Lung Cancer Risk from Radon and Progeny and Statement on Radon,” *ICRP Publication 115*, Ann. ICRP 40 (1), 2010.
38. CEN/TR 17113. “Construction Products - Assessment of Release of Dangerous Substances - Radiation From Construction Products - Dose Assessment of Emitted Gamma Radiation,” European committee for standardization, CEN, 2017, pp. 47.



DOI: 10.2478/ncr-2018-0003

ISSN online 2545-2819

ISSN print 0800-6377

© Article authors. This is an open access article distributed under the Creative Commons Attribution-NonCommercial-NoDerivs licens. (<http://creativecommons.org/licenses/by-nc-nd/3.0/>).

Received: Feb. 16, 2018

Revision received: April 19, 2018

Accepted: April 19, 2018

Frost Destruction of Concrete – A Study of the Validity of Different Mechanisms



Göran Fagerlund
Professor em.
Div. Building Materials
Lund Institute of Technology
Box 118
SE-221 00 Lund
E-mail: goran.fagerlund@byggtek.lth.se

ABSTRACT

Well-known frost destruction mechanisms applicable to concrete not exposed to salt are, (1) hydraulic pressure during freezing, (2) growth of ice-bodies in capillaries during freezing. Theories behind these mechanisms are presented. A third mechanism, ice expansion during heating of frozen concrete, is put forward. The validity of a certain mechanisms is discussed by analyzing its ability to explain experimental observations.

Key words: Frost damage mechanisms, hydraulic pressure, ice growth, thermal deformation

1. EXPERIMENTAL OBSERVATIONS

Investigations of the validity of a certain frost destruction mechanisms are best performed on specimens that are isolated from water exchange with the environment during freeze/thaw. Typical results of such experiments are seen in Figures 1-4. All these experimental observations must be explained by the destruction theory if this is to be valid.

1.1 Critical water content, critical air-pore spacing

The water content in concrete can be expressed in terms of degree of saturation, S , where $S = 0$ and $S = 1$ correspond to complete dryness and complete saturation (all pores including air-pores and pores in aggregate water filled). Above a certain critical degree of saturation damage occurs at freezing while no damage occurs below the critical value. The critical value is independent of the number of freeze-thaw cycles and rate of freezing but might be somewhat dependent on the lowest freezing temperature. The concept critical degree of saturation is discussed in detail in [1]. An example of the experimental determination of the critical degree of saturation is shown in Figure 1, published in [1]. Each specimen had an individual water content that was kept constant during the test.

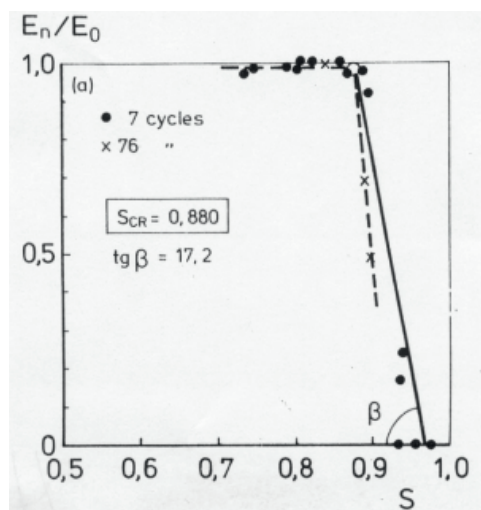


Figure 1 - Determination of the critical degree of saturation of an OPC-concrete with w/c-ratio 0.45 and 6% air. E_0 and E_n are the E-modulus before freeze/thaw and after n freeze/thaw cycles [1].

The critical degree of saturation will normally not be reached until a certain fraction of the air-pore system has been water-filled. The fact that the critical saturation exists indicates that there must exist a certain critical flow distance between places where water freezes and air-pores not filled by water. The critical flow distance is individual for each type of concrete but independent of the shape of the air-pore system. A theoretical analysis of the relation between the critical degree of saturation and the critical flow distance is performed in [2]. Analysis performed for an OPC-concrete with w/c-ratio 0.57 gave the critical flow distance 0.33 mm. The critical flow distance for other types of concrete might be somewhat different.

1.2 Effect of water content on length change

Figure 2 shows measurements of length changes during freezing and thawing of two moisture sealed cement pastes with the same w/c-ratio but with two different water contents. Temperature is measured in the Centre of the specimen. The amount of frozen water is only about 4 grams

higher in the paste with big expansion. The measurements were made in a combined calorimeter/dilatometer [3]. The following observations are made:

- Freezing is not initiated until pore water has been super-cooled to about -5°C . Then, temperature is rapidly increased to about -1°C at the same time as the specimen expands momentarily and reversibly.
- The specimen contracts more than normal thermal contraction when the water content is below the critical value.
- The specimen expands when the water content is above the critical value.
- At thawing, the expanded specimen maintains its expanded state, or even expands a bit further, until temperature has increased to about -10°C when big contraction occurs until the entire specimen is thawed.
- When the water content is above the critical value there is big permanent expansion of the specimen after complete thawing.

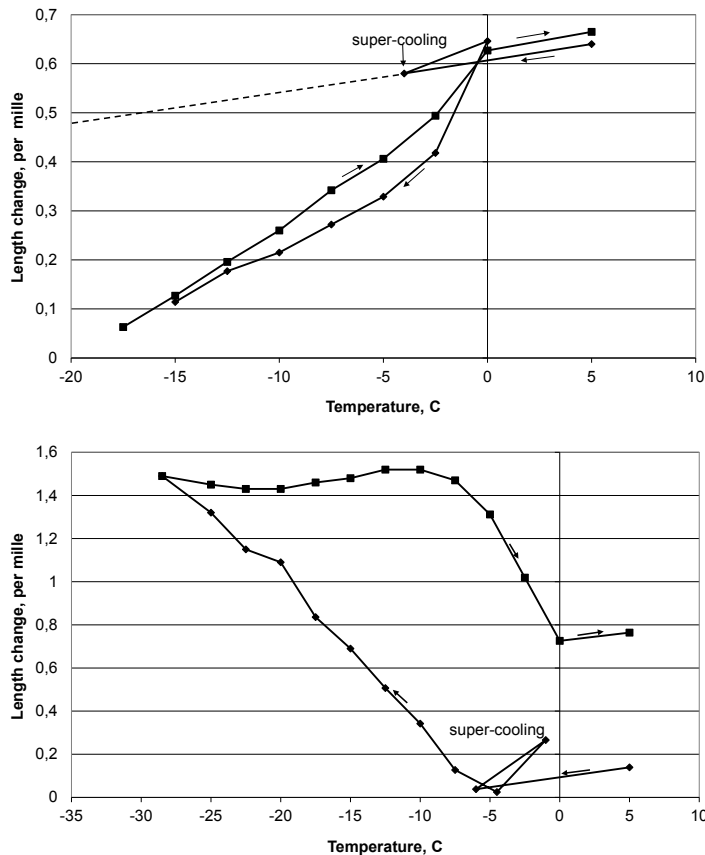


Figure 2 - Length change measurements during freezing and thawing of a non-air entrained cement paste specimen with w/c-ratio 0.83. Specimen volume, 100 cm^3 . Pore volume, 59 cm^3 . Temperature measured inside the specimen. Upper figure: Specimen saturation 0.83 which is below critical. Total volume of ice is 22 cm^3 at -10°C . Lower figure: Specimen saturation 0.90 which is above critical. Total volume of ice is 30 cm^3 at -27°C .

1.3 Effect of temperature curve and air on length change

Measurements of length changes of moisture sealed concrete specimens frozen and thawed in air are shown in Figure 3 [4]. Temperature was measured on the surface of the specimen. Temperature in the freezing cabinet was held constant at -15°C and -30°C during 12 hours. The specimen surface rapidly adopted the same constant temperatures. The following observations are made:

- *Non-air-entrained concrete with water content above critical:* the concrete expands during freezing. After 7 hours the specimen expands rapidly due to terminated super-cooling. At further cooling, expansion continues. When temperature is held constant at -15°C and at -30°C expansion immediately stops. When temperature continues to decrease, expansion continues.
- *Air-entrained concrete with water content below critical:* the concrete contracts during freezing. When temperature is held constant at -15°C and -30°C contraction immediately stops. When temperature continues to decrease, contraction continues.

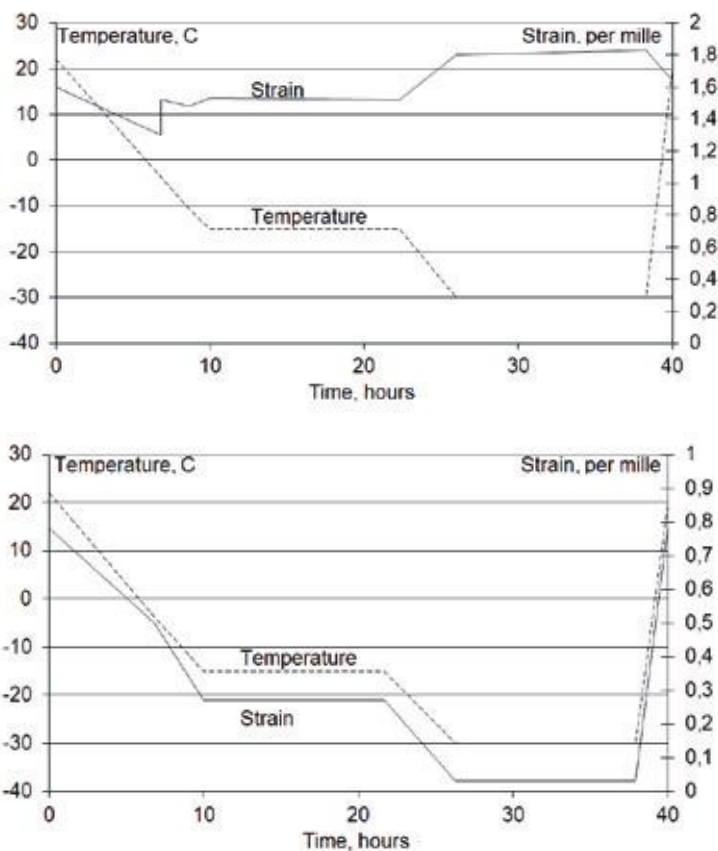


Figure 3 - Length changes versus temperature curve for concrete with water-cement ratio 0.60. Temperature measured on the specimen surface. Data from [4]. Upper figure: non-air-entrained concrete. Lower figure: air-entrained concrete, air content 6%.

More examples of this type of effect of the temperature curve on length change of moisture sealed concrete are found in [4].

1.4 Effect of temperature-time curve on ice formation

An example of the amount of ice in concrete as function of temperature and time is shown in Figure 4, [4]. The following observations are made:

- When temperature lowering halts, ice formation immediately stops
- When temperature lowering is resumed, ice formation immediately re-starts.

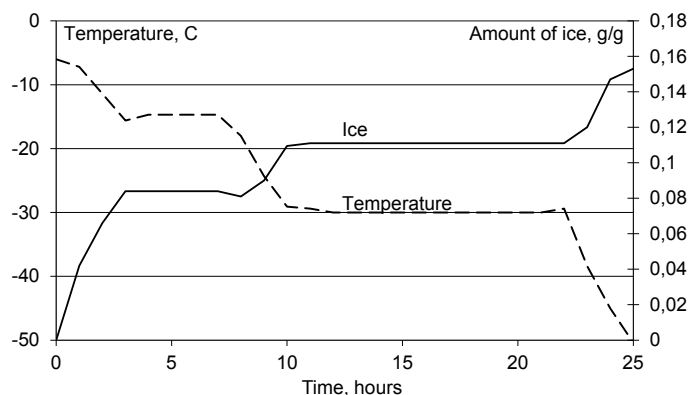


Figure 4 - Relation between temperature-time curve and ice formation. w/c-ratio 0.40. No air entrainment. Data from [4].

1.5 Hysteresis between ice formation and ice melting

A result of a calorimeter measurement of ice formation and melting is shown in Figure 5, [4]. Temperature was measured in the calorimeter compartment. The specimen temperature is somewhat higher during cooling and somewhat lower during heating due to time lag between calorimeter and specimen. There is big hysteresis between the amount of ice formed and ice melted at all temperatures. The reason is that water is super-cooled in isolated capillaries during the cooling phase while it melts at a temperature which corresponds to the pore radius. When temperature is about -45°C no super-cooling exists but water freezes homogeneously.

Results show that the rate of freezing has no influence on the amount of ice formed at a given temperature [4].

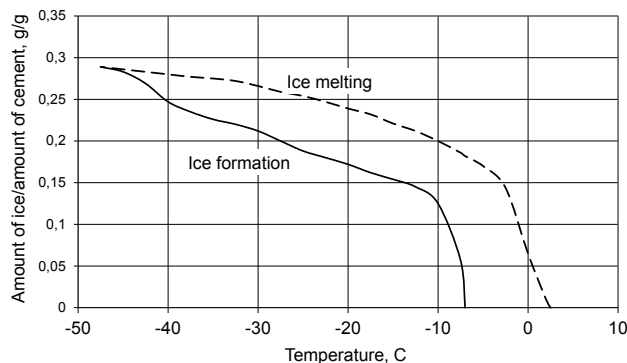


Figure 5 - Example of the hysteresis between ice formation and ice melting. w/c -ratio 0.60, no air entrainment. Freezing rate $3.6^{\circ}\text{C}/\text{h}$ and $7.8^{\circ}\text{C}/\text{h}$. Data from [4]. Temperature measured in the calorimeter compartment.

2. DESTRUCTION MECHANISM - HYDRAULIC PRESSURE

2.1 Theory

When water freezes in capillaries and in water-filled air-pores, excess water caused by the 9% increase in water volume when transformed into ice has to flow to the nearest air-filled spaces. There are two parts in the freezing process during which hydraulic pressure might be relevant:

Part 1: When temperature is gradually lowered after termination of super-cooling there will be a gradual increase in ice formation. The rate of ice formation is normally rather low, but permeability is also low due to ice formation. At high degree of saturation the only possibility for excess water to escape is through the narrow gel pore system since gel pore water is unfreezable. Increased amount of frozen water can therefore be accompanied by continuous expansion provided the water content is high.

Part 2: When initial super-cooling is interrupted, temperature rapidly increases and a certain amount of water freezes in a very short time.

Part 1: Gradually lowered temperature and increase in ice formation

Water transport takes place in a narrow and partly ice-filled pore system and it will exert pressure to the pore walls. Fracture occurs when the pressure exceeds the tensile strength of the cement paste. When this happens, the flow distance t exceeds a critical value t_{CR} (m). The mechanism was presented and discussed by Powers [5]. The model in Figure 6 is used for calculating the pressure and the critical flow distance.

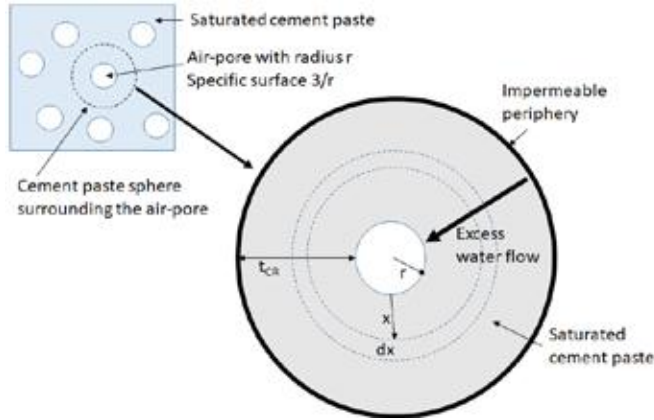


Figure 6 - Model for calculating the hydraulic pressure: saturated spherical cement paste shell with impermeable outer surface surrounding an empty spherical air-pore with radius r .

Water can only flow towards the void, since water outside the sphere has to move to voids in neighboring spheres. The rate of total excess water W_x (m^3/s) formed within the outer shell with thickness $t_{CR} - x$ is:

$$W_x = 0,09 \cdot \frac{dw_f}{d\theta} \cdot \frac{d\theta}{dt} \cdot \left[\frac{4\pi}{3} (t_{CR} + x)^3 - \frac{4\pi}{3} (r + x)^3 \right] \quad (1)$$

Where,

$dw_f/d\theta$ ice formation as function of the freezing temperature, $\text{m}^3/(\text{m}^3 \cdot \text{degree})$
 $d\theta/dt$ rate of temperature change in cement paste during freezing, degree/s
 t_{CR} the critical shell thickness, i.e. the critical flow distance, m

The area A_x (m^2) across which this flow takes place is:

$$A_x = 4\pi \cdot (r + x)^2 \quad (2)$$

Water flow creates pressure that is described by Darcy's law:

$$W_x = K \cdot A_x \cdot \frac{dP}{dx} A = \pi r^2 \quad (3)$$

Where,

dP/dx pressure gradient, Pa/m
 K permeability coefficient, $\text{m}^2/(\text{Pa} \cdot \text{s})$

Pressure is zero at the periphery of the void. It is highest at the outer periphery. Inserting values for W_x and A_x in Equation (1) and integrating over the shell thickness gives the following expression for the maximum pressure:

$$P_{max} = \frac{0,09 \frac{dw_f}{d\theta} \cdot \frac{d\theta}{dt}}{3K} \cdot \int_0^{t_{CR}} \frac{(r + t_{CR})^3 - (r + x)^3}{(r + x)^2} dx \quad (4)$$

The critical flow distance is obtained when max pressure equals the tensile strength f_t of the cement paste; $P_{max} = f_t$. Solution of Equation (4) gives the following expression for the critical flow distance (the radius r of the void is exchanged for its specific surface α , i.e. $r = 3/\alpha$):

$$t_{CR}^2 \left(\frac{t_{CR} \cdot \alpha}{9} + \frac{1}{2} \right) = \frac{f_t \cdot K}{0,09 \frac{dw_f}{d\theta} \cdot \frac{d\theta}{dt}} \quad (5)$$

The validity of the hydraulic pressure theory can be checked by introducing data for the parameters on the right hand side of the equation and thereby calculating the value of the critical flow distance. The calculated value is compared with the experimentally determined value. Agreement between the two values is an indication of the validity of the theory. There are three obstacles:

1. The critical flow distance must be known.
2. The specific surface of the air-filled part of the air-pore system when t_{CR} is reached must be known.
3. The permeability of the partly frozen cement paste must be known.

The critical flow distance can be calculated from an experimentally determined value of the critical degree of saturation. The calculation also gives the value of the “critical specific surface” α corresponding to the critical flow distance. The only information required is the air-pore size distribution. The method is described in [2]. The following critical specific surface was obtained for an OPC-concrete with water-cement ratio 0.57: $\alpha = 9.3 \text{ mm}^{-1} = 9.3 \cdot 10^3 \text{ m}^{-1}$. Inserting this value and the observed critical flow distance $0.33 \text{ mm} = 0.33 \cdot 10^{-3} \text{ m}$ gives:

$$9.2 \cdot 10^{-8} = \frac{f_t \cdot K}{0,09 \cdot \frac{dw_f}{d\theta} \cdot \frac{d\theta}{dt}} \text{ m}^2 \quad (6)$$

All parameters except the permeability can be experimentally determined. Uniaxial tensile strength of cement paste with w/c-ratio 0.57 is at least 6 MPa (tensile strength of the solid material on micro-level is about 200 MPa [7]). The strength is reduced by porosity, P , according to the following approximate relation $f_t \approx 200(1-P)^3 \text{ MPa}$, where $P \approx 0.6$. Thus $f_t \approx 12 \text{ MPa}$. This value is further halved due to possible effects of micro-defects). Experiments show that $dw_f/d\theta \approx 10^{-3} \text{ m}^3/\text{m}^3 \cdot \text{degree}$ [4]. This value is valid during a big temperature interval for a concrete with w/c-ratio 0.60 once the rapid ice formation after super-cooling has occurred, see Figure 5. The value is not influenced by the freezing rate, which was shown experimentally. The freezing rate used for determination of t_{CR} was $d\theta/dt \approx 10^{-3} \text{ degree/s}$ (3,6 degree/hour). This is representative for the freezing rate of outdoor air. Then, the following maximum permeability is needed for obtaining the actual observed critical flow distance:

$$K = \frac{9.2 \cdot 10^{-8} \cdot 0,09 \cdot 10^{-3} \cdot 10^{-3}}{6 \cdot 10^6} = 1.4 \cdot 10^{-21} \frac{\text{m}^2}{\text{Pa} \cdot \text{s}} \quad (7)$$

The only pores that are not blocked by ice when a large fraction of ice has been formed are the gel pores since water in these is not freezable. According to measurements by Powers [6] the permeability of gel pores at room temperature is $7 \cdot 10^{-11}$ darcy corresponding to $7 \cdot 10^{-20}$ $\text{m}^2/(\text{Pa} \cdot \text{s})$. The permeability is decreased at lowered temperature due to lower water viscosity. According to [8] the viscosity of super-cooled water at -20°C is 4 times higher than at $+20^\circ\text{C}$. Thus, the permeability of gel water at -20°C is about $2 \cdot 10^{-20}$ $\text{m}^2/(\text{Pa} \cdot \text{s})$. This value is 7 times higher than the required permeability according to the hydraulic pressure theory. One cannot exclude, however, that ice in capillaries blocks water transfer from gel pores before it can reach air-filled spaces, which makes permeability even lower than for un-blocked gel pores. Therefore, the calculation of the required permeability above does not necessarily contradict the hydraulic pressure theory.

Part 2: Interrupted super-cooling

Examples of interrupted super-cooling and the accompanied rapid increase of specimen length are seen in Figures 2 and 3. The expansion shown in Figure 2 for the cement paste specimen with high degree of saturation is immediately reversed when rapid ice formation ends, which indicates that the reason for expansion is hydraulic pressure. The super-cooling is about -6°C and the expansion about 0.2 %. The fact that contraction occurs shows that the expansion was not big enough to harm the specimen. Figure 3 (upper figure) shows big expansion of a concrete specimen when super-cooling is terminated at about -7°C . Also in this case the expansion is about 0.2%. This is of the same order as the fracture strain of concrete.

The amount of ice formed when super-cooling is terminated can be calculated from the “instantaneous” temperature rise when super-cooling is terminated. The process is almost adiabatic. The amount of ice formed within a materials volume V can then be calculated by:

$$W_f = \frac{\gamma_m \cdot c_m}{\rho_w \cdot \Delta h} \cdot \Delta T \cdot V \approx 0.006 \cdot \Delta T \cdot V \quad (8)$$

Where,

| | |
|------------|--|
| W_f | amount of frozen water, m^3 |
| ΔT | instantaneous temperature rise at termination of super-cooling, K |
| ρ_w | density of water, $1000 \text{ kg}/\text{m}^3$ |
| Δh | heat of fusion of water, $333 \cdot 10^3 \text{ J}/\text{kg}$ |
| γ_m | density of material, $\approx 2200 \text{ kg}/\text{m}^3$ |
| c_m | specific heat of material, $\approx 0.9 \cdot 10^3 \text{ J}/(\text{kg} \cdot \text{K})$ |
| V | materials volume within which ice formation is very rapid, m^3 |

All parameters on the right hand side, except volume V are known. ΔT is directly observed by the actual temperature-time curve. The volume of the specimen in Figure 2 is 10^{-4} m^3 (100 cm^3) and the temperature rise 5°C . Thus, the maximum amount of ice rapidly formed is $0.006 \cdot 5 \cdot 10^{-4} = 3 \cdot 10^{-6} \text{ m}^3$ or 3 cm^3 . This is about 6% of the total amount of water in the specimen. The volume expansion of this ice is $0.1 \cdot 3.6 = 0.36 \text{ cm}^3$. The observed volume expansion is $3 \cdot 0.2 \cdot 10^{-3} \cdot 100 = 0.06 \text{ cm}^3$. Thus, as expected, expansion due to hydraulic pressure is smaller than the expansion of water when it freezes.

Ice formation is initiated at some point in the specimen and is then spread by a velocity of about $10 \text{ mm}/\text{s}$ [9]. This means that all water in a fictitious sphere with radius r m

surrounding the point of nucleation is nucleated within time $r \cdot 1000/10 = 100 \cdot r$ s. The volume of this sphere is supposed to be equal to the actual specimen volume 10^{-4} m^3 , which gives a fictitious radius of $2.9 \cdot 10^{-2} \text{ m}$. The nucleation time is $100 \cdot 2.9 \cdot 10^{-2} = 2.9 \text{ s}$.

The average rate of ice formation in the sphere is:

$$\frac{dw_f}{dt} = \frac{W_f}{V} \cdot \frac{1}{\Delta t} = \frac{3 \cdot 10^{-6}}{10^{-4}} \cdot \frac{1}{2.9} = 10^{-2} \frac{\text{m}^3}{\text{m}^3 \cdot \text{s}} \quad (9)$$

This value is 10 000 times higher than the value in Part 1 above, which is: $dw_f/dt = 10^{-6} \text{ m}^3/(\text{m}^3 \cdot \text{s})$. The two freezing rates cannot be directly compared, however, since they are valid for different materials; cement paste with w/c-ratio 0.83 and concrete with w/c-ratio 0.57. It seems obvious, however, that the rate of ice formation is considerably higher when super-cooling is interrupted than when the more slow temperature change takes place thereafter. The reason why damage does not necessarily occur is that only a small amount of ice is formed and permeability therefore still rather high.

2.2 Relation to observations

The following observations can be explained by the hydraulic pressure theory:

- 1: The existence of a critical flow distance and hence the existence of a critical degree of saturation, Figure 1.
- 2: The fairly good relation between the experimentally determined and the theoretically calculated critical flow distance, Equation (6) and (7).
- 3: the rapid expansion followed by the rapid contraction when super-cooling is terminated, Figure 2 and 3.
- 4: The fact that air entrainment seems to have small or no effect on frost resistance of concrete with very low water-cement ratio [10]. The permeability of this type of concrete might be so low that water is freezing more or less as in a “closed container”. Theoretically, also a very small amount of freezable water might destroy concrete under such conditions.
- 5: The fact that porous coarse aggregate grains can destroy concrete during freezing.

The following observation seems to contradict the hydraulic pressure theory: when temperature is held constant no more ice is formed, Figure 4. Therefore, theoretically, hydraulic pressure should vanish and the specimen should contract. This does not happen however, Figure 3 (upper figure). A plausible explanation is that damage caused during freezing that precedes the halt in temperature lowering has caused so much damage to the concrete that contraction cannot take place. The fracture tensile strain of concrete is about 0.15 %. But as seen by Figure 3 the strain caused by freezing before the halt in temperature is about 0.2 %.

3. DESTRUCTION MECHANISM-EXPANSION OF ICE DURING THAWING

At heating of a frozen specimen damaged by frost, there might be a period of maintained expansion showing that there is no relaxation of tensile stresses. One example is seen in Figure 2 (lower figure); contraction caused by melting of ice does not start until temperature has been reduced to about -7°C . The reason behind this phenomenon must be the big hysteresis between

ice formation and ice melting, Figure 5. Thermal expansion of ice is higher than that of concrete. Therefore, thermal expansion of ice before it melts might cause damage.

The coefficient of thermal expansion of a frozen material containing ice, α , can be calculated by the following composite material expression:

$$\alpha = \frac{\alpha_i \cdot V_i \cdot E_i + \alpha_m \cdot V_m \cdot E_m}{V_i \cdot E_i + V_m \cdot E_m} \quad (10)$$

Where,

α expansion coefficient m/m

V volume fraction, m³/m³

E E-modulus, Pa

Indices i and m represent ice and unfrozen material.

Example 1:

The following data are valid for the cement paste in Figure 2 lower:

$\alpha_i \approx 50 \cdot 10^{-6}$ m/m, $\alpha_m \approx 10 \cdot 10^{-6}$ m/m, V_i and V_m vary with temperature, for -27°C the following values are approximately valid, $V_i = 0.30$, $V_m = 0.70$, $E_i \approx 10\text{GPa}$, $E_m \approx 3\text{GPa}$ ($E_m = 40(1-P)^3$ GPa [11], where P is paste porosity, which is about 60%). This gives:

$$\alpha = \frac{50 \cdot 10^{-6} \cdot 0.30 \cdot 10 \cdot 10^9 + 10 \cdot 10^{-6} \cdot 0.70 \cdot 3 \cdot 10^9}{0.30 \cdot 10 \cdot 10^9 + 0.70 \cdot 3 \cdot 10^9} = 33 \cdot 10^{-6}$$

This is more than the thermal expansion of cement paste containing no ice, which according to the contraction curve for temperature above 0°C is $10 \cdot 10^{-6}$ m/m. Additional expansion caused by ice during the temperature interval -27°C to -10°C for the specimen in Figure 2, provided no ice is melted, is:

$$\Delta\varepsilon = (33 - 10) \cdot 10^{-6} \cdot (27 - 10) = 0.39 \text{ per mille} \quad (11)$$

This is a high value. Therefore, one cannot exclude that ice expansion caused by heating will add to damage previously caused by freezing.

4. DESTRUCTION MECHANISM - PRESSURE FROM GROWING ICE

4.1 Principles

The principles for this mechanism were presented by Powers [12]. The mechanism is illustrated by Figure 7. At a certain instance below freezing temperature four water phases co-exist: (1) ice bodies completely filling coarser capillaries, (2) some ice in air-pores, (3) unfrozen water in very small capillaries and gel pores caused by freezing point depression and by super-cooling, (4) unfrozen gel water in saturated cement gel. The distance from ice in the capillary to the nearest air-pore is t . No consideration is taken below to geometrical arrangements of pores, ice and water.

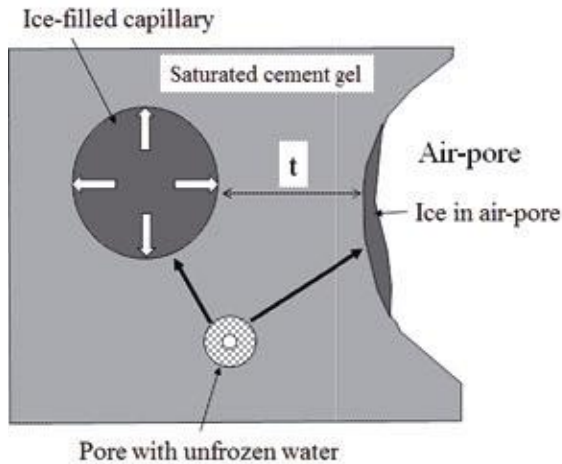


Figure 7 - Illustration of the destruction mechanism growing ice pressure. Unfilled arrows indicate pressure from growing ice. Filled arrows indicate water flow to ice bodies. The un-filled circle in pore with unfrozen water indicates drying caused by water transfer.

The system is supposed to be at equilibrium. When temperature is lowered by dT the free energy of ice and water is changed. However, free energy of stress-free ice will be lower than that of unfrozen water. The change in free energy at constant pressure is:

For unfrozen bulk water:

$$dG_w = \left(\frac{\partial G_w}{\partial T} \right)_P \cdot dT = -S_w \cdot dT \quad (12)$$

For bulk ice:

$$dG_i = \left(\frac{\partial G_i}{\partial T} \right)_P \cdot dT = -S_i \cdot dT \quad (13)$$

Where,

G_w and G_i free energy of super-cooled water and ice, J/mole

S_w and S_i entropy of unfrozen water and ice, J/(mole·K)

The difference in free energy is:

$$dG_T = (dG_w - dG_i) \cdot dT = (-S_w + S_i) \cdot dT \quad (14)$$

Example 2:

The absolute entropies at 0°C for unfrozen water and ice are, $S_w \approx 63$ J/(mole·K), $S_i \approx 41$ J/(mole·K). Temperature reduction $-\Delta T$ gives the following difference in free energy:

$$\Delta G_T = (-63 + 41) \cdot (-\Delta T) \quad (15)$$

In order to restore equilibrium, water will move from the water-filled pores towards ice bodies in ice-filled capillaries and towards ice in air-pores. The rate of water transfer is determined by

the difference in vapour pressure between super-cooled water and ice. This is about 26 Pa at -10°C and 22 Pa at -20°C . The water transfer takes part within the water-filled cement gel. Water is transformed into ice when arriving to the ice bodies causing these to grow and exert pressure to the pore walls. Water transfer does not stop until pressure in the ice has become so high that its free energy is equal to the free energy of unfrozen water. Before this happens the concrete might be fractured. Ice growth will also stop if water is exposed to sufficiently high under-pressure (suction). The distance water has to flow from water-filled capillaries to ice-filled capillaries is very short. Therefore, for normal freezing rates, new equilibrium is rapidly reached when temperature lowering is stopped. Consequently water transport and ice growth stops.

There are two scenarios:

1. The concrete stays completely water-saturated during the freezing process. This is valid for a structure that is exposed to unfrozen water during freezing, like a foundation exposed to frost at one part and at the same time sucking ground water at a lower part, or a in a dam where the downstream part freezes while the upstream part is exposed to unfrozen water. It will also be valid for fresh concrete where the surface part freezes while the inner part of the structure contains unfrozen mixing water.
2. The concrete is isolated so that no water can enter or leave during the freezing process. This is typical for most real structures and for specimens freeze-tested in the lab.

In both cases ice growth might take place simultaneously in capillaries and in air-pores.

4.2 Scenario 1: The concrete stays saturated. Ice growth in ice-filled capillaries

Ice pressure is transferred to the solid pore walls through a liquid water phase. Ice bodies confined in capillaries cannot grow freely so ice formation will cause pressure against pore walls and within the ice. Ice growth exerts pressure to the water phase which in turn transfers pressure to the solid pore wall. Ice pressure will increase the free energy of ice according to the Equation below:

$$dG_i = \left(\frac{\partial G_i}{\partial T}\right)_P \cdot dT + \left(\frac{\partial G_i}{\partial P}\right)_T \cdot dP_0 = -S_i \cdot dT + v_i \cdot dP_0 \quad (16)$$

Where,

dP_0 increase of compressive pressure in ice, N/m^2

v_i molar volume of ice, m^3/mole ($v_i=19.6 \cdot 10^{-6} \text{ m}^3/\text{mole}$)

$$dG_w = \left(\frac{\partial G_w}{\partial T}\right)_P \cdot dT + \left(\frac{\partial G_w}{\partial P}\right)_T \cdot dP_0 = -S_w \cdot dT + v_w \cdot dP_0 \quad (17)$$

The following relation is valid at equilibrium. (The relation is equivalent to the Clapeyron Equation):

$$\frac{\Delta P_0}{\Delta T} = \frac{(-S_w + S_i)}{v_i - v_w} \quad (18)$$

Example 3:

Temperature is decreased by 5°C from 0°C. Ice density and entropies are approximately constant during this small temperature change. The ice pressure when ice growth stops is:

$$\Delta P_0 \approx \frac{-63 + 41}{19.6 \cdot 10^{-6} - 18 \cdot 10^{-6}} \cdot (-5) = 68.8 \text{ MPa} \quad (19)$$

Thus, very high pressure must be exerted on ice in order to stop its growth.

Note: This high pressure will only appear when the ice body is enclosed in a completely rigid, incompressible and un-fractured pore (container). In reality, the material will be fractured long before this pressure is reached.

4.3 Scenario 2: The concrete is moisture isolated. Ice growth in capillaries

In the normal case there is no ingress of water from outside during freezing. Water transfer to ice-bodies in capillaries will therefore cause drying of pores containing unfrozen water. This will increase the hydrostatic tension in water, decreasing its free energy:

$$dG_{w,d} = - \left(\frac{\partial G_w}{\partial P} \right)_T \cdot dP_w = -v_w \cdot dP_w \quad (20)$$

Where,

$dG_{w,d}$ change of free energy of water caused by drying, J/mole

dP_w increase of hydrostatic tension in water, N/m²

v_w molar volume of water, m³/mole ($v_w=18 \cdot 10^{-6}$ m³/mole)

The free energy of water is changed to:

$$dG_w = -S_w \cdot dT + v_w \cdot dP_0 - v_w \cdot dP_w \quad (21)$$

The free energy of ice, Equation (16), is unchanged. Equilibrium occurs when:

$$-S_w \cdot dT + v_w \cdot dP_0 - v_w \cdot dP_w = -S_i \cdot dT + v_i \cdot dP_0 \quad (22)$$

Hydrostatic tension can be expressed in terms of relative humidity:

$$P_w = - \frac{R \cdot T}{v_w} \cdot \ln \phi \quad (23)$$

Where,

R the gas constant, 8.314 J/(mole·K)

T absolute temperature, K

ϕ Relative Humidity (RH)

Inserting this value in Equation (22) gives the following pressure at equilibrium:

$$\Delta P_0 = \frac{(-S_w + S_i)}{v_i - v_w} \cdot \Delta T + \frac{8.314 \cdot T}{v_i - v_w} \cdot \ln \phi \quad (24)$$

Example 4:

Temperature is decreased by 5°C from 0°C. As in Example 3 relative humidity is changed to 0.97. Ice pressure in a completely rigid, incompressible ice-filled pore (container) becomes:

$$\Delta P_0 = \frac{(-63 + 41)}{(19.6 - 18)10^{-6}} \cdot (-5) + \frac{8.314 \cdot 268}{(19.6 - 18)10^{-6}} \cdot \ln 0.97 = 26 \text{ MPa} \quad (25)$$

The calculation shows that even small drying might substantially reduce ice pressure. According to the equation, water flow stops when RH is reduced to 95%. Drying will cause the cement paste to contract which will compensate for ice expansion. Lowering temperature further will cause bigger reduction of hydrostatic pressure causing bigger contraction.

4.4 Ice growth in air-pores

Water is also transferred towards ice contained in air-filled air-pores by the same mechanism as water flow to capillary ice. Air-pore ice can, however, grow in stress-free condition.

Concrete stays saturated

Ice growth will continue as long as temperature is reduced since no ice pressure is built up.

Concrete is moisture isolated

Ice growth in air pores will stop when the hydrostatic tension in unfrozen pore water is sufficiently big. Ice is not exposed to pressure. Its free energy is given by Equation (13). Free energy of water is affected by hydrostatic tension. It is:

$$dG_w = -S_w \cdot dT - v_w \cdot dP_w \quad (26)$$

The condition for stop of ice growth, $G_i = dG_w$, becomes:

$$\frac{\Delta P_w}{\Delta T} = \frac{-S_w + S_i}{v_w} \quad \text{or} \quad \ln \phi = -\frac{P_w \cdot v_w}{8.314 \cdot T} \quad (27)$$

Example 5:

Temperature is decreased by 5°C from 0°C. Ice growth stops when the hydrostatic tension in pore water and the remaining relative humidity are:

$$P_w = \frac{-63 + 41}{18 \cdot 10^{-6}} \cdot (-5) = 6.1 \text{ MPa} \quad (29)$$

$$\ln \phi = -\frac{6.1 \cdot 10^6 \cdot 18 \cdot 10^{-6}}{8.314 \cdot 268} \quad \phi = 0.95 \quad (30)$$

4.5 Relation to observations

The following observations can be explained by the ice growth theory:

1: The existence of a critical flow distance and therefore a critical degree of saturation. Since ice growth in air-pores may occur in stress-free condition water transfer will primarily go towards air-pore ice. The shorter the distance between air-pores, the smaller the pressure built up in capillaries. Since free energy of ice under pressure is higher than that of stress-free ice it might also be that pressure in ice initially formed in capillaries will be gradually reduced. Hypothetical curves of ice pressure versus air-pore spacing are shown in Figure 8. Unfortunately it is difficult to express the critical distance theoretically in similar manner as was the case for hydraulic pressure.

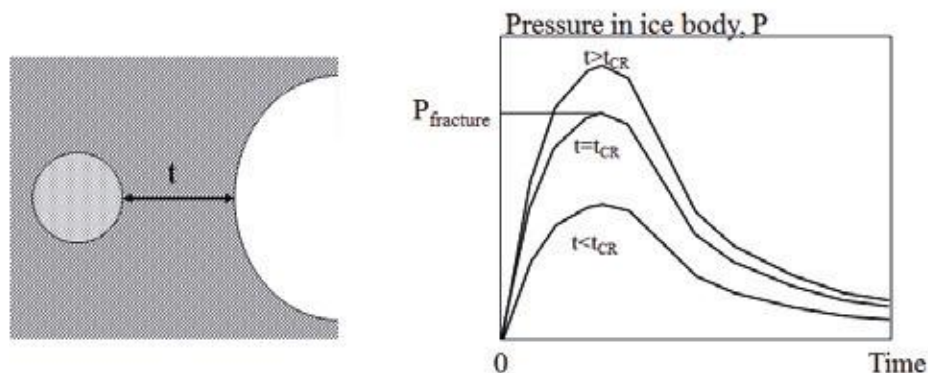


Figure 8 - Hypothetical pressure time curves for different values of the distance t between an ice-filled pore and the nearest air-filled pore.

2: The fact that expansion of moisture insulated concrete containing water content above critical stops when temperature is held constant. As seen by Figure 4 ice formation stops when temperature is held constant.

3: The fact that contraction takes place when water content is below critical, Figure 2 (upper figure) and Figure 3 (lower figure). According to theory, drying caused by transfer of water to ice would cause contraction. However, drying before ice growth stops is rather small as calculated by Equation (24) and could therefore hardly explain the big contractions observed. An alternative explanation to the big contraction is the composite material model described in paragraph 3, viz. the fact that the contraction coefficient of ice is bigger than that of unfrozen material, Equation (10). This is demonstrated by Examples 6 and 7.

Example 6:

The following data are valid for the cement paste in Figure 2 (upper figure): V_i and V_m vary with temperature, for -10°C the following values are approximately valid, $V_i = 0.22$, $V_m = 0.78$, $E_i \approx 10\text{GPa}$, $E_m \approx 3\text{GPa}$. This gives:

$$\alpha \approx \frac{50 \cdot 10^{-6} \cdot 0.22 \cdot 10 \cdot 10^9 + 10 \cdot 10^{-6} \cdot 0.78 \cdot 3 \cdot 10^9}{0.22 \cdot 10 \cdot 10^9 + 0.78 \cdot 3 \cdot 10^9} = 29 \cdot 10^{-6} \quad (31)$$

Thus, the contraction coefficient for frozen cement paste is about 3 times higher than that of unfrozen material. But, the observed contraction coefficient is also about $30 \cdot 10^{-6}\text{m/m}$. This means that most of the contraction coefficient observed might depend on contraction of ice and not on drying caused by water transfer to ice in capillaries or air-pores.

Example 7:

An additional example of this composite material effect is seen in Figure 9 showing the temperature time curve of a hard-burnt clay brick frozen below its critical degree of saturation. This is a material with negligible moisture shrinkage, but despite this the thermal shrinkage at minus temperature is big. The following data are valid: $V_i = 0.21$ (all ice is formed in the interval 0-5°C), $V_m = 0.79$, $E_m = 20$ GPa, $\alpha_m = 8$ GPa. The theoretical contraction coefficient at freezing temperature is:

$$\alpha \approx \frac{50 \cdot 10^{-6} \cdot 0.21 \cdot 10 \cdot 10^9 + 8 \cdot 10^{-6} \cdot 0.79 \cdot 20 \cdot 10^9}{0.21 \cdot 10 \cdot 10^9 + 0.79 \cdot 20 \cdot 10^9} = 13 \cdot 10^{-6} \frac{m}{m} \quad (32)$$

This is 60% higher than for unfrozen material. The observed contraction coefficient of frozen material is $15 \cdot 10^{-6}$ m/m.

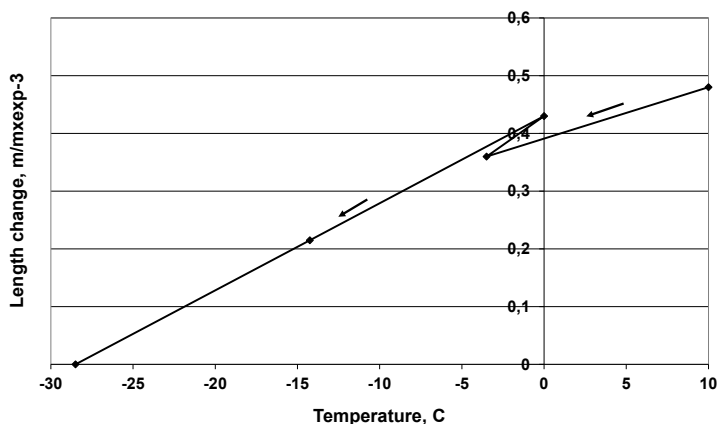


Figure 9 – Length change-temperature curve of hard-burnt clay brick during freezing. Degree of saturation is 0.68. Critical degree of saturation is 0.75. Porosity is 0.31.

4.6 Effect of the water-cement ratio

The amount of unfrozen water required for ice growth in concrete with water content high enough to cause frost damage is big for all w/c- ratios, see Table 1. However, the water flow needed for ice growth to stop by high water under-pressure is more restricted the lower the w/c-ratio. Water transport needed for decreasing relative humidity from 100% to 95% and 90% are given in Table 1.

Table 1- Unfrozen water, w_{nf} kg/m³ at -10°C based on measurements in [13]. Moisture flow Δw kg/m³ required to lower RH to 95% and 90%. Based on desorption isotherms in [14].

| w/c | w_{nf}/c ¹⁾ | | moisture flow to reduce RH in pores, $\Delta w/c$ | |
|-----|--------------------------|--------------------------------------|---|-------------|
| | undried ²⁾ | dried and re-saturated ³⁾ | 100% to 95% | 100% to 90% |
| 0.3 | 0.19 | 0.09 | 0.02 | 0.03 |
| 0.4 | 0.26 | 0.12 | 0.04 | 0.06 |
| 0.6 | 0.36 | 0.18 | 0.09 | 0.13 |
| 0.8 | 0.42 | 0.23 | 0.16 | 0.22 |

1) c is the cement content, kg/m³.

- 2) Saturated, never dried.
- 3) Pre-dried at +105°C and then re-saturated.

Normal cement content for concrete with w/c-ratio 0.30 is about 500 kg/m³. Therefore, according to Table 1, the water flow from 100% to 95% RH is 10 liter/m³. The volume expansion when this water freezes is 1 liter/m³ which gives a volume expansion of concrete of 1‰ when it is completely saturated. For concrete with w/c-ratio 0.4, 0.6 and 0.8 and cement contents 400, 300 and 250 kg/m³ the volume expansions are round 1.6, 2.7 and 4.0‰. Thus, it seems as the ice growth mechanism might have biggest effect for concrete with normal w/c-ratio, and will be of less importance for high performance concrete with very low w/c-ratio.

5. CONCLUSIONS

The following frost destruction mechanisms are presented and discussed:

- 1: Hydraulic pressure occurring when excess water formed by the 9% volume increase of water when transformed into ice is forced through a narrow and partly ice-filled pore system.
- 2: Ice growth caused by transfer of unfrozen water to ice bodies in capillaries.
- 3: Volume expansion of ice during thawing due to hysteresis between ice formation and ice melting.

The validity of different destruction mechanisms is tested by confronting the theories with experimental results.

Both the hydraulic pressure mechanism and the ice growth mechanism predict the existence of a critical flow distance from the place where ice formation takes place to the nearest air-filled pore. This means that critical water contents exist, that besides the critical distance depend on the air-pore size distribution. An example is shown in Figure 1. In a previous article the critical distance was experimentally found to be 0.33 mm for a concrete with w/c-ratio 0.57, [2]. A theoretical analysis based on the hydraulic pressure mechanism, Equation (5), using measured and realistic data for tensile strength, rate of ice formation and permeability gives a value of the critical flow distance that is of the same order as the observed value. This is an indication of the validity of the hydraulic pressure mechanism. Hydraulic pressure will explain the rapid expansion when super-cooling is interrupted, Equation (9).

Ice growth in capillaries is caused by the appearance of a difference in free energy between ice and unfrozen water, when temperature is lowered. In theory, ice pressure might be high enough to destroy the concrete, particularly if the concrete has possibility to absorb water during the freezing process. For normal moisture conditions, where the structure is protected from moisture uptake during freezing, water transfer to ice-bodies will cause the cement paste to dry. Therefore, hydrostatic tension will appear in unfrozen water, which will reduce pressure and even stop it after rather small drying. Thus, the ice growth mechanism might be most important for concrete with limited moisture shrinkage, Table 1. The fact that concrete that is unharmed by frost contracts more than normal during freezing is often explained by the drying effect caused by water transfer to ice. It is shown that an additional, and possibly more plausible reason for contraction, might be thermal contraction of ice in pores. Ice in air-pores will grow in stress-free condition and will therefore reduce ice growth in capillaries. Air will therefore protect concrete.

When frozen concrete is heated, un-melted ice in the pore system will expand and possibly cause damage to the concrete. A theory for this is given, Equation (10). The reason why ice is

present during a big part of the warming process is the big hysteresis between ice formation and melting caused by local super-cooling of water in pores.

Comments:

The theories presented above relate to freezing in a salt-free environment. Then, damage does primarily take place inside the concrete. When concrete is exposed to salt from outside, like in a salt scaling test, damage does normally take place on the surface as scaling. The theories presented may, however, still be applicable provided the effect of salt ions in pore water is introduced in the theories. Moreover, consideration must also be taken to water and ion flow across the concrete surface during freeze/thaw. A thorough discussion of the salt scaling mechanism is performed in [15].

REFERENCES

1. Fagerlund G: “A service life model for internal frost damage in concrete,” *Report TVBM-3119*, Div. of Building Materials, Lund Institute of Technology, Lund, Sweden, 2004.
2. Fagerlund G: “The critical flow distance at freezing of concrete – theory and experiment,” *Nordic Concrete Research*, No. 56, 2017, pp. 35-53.
3. Fagerlund G: “Significance of critical degrees of saturation at freezing of porous and brittle materials,” *Special Publication SP-47-2 “Durability of Concrete,”* American Concrete Institute. Detroit, USA, 1973.
4. Fridh K.: “Internal frost damage of concrete. Experimental studies of destruction mechanisms,” *Report TVBM-1023*, Div. of Building Materials, Lund Institute of Technology, Lund, Sweden, 2005.
5. Powers T.C.: “The air requirement of frost-resistant concrete,” *Highway Research Board Proceedings*, No 29, 1949, pp. 184-202.
6. Powers T.C.: “Structure and physical properties of hardened Portland cement paste,” *J. American Ceramic Soc.*, Vol 41, 1958.
7. Qian Z., Ye G., Schlangen E., van Breugel K.: “Modeling fracture behaviour of cement paste based on its microstructure”, *Proceedings*, 4th Int. Workshop of Young Doctors in Geomechanics. 21-23 Nov. 2012. École des Ponts, Paris Tech., Paris, France.
8. Zwolinsky B.J. & Eicher L.D.: “High-precision viscosity of super-cooled water and analysis of the extended range temperature effect,” *J. Phys. Chem.*, 71(13), 1971.
9. Helmuth R.A.: “Capillary size restriction on ice formation in hardened Portland cement paste,” *Proceedings*, 4th Int. Symposium on Chemistry of Cement. Vol II. Nat. Bureau of Standards, Washington DC., USA, 1960.
10. Malhotra M.V., Painter K.A., Bilodeau A.: “Mechanical properties and freezing and thawing resistance of high strength concrete incorporating silica fume,” *Cement, Concrete and Aggregate*. Vol 9, No 2. ASTM, Washington DC., USA, 1987.
11. Helmuth, R.A., Turk, D. Elastic moduli of hardened Portland cement paste and tricalcium silicate pastes. *Highway Research Board*, Special report 90, 1966.
12. Powers T.C: “Resistance of concrete to frost at early ages,” *Proceedings*, RILEM Symposium on Winter Concreting, Copenhagen, Denmark, 1956. The Danish National Institute of Building Research. Session C, General report, pp 1-50.
13. Vuorinen J.: “On determination of effective degree of saturation of concrete,” Concrete and soil laboratory, Imatran Voima OY. Oulu, Finland, 1973.
14. Nilsson L-O.: “Fuktproblem vid betonggolv” (“Moisture problems in concrete floors”), *Report TVBM-3002*, Div. of Building Materials, Lund Institute of Technology, Lund, Sweden, 1977. (In Swedish.)

15. Lindmark S.: “Mechanisms of salt frost scaling of Portland cement-based materials: Studies and hypothesis,” *Report TVBM-1017*, Div. of Building Materials, Lund Institute of Technology, Lund, Sweden, 1998.



DOI: 10.2478/ncr-2018-0004

ISSN online 2545-2819

ISSN print 0800-6377

© Article authors. This is an open access article distributed under the Creative Commons Attribution-NonCommercial-NoDerivs licens. (<http://creativecommons.org/licenses/by-nc-nd/3.0/>).

Received: March 18, 2018

Revision received: May 15, 2018

Accepted: May 15, 2018

Full-scale Test of an Unreinforced Concrete Dome Plug for the Spent Nuclear Fuel Repository



Richard Malm
Ph.D., Researcher
KTH Royal Institute of Technology
Division of Concrete Structures
SE-100 44 Stockholm
e-mail: richard.malm@byv.kth.se

ABSTRACT

In the planned Swedish repository for spent nuclear fuel, plugs are designed to close the deposition tunnels. The outer part of these plugs consists of a concrete dome made with self-compacting-concrete, designed to have low pH to reduce negative effects on the bentonite clay buffer. A full-scale test has been performed to evaluate the performance of the plug, to test the installation and to verify underlying design assumptions. In this paper, the behaviour of the concrete dome is evaluated based on measurements, from casting the concrete until it was subjected to 4 MPa hydrostatic water pressure.

Key words: Nuclear, full-scale testing, concrete plug, shrinkage, cooling.

1. INTRODUCTION

1.1 The Swedish nuclear repository

The Swedish Nuclear Fuel and Waste management Co (SKB) is responsible for developing the repository for spent nuclear fuel in Sweden. In the proposed concept for deposition, called KBS-3, the spent fuel will be installed in copper canisters with iron inserts. These will be placed in the crystalline rock at depth of about 500 m below ground in the repository in Forsmark. The canisters are placed in vertical holes in floor of the deposition tunnels and are enclosed with a pre-packed bentonite buffer. After all canisters are installed in a deposition tunnel, the tunnel will be filled with the pre-packed bentonite backfill. At the tunnel entrance, a plug will be placed as a temporary closure to allow for further deposition in the other deposition tunnels as

seen in Figure 1. In total, about 100 deposition tunnels are planned to be built in the repository. The designed life-span of these plugs is only during the operation period of the repository, i.e. maximum of 100 years. When all deposition tunnels are backfilled and plugged, the adjacent main tunnel will also be filled with bentonite clay and in the end, all tunnels and shafts will be filled all the way up to the ground level, [1].

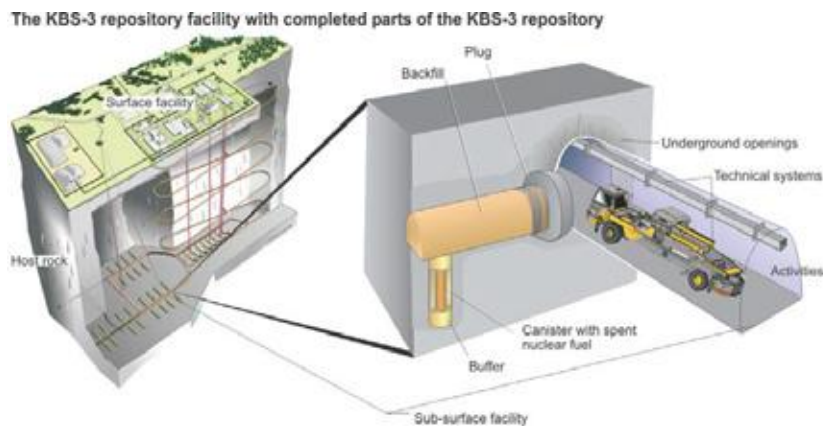


Figure 1 – Illustration of the KBS-3 repository, from [1].

The plug used to seal the deposition tunnels consists of several material layers, each with its specific purpose, see Figure 2. The main parts of the plug are; filter, bentonite seal and a concrete dome. The filter is needed to control ground water inflow during casting and hardening of the concrete dome through drainage pipes. The bentonite seal is intended to be the water-tight seal of the plug and should thereby prevent that leakages occur from the backfilled deposition tunnel to the adjacent main tunnel. The concrete dome constitutes the mechanical resistance intended to transfer the loads from swelling pressure of bentonite and the hydrostatic water pressure to the surrounding rock. The concrete dome has an octagonal shape with a concave downstream surface, and thereby carrying the horizontal pressure loads as a dome. The concrete dome is unreinforced and built with a specially developed concrete mix that is intended to have a lower pH than conventional concrete. The low pH-concrete is described further in detail in the following section. Between these material layers, different delimiters are installed only to separate the materials. The delimiter closest to the concrete dome consists of concrete beams.

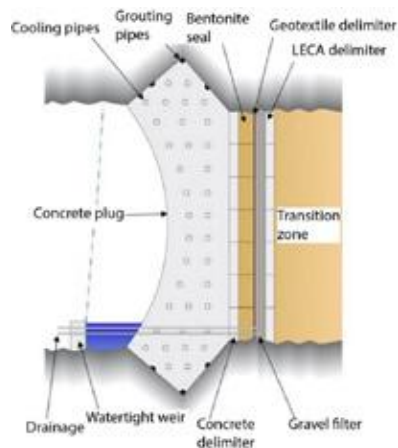


Figure 2 – Illustration of the reference design of plugs for the KBS-3 repository, from [1].

The concrete dome will theoretically be subjected to high pressure loads during the operation phase. The swelling pressure in the backfill is expected to be very high and therefore, the backfill closest to the plug (backfill transition zone) will be designed to reduce the swelling pressure acting on the concrete dome plug to 2 MPa. However, considering uncertainties in the expected swelling pressure, the concrete dome has been designed for a swelling pressure of 4 MPa. Thereby, the total pressure that the plug is designed for is 9 MPa, including the maximum hydrostatic water pressure of 5 MPa, i.e. 500 m of hydraulic head. The expected water pressure during operation of the repository is likely lower than this, considering that the remaining part of the tunnel system is open and the expected low natural inflow of water which means that it will take many years before the water pressure has been built up in the deposition tunnels. After the main tunnels (i.e. downstream of the plug) also are filled with bentonite, the concrete dome will be subjected to water pressure and swelling pressure from both sides and the plug does not fill any function in the repository after this.

In order to verify the concept for plugging the deposition tunnels, a full-scale test has been performed in Äspö Hard rock laboratory (HRL). The purpose of the full-scale test was firstly to test how the installation could be made and to ensure that it was possible to build the plug according to the design specifications. In addition, the purpose was also to evaluate that the design acted as expected during hardening and the serviceability state when it is subjected to hydrostatic pressure. Finally, the purpose was also to estimate the water tightness of the structure. However, in this paper the focus will be on the early age behaviour and especially to assess if the cooling of the dome worked as intended to break the bond between concrete and rock prior to grouting.

1.2 Low pH-concrete

The concrete mix used in the nuclear repository needs to have lower pH than conventional concrete. The reason for this is that high pH may influence the swelling properties of the bentonite clay. Therefore, a specific concrete mix had previously been developed and tested for this purpose that result in a pH value below 11, see [2]. The concrete mix is called B200 and is self-compacting and contains ordinary Portland cement, densified silica fume, limestone filler,

superplasticizer, high quality natural fine aggregates and average quality crushed coarse aggregate, see Table 1.

Due to the low amount of cement used, the heat development due to hydration is low, which results in slower maturity. The strength development at early age is slow, but after 28 days the expected cylinder strength is about 42 MPa and about 62 MPa after three months. Several experimental studies of the material properties of the B200 low pH-concrete have been performed and these are presented by [1] and [2].

Table 1 – Material composition of B200, from [2].

| Constituent | Amount (kg / m ³) |
|------------------------------------|----------------------------------|
| CEM I 42.5 MH/SR/LA | 120 |
| Silica fume (densified) | 80 |
| Water | 165 |
| Limestone filler L25 | 369 |
| Sand 0-8 mm (65% of aggregates) | 1037 |
| Gravel 8-16 mm (35% of aggregates) | 558 |
| Glenium 51 | 6.38 |
| water/cement | 1.38 |
| water/binder | 0.83 |
| water/powder | 0.29 |

Typically for higher strength concrete, the autogenous shrinkage is relatively high, and especially for the first three months. The high autogenous shrinkage could potentially cause cracking in the dome unless measures were used. The early autogenous shrinkage from one hour to 24 hours after casting was about 0.8 mm/m, and the additional autogenous shrinkage from 24 hours after casting to 90 days was about 0.2 mm/m, i.e. resulting in a total autogenous shrinkage after 90 days of about 1.0 mm/m, according to [2]. Some of this shrinkage will of course be compensated for by a slow casting rate. One of the design requirements for the concrete plug was that it should be considered as stress free after 90 days. This means that the shrinkage during the first 90 days must be considered as free shrinkage, i.e. without restraint, and therefore the concrete plug should release from the rock surface during this time, [3]. Therefore, to avoid the risk of cracking, an advanced cooling sequence was utilized with the intention to break the bond between the concrete and rock.

2. THE DOMEPLU FULL-SCALE TEST

The Dome plug (DomePlu) full-scale test started with excavation of the test tunnel, which was performed early in 2012. The excavation was made with a drilling and careful blasting technique to minimize the excavated damage zone in the rock. The tunnel is horse-shoe shaped with a width of 4.2 m and a height of 4.8 m and a total length of about 14 m, see Figure 3 a) and Figure 3 b). After the excavation was done, wire-sawing was used to excavate a slot in the rock. This slot constitutes the abutment for the concrete dome. The excavation of the slot was made by

drilling eight 250 mm cores from the downstream side and eight 250 mm holes from the upstream side that intersected the previously drilled holes. The holes were inclined to form an octagonal shape after this wire-sawing with a pushing cut was made to create the slot, see Figure 3 b).



Figure 3 – a) Illustration of the excavated test tunnel based on laser scanning, b) Photo of the excavated slot, in the photo the project leader Pär Grahm (SKB) is shown.

The plug that was built in the full-scale test deviated to a small extent compared to the reference design of plugs shown previously in Figure 1. The reason for this was that the length of the test tunnel, which was excavated a shorter length compared to the deposition tunnels due to practical reasons, considering that this test was aimed to evaluate the plug. At the end of the excavated tunnel, a concrete wall was cast to ensure a smooth vertical surface for the installation of the backfill bentonite blocks, see Figure 3 b). Thereby, no transition zone as shown in Figure 1 was installed.

After the tunnel excavation was finalized, the different material layers in the plug was installed. From the upstream side, the tested plug consisted of the following layers

- Backfill zone – 100 cm
- LECA Beams – 30 cm
- Macadam filter – 30 cm
- Geotextile
- Bentonite seal – 50 cm
- Concrete beams – 30 cm
- Two-ply geotextile
- Concrete dome ~ 180 cm (in the centre)

In the following, only the installation of the concrete dome will be described. The installation of the other material layers is described in detail in [1].

2.1 Building the concrete dome plug

Casting of the concrete dome was performed on March 13th in 2013. The concrete was delivered to the site in Äspö HRL by 13 lorries from the factory in Kalmar. It was highly important that correct properties were achieved of the fresh concrete, especially when using self-compacting concrete, to ensure a successful pour and casting. Therefore, extensive testing was performed on site for each batch of concrete, where slump flow, air content and density were measured on-site. Besides this, 12 cubes were cast at the factory and at the site and these were used to determine the cube strength and the tensile splitting strength.

The estimated time needed for transport was about 2 hours from the factory to the site underground and then additionally 45 minutes were needed for casting. The concrete was pumped through a pipeline to the concrete dome plug. The casting of the dome was made with a maximum casting height of 100 cm per hour which resulted in a total time for casting of approximately 10 hours.

The concave downstream shape of the dome and the use of self-compacting concrete resulted in a rather complex formwork designed to carry the full hydrostatic pressure, as seen in Figure 4 a). On the upstream side, the concrete beams act as formwork and a geotextile had been installed to prevent bond between the concrete dome and the concrete beams, as seen in Figure 4 b).

Cooling pipes were installed for cooling of the concrete dome. The cooling pipes were made of copper with a diameter of $\phi 25$ mm, and consisted of three separate sections where each section had a length of 80 m. Since there was no reinforcement in the concrete dome, a supporting steel scaffolding was installed to carry the self-weight of the cooling pipes, as seen in Figure 4 b). A design criterion for the steel frame was that it should not be attached to the rock in both the top and bottom, i.e. so that it could cause restraint forces in the concrete dome due to shrinkage. One cooling machine of at least 20 kW was needed for the cooling. However, since the cooling was vital for the construction, a redundant (backup) cooling machine was also placed on site, if the first one would fail for some reason. The flow of the cooling media was controlled by temperature where the allowed difference between inlet and outlet temperature was defined as 2 °C.



a)



b)

Figure 4 – Photos from construction of the dome plug, a) formwork, b) cooling pipes and their scaffolding.

Considering that the concrete dome is unreinforced the intention was to allow for free shrinkage during the first three months. This would be achieved by an advanced cooling procedure, where the concrete was cooled during hardening (stage A) and when sufficient strength has been developed, the intention was to cool the concrete significantly to break the bond between concrete and rock (stage B). This procedure would thereby allow for free shrinkage and after about three months the concrete dome would be cooled once again (stage C) to make it shrink as much as possible to allow for contact grouting between the dome and the rock surface. The cooling during contact grouting would also result in thermal pre-stressing of the dome when the cooling was ended. The temperature in the tunnels was about 14 °C and the temperature in the inlet of the cooling pipes was at most reduced to 1 °C. The temperature in the concrete varied and was naturally higher than this, as later presented in Section 4.2. The cooling procedure of the dome is illustrated in Figure 5, where the three stages A, B and C are illustrated.

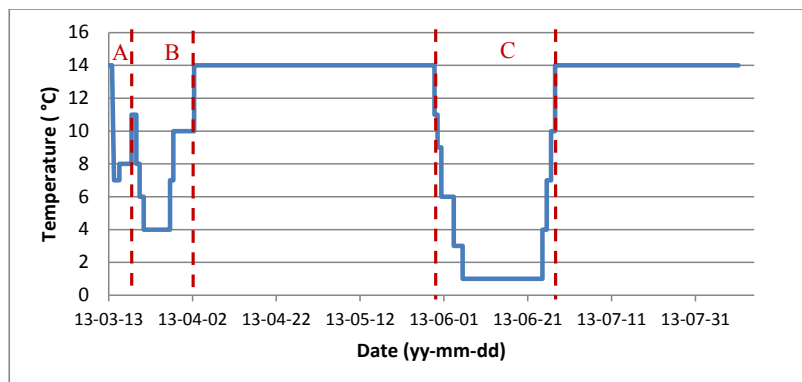


Figure 5 – Illustration of inlet temperature in the cooling pipes during the cooling procedure, with the three stages (A) cooling during hydration, (B) cooling to force the dome release from the rock and (C) cooling during contact grouting plug used in the full-scale test.

In the wire sawn slot, grouting pipes were installed as shown previously in Figure 2. The purpose of the grouting tubes was to ensure water tightness of the dome. In addition, the thermal pre-stress of the dome will minimize the risk of cracking and thereby lead to reduced leakage. After about three months, contact grouting was performed. The purpose of the contact grouting was to seal gaps that had occurred between the concrete dome plug and the surrounding rock. Due to the high amount of shrinkage during the first 90 days according to the experiments and the thermal cooling of the concrete dome plug, it was intended to create a gap between the rock and concrete plug. According to [3], the estimated gap due to shrinkage at the time of grouting would be about 3.7 mm in the top of the dome plug, under the assumption that the plug has released from the rock. In addition, since cooling was performed prior to contact grouting, the gap between concrete and rock was planned to increase even further up to 4.2 mm. First the inner tube on the upstream side was grouted and after this the outer tube, i.e. on the downstream side. Both were performed on the same day, June 11th, 2013. In the first stage, a total of 105 litres were used and the pressure was stable and ended at 10 bars. During the second stage, i.e. grouting of the outer tube, when about 42 litres of grout had been used, a small area with leakage of grouting could be detected near the top of the dome. The total amount of grout was about 93 litres where the final pressure was 10.7 bar. The third and final grouting stage was performed about one week after the first two. In the third grouting stage, the centre tube was grouted with a total of 406 litres, ending up with a final pressure of 61 bar, i.e. 6 MPa, with a pressure increase of 10 bar/min. During the grouting of the last tube, no leakage was detected by

the workers on site. The grouting pressure was maintained for 30 minutes before the grouting was ended.

A total volume of 654 litres was thereby used for grouting, which is almost three times as much as needed to fill the gap between concrete dome and the rock according to a simplified estimation of the expected gap. It is thereby likely to assume that grout also may have filled voids or cracks/fractures within the rock and or within the concrete dome, such as between cooling pipe and concrete dome. It is also possible that the top of the dome was not filled completely during casting or that grout may have filled voids in between the concrete beams.

2.3 Pressurization

The swelling pressure acting on the dome is expected to be about 2 MPa, but this develops over many years if only natural inflow of water occurs. The purpose of the test was to subject the plug to its serviceability loads. Therefore, to decrease the time needed for the experiment, a pressurization system was used to control the water pressure in the filter of the plug. Owing to the pressurization of water, it was possible to increase the rate of saturation of the bentonite seal so that the maximum swelling pressure should be reached during the test period.

The pressurization of the plug started initially with only natural inflow of water. After about 0.8 MPa of water pressure was reached in December 2013, the pumps started which continuously increased the water pressure until 4 MPa, i.e. a hydraulic head of 400 m, was reached. The intention was to increase the water pressure up to 7 MPa, however due to the conditions of the surrounding rock at the experimental site it was not possible. After the water pressure had been increased to about 3 MPa, a significant leakage in the rock occurred in the adjacent tunnel, about 15 m from the plug. Water leakage through rock fractures had been recognized as one major project risk since the rock at Äspö HRL is significantly fractured in general. Due to the encountered rock fracture, by-passing the plug, it was decided to limit the water pressure in the plug to 4 MPa and perform continuous measurements of the observed leakages at this level. This pressure could successfully be maintained by the water pressurization system for about three years. The pressurization curve from the full-scale test is shown in Figure 6.

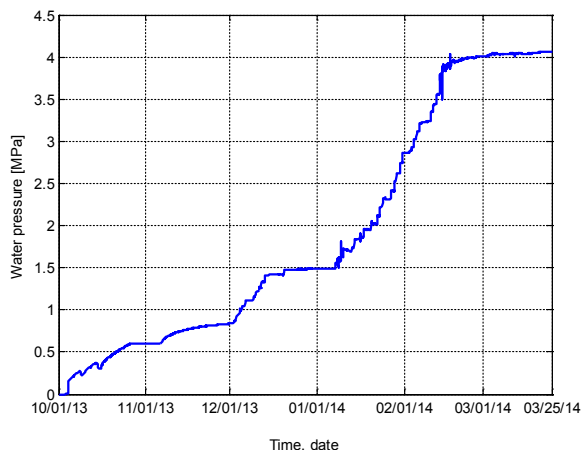


Figure 6 – Pressurization sequence of the plug, where the pressure was increased to 4 MPa.

3. INSTRUMENTATION PROGRAM

The full-scale test of the plug was instrumented with several types of sensors. However, in this paper, only the sensors used to monitor the concrete dome are described.

3.1 Monitoring of the concrete dome

The concrete dome was instrumented with several sensors, where most of them were embedded inside the concrete dome. Some sensors were only used for a shorter period, such as measuring the pressure on the formwork, while the others were used to monitor the behaviour from the hardening process and continued for about five years.

The different types of recordings were; temperature in the concrete dome and the ambient air, strain in the concrete dome, displacement sensors measuring the displacement of the dome and the joints between concrete and rock. In total, the response of the concrete dome was measured with 62 recorded signals where the following types of sensors were used [3]:

- 5 pressure sensors (Wika S11) – pressure on the formwork
- 6 joint meters (TML type KJA-A) – relative displacement between concrete and rock
- 3 LVDT (HBM type WA) – displacement of the concrete dome
- 14 strain gauges (TML type KM-AT) – strain and temperature in the concrete dome
- 10 strain gauges (TML type KM-A) – strain in the concrete dome
- 4 strain gauges (Geokon 4200) – strain and temperature in the concrete dome
- 2 temperature sensors (PT 100) – ambient air temperature

In this paper, the focus is on evaluating the early age behaviour and the response during initial pressurization. Therefore, all results from this full-scale test will not be presented in this paper. In Figure 7, a photo of installed strain gauges and cooling pipes is shown in addition to a sketch illustrating the placement of sensors.

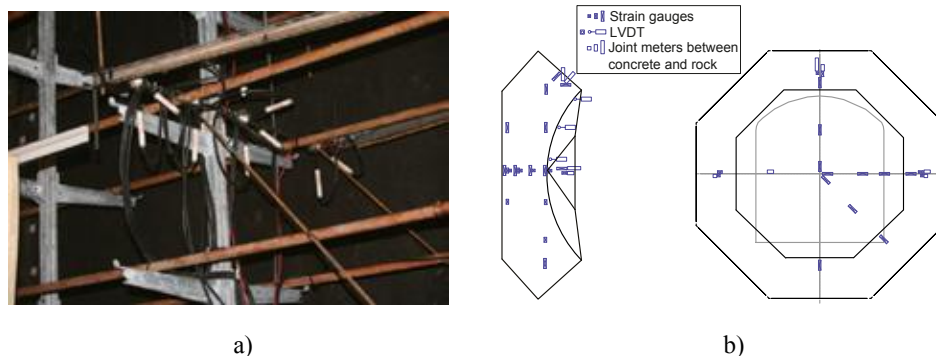


Figure 7 – Installed sensors, a) strain gauges in the centre, b) placement of sensors.

Numerical analyses had been used before the full-scale test to determine suitable measuring ranges and to select the placement of the sensors, see [1]. The structural response from shrinkage and water pressure is expected to be the same regardless which quarter of the dome the sensors were placed in as long as the sensors are placed at the same depth and radius, due to

symmetry of the dome. However, due to the gravity force, largest stresses will occur in the upper half of the dome due to bond between concrete and rock. Therefore, the instrumentation of the concrete dome was primarily made in one quarter (in the upper half) of the concrete dome. In the monitoring program for the concrete dome, some redundancy was included to increase the probability that the behaviour would be measured even if some sensors failed. This was achieved both by using the symmetry and placing sensors at positions that were expected to give similar results (i.e. placed at similar radius and depth) and in addition of using sensors from different manufacturers.

The following instrumentation loggers were used for the different sensors;

- HBM Spider8 – For sensors measuring the pressure on the formwork
- Gantner Q.bloxx A104 – For Geokon strain gauges (including their temperature signals). A Vib Wire-108 module was used to convert the signal from the sensors
- Gantner Q.bloxx A106 – For TML strain gauges, joint meters and LVDT sensors
- Gantner Q.bloxx A107 – For ambient air temperature sensors and thermocouple signal of TML strain gauges

The sampling rate in the measurements of the pressure on the formwork was one reading each minute and for all other measurements a sampling rate of one reading every five minutes was used.

3.2 Instrumentation

In total, 28 strain gauges were embedded in the concrete dome with the intention to capture its behaviour from hardening until the test was ended. The placement of all embedded strain gauges is illustrated in Figure 8. Sensors were placed at four depths in the centre of the dome and in three directions to capture the distribution of strain. In addition, several strain gauges were placed close to the interface between concrete and rock. Almost all strain gauges were placed on shorter reinforcement bars that were mounted on the cooling pipes, except for the strain gauges closest to the rock. In this case it was not possible to attach these to the cooling system, so instead reinforcement bars were installed in the rock on which the strain gauges were attached. The concrete cover was at least 400 mm for the sensors closest to the surfaces to minimize the risk of the sensors being subjected to high water pressure.

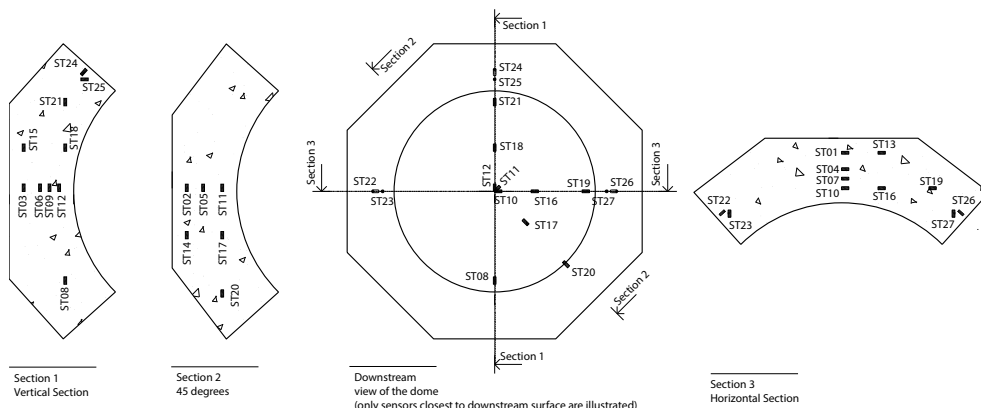


Figure 8 – Placement of installed strain gauges.

Joint meters were installed to measure the relative displacement between the concrete dome and the rock. In total, 6 joint meters were installed; two sensors each at the left- and right-hand side and two in the top. All these sensors were drilled into the rock at the downstream side of the slot, where one was placed perpendicular to the rock surface and the other one was placed vertically (in the top) or in the tunnel axis direction (left- and right-hand side). The intention of these sensors was to observe if the concrete dome released from the rock. It was expected that the concrete dome would release from the rock during the second cooling stage (B), and that the downstream side would be compressed when the dome was subjected the water pressure.

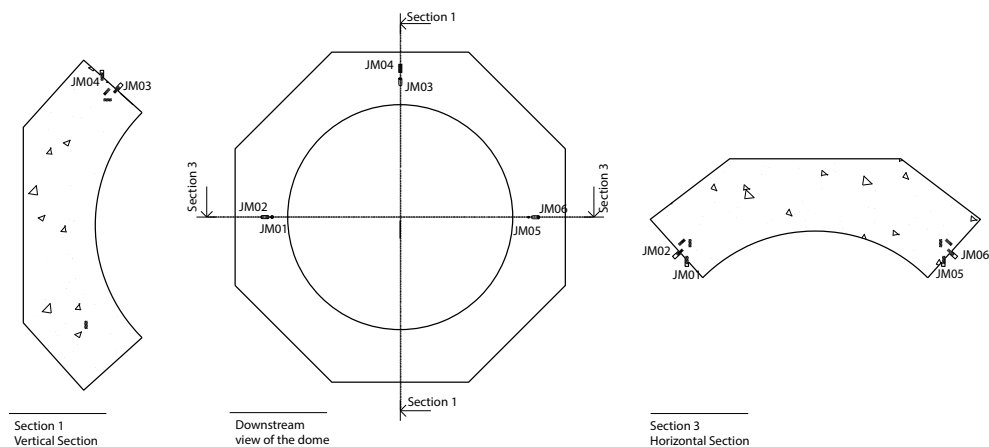


Figure 9 – Placement of installed joint meters gauges.

3.2 Signal processing the measured data

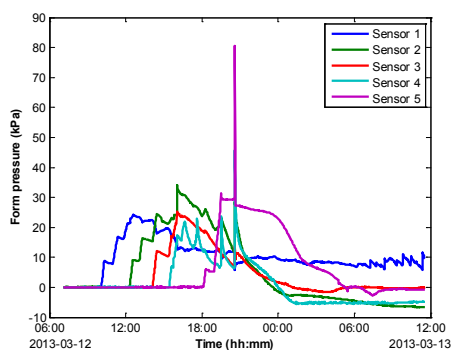
All sensors have been temperature compensated based on the difference in thermal expansion of the sensors and the concrete. This is described in detail in [4]. In addition, all measured signals have been subjected to signal processing to remove effect from background noise and from spurious voltage impulses that occurred. All signal processing has been performed with the signal processing toolbox in Matlab by using smoothing filters. For the Geokon sensors, local regression using weighted linear least squares and a 1st degree polynomial models that assigns lower weight to outliers (denoted “rlowess”) were used primarily to reduce the influences of the spurious voltage impulses. For all other signals, the filtering was made with Savitzky-Golay, a generalized moving average filter from unweighted linear regression, primarily to attenuate the background noise. More information about the signal processing can be found in [4].

4. RESULTS

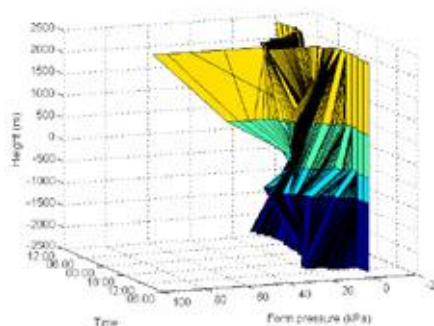
4.1 Pressure on the formwork during concrete hardening

The pressure on the formwork was measured at five locations over the height of the form/dome. The sensors were numbered from 1 to 5 based on their height above the ground, meaning sensor no 1 was at the bottom and sensor no 5 was close to the top. In Figure 10 a), the pressure is shown as a function of time, measured at each sensor and in Figure 10 b) the same result is

presented in a 3D plot (height, pressure and time). As can be seen, the maximum pressure at each location of the sensors a few hours after the level of concrete reached that position. This means that the hardening of concrete in the bottom started before the whole plug was cast. Thereby, the maximum theoretical hydrostatic pressure of 160 kN/m^2 (at the bottom) never occurred. Instead the maximum pressure measured close to the bottom was approximately 25 kN/m^2 . The maximum form pressure was typically 35 kN/m^2 measured at all sensor positions. However, there was a significant increase measured at the sensor in the top where it increased from about 30 kN/m^2 to a maximum of approximately 80 kN/m^2 for a period of four minutes. This was however after casting was completed. According to the staff at site during casting, the contact grouting tubes were pressurized at the end of casting to cleanse the tubes. This pressure impulse, is likely a result of this action.



a)



b)

Figure 10 – Recorded pressure on the formwork.

4.2 Temperature development during concrete hardening

The temperature in the ambient air in the tunnel varied typically between 13 and $15 \text{ }^\circ\text{C}$ during the measuring period. The initial temperature for all batches of concrete was about $10 \text{ }^\circ\text{C}$ prior to casting. After the hydration of the concrete had started, the cooling pipes started to reduce the temperature in the concrete. The cooling sequence was conducted in smaller steps as shown in Figure 5. The aim of the concrete cooling during hydration (stage A) was to ensure that the temperature in the dome was less than $20 \text{ }^\circ\text{C}$. As it can be seen in Figure 11, the maximum temperature in the concrete was slightly below $18 \text{ }^\circ\text{C}$ during hydration. After this, the cooling stage B was performed, intended to break the bond between concrete and rock. During this stage, the temperature in the cooling pipes was reduced to $4 \text{ }^\circ\text{C}$ and maintained at this level for 6 days. This resulted in a temperature in the concrete between 6 and $10 \text{ }^\circ\text{C}$. After this the temperature increased as the cooling equipment was turned off.

Finally, after about three months, the cooling system was used once again to cool the concrete dome as much as possible to allow for effective contact grouting. During this cooling stage (C), the inlet temperature in the cooling pipe was reduced to $1 \text{ }^\circ\text{C}$ to create a large thermal pre-stressing of the concrete dome, i.e. to introduce compressive forces into the dome after the cooling was completed. The measured temperature during the cooling period prior to the contact

grouting (stage C), decreased to a minimum of 3 °C and was about 8 °C as maximum, as seen in Figure 11.

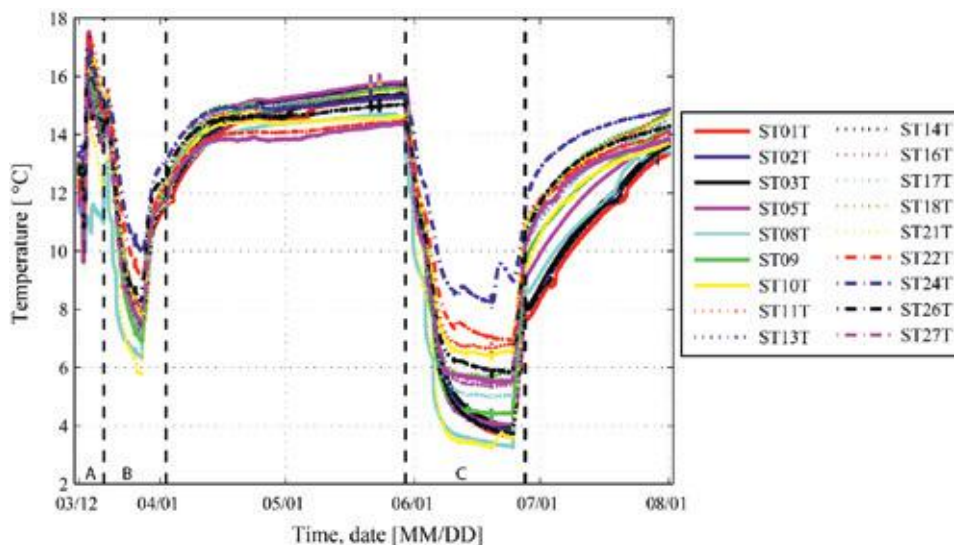


Figure 11 – Recorded temperatures in the concrete during the first five months.

The advanced cooling sequence had worked and no visible cracks could be detected in the concrete dome. However, whether the concrete dome had released from the rock or not during cooling stage B was uncertain. Therefore, different methods were used to evaluate this based on the measurements as shown in the following sections.

4.3 Relative displacement between concrete and rock

The joint meters measured the relative displacement between concrete and rock at six locations, as previously shown in Figure 9. The results up to the point after contact grouting is shown in Figure 12. As can be seen in Figure 12, the joint meters show small relative movement between concrete and rock which indicates no direct crack opening during the first stages. The maximum relative displacement is 0.1 mm during cooling prior to grouting (stage C). If the concrete dome had released from the rock, a relative displacement of about 4.2 mm had occurred according to [3]. This shows that the concrete dome did not release from the rock on the downstream side of the slot, at least not at these locations. The relative displacements are in general so small, and most likely corresponds to elastic strains in the concrete. However, all joint meters show a slightly larger value after grouting than before, which indicates that at least some parts of the slot have been grouted. The largest difference before and after grouting is seen on JM05 which measures the relative displacement in the tunnel axis and is located on the right-hand side (viewed from the downstream side).

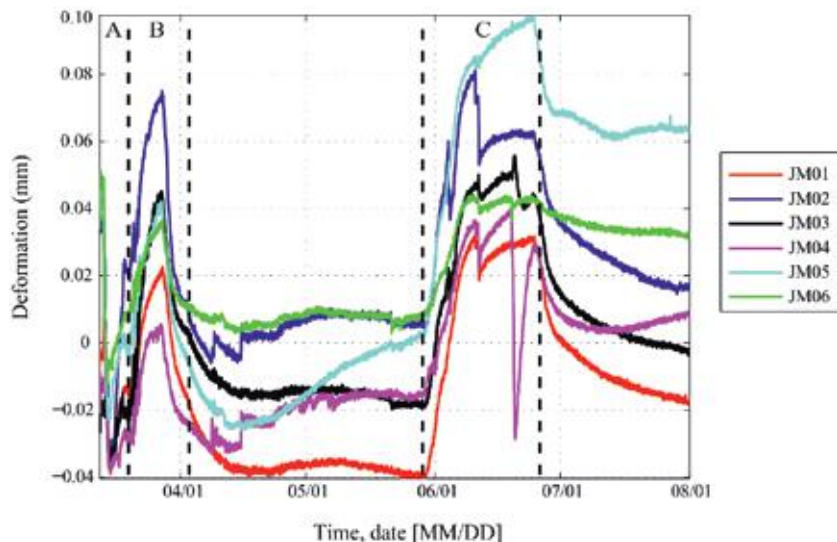


Figure 12 – Variation in relative displacement at the interface between concrete and rock.

4.4 Induced strains in the concrete

The difficulty with analysing the induced strains in the concrete is to determine at which point sufficient bond between concrete and the sensors has been reached. During the first hours after pouring the concrete, the concrete behaves completely plastic and no reliable strains can be measured. After this, as the hydration initiates and the concrete strength starts to develop and due to the increased temperature from the hydration, compressive stresses occur in the concrete. When the heat generated by the hydration reduces which result in decreased temperature in the concrete, where tensile stresses develop, [5].

In the full-scale test, two different type of strain gauges were used. The strain gauges with larger flanges (Geokon 4200) at the ends, were significantly easier to evaluate regarding the early age behaviour since they quite early recorded reliable strains in the concrete. In Figure 13, the development of strain from one of these sensors is shown as an example for the early age strain development in the dome. In the figure, the corresponding measured temperature at this sensor is also presented. In the figure, the graph is presented from the start of casting (at 07:00 in the morning). The presented sensor is however located in the centre of the dome and hence was not embedded in concrete until about seven hours after casting begun.

For the other strain gauges, with smaller flanges it was much more difficult to capture the early behaviour since several sudden changes in strain occurred in these signals during the casting and early in the hydration process. Methods to find suitable zero-reference level for the strain gauges used in case have been presented by [3] and [6]. The determination of the zero-reference value is, however, only important for obtaining the absolute value of the strain and to predict induced stresses. In this case, it is more interesting to find the influence from the advanced cooling and to quantify the effect from the thermal pre-stress. Thereby, to achieve this only the relative difference of the strain before and after the third cooling stage (stage C) as shown in Figure 14 should be considered, which is described in Section 4.5.

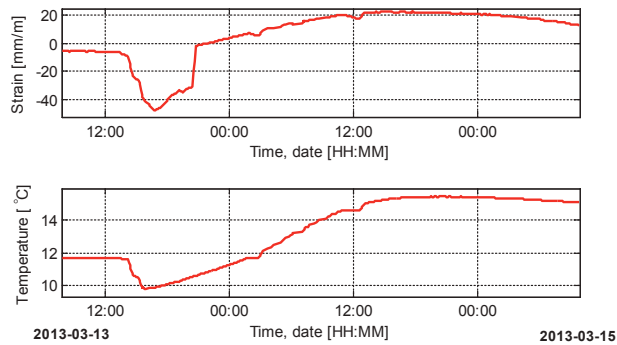


Figure 13 – Early strain/stress development in concrete. Measured strain development in the dome plug with a Geokon sensor (top), temperature development from the same Geokon sensor (bottom).

Two of the strain gauges failed during the third and final grouting stage. The two strain gauges that failed (ST23 and ST25) were placed adjacent to the joint meters (JM01 and JM03). As it can be seen in Figure 15, these sensors were installed on reinforcement bars drilled in to the rock. However, these reinforcement bars were placed close to the centre tube that was grouted in the final grouting stage. It is therefore believed that the grout travelled along the reinforcement bar up to the strain gauges and the high grout pressure of 6 MPa destroyed these gauges.

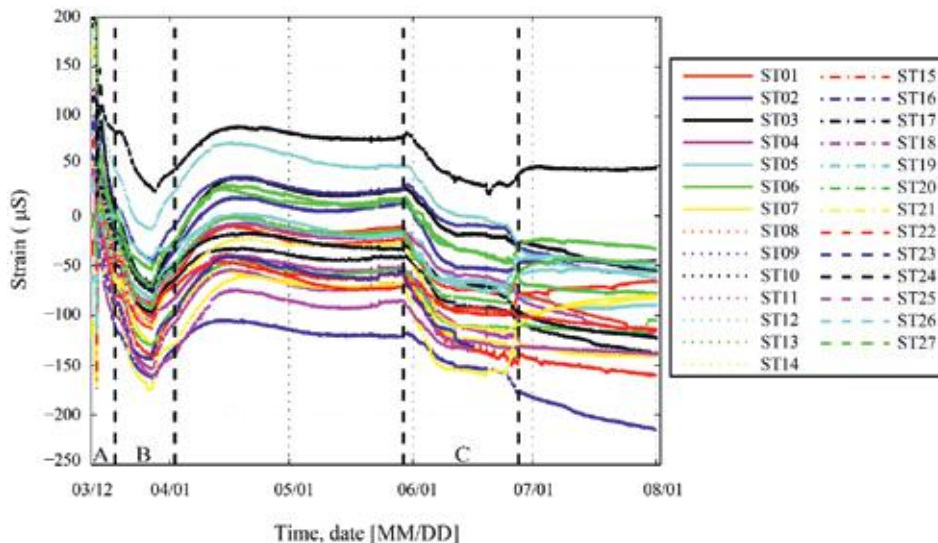


Figure 14 – Variation in measured strain based on all strain gauges.



Figure 15 – Photos of strain gauges that failed during the third grouting, a) strain gauge ST23 and b) ST25. Also seen in the photo: the installed joint meters, a) JM01 and JM02 and b) JM03 and JM04.

4.5 Effect of the thermal pre-stress

To estimate the effect from the thermal pre-stress, the relative difference in strain before and after cooling stage C) was analysed for all strain gauges. The time points for the start and stop of the third cooling cycle was illustrated with two black lines in Figure 14. Here the strain difference has been multiplied with the elastic modulus of concrete (33.9 GPa according to [2]) to calculate the compressive pre-stress. The calculated compressive stresses induced due to grouting is presented in Figure 16 a). As seen in the figure, the thermal pre-stress (i.e. compressive) varies from about 0.5 MPa to 3.5 MPa in the concrete dome. It should be noted that the two strain gauges that failed during grouting are shown as zero stress in the figure.

If no grouting could be inserted between the concrete dome and the rock, then the strain would be identical before and after. For a case without bond between the concrete and rock, the full temperature reduction from cooling would result in thermal pre-stress. Here, the temperature difference is based on the difference in temperature for each sensor between maximum temperature during hydration (between 15 and 18 °C) and minimum temperature during cooling prior to contact grouting (between 3 and 8 °C). The maximum temperature during hydration is considered as the strain free temperature for the concrete. This is denoted as the maximum thermal pre-stress and is shown in Figure 16 b). Considering that the temperature varies in the concrete dome to some extent, this results in a variation in maximum theoretical thermal pre-stress between 3 and 4.5 MPa.

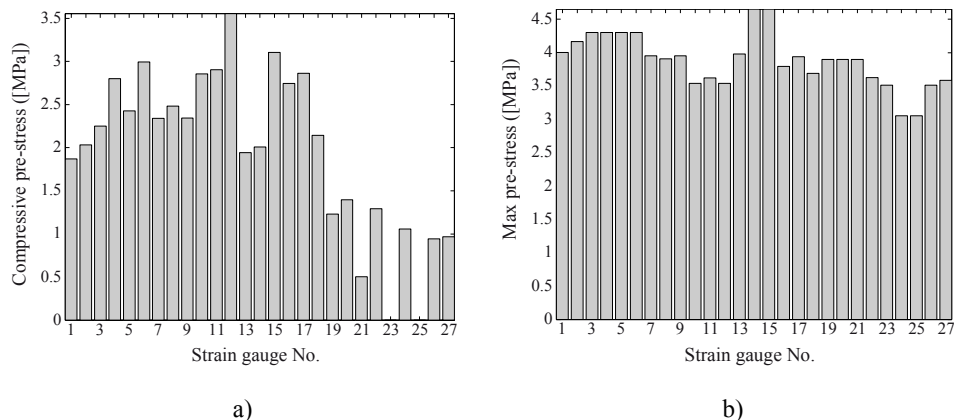


Figure 16 – Calculated effect from the thermal pre-stress during grouting, a) induced compressive strain based on the strain gauges, b) maximal stresses due to the variation in temperature.

Finally, the ratio between the obtained strain difference before and after grouting (Figure 16 a) and the maximum thermal pre-stresses (Figure 16 b) indicates the degree of achieved pre-stress in the dome. By calculating the relative ratio of the induced pre-stress, the results are no longer dependent on the estimated elastic modulus of the concrete and is thereby only dependent on the measured quantities. It can be seen in Figure 17 that one sensor gives 100%, i.e. where the obtained pre-stress is equal the theoretical maximum. This sensor is denoted ST12 and is mounted in the centre of the dome, about 400 mm from the upstream surface and measures in the vertical direction. The two sensors close to this, ST10 and ST11 also show high utilization of pre-stress, about 80% of the maximum theoretical value. In common for the five sensors, that show highest achieved relative pre-stress, is that all are mounted on the upstream side of the dome. Most of the strain gauges show relatively low pre-stress compared to the theoretical maximum where the average utilization is 53%. Thereby, based on the calculated effect of thermal pre-stress it can be concluded that the dome plug had partially released from the rock and it is likely that the upstream side of the slot released to a greater extent than the downstream side (i.e. where the joint meters are located).

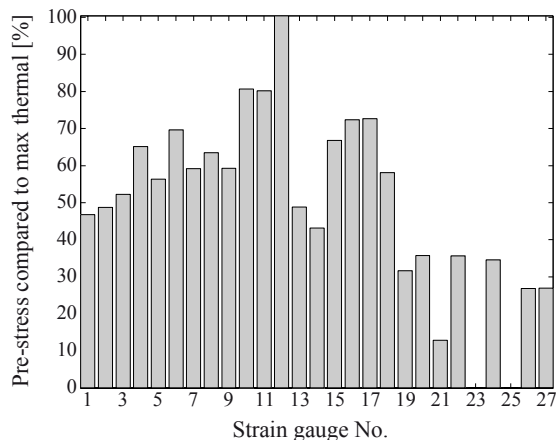


Figure 17 – Achieved pre-stress compared to maximum thermal stress.

4.6 Pressurization 4 MPa and long-term behaviour

As shown previously, the pressurization of the plug was performed to a water pressure of 4 MPa. When the water pressure reached about 3.5 MPa, a significant change for the two sensors in the top of the dome (JM03 & JM04) occurred as seen in Figure 18. This is likely caused by the dome releasing on the upstream side of the slot and thereby all loads are carried by to the downstream side of the slot in this region. Thereby, the joint meters were compressed and stopped recording reliable displacements when it was compressed beyond its measuring range. A water pressure sensor had been installed on the rock on the upstream side of the slot in this region. This sensor showed that water pressure increased in a similar manner as shown in Figure 6 before the sensor failed.

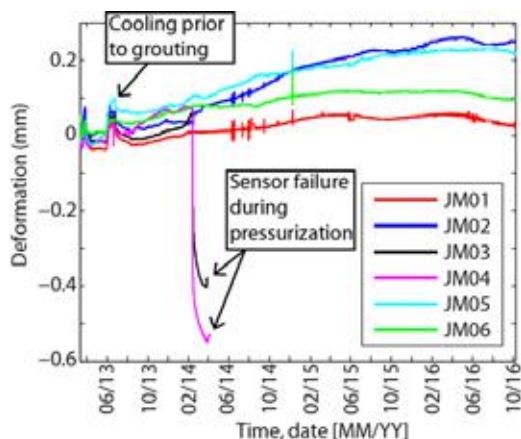


Figure 18 – Installed strain gauges.

Thereby, the concrete has most likely released on the upstream side of the slot in this region during the increasing water pressure, as illustrated in Figure 19 a). In addition, a small leakage

between concrete and rock was observed near the top of the concrete as seen in Figure 19 b). It should be noted that this is the same location where leakage of grout occurred during grouting. It is therefore likely that this location had not been sufficiently grouted which caused this leakage path. All leakage from the plug was gathered in a weir installed downstream of the concrete dome, see Figure 2. To prevent loss of water due to evaporation, a plastic sheet had been installed that enclosed the area upstream of the weir. From this weir, the leakage water was collected and measured automatically. The total leakage through the plug and the adjacent rock that was collected in the weir was 108 ml/min at this point and after this, the leakage at the top successively decreased and was 43 ml/min after 6 months, according to [1].

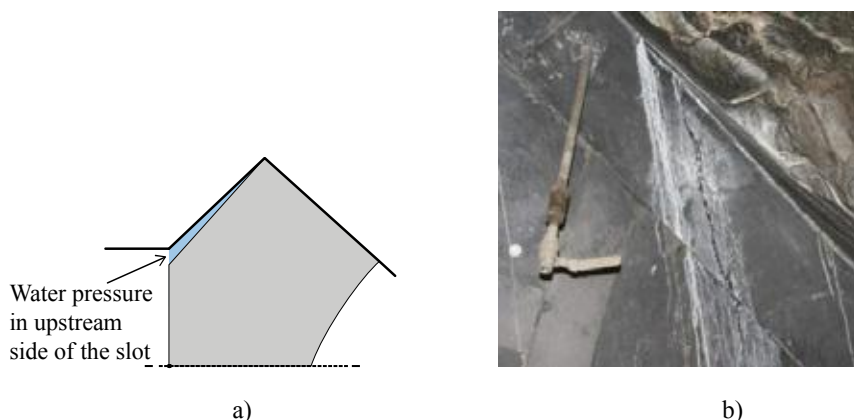


Figure 19 – a) Illustration of water pressure in upstream side of the slot, b) photo of small leakage near the top of the concrete dome.

5. CONCLUSIONS

In this paper, a full-scale test of the Dome plug intended to be used in the future repository for spent nuclear fuel in Sweden has been presented. The purpose of the full-scale test was to verify that it was possible to build the plug according to the design specifications. In addition, the purpose was also to evaluate that the design acted as expected during hardening and the serviceability state when it was subjected to hydrostatic pressure and estimate the water tightness of the structure.

The full-scale test showed that it was possible to build a plug according to the specifications and the whole installation worked as planned. The test showed that it was possible to build a concrete dome that could both carry its serviceability loads and be sufficiently water tight to allow for the bentonite seal to homogenize.

Due to the high autogenous shrinkage, the design was made for the unreinforced concrete to release from the rock during the hardening process by means of cooling. The measurements showed however that this was difficult to accomplish.

Based on the results from the strain gauges it can be observed that the contact grouting resulted in a thermal pre-stressing of the concrete dome plug. The obtained pre-stress varied between 0.5

MPa and 3.5 MPa in the concrete dome, depending on the direction and location of the sensors. Only one sensor obtained the actual theoretical level of pre-stress and a few other sensors showed pre-stress above 70% of the theoretical value. The average pre-stress obtained from all strain gauges in operation was 53%. If the concrete dome had released from the rock during the cooling stages, it is expected that all sensors would obtain their theoretical value. This indicates that the concrete dome only partially released from the rock in the top of the dome.

According to the measurements it is likely that the dome released partially, especially on the upstream side. At the location of the joint meters on the downstream side of the slot, the dome seems to have been constrained to the rock during the whole test. There could be several reasons for this. Naturally, the bond strength may have been higher than the previous test values that were used in design. However, if this was the case then numerical analyses showed that there would be a significant risk of cracking in the dome if it was subjected to the design values of the shrinkage without releasing from the rock. The full-scale test did however not show any visible cracks or leakages through the concrete (except for a small area in the interface between concrete and rock in the top of the dome as shown in Figure 19 b). Other reasons for the discrepancy could of course be that numerical analyses were conservative or that the autogenous shrinkage of the concrete was less than assumed in the design.

6. FURTHER RESEARCH

Considering that this is an extensive project, it has not been possible to present all results from the full-scale test. In this paper, the focus was on the early age behaviour and, especially, to evaluate if the concrete released from the rock as expected prior to grouting. The project is currently on-going and has moved in to the second phase. At the end of the serviceability load test (sustained load of 4 MPa load for 3 years), a strength integrity test will be performed where the water pressure will be increased up to 9 MPa. After this, the whole plug will be demolished where a lot of test samples will be taken out. Before demolition, non-destructive testing will be performed to find if any internal damages are visible which could indicate interesting locations for core samples, etc. During the demolition, the thickness of the grout will be studied which will show the efficiency of the grouting and the results can be used to verify the results from the monitoring. Thereby, the results from the evaluations in this paper will be possible to verify with actual observations and measurements of the bond between concrete and rock and thickness of the grout in the future.

SKB will also continue to develop the concept for sealing deposition tunnels. The findings presented in this paper showed areas for improvement and further work. For instance, one important aspect is to study if the cooling scheme could be simplified and determine if the second cooling stage (stage B) is necessary. Another important aspect for further work is to continue develop the formwork used for the dome plug. As the test showed, the pressure on the formwork was much lower than the hydrostatic pressure due to the low casting rate.

7. ACKNOWLEDGEMENT

The work presented in this paper regarding the full-scale test of the Dome plug that has been carried out in cooperation between SKB and Posiva Oy. The main project team consisted of the following people:

| | |
|---------------------|---|
| SKB | Pär Gramh (Project leader), Patrik Hagman, Karin Nilsson, Anna Blomqvist, Behnaz Aghili, Pär Viberg, Mats Lundquist, Gunnar Ramqvist, Stefan Grandin Svärth, Mikael Hedin |
| Posiva Oy: | Petri Koho (Project partner), Petri Korkeakoski, Sanna Mustonen. |
| NCC: | Hans Wimelius, Jonas Magnusson, Alexandre Mathern, Lars-Olof Dahlström, Christina Claeson-Jonsson. |
| Clay Technology: | Lennart Börgesson, Torbjörn Sandén, Mattias Åkesson, Linus Andersson, Viktor Jensen. |
| KTH: | Richard Malm, Stefan Trillkott, Claes Kullberg. |
| SWECO: | Richard Malm, Daniel Eriksson. |
| Palmer Engineering: | Sten Palmer (Technical supervisor). |
| Vattenfall Teknik: | Tobias Gasch. |
| Uppländska berg: | Rickard Karlzén |

REFERENCES

1. Gramh P, Malm R, Eriksson D: “System design and full-scale testing of the Dome Plug for KBS-3V deposition tunnels – Main report,” *Technical Report* TR-14-23, Swedish Nuclear Fuel and Waste Management Co, Stockholm, Sweden, 2015, 206 pp.
2. Vogt C, Lagerblad B, Wallin K, Baldy F, Jonasson J-E: “Low pH self-compacting concrete for deposition tunnel plugs,” *Report* R-09-07, Swedish Nuclear Fuel and Waste Management Co, Stockholm, Sweden, 2009, 78 pp
3. Malm R: “Low-pH concrete plug for sealing the KBS-3V deposition tunnels,” *Report* R-11-04, Swedish Nuclear Fuel and Waste Management Co, 2012, 149 pp.
4. Malm R: “Instrumentation and evaluation of the concrete dome plug DOMPLU,” TRITA-BKN *Report* 147, Department of Civil and Architectural Engineering, KTH Royal Institute of Technology, Stockholm, Sweden, 2014, 106 pp.
5. Emborg M: “Thermal stresses in concrete structures at early ages,” *PhD thesis*, report 1989:73 D, Department of Civil, Environmental and Natural Resources Engineering, Luleå University of Technology, Luleå, Sweden, 1989, 280 pp.
6. Kristiansson A: “Evaluation of a concrete plug: From the Dome Plug Experiment DOMPLU at Äspö HRL,” *MSc thesis*, TRITA-BKN-Master Thesis 418, Department of Civil and Architectural Engineering, KTH Royal Institute of Technology, Stockholm, Sweden, 2014, 121 pp.



DOI: 10.2478/ncr-2018-0005

ISSN online 2545-2819

ISSN print 0800-6377

© Article authors. This is an open access article distributed under the Creative Commons Attribution-NonCommercial-NoDerivs licens. (<http://creativecommons.org/licenses/by-nc-nd/3.0/>).

Received: March 15, 2018

Revision received: May 7, 2018

Accepted: May 7, 2018

The Influence of Supplementary Cementitious Materials on Climate Impact of Concrete Structures Exposed to Chlorides



Nadia Al-Ayish
Ph.D. candidate
RISE CBI Betonginstitutet
Drottning Kristinas v. 26, 114 28 Stockholm
e-mail: nadia.al-ayish@ri.se



Otto During
M.Sc.
RISE CBI Betonginstitutet
Drottning Kristinas v. 26, 114 28 Stockholm
e-mail: otto.during@ri.se



Katarina Malaga
Ph.D. Associate professor
RISE CBI Betonginstitutet
Drottning Kristinas v. 26, 114 28 Stockholm
e-mail: katarina.malaga@ri.se



Nelson Silva
Ph.D.
RISE CBI Betonginstitutet
Drottning Kristinas v. 26, 114 28 Stockholm
e-mail: katarina.malaga@ri.se



Kjartan Gudmundsson
Ph.D. Associate professor
Royal Institute of Technology (KTH), Department of Civil and Architectural Engineering, Brinellv. 23, 10044 Stockholm,
Kjartan.gudmundsson@byv.kth.se

ABSTRACT

Addition of fly ash or GGBS in concrete has shown to increase the durability and thus the service life of concrete structures exposed to chlorides. Currently, the durability relies on

regulations, which beside a minimum cover thickness also put constraint on amount and type of SCM in different environments. Swedish regulations do not, however, consider the actual durability of different binders. As a consequence, a LCA might be misleading. This paper investigates the climate impact of concrete with SCM in chloride environment. Current prescriptive design approach is compared with a performance based service life approach and applied to bridge parts.

Key words: chloride induced corrosion, Supplementary Cementitious Materials (SCM), climate impact, bridge, service life, LCA, concrete.

1. INTRODUCTION

The Swedish Transport Administration (STA) has identified a need to reduce greenhouse gases from infrastructures at a life-cycle perspective. In order to reduce these emissions STA has set a vision to reduce the climate impact of infrastructures by 15 % until 2020, 30 % until 2025 and zero emissions by 2050, compared to levels from 2015. For this reason STA has since 2016 set a demand that all infrastructure projects with an investment cost above 50 million SEK (approximately 5 million EUR) have to declare their climate impact [1]. Since concrete is the most common material used in bridges, efforts to reduce its climate impact will have a big effect on the overall reduction potential of the infrastructure [2].

There are different ways to reduce the climate impact of concrete structures. One way is to use the resources more efficiently by reducing the total clinker content in the concrete mix. This can be achieved for example by replacing part of the Portland cement (CEM I) with supplementary cementitious materials (SCM) from industrial waste products such as fly ash (FA) and ground-granulated blast furnace slag (GGBS). Another way to reduce the climate impact is by increasing the durability of the structure and thereby extending the service life and reducing the need for repair and replacement. Müller et al. [3] propose that the sustainability potential of a concrete structure should be defined as the relationship between the lifetime performance and the environmental impact. According to this definition the authors suggest three approaches to enhance the sustainability: 1) lowering the environmental impact of the concrete mix; 2) improving the concrete performance, i.e. reduction of cross-section of members through high load bearing capacity and 3) by extending the life span of the material and the structure. By reducing the need for repair and replacement there can be a significant reduction in environmental impact over the life span of a construction.

A bridge part that is frequently maintained and repaired is the edge beam. It is exposed to harsh conditions such as freezing and as a consequence also to chlorides due to the de-icing salts. According to a study by Racutanu the edge beam system is one of the bridge parts that gets damaged the most and stands for 33 % of all damages noted in a large sample of Swedish concrete bridges [4]. Based on statistical data, the average age before replacing an edge beam is 45 years [5]. According to this research the time before replacement depends on the location where an edge beam in heavy traffic is replaced more frequently than in non-heavy traffic. This is also due to use of de-icing salts. Moreover, a study by Safi found that the life cycle measures (LCM) applied to an edge beam are: repair every 20 years, replacement every 60 years and impregnation every 20 years [6]. According to Veganzones et al. [7], except for high LCM costs, repair and replacement of bridge edge beams also cause user and societal costs due to traffic disturbance.

One of the main deterioration problems in reinforced concrete (RC) structures is chloride induced corrosion [8]. In order to protect the reinforcement from corrosion and obtain a certain service life a minimum concrete cover thickness is needed. At present, this cover thickness is mainly based on current regulations in Sweden that do not differentiate between cement types and concrete compositions. A study on chloride ingress in Swedish conditions by Tang and Löfgren [9] concludes, however, that this cover thickness should also depend on the addition of SCM. The aim of this study is therefore to evaluate the global warming potential (GWP) of RC structures exposed to chlorides considering the durability of SCMs. Although researches have shown the link between environmental impact and durability there is still a lack of LCA studies that include the actual performance of reinforced concrete structures with different mix designs. This study evaluates the climate impact of mix designs with various amounts of SCM based on their influence on concrete performance. The mix designs are applied on two bridge parts, a bridge edge beam, which is exposed to de-icing salt and a bridge pier, which is exposed to constant chloride diffusion. The performance based approach is based on recent research [9] and compared with current prescriptive approach. Chloride induced corrosion is the only deterioration mechanism that is considered in this study.

2. DURABILITY OF CHLORIDE EXPOSED CONCRETE WITH SCM

Durability of steel reinforced concrete depends on several factors such as concrete properties, environmental exposure, ageing of concrete and steel quality. Steel reinforcement in concrete is protected from corrosion by a passivating film that is created due to the high alkalinity of the pore solution. When concrete carbonates, the pH in the pore solution drops, activating the corrosion process. However, a pH reduction is not the only corrosion inducing process. When chloride ions penetrate the concrete and reach a certain concentration at the depth of the reinforcement, a so called threshold value, an electrochemical process starts the corrosion of steel, even without a drop in pH. There are three mechanisms leading to chloride induced corrosion [10]; 1) The chloride ions in the electrolyte may penetrate through the passive film to the steel surface due to the high potential difference across the film. 2) The film may break due to discontinuities in the film. 3) And lastly, adsorption of ions to the film may lead to progressive thinning.

When chloride ions diffuse through pores into the concrete, some of the ions will be bound chemically to the aluminat phase in the cement [11], some will be physically bound to the pore walls [12] and some will be free in the pore solution. The reaction of steel is dependent on the concentration of free chloride ions. However, when defining a chloride threshold value it is difficult to measure the free ions only and a total chloride content is therefore used. The resistance of concrete to chloride diffusion depends on several factors of which one is the addition of SCM. In previous times addition of fly ash or ground-granulated blast furnace slag (GGBS) has been linked to an increased risk of corrosion due to a lower alkalinity in the pore solution [13,14]. More recent studies, however, have shown that fly ash and GGBS contain a higher amount of alumina which leads to an increased chemical binding of chlorides [15,11], thus increasing chloride threshold. Additionally, a denser microstructure in fly ash and GGBS incorporated concrete has also been observed which means that the diffusion coefficient might also be lower [16]. A literature study by Shi et al. [17] concluded that concrete with SCMs has an overall improved resistance to chloride ingress.

The chloride threshold is an important parameter regarding service life modelling. There is however a large scatter in the literature. According to Angst et al. [15] the scatter of the chloride threshold value is smaller for field studies.

3. SERVICE LIFE PREDICTION

Sustainability of a structure is greatly dependent on the technical performance under the designed service life. The more durable the structure is the lower are the repair costs and the environmental impact. The difficulty in a LCA model is the service life prediction. There is statistical data on repair and maintenance, but they do not consider the durability of different concrete mix designs and binders. The consequence is therefore a significant gap when designing a sustainable concrete structure.

The design service life should include an anticipated maintenance, but without the necessity of a major repair. ISO 16204 defines 4 methods with different levels of sophistication to verify the design service life, namely: full probabilistic (DuraCrete model in Fib bulletin 34) [18], partial factor, deemed-to-satisfy and avoidance of deterioration [19]. This paper compares a performance based service life model for chloride ingress with a prescriptive service life approach.

3.1 Today's prescriptive service life design

In a prescriptive or deemed-to satisfy service life approach the service life is designed through constrains on minimum cover thickness and on concrete properties in different environmental exposures such as water to cement ratio, clinker content and amount of SCM content in binder [20]. The concrete cover does not, however, vary with type of binder. It only depends on the water to cement (w/c) ratio.

Table 1 demonstrates the allowable limits for reinforced concrete in different chloride environments in order to reach a service life of 100 years as defined in the Swedish application of the European construction standards, EKS 10 [21,22].

Table 1 – Allowable limits for the chloride exposure classes used in this research. The material properties are from SS EN 137003 [21] while the cover thicknesses are from EKS 10 [22].

| | XS2 (submerged in sea) | XD3 (de-icing salt) | XF4 (frost) |
|-----------------------------------|---------------------------|------------------------|----------------|
| W/C(eq) [-] | 0.45 | 0.40 | 0.45 |
| Max addition [% of binder] | | | |
| FA | 35 | 35 | 20 |
| GGBS | 65 | 35 | 20 |
| Concrete cover for: | | | |
| W/C 0.4, 100yr [mm] ¹ | 45 | 45 | NA |
| W/C 0.45, 100yr [mm] ¹ | 50 | - | NA |

¹Excluding 10 mm tolerance

3.2 Performance based service life design

There are several models for calculating the chloride ingress in reinforced concrete structures. Some models are: the simple ERFC model, the Mejlbro-Poulsen's model, the DuraCrete model, ACI Life 365 and the ClinConc model [9]. The first four models use the total chloride content as the main driving force in the transport function while the ClinConc model takes into account the free chlorides in the pore solution. What the models have in common is the assumption of a crack-free concrete and that they are based on Fick's 2nd law of diffusion.

The best curve fitted model is, according to Tang et al. [23], the ClinConc model which considers the free chlorides in the pore solution. Tang and Löfgren [9] used this model to evaluate the durability of concrete with SCM exposed to chlorides. The chloride ingress was modeled for marine and road environments with a service life of 100 years and chloride threshold at 1.0 % and 0.4 % of mass of binder respectively. Field data from concrete exposed to Swedish seawater under a period of 20 years were used for validating the study. Tang and Löfgren concluded that an addition of FA and GGBS in concrete improves the resistance to chloride ingress and that current prescribed cover thicknesses are not enough for concrete without SCM. The authors proposed therefore modified concrete cover thicknesses which also consider the addition of FA and GGBS. Table 2 shows the proposed cover thicknesses for the environmental classes XS2 and XD3 and water to binder (w/b) ratios 0.40 and 0.45.

Table 2 – Suggested concrete cover thicknesses (in mm) for chloride environment [9].

| | CEM I | CEM II/A-S | CEM II/A-V or CEM II/B-V | CEM II/B-S | CEM III/A |
|-------------------------------------|-------|------------|--------------------------------|------------|-----------|
| <i>XS2 (east coast¹)</i> | | | | | |
| w/b 0.45 | 90 | 60 | 60 | 60 | 50 |
| w/b 0.40 | 80 | 50 | 45 | 50 | 45 |
| <i>XD3</i> | | | | | |
| w/b 0.40 | 70 | 45 | 45 | 45 | 45 |

¹Refers to the east coast of Sweden which has a chloride concentration of about 0.4% by mass of seawater.

To evaluate the sensitivity of the cover thicknesses Tang and Löfgren [9] included the uncertainties of the input parameters; chloride threshold, diffusion coefficient at 6 months, surface chloride content and temperature. The results showed that a 10 % variation of the input parameters resulted in a 3 to 5 % variation of the determined cover thicknesses independent of type of concrete. The chloride threshold value was shown to have the lowest influence on the cover thickness (approximately 3 %).

4. LCA OF RC STRUCTURES IN CHLORIDE ENVIRONMENT – A CASE STUDY

The environmental effect of using today's prescriptive cover thicknesses is investigated. The cover thicknesses in Table 1 are compared to the performance based cover thicknesses in Table 2 for concrete mix designs with and without SCM and two w/b ratios.

The following aspects are investigated in the analysis:

- The effect of SCM on service life and material consumption during a period of 100 years. To what extent does the improved durability of concrete with SCM reduce the GWP?
- The effect of introducing a performance based cover thickness on GWP. What would a difference in cover thickness mean?
- The difference in w/b ratio on GWP of RC structure. Concrete with higher w/b ratio has a lower durability and needs therefore a thicker concrete cover but has on the other hand lower clinker content. Is it better for the climate to use concrete with lower w/b ratio or higher?
- The consequences of using today's prescribed cover thicknesses.

4.1 Case study

A bridge edge beam and a bridge pier have been chosen as case studies for the LCA. The bridge edge beam is a sensitive part of a bridge in terms of damages and has a high repair cost and environmental impact due to traffic disturbances. In this case study the edge beam is part of a road bridge and is exposed to de-icing salt which means that it is subjected to chlorides through spraying. This is exposure class XD3 according to EN 206 and limits the w/c ratio to maximum 0.40.

A bridge pier has a load carrying function and is subjected to different chloride exposures which are related to the atmospheric zone, tidal/splash zone and the submerged zone. From a 20 year field study on chloride ingress it has been observed that the submerged zone is the most severe case [24]. For that reason the submerged zone is chosen for the analysis in this case study. The influence of using different w/c ratios is investigated for the pier only as XD3 does not allow a w/b ratio of 0.45. The question is if it is more environmentally friendly to have a concrete with a higher w/c ratio and thus lower clinker content or more beneficial to have a lower w/c ratio where the concrete has a denser structure.

Both case studies are fictive and not related to a specific type of bridge which means that the maintenance will be unknown. Instead a theoretical figure for repair and replacement is used. A cast in situ concrete is assumed for both cases. The reference dimensions for both cases are shown in Table 3 and are based on concrete cover thicknesses according to EKS 10. An adequate distance between piers is assumed.

Table 3 – Specifications of the reference cases.

| Reference case | w/c ratio | Cover thickness | Cross section | Length | Reinforcement |
|------------------|-----------|-----------------|---------------------------|--------|-----------------------------|
| Bridge edge beam | 0.40 | 45 mm | Rectangular 0.5 m x 0.5 m | 10 m | 4 weight-% |
| Bridge pier | 0.40 | 45 mm | Circular 1 m diameter | 6 m | 4 % of cross sectional area |

When the concrete cover thickness is varied it is assumed that the reinforcement position and amount are constant. This means that there will be a change in cross sectional area and thus concrete volume which could be the case when the amount of reinforcement is already optimized and moving the reinforcement inward is not an option. Additionally, it is also a

conservative way of performing the LCA because it adds an extra GWP to the performance based cover thicknesses.

4.2 Concrete mix design

In this study 8 different concrete mix designs, which were developed within a STA project, have been evaluated (Table 4). The mix designs consist of 4 types of binders with varying amount of FA and GGBS and two w/b ratios. No efficiency factor (i.e., a factor = 1) was used in the concrete mixes with SCM which means that w/b ratio is equal to w/c ratio. Mixes with a binder that contains 20 weight-% SCM or less meets the requirements for frost resistance according to SS 137003, the Swedish application of EN 206 [22]. The concrete mixes with 29 % GGBS exceeds the limit but is still included due to a recent study which shows that a GGBS content of up to 40 % of binder may be acceptable with respect to the salt-frost scaling resistance [25]. The mixes also contain superplasticizers and air-entrainer which are not shown in Table 4. This is due to the small amounts used which are assumed to have only a negligible effect on the outcome of the environmental impact.

Table 4 – Mix design of the concretes used in this analysis.

| Mix ID | w/b | OPC [kg/m ³] | FA [kg/m ³] | GGBS [kg/m ³] | Aggregates, crushed [kg/m ³] | Aggregates, natural [kg/m ³] |
|---------------|------|-----------------------------|----------------------------|------------------------------|--|--|
| CEM I 0.40 | 0.40 | 425 | | | 846 | 864 |
| 16% FA 0.40 | 0.40 | 353 | 69 | | 844 | 863 |
| 20% GGBS 0.40 | 0.40 | 340 | | 85 | 842 | 861 |
| 29% GGBS 0.40 | 0.40 | 302 | | 123 | 836 | 854 |
| CEM I 0.45 | 0.45 | 400 | | | 846 | 864 |
| 16% FA 0.45 | 0.45 | 336 | 64 | | 842 | 861 |
| 20% GGBS 0.45 | 0.45 | 320 | | 80 | 841 | 859 |
| 29% GGBS 0.45 | 0.45 | 284 | | 116 | 839 | 858 |

4.3 LCA method

In order to calculate the GWP of the aforementioned concrete structures a LCA method in accordance with EN 15804 [26] is applied. EN 15804 provides core product category rules for construction products and services and also the means for developing a Type III environmental declaration. The GWP is calculated by using the method by IPCC (Intergovernmental Panel on Climate Change) 2013 GWP100a.

The LCA includes the following life-cycle stages:

- Production stage (module A1-A3). It includes raw material extraction, transport of raw material to factory and manufacturing)
- Replacement (module B4). With a system boundary of 100 years.

The service life of the edge beam and pier is included through the replacement stage. For example, if a structure has a service life of 80 years and the system boundary is 100 years, then it would mean that the structure needs to be replaced theoretically 0.25 times to reach those 100 years. In reality, not all structures with a specific service life are repaired at the same time. Some might be repaired earlier and some might be repaired later. This theoretical number represents an average value.

The functional units for the cases are:

1. 1 length meter bridge edge beam with a service life of 100 years. Exposed to de-icing salt.
2. 1 length meter bridge pier with a service life of 100 years. Exposed to marine environment with a 0.4 % chloride concentration.

It should be noted that the LCA does not take into account the construction and maintenance activities at site such as machinery. It only considers the material use.

Life-cycle inventory data were mainly gathered from environmental product declarations (EPD) for the Swedish market and the LCA database ecoinvent version 3 [27]. An inventory of materials and energy is described in Table 5.

Regarding waste products and secondary materials, they are considered to have no environmental burden allocated from the main product unless they have a contribution to the overall revenue that is higher than 1 %. An economic evaluation was performed which showed that the revenue of fly ash and the slag leaving the industrial process can be considered to be very low according to EN 15804 [26]. Hence there is no environmental burden allocated to fly ash and slag waste. However, while fly ash can be utilized directly in the concrete mix without further processing GGBS needs to be grinded and dried before applied. This adds an extra environmental burden to GGBS. Information about GGBS processing was delivered through personal contact with Merox AB [28].

The required energy at the factory is based on information from a Thomas Concrete Group factory in Sweden and has an energy consumption of 18 kWh/m³ electricity and 15 kWh/m³ district heating [29]. The district heating is based on a Swedish mix from Svensk fjärrvärme during the reference year 2014 [30] where the fuels were gathered from ecoinvent v.3. All materials, except for the reinforcement, are transported from real manufacturing places to a concrete factory located in Stockholm. The reinforcement is instead transported directly to the construction site. Data for transport were gathered from Network for Transport Measures (NTM) [31].

Table 5 – GWP of materials and energy sources.

| Resource | Unit | GWP [kg CO ₂ -eq] | Reference |
|----------------------------|-------|------------------------------|----------------------------|
| OPC | 1 ton | 678 | EPD-HCG-20140186-CAD1-EN |
| FA | 1 ton | 0 | |
| GGBS | 1 ton | 88 | [28] |
| Water | 1 ton | 0.28 | Ecoinvent v.3 |
| Aggregates, crushed | 1 ton | 2.4 | Ecoinvent v.3 ¹ |
| Aggregates, natural | 1 ton | 1.7 | Ecoinvent v.3 ¹ |
| Carbon steel reinforcement | 1 ton | 370 | EPD S-P-00305 |
| District heating | 1 kWh | 0.092 | [30] |
| Swedish electricity mix | 1 kWh | 0.056 | Ecoinvent v.3 |

¹ Modified for Swedish conditions.

4.4 Service life modelling

According to Tang and Löfgren [9] the prescribed cover thicknesses for a service life of 100 years are not always sufficient and need therefore to be updated. In order to calculate the service life of reinforced concrete designed with current Swedish regulations, the ERFC (error function complement) model for chloride diffusion in an infinite half-space was used. The influence of concrete ageing is excluded in the model which is a conservative way of calculating the service life.

For the reason that the chloride profile is fixed for each concrete mix due to the same environmental exposures and chloride diffusion properties then the service life will only depend on the relation between two cover thicknesses. This is expressed in equation (1). The service life can be calculated by using the figures of Tang and Löfgren [9], also expressed in Table 2, as a reference which the calculated service life relates to. For example, if a reinforced concrete structure of a certain mix has a cover thickness of 45 mm and it is assumed that the corresponding service life is 100 years then a cover thickness of 40 mm will result in a service life of t years. In this case a 45 mm cover thickness and a service life of 100 years will be the reference.

$$t = t_{ref} \cdot \left(\frac{x}{x_{ref}} \right)^2 \quad (1)$$

Where:

t = service life of concrete with x cover thickness [year]

t_{ref} = service life of reference concrete with x_{ref} cover thickness [year]

x = cover thickness of concrete [mm]

x_{ref} = cover thickness of reference concrete [mm]

5. CLIMATE IMPACT AND SERVICE LIFE OF THE CASE STUDY

5.1 Impact of concrete mix design

It is well known that the climate impact of a concrete mix is highly dependent on the clinker content. When a part of the clinker is replaced with FA or GGBS the climate impact is expected to decrease accordingly. Figure 1 shows the GWP of the concrete mix designs used in this study divided into the life cycle stages: material production, transport to factory and production at factory. It can be noted that a clinker replacement with 16 % FA results in a 15 % reduction of GWP compared to CEM I concrete for both w/b ratios. An increase in w/b ratio results in an approximately 6 % decrease in GWP. Transport to factory and production at factory has a slight impact on the GWP.

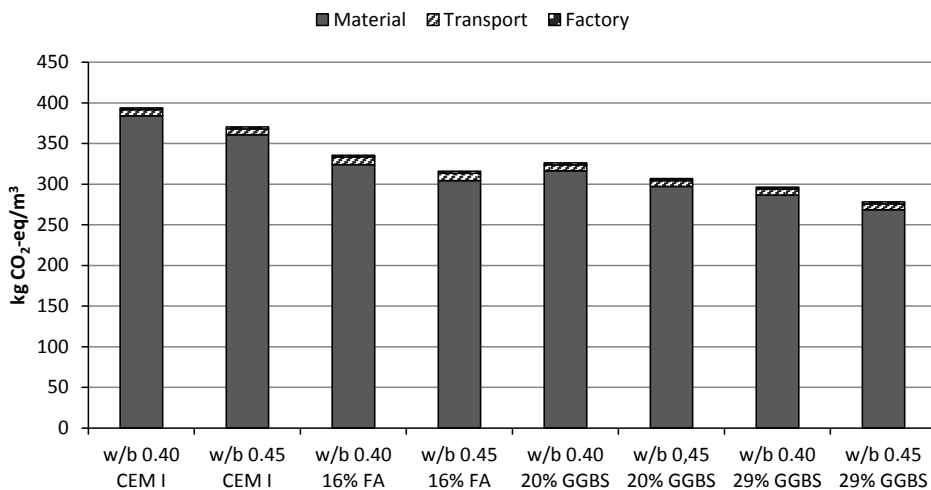


Figure 1 – GWP of 1 m³ of concrete mixes used in this research, divided into three life cycle stages

5.2 Impact of edge beam and pier during production stage

When the concrete mixes are applied to a reinforced bridge edge beam with a cover thickness according to today's Swedish regulations the result show a decrease in GWP of 14 %, 16 % and 23 % for the concrete mixes with 16 % FA, 20 % GGBS and 29 % GGBS respectively, compared with CEM I (Figure 2). These greenhouse gases are emitted during the production stage of the concrete and reinforcement. For the proposed performance based concrete cover thicknesses the effect of lower chloride ingress due to addition of SCM may be visualized. In order to have a sufficient cover thickness which enables a service life of 100 years the cover needs to be increased by 25 mm. This leads, in this case, to an increase in volume which in turn results in an increase in GWP by 19 %. According to the performance based approach an addition of 16 % FA have the potential to lower the GWP by 27 %, which is a big impact.

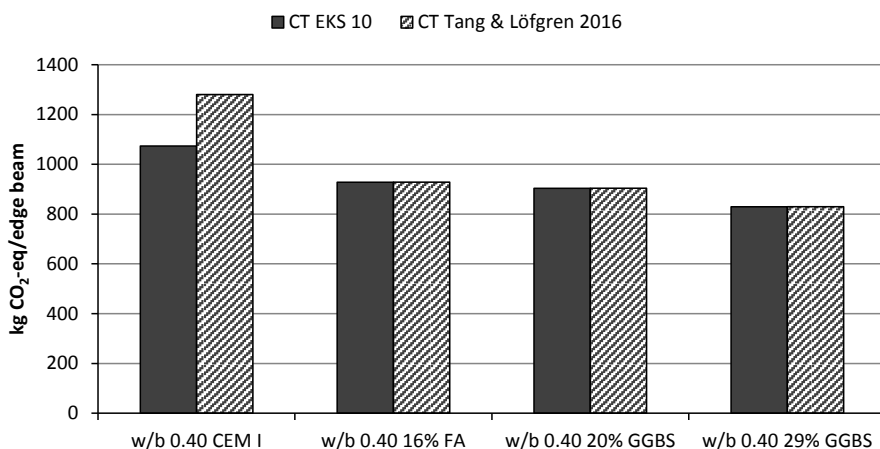


Figure 2 – GWP from production of one bridge edge beam.

Concerning the bridge pier, except for an addition of SCM the effect of w/b ratio on the GWP has also been investigated. The results revealed that there is not a significant difference between w/b ratios as the extra cover thickness compensate for a reduction in clinker content (Figure 3). Still there is a notable difference between CEM I and concrete with SCM.

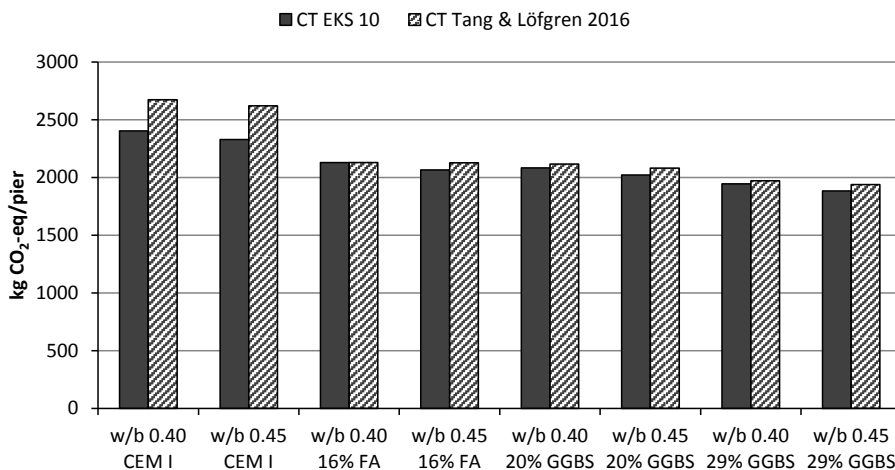


Figure 3 – GWP from production of one bridge pier.

The GWP of the reinforcement is 7 % of the total GWP for the edge beam and 20 % for the pier.

5.3 Impact of edge beam and pier including service life

The cover thicknesses according to Tang and Löfgren [9] represent a service life of 100 years. The cover thicknesses according to standard are fixed and do not vary with binder type which

leads to a variation in service life. Table 7 shows the calculated service lives for a fixed concrete cover according to the standard using Eq. (1).

Table 7 – Calculated service life of edge beam and pier with a cover thickness according to EKS 10 [22].

| | Cover thickness | Mix – CEM I [years] | Mix – 16%FA [years] | Mix – 20%GGBS [years] | Mix – 29%GGBS [years] |
|--------------------|-----------------|---------------------|---------------------|-----------------------|-----------------------|
| Edge beam w/b 0.40 | 45 mm | 41 | 100 | 100 | 100 |
| Pier w/b 0.40 | 45 mm | 32 | 100 | 81 | 81 |
| Pier w/b 0.45 | 50 mm | 31 | 69 | 69 | 69 |

When the service life and hence the need of repair and replacement is included in the LCA the effect of the chloride ingress becomes clearer. If a fixed cover thickness is used for all binder types then the results reveal that there will be a dramatic increase in GWP for concrete with CEM I for both exposure classes due to the better durability performance of concrete with SCM. For the bridge edge beam with CEM I this would mean a replacement of 1.4 times during a period of 100 years which equals a total GWP of 2597 kg CO₂-eq (Figure 4). An addition of fly ash could in this case reduce both CO₂ emissions and costs. Regarding the pier the results show an even bigger difference with a replacement ratio of 1.7 times which equals a total GWP of 7598 kg CO₂-eq (Figure 5). However, a bridge pier is rarely replaced and not all of the reinforcement is replaced either which could mean a lower GWP in reality. Nevertheless, there is still a significant difference in GWP for concrete with and without SCM.

If a w/b of 0.45 was to be used instead of a w/b of 0.40 when designing a pier according to EKS 10 [22] then this would lead to a reduced service life for all binder types. A small increase in cover thickness has a big reduction in GWP. When a performance based cover thickness is applied then there is not a significant difference between w/b ratios 0.40 and 0.45.

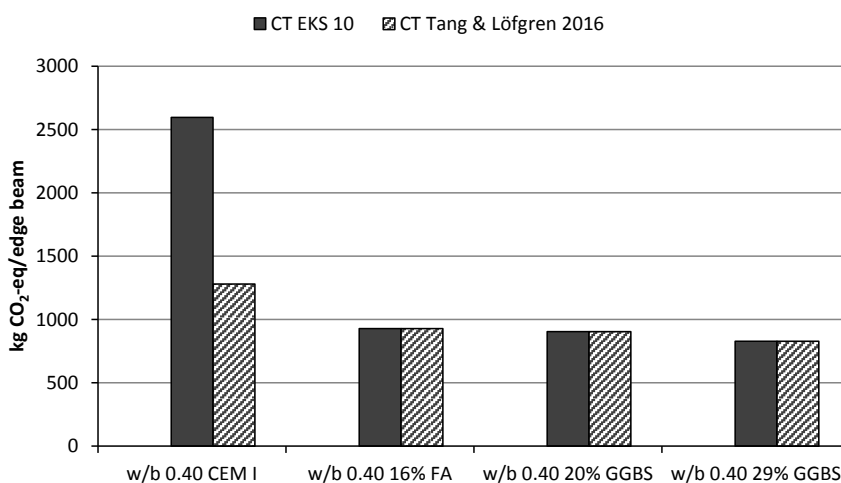


Figure 4 – GWP from production and replacement of bridge edge beam.

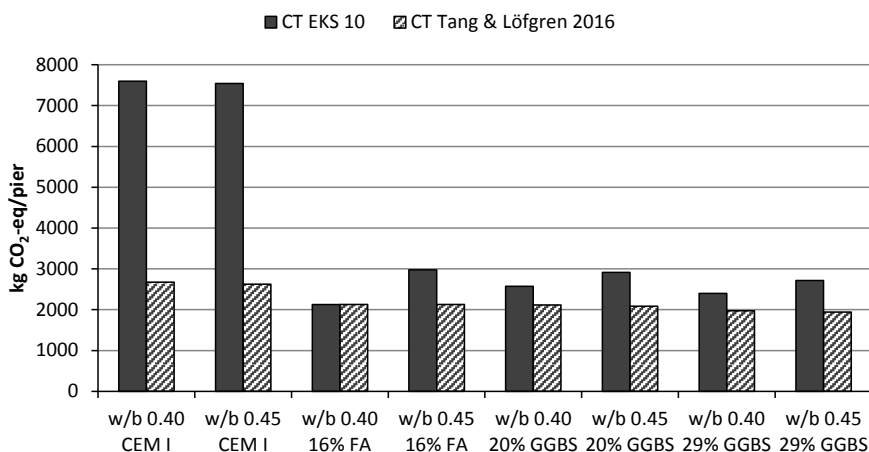


Figure 5 – GWP from production and replacement of bridge pier.

5.4 Influence of SCM on service life design and CO₂

The results in this study show that an addition of FA and GGBS lowers the climate impact not only due to lower clinker content but also by increasing the durability properties of concrete exposed to chlorides. By adapting the cover thickness after type of binder major savings in GWP can be achieved. The relation between cover thickness, service life, binder type and GWP for a bridge pier with two dimensions, 0.5 m and 1 m in diameter, is expressed in Figure 6. Only the concrete has been taken into consideration. In this case where the reinforcement is fixed a GWP for a specific type of reinforcement can be added to the GWP for a total climate impact of the structure. The binder types which are analyzed in a performance based approach are CEM I and 16 % FA for w/b 0.40.

Figure 6 shows that when designing a pier to last a certain amount of years, a cover thickness and GWP will be obtained depending on binder type. For example would a service life of 100 years result in a cover thickness of 80 mm for CEM I and 45 mm for a binder with 16 % FA. The GWP would then be 1.0 kg CO₂-eq/m year for CEM I and 0.66 kg CO₂-eq/m year for 16 % FA, a 34 % difference. The GWP can also be calculated the other way around by first choosing cover thickness. If a pier is designed to have a concrete cover of 50 mm then using a binder with 16 % FA instead of CEM I would increase the service life by 80 years which is equal to a 72 % decrease in GWP.

The cross-section area also has an influence on the GWP. The smaller the cross-section area is the greater will it be affected by the binder type and thus cover thickness. The reason is that the total relative volume change due to an increase or decrease in cover thickness will be greater.

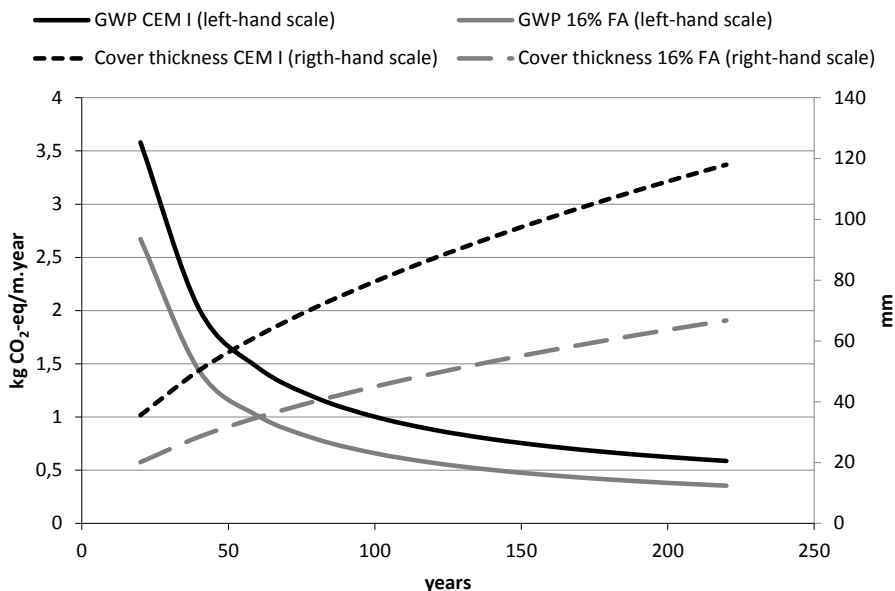


Figure 6 – Relation between GWP, service life, cover thickness and binder type.

6. DISCUSSION

This study shows that there is a twofold effect of SCM on the GWP of reinforced concrete structures exposed to chlorides. Not only does it reduce the climate impact by lowering the clinker content but it also extends the service life through an improvement in durability. This reduces the demand for repair and replacement, thus saving resources through the whole life cycle.

The results showed that today's cover thicknesses are, for the most part, not adequate in order to reach a service life of 100 years. For an edge beam with CEM I and w/b 0.40 this would result in 1.4 replacements during the service life which is in line with today's maintenance of 1 replacement and 3 repairs. If, however, the cover thickness is instead increased from 45 mm to 70 mm or if fly ash is added then the need for repair would be dramatically reduced resulting in a lower GWP. A reduced maintenance does not only reduce the climate impact it also reduces user and societal costs significantly, especially for heavily trafficked road bridges.

For a submerged condition, XS2, an even bigger reduction in GWP can be made. The analysis also revealed that there is not a significant difference between w/b 0.40 and 0.45. Nevertheless, this analysis investigates the effect of the concrete volume only, meaning that the reinforcement is fixed to a constant amount and location. Another approach is to also investigate the effect of the reinforcement by fixing the cross-section area.

Consequences of ignoring the durability in LCA are wrong assumptions for the service life and maintenance which result in misleading environmental impact results. Durability and service life should be included in the environmental optimization of reinforced concrete structures.

Introducing a performance-based approach for service life design could help reducing the GWP as it could open up for usage of new binder types and concrete mix design.

To reduce the climate impact of concrete infrastructures it is suggested that a minimum amount of FA or GGBS is encouraged by STA for bridges exposed to chlorides. It would not only improve the durability but also the sustainability potential defined by Müller et al. [3] by all three approaches; lower GWP in mix design, reduction in concrete volume and increased service life.

7. CONCLUSIONS AND FUTURE RESEARCH

Based on the results of this study it can be concluded that there is a need to implement performance based cover thicknesses. The following observation could be made for concrete with SCM in a chloride environment:

- A lower climate impact per cubic meter of concrete due to lower clinker content.
- No significant difference between w/b ratios due to a compensation of an increase in concrete volume.
- A longer service life for bridges due to lower maintenance which results in a lower climate impact per year.
- Lower owner, user and societal costs in the case of bridge edge beams.

Addition of FA or GGBS in concrete is an efficient way to reduce the climate impact of the built environment. Also, by adapting performance based concrete cover thicknesses that include SCMs as well would greatly improve the quality of LCA and LCC of new projects and help pushing the industry towards a more sustainable development and an increased demand of existing and new SCMs.

The following directions for future research are suggested:

- Including an analysis of the reinforcement by keeping the cross-section area of the edge beam or pier constant while changing the amount and location of the reinforcement.
- A structural analysis could also be included in this type of study by adding the load bearing capacity to the functional unit. In that way different design options could be investigated.
- Including other durable materials such as ultra-high performance concrete and taking into consideration the possibility for a more slender structure.
- Investigating other deterioration mechanisms such as frost attack or the effect of multiple deterioration mechanisms.
- Adding LCC to the analysis.

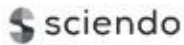
ACKNOWLEDGEMENT

This study was financed by the Swedish Transport Administration and the CBI Foundation. The authors would also like to acknowledge Majid Solat Yavari for contributing with a bridge pier case.

REFERENCES

1. Trafikverket: ”Klimatkrav i byggprojekt - ett viktigt steg mot klimatneutral infrastruktur,” <http://www.trafikverket.se/om-oss/nyheter/Nationellt/2016-02/klimatkrav-i-byggprojekt---ett-viktigt-steg-mot-klimatneutral-infrastruktur/>, accessed 2017. (In Swedish.)
2. Du G: “Life cycle assessment of bridges, model development and case studies,” *Doctoral thesis*, KTH Royal Institute of Technology, Dept. of Civil & Architectural Engineering, Stockholm, Sweden, 2015, 151 pp.
3. Müller H, Haist M & Vogel M: “Assessment of the Sustainability Potential of Concrete and Concrete Structures Considering their Environmental Impact, Performance and Lifetime,” *Construction and Building Materials*, Vol. 67, 2014, pp 321-337.
4. Racutanu G: The Real Service Life of Swedish Road Bridges - A Case Study, *Doctoral thesis*, KTH Royal Institute of Technology, 2001.
5. Mattsson HÅ: “Integrated Bridge Maintenance - Evaluation of a pilot project and future perspectives,” *Doctoral thesis*, KTH Royal Institute of Technology, Dept. of Civil & Architectural Engineering, Stockholm, Sweden, 2008.
6. Safi M: “Life-Cycle Costing: Applications and Implementations in Bridge Investment and Management,” *Doctoral thesis*, KTH Royal Institute of Technology, Dept. of Civil & Architectural Engineering, Stockholm, Sweden, 2013.
7. Veganzones J, Sundquist H, Pettersson L & Karoumi R: “Life-Cycle Cost analysis as a tool in the developing process for new bridge edge beam solutions,” *Structure and Infrastructure Engineering*, Vol. 49, 2015, pp 1737-17746.
8. Tang L, Utgenannt P & Boubitas D: “Durability and Service Life Prediction of Reinforced Concrete Structures,” *Journal of the Chinese Ceramic Society*, Vol 43, 2015.
9. Tang L & Löfgren I: “Evaluation of Durability of Concrete with Mineral Additions with regard to Chloride-Induced Corrosion,” *Report No. 2016-4*, Chalmers University of Technology, Dept. of Civil Engineering, Gothenburg, Sweden, 2016.
10. Streblov HH: “Mechanisms of pitting corrosion, Corrosion mechanism in theory in practice,” 2nd edition (P. Marcus), Marcel Dekker Inc., New York, USA, 2002.
11. Arya C, Buenfeld NR & Newman JB: “Factors Influencing chloride binding in concrete,” *Cement and Concrete Research*, 20(2), 1990, pp 291-300.
12. Nilsson LO, Poulsen E, Sandberg P, Sorensen HE & Klinghoffer O: “Chloride penetration into concrete – state of the art: Transport processes, corrosion initiation, test methods and prediction models,” *HETEK Report No. 53*, Danish Road Directorate, Copenhagen, Denmark, 1996.
13. Tuutti K: “Corrosion of steel in concrete,” *CBI research FO 4:82*, Swedish Cement and Concrete Research Institute, Stockholm, Sweden, 1982.
14. Byfors K: “Influence of silica fume and flyash on chloride diffusion and pH values in cement paste,” *Cement and Concrete Research*, Vol. 17, 1987, pp. 115-130.
15. Angst U, Elsener B, Larsen CK & Vennesland Ø: “Critical chloride content in reinforced concrete – a review,” *Cement and Concrete Research*, Vol. 39 (12), 2009, pp 1122-1138.
16. Khan MI: “Nanostructure and microstructure of cement concrete incorporating multicementitious composites,” *Transportation Research Record: Journal of the Transportation Research Board*, No. 2141, Washington D.C., 2010, pp. 21-27.
17. Shi X & Xie N: Fortune, K. & Gong, J.: “Durability of steel reinforced concrete in chloride environments: An overview,” *Construction and Building Materials*, 2012, pp 125-138.
18. Fib bulletin 34: “Model code for service life design”, fédération internationale du béton (fib), Lausanne, Switzerland, 2006.

19. SS-ISO 16204:2012: “Durability – Service life design of concrete structures,” Swedish Standards Institute, Stockholm, Sweden, 2015.
20. CEN: “Concrete – Specification, performance, production and conformity EN 206:2013, European committee for standardization,” Brussels, Belgium, 2013.
21. SS 137003:2015: “Concrete – Application of SS-EN 206 in Sweden,” Swedish Standards Institute, Stockholm, Sweden 2015.
22. Boverket: ”Boverkets byggregler - EKS 10,” Boverket, Karlskrona, Sweden 2016. (In Swedish).
23. Tang L, Utgenannt P & Boubitsas D: “Durability and Service Life Prediction of Reinforced Concrete Structures,” *Journal of the Chinese Ceramics Society*, 2015, pp 1408-1412.
24. Boubitsas D, Tang L & Utgenannt P: “Chloride Ingress in Concrete Exposed to Marine Environment - Field data up to 20 years’ exposure,” *CBI Report* to SBUF Project 12684, Swedish Cement and Concrete Research Institute, Stockholm, Sweden., 2014.
25. Löfgren I, Esping O & Lindvall A: “The influence of carbonation and age on salt frost scaling of concrete with mineral addition,” *Proceedings*, International RILEM Conference on Materials, Technical University of Denmark, Lyngby, Denmark, 22-24 August 2016.
26. CEN: “Sustainability of Construction Works – Environmental Product Declarations – Core Rules for the Product Category of Construction Products EN 15804, European committee for standardization,”, Brussels, Belgium, 2012.
27. Wernet G, Bauer C, Steubing B, Reinhard J, Moreno-Ruiz E & Weidema B: “The ecoinvent database version 3 (part I): overview and methodology,” *International Journal of Life Cycle Assessment*, [online] 21(9), pp.1218–1230. 2016. Available at: <<http://link.springer.com/10.1007/s11367-016-1087-8>>.
28. Personal communication with Merox AB, 2012.
29. Personal communication with Thomas Concrete Group, 2016.
30. Svensk Fjärrvärme: Fjärrvärmestatistik, <https://www.energiforetagen.se/statistik/fjarrvarmestatistik/tillford-energi/> , 2014.
31. Network for Transport Measures: NTMcalc – Calculation of Environmental Impact, <https://www.transportmeasures.org/en/> , accessed 2016.



DOI: 10.2478/ncr-2018-0006

ISSN online 2545-2819

ISSN print 0800-6377

© Article authors. This is an open access article distributed under the Creative Commons Attribution-NonCommercial-NoDerivs licens. (<http://creativecommons.org/licenses/by-nc-nd/3.0/>).

Received: March 15, 2018

Revision received: May 11, 2018

Accepted: May 11, 2018

Dynamic Measurements for Determining Poisson's Ratio of Young Concrete



Lamis Ahmed
Ph.D., Assistant Professor
KTH Royal Institute of Technology
Division of Concrete Structures
SE-100 44 STOCKHOLM, Sweden
e-mail: lamis.ahmed@byv.kth.se

ABSTRACT

Knowledge of the elastic properties of concrete at early age is often a pre-requisite for numerical calculations. This paper discusses the use of a laboratory technique for determining Poisson's ratio at early concrete age. A non-destructive test set-up using the impact resonance method has been tested and evaluated. With the method, it has been possible to obtain results already at 7 hours of concrete age. Poisson's ratio is found to decrease sharply during the first 24 hours to reach a value of 0.08 and then increase to approximately 0.15 after seven days.

Key words: Modelling, testing, Poisson's ratio, young concrete

1. INTRODUCTION

Young concrete is studied, with a special focus on the period from the first contact between cement and water and up to 12 hours of age, which often is regarded as the most critical period with respect to e.g. vibration damage [1]. In some structural applications, for example in tunnelling, mining, bridge deck maintenance, construction of hydropower and nuclear power facilities, there is a need to control the response of young concrete that can be subjected to different types of dynamic loads, for example from impact vibration. Due to difficulties in performing experiments on young concrete, for example early formwork removal problems, simulation models are needed as a complement. These models require insertion of material data for concrete, such as the development of compressive strength, tensile strength, modulus of

elasticity and Poisson's ratio. It is very important to understand how elastic properties of concrete develop with time, which can be subjected to the effects of thermal gradients and autogenous shrinkage. In numerical tests [1], it was found that Poisson's ratio has a significant effect on maximum crack width for young concrete models. For example, the simulated maximum crack widths decreased from 0.8 to 0.4 mm when the Poisson's ratio was reduced from 0.2 to 0.1.

Of previous studies that measured Poisson's ratio at an early age, most concluded that this parameter is insensitive to age, i.e. the measured Poisson's ratio shows practically the same value for all ages and curing conditions. Poisson's ratio can be obtained from both static and dynamic test methods. The static test is the most commonly used to determine Poisson's ratio where a concrete cylinder is subjected to a force in the longitudinal direction. The concrete cylinder will be shorter in this direction, but also thicker in the transversal direction. The relation between transversal deformation and the longitudinal direction is called Poisson's ratio. The static Poisson's ratio normally for hardened concrete varies between 0.15-0.25 [2]. For a fluid like material, the Poisson's ratio is 0.5. Fresh concrete can be regarded as a fluid. This means that Poisson's ratio for concrete at a very early age should be close to 0.5 but cannot exceed this value [3].

In static tests, however, compressive forces produce deformations which result in a reduction in the volume of the specimen, whereas the dynamic tests cause little or no deformation. In one study, a hypothetical relation between the static and dynamic values of Poisson's ratio and age for saturated concrete mixes was developed, see Figure 1. In this relationship, the static value of Poisson's ratio tends towards a dynamic value of Poisson's ratio at the infinite time. The basis of this hypothesis is that weak, porous or dry paste, mortars and concrete will have a low Poisson's ratio due to the occurrence of plastic deformations and reductions in volume which are more significant than in strong pastes [2].

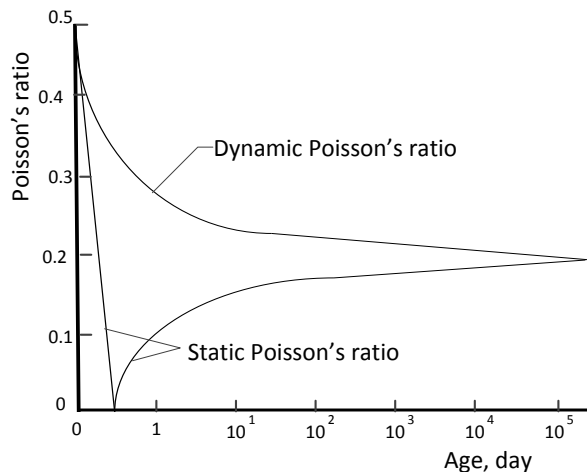


Figure 1 – Hypothetical relation between the static and dynamic Poisson's ratios and age for saturated concrete mix [2].

However, two important studies [3] and [4], describe a significant decrease in Poisson’s ratio at very early ages. A static test was performed in [3] and showed decreasing trends for static Poisson’s ratio, from approximately 0.4 to 0.1 during the first 10-15 hours, at a compressive strength of about 1 MPa, Figure 2 (a). After this, Poisson’s ratio increases with strength growth. Poisson’s ratio was determined via the deformations obtained at a stress level of 1/3 of the compressive strength. The results of an investigation on high-performance concrete using the pulse velocity method [4] are showed a similar trend. It can be shown from this dynamic test that dynamic Poisson’s ratio is decreasing during a short period of about 9 to 18 hours, reaching a value of 0.14, then increasing to its final value after seven days, Figure 2 (b). Although some experimental results [5] show increasing values of Poisson’s ratio with age during the first 12 hours, for example up to about 25%, this is often considered as a close to constant value. To date, there is no information given in the Eurocode 2 [6] about how to specify Poisson’s ratio at early ages.

It is thus likely that this parameter has a significant effect on numerical results for early age concrete [1]. Knowing Poisson’s ratio is required to simulate experimental behaviour by numerical analyses. Therefore, a small-scale laboratory test was performed to find a technique to measure Poisson’s ratio at early concrete age, which is here summarized. Moreover, the aim was to investigate the influence on the static and dynamic Poisson’s ratios according to the lines suggested in Figure 1.

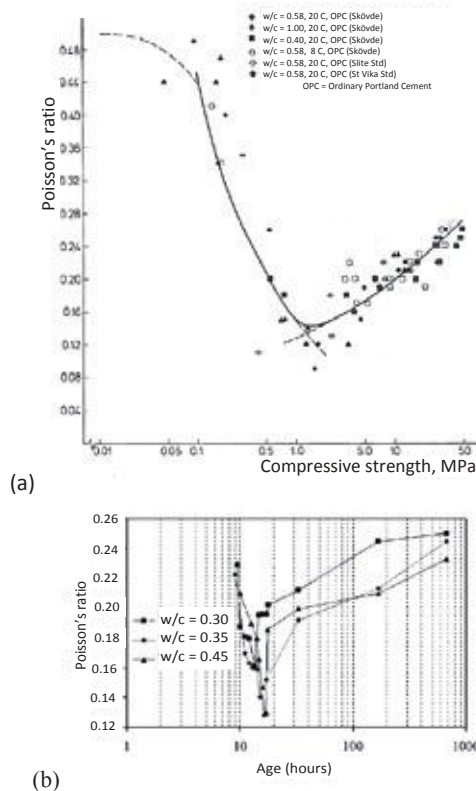


Figure 2 – Evolution of Poisson’s ratio at early age; (a) static test [3] and (b) dynamic test [4].

2. EXPERIMENTAL WORK

2.1 Materials

In this study, two concrete prisms of $160 \times 100 \times 800 \text{ mm}^3$ were cast. The concrete composition is presented in Table 1, chosen on the basis of laboratory investigations performed in [7]. A series of 150 mm cubes was cast to determine the development of compressive strength which was possible from 10 hours. The equation, where t is concrete age in days, is derived from tested cubes, giving the relation between the age of concrete and compressive strength (f_c) [7] as:

Table 1 – Compositions and mechanical property of the concrete used in the tests.

| Composition | Content |
|--|---------|
| Cement (CEM I 42.5 N – SR 3 MH), kg/m^3 | 495 |
| Water, kg/m^3 | 220 |
| Aggregate 0-8 mm, kg/m^3 | 1540 |
| Silika U/D, kg/m^3 | 20 |
| Glenium, kg/m^3 | 4 |
| Compressive strength, cube test MPa | 84 |

$$f_c(t) = 106.9 e^{-1.79/t^{0.51}} \text{ for } 0 \leq t \leq 112 \text{ days} \quad (1)$$

Eurocode 2 [6] provides an empirical equation to estimate the relative compressive strength of concrete at various ages as follows:

$$f_{cm}(t) = \beta_{cc}(t) \cdot f_{cm} \quad (2)$$

$$\beta_{cc}(t) = e^{s \cdot [1 - \frac{28}{t}]^{0.5}} \quad (3)$$

where:

- $f_{cm}(t)$ mean compressive strength of concrete at age t , MPa
- f_{cm} mean compressive strength of concrete at age 28 days and equals to 0.8 of cube strength, MPa
- $\beta_{cc}(t)$ function to describe the development of compressive strength with time
- s coefficient which depends on the type of cement and is here assumed to be 0.2 for f_{cm} greater than 60 MPa [6].

2.2 Determination of resonant frequencies

The focus of this pilot test was to evaluate some dynamic properties of concrete using impact resonance method [8] where a supported specimen is struck with a small impactor and the specimen response is measured by three accelerometers on the specimen $p1$, $p2$ and $p3$. The output of the accelerometer is recorded. Three accelerometers were positioned onto the specimen, as shown in Figure 3, enabling recording of particle accelerations as the three fundamental longitudinal, torsional and transverse resonant frequencies of the concrete, respectively. The fundamental frequencies for the three different modes of vibration are obtained by proper location of the impact point and the accelerometers. The recording time was

approximately 0.035 s with a sampling frequency of 9600 Hz, the highest possible. According to [9], the recorded signals of impact must be low-pass filtered before the data are sampled. In order to prevent out-of-band signals from being improperly interpreted within the analysis range, a phenomenon known as 'aliasing', the transducer signals were filtered using a low-pass (Bessel) filter with a cut-off frequency 2400 Hz, of available in the data acquisition system.

Frequency spectra were obtained using the fast Fourier transform (FFT) routines of the Matlab numeric software [10]. Using the FFT introduces limitations in the resolution of the spectrum so that it is only possible to obtain information on frequencies up to the Nyquist sampling frequency [9], i.e. here 4800 Hz. It should be noted that the number of longitudinal resonance frequencies measured up to this frequency depends on the material and the boundary condition. For example, the acceleration–frequency spectra for the three points are plotted in Figure 4. The obtained longitudinal and torsional frequencies are given in Table 2.

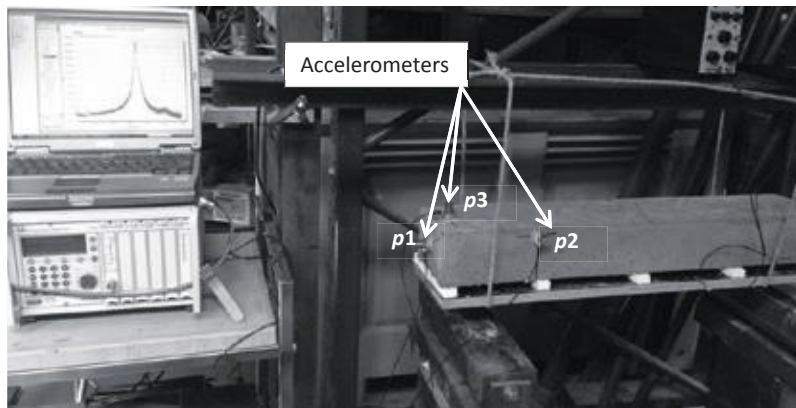
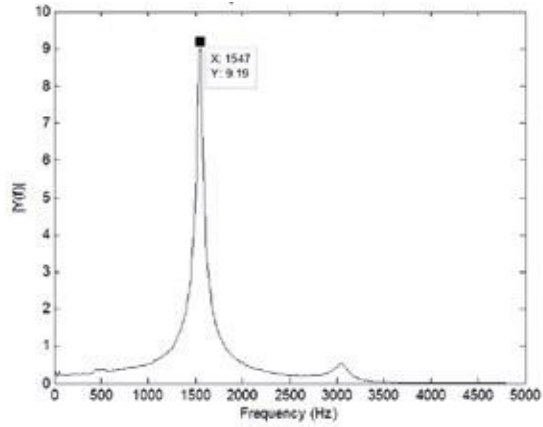


Figure 3 – The suspended prism and the position of the accelerometers according to the testing standard [7].

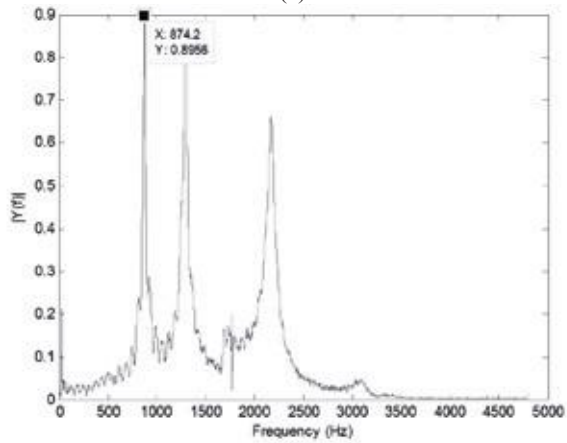
Table 2 – Measured frequencies and calculated longitudinal and torsional modulus of elasticity and Poisson's ratios

| Curing age (hours) | Longitudinal frequency (Hz) | Torsional frequency (Hz) | Longitudinal modulus of elasticity (GPa) | Torsional modulus of elasticity (GPa) | Estimated Poisson's ratio |
|--------------------|-----------------------------|--------------------------|--|---------------------------------------|---------------------------|
| 7.0 | (526) | (271) | 1.59 | 0.61 | 0.294 |
| 7.5 | 951 | 277 | 5.25 | 2.11 | 0.242 |
| 8.0 | (693) | (374) | 2.75 | 1.17 | 0.179 |
| 8.5 | (749) | (412) | 3.22 | 1.42 | 0.135 |
| 9.0 | (880) | (447) | 3.89 | 1.72 | 0.131 |
| 9.5 | (824) | (454) | 4.44 | 1.98 | 0.121 |
| 10.0 | (941), 1369 | (520), 773 | 5.08, 10.74 | 2.26, 4.99 | 0.103* |
| 11.0 | (1049), 1460 | (590), 829 | 6.31, 12.22 | 2.91, 5.74 | 0.084* |
| 12.0 | 1547 | 874 | 12.22 | 5.74 | 0.076 |
| 14.0 | 1730 | 975 | 13.72 | 6.38 | 0.081 |
| 15.0 | 1787 | 1003 | 17.16 | 7.93 | 0.090 |
| 18.0 | 1927 | 1076 | 18.30 | 8.40 | 0.101 |
| 24.0 | 2041 | 1140 | 21.28 | 9.66 | 0.101 |
| 30.0 | 2110 | 1175 | 23.88 | 10.85 | 0.107 |
| 72.0 | 2295 | 1255 | 25.52 | 11.52 | 0.148 |
| 144.0 | 2375 | 1300 | 30.19 | 13.14 | 0.148 |
| 168.0 | 2385 | 1304 | 30.19 | 13.14 | 0.146 |

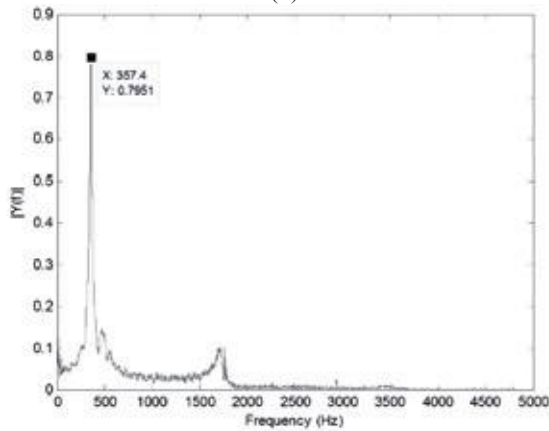
- The values within parentheses refer to prism No. 2., - * average value of two prisms



(a)



(b)



(c)

Figure 4 – Example of the acceleration–frequency spectra of (a) longitudinal (b) torsional and (c) transverse vibrations of 12 hr concrete curing age.

2.3 Determination of dynamic moduli of elasticity

To estimate the dynamic modulus of elasticity of concrete, a resonance frequency tests according to ASTM C215-14 [8] was used. The dynamic modulus of elasticity is generally greater than the static modulus. The difference between dynamic and static moduli might be based on the fact that the nonhomogeneous characteristics of concrete affect the two moduli in different ways [11]. The Eurocode 2 [6] provides an empirical equation to estimate the static modulus of elasticity at the early concrete age as follows:

$$E_{ci}(t) = \beta_E(t) \cdot E_{ci} \quad (4)$$

$$\beta_E = [\beta_{cc}(t)]^{0.5} \quad (5)$$

$$E_{ci} = E_{c0} \cdot \alpha_E \left(\frac{f_m}{10}\right)^{1/3} \quad (6)$$

where:

| | |
|-------------------------|---|
| $E_{ci}(t)$ | tangent modulus of elasticity of concrete at age t |
| E_{ci} | tangent modulus of elasticity of concrete at age of 28 days, MPa |
| $E_{c0} \cdot \alpha_E$ | equal to 20.5 GPa, where a quartzitic aggregate type is assumed. |
| β_E | function to describe the development of modulus of elasticity with time |
| $\beta_{cc}(t)$ | coefficient according to Eq. 3 |

From the longitudinal frequency in Table 2, the dynamic modulus of elasticity (E_{dy}) was calculated according to [7] as follows:

$$E_{dy} = Dm f_L^2 \quad (7)$$

where:

| | |
|-------|--|
| m | mass of specimen, kg |
| D | $4(L/bd)$, m^{-1} for a prism, L is the length, b is the width and d is the depth |
| f_L | fundamental longitudinal frequency, Hz |

The longitudinal resonant frequency is measured for each specimen immediately after removal from the frame at the specified age. The density of the concrete is assumed as 2265 kg/m^3 , equal to the concrete type used in Table 1 [7]. The calculated longitudinal moduli of elasticity are presented in Table 2.

2.4 Determination of Poisson's ratio of young concrete

To calculate the dynamic Poisson's ratio (μ) the ratio of lateral to longitudinal strain for an isotropic solid was used, as follows [8]:

$$\mu = \left(\frac{E}{2G}\right) - 1 \quad (8)$$

where:

| | |
|-----|-----------------------|
| E | modulus of elasticity |
| G | modulus of rigidity |

In this study, the longitudinal modulus of elasticity, presented in Table 2 is calculated according to Eq. (7). Based on the fundamental torsional frequency, the modulus of rigidity was calculated as follows [8]:

$$G = Bm f_{T0}^2 \quad (9)$$

where:

f_{T0} fundamental torsional frequency, Hz,
 B $(a/b + b/a)/[4a/b - 2.52(a/b)^2 + 0.21(a/b)^6]$ for a rectangular prism whose cross-sectional dimensions are a and b , m, with a less than b .

The torsional moduli of elasticity and Poisson’s ratio are calculated and presented in Table 2.

3. RESULTS AND DISCUSSIONS

The growth of the Poisson’s ratio during the seven days is shown in Figure 5 (a). This demonstrates the evolution of Poisson’s ratio as a function of time for two test prisms. It can be seen that during the first 12 hours, a significant decrease of Poisson’s ratio occurs, which after that stabilises. By using Eq. (1), a corresponding curve for the relationship between compressive strength and Poisson’s ratio can also be presented in Figure 5 (b).

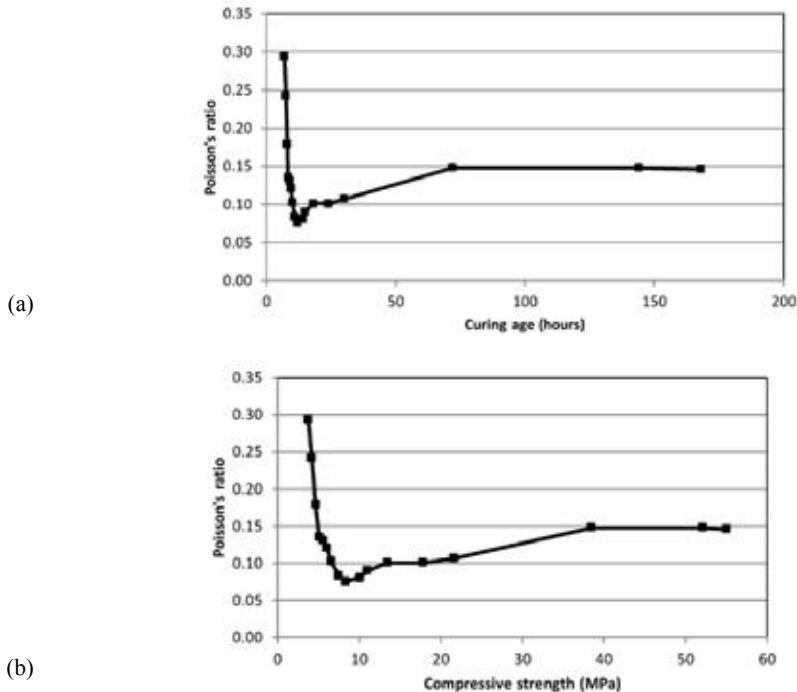


Figure 5 – Poisson’s ratio versus (a) curing age and (b) compressive strength.

The growth of the compressive strength by applying different formulas, i.e. Eq. (1) and (2) according to [7] and Eurocode 2 [6] respectively, is shown in Figure 6. This figure shows that the Eurocode 2 equation (Eq. 2) worked well to predict the development of the compressive strength of the experimental values obtained from [7]. It should be noted that Eq. (1) has been derived from test data of concrete cubes that were conditioned in +20°C and 100% humidity (in water) before testing.

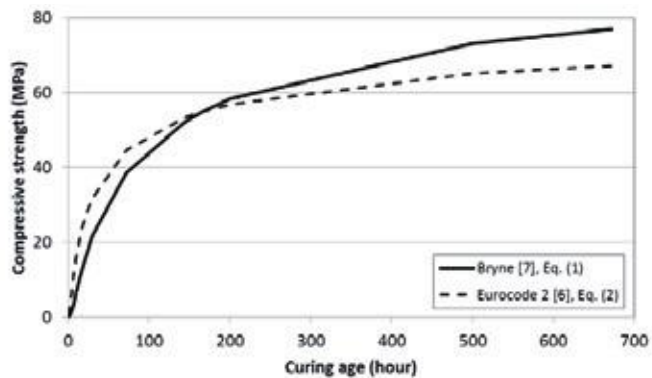


Figure 6 – Development of the compressive strength with time.

The growth of the dynamic modulus of elasticity based on the longitudinal resonant frequency and during the first 7 days is shown in Figure 7, together with the corresponding curve for the static modulus of elasticity by using Eq. (4). As expected, E_{dy} is always greater than E_{ci} . The difference between the two moduli decreases as concrete strength develops with time. The dynamic elastic modulus is generally 60, 33, and 14 % higher than the static elastic modulus for 1, 3 and 7 days curing age, respectively.

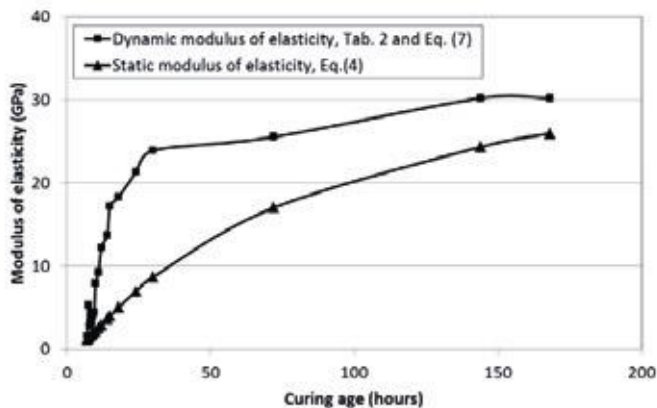


Figure7 – Development of the static and dynamic moduli of elasticity with time.

4. CONCLUSION

The purpose of this study was to test and evaluate an experimental technique for estimation of the development of Poisson's ratio and to obtain a better understanding of the test used to compute the dynamic Poisson's ratio. From the results, it can be observed that the Poisson's ratio to a great extent depends on concrete age during the first few hours after casting, see Figure 5 (a). The measurement results showed similar decreasing trends as previously suggested for other concrete types and methods in [3,4]. It can be observed that the possible relationship of dynamic Poisson's ratio with age in Figure 1 is not valid and the static and dynamic Poisson's ratios in concrete have similar decreasing trends. This behaviour may be caused by the composite nature of concrete rather than the used test method.

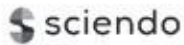
Both static and dynamic moduli of elasticity were calculated. As expected the values of dynamic modulus of elasticity is higher than static modulus for this concrete mix, in which dynamic modulus might trend towards static at the hardened concrete stage.

The used impact resonance method, in this study, was sensitive to the specimen dimensions and density of the concrete. This study can be used as a means for a more comprehensive programme research to investigate the characteristic of the mix on the Poisson's ratio. Not only would it provide a better understanding of internal mechanisms, but also to establish consistent and accurate formulas to compute Poisson's ratio that has an important role in the model analysis.

REFERENCES

1. Ahmed L, Ansell A & Malm R: "Numerical Modelling and Evaluation of Laboratory Tests with Impact Loaded Young Concrete Prisms," *Materials and Structures*, Vol. 49, No. 11, November 2016, pp. 4691-4704.
2. Anson M & Newman K: "The Effect of Mix Proportions and Method of Testing on Poisson's Ratio for Mortars and Concretes," *Magazine of Concrete Research*, Vol. 18, No. 56, September 1966, pp. 115-130.
3. Byfors J: "Plain Concrete at Early Ages," Research Fo 3:80, Swedish Cement and Concrete Institute, Stockholm, 1980, 464 p.
4. Mesbah H A, Lachemi M & Aitcin P-C: "Determination of Elastic Properties of High-Performance Concrete at Early Ages," *ACI Material Journal*, Vol. 99, No.1, January 2002, pp. 37-41.
5. Oluokun F A, Burdette E G & Deatherage J H: "Elastic Modulus, Poisson's Ratio and Compressive Strength Relationship at Early Ages," *ACI Journal*, Vol. 88, No.1, January 1991, pp. 3-10.
6. EN 1992-1-1: "Eurocode 2: Design of Concrete Structures," Part 1-1 "General Rules and Rules for Buildings," European Committee for Standardisation (CEN), Brussels, 2004, 236 p.
7. Bryne L E: "Time Dependent Material Properties of Shotcrete," *Bulletin* No. 124, Dept. of Civil and Architectural Engineering, KTH Royal Institute of Technology, Stockholm, Sweden, 2014, 79 p.
8. ASTM C215 – 14: "Standard Test Method for Fundamental Transverse, Longitudinal, and Torsional Frequencies of Concrete Specimens," ASTM International; West Conshohocken, Pa, USA, December 2014, 7 p.

9. Hewlett-Packard: “The Fundamentals of Signal Analysis,” Application Note 243, Agilent Technologies, USA, 2000, 86 p
10. Mathworks *Matlab*. See <http://www.mathworks.com/products/matlab/> for further details. Accessed 14/03/2018.
11. Philleo R E: “Comparison of Results of three Methods for Determining Young's Modulus of Elasticity of Concrete,” *ACI Journal*, Vol. 26, No. 5, January 1955, pp. 461–469.



DOI: 10.2478/ncr-2018-0007

ISSN online 2545-2819

ISSN print 0800-6377

© Article authors. This is an open access article distributed under the Creative Commons Attribution-NonCommercial-NoDerivs licens. (<http://creativecommons.org/licenses/by-nc-nd/3.0/>).

Received: Feb. 25, 2018

Revision received: May 27, 2018

Accepted: May 28, 2018

Filler and Water Reducer Effects on Sedimentation, Bleeding and Zeta-Potential of Cement Paste



Ya Peng
Post Doc. Researcher
Dept of Structural Eng., NTNU
N-7491 Trondheim
yapeng2007@hotmail.no



Bård Pedersen
Senior Principal Engineer
Norwegian Public Roads Administration (NPRÅ)
N-0033 Oslo
baard.pedersen@vegvesen.no



Serina Ng
Scientist
Building and Infrastructure, Sintef
N-7491 Trondheim
akfc@hotmail.sg



Klaartje de Weerd
Associate Professor
Dept of Structural Eng., NTNU
N-7491 Trondheim
klaartje.d.weerd@ntnu.no



Stefan Jacobsen
Professor
Dept of Structural Eng., NTNU
N-7491 Trondheim
stefan.jacobsen@ntnu.no

ABSTRACT

Bleeding and sedimentation quantify the stability of fresh cement paste, whereas the addition of fillers and water reducers affect the stability. The effect of various types of fillers and water reducers was investigated by measuring bleeding, hydrostatic pressure and electroacoustic zeta-potential. Depending on their characteristics and use, fillers can improve stability by reducing sedimentation rate and bleeding. The combined effects of fillers and water reducers on the sedimentation rates, quantified as time-dependent hydrostatic pressure changes (dp/dt) in fresh matrix, correspond to their effects on zeta-potentials. The influence of the water reducers on sedimentation and bleeding exceed that of filler type.

Key words: stability, sedimentation, bleeding, zeta-potential, filler, water reducer

1. INTRODUCTION

Concrete can generally be regarded as a two phase material with a fluid phase and a particle phase. The properties of a given concrete are determined by the properties of each phase and the proportions between the two phases. Many models have defined the materials in each phase, among which the Particle-Matrix model (PM model) [1] suggests all particles $> 125 \mu\text{m}$ as the particle phase and all fluids and particles $\leq 125 \mu\text{m}$ as the matrix phase. Self-compacting concrete (SCC) was developed and is used for its advantage of not needing vibration. Two important properties of SCC are its flowability and its stability. Based on the PM model, the low yield stress and viscosity of the matrix and the density difference between the particles and the fluid causes particles to sink, resulting in sedimentation and bleeding, which are important factors in the instability of SCC [2]. According to Hammer et al. [3], the stability of the matrix itself affects the fresh properties of SCC by contributing to the bleeding and/or inhomogeneity of the concrete. Traditionally, bleeding has been seen as the main form of cement paste and matrix instability. However, sedimentation is also a part of the bleeding process and it has been suggested that the sedimentation rate can be used to evaluate the stability of modern cement matrix with admixtures and mineral additives [4].

For cementitious materials, filler addition is a good way to improve both the flow and stability simultaneously because it increases the matrix volume without adding extra cement [5]. Cement can be replaced by filler to reduce the cost and optimize some fresh properties of concrete such as rheology and stability. However, requirements for strength and durability in terms of w/c or water binder ratio must always be met. Filler can therefore be applied to concrete in two different ways: either to add it to decrease the water to powder ratio (w/p) while keeping w/c unchanged, or to increase w/c by replacing part of cement while keeping w/p constant. Addition and replacement both influence the sedimentation process by changing the solid fraction, the particle size distribution and the total surface area. As the solid fraction Φ increases or the particle size decreases, the influence of surface forces relative to body forces increases. Flocculation occurs in colloidal mixtures (suspensions consisting of colloid particles with one or more linear dimension between about 1 nm and 1 μm suspended in a fluid [6]). The particles, both the flocs and the single particles, have associated and/or adsorbed ions, molecules and/or liquid pockets so that the volume or thickness of “free” suspending fluid can vary greatly. The addition of admixtures influences the flocculation state of the suspension by electrostatic repulsion and steric hindrance. These interactions affect the effective “particle” sinking velocity during sedimentation. Depending on filler characteristics (particle size, specific surface, flocculation state, etc.) and combination with water reducer, the filler can affect the stability to various degrees.

Theories including Stokes' Law [7], Richardson-Zaki Equation (*R-Z*) [8], Kynch theory [9], Kozeny-Carman Equation (*K-C*) [10, 11] etc. describe particle sedimentation and bleeding. As to the experimental method, it has long been recognized that the zeta-potential is a good index of the interaction magnitude between colloidal particles. For colloidal stability, the repulsive forces must be dominant i.e. the greater the zeta-potential the more likely that the suspension is stable. If the zeta-potential is close to zero, the tendency for flocculation increases [12, 13]. Measurements of zeta-potential are commonly used to assess the stability of colloidal systems [14]. On the other hand, non-intrusive methods such as X-ray, gamma-ray and ultrasonic techniques have been developed which allow a full determination of the distribution of the dispersed material [15]. In our earlier research, a conceptual model [16] was proposed which described the stability of cement paste as the changing process of different zones. Several parallel test methods including HYdroStatic Pressure Test (*HYSPT*), in situ volume fraction measurements and total bleeding test were introduced for matrix stability study [16, 17]. *HYSPT* relies on the fact that the mainly restricted Stokesian settlement of particles causes changes in solid fraction and fresh density at a given height and time. During particle sedimentation, the hydrostatic pressure can be calculated in accordance with Eq. (1) [16], assuming a homogeneous zone below a sharp bleeding front:

$$p = \rho_l g \cdot h_b + \rho_m \cdot g \cdot (h - h_b) = \rho_l g \cdot h_b + [\rho_s \Phi + \rho_l (1 - \Phi)] \cdot g \cdot (h - h_b) \quad (1)$$

Where p (*Pa*) is the pressure, h and h_b (*m*) are the middle depth and bleeding height respectively, ρ_l , ρ_s and ρ_m are the density of the liquid, solid and mixture respectively. The mixture between the bleeding front and the middle test level is assumed to be homogeneous with solid fraction Φ [16]. It can be calculated by inserting the pressure and bleeding measurement results into Eq. (1), see Eq. (2).

$$\Phi = (p - \rho_l g h) / [(\rho_s - \rho_l) \cdot g \cdot (h - h_b)] \quad (2)$$

The scope of this research was to investigate the effect on the sedimentation process of adding and replacing two different fillers in pastes of $w/c = 0.5$ and 0.7 when combined with various water reducers. Bleeding, hydrostatic pressure and zeta-potential were measured to study how the interactions between particles affect the effective sinking velocity.

2. MATERIALS AND EXPERIMENTS

2.1 Materials

An ordinary Portland cement, *CEM I 42.5* in accordance with EN 197-1, was used for the experiments. Two different fillers, crushed Årdal and limestone, were applied both as partial replacement for, and as addition to the cement. The limestone filler consists of almost 85% calcite in addition to clay minerals. The Årdal filler originates from glaciouflovial aggregate and mostly consists of granite and gneiss. The main minerals are feldspars (plagioclase and potassium feldspar) (approx. 65%), quartz (approx. 18%) and mica (approx. 10%), in addition to some chlorite and amphibolite. The oxide compositions of these two fillers and the cement are shown in *Table 1*. The particle size distributions of the cement and the fillers determined by a Mastersizer laser granulometer are shown in Figure 1. The limestone powder is much finer than the Årdal filler, but coarser than the cement particles. This is also reflected in their respective Blaine values. Two different types of water reducer, polycarboxylate (*PCE*) and lignosulfonate (*LS*) were applied. *Table 2* gives the main characteristics of the water reducers. The dosages for all the samples are the solid of the water reducer by the mass of powder including cement and filler (*sbwp*, solid by the weight of the powder), see *Table 3*.

Table 1 - The oxide compositions of the powder materials detected by X-ray fluorescence (XRF).

| Compositions | STD-CEM I | Limestone | Årdal |
|--------------------------------------|-----------|-----------|--------|
| SiO ₂ | 20.98% | 16.03% | 63.56% |
| Al ₂ O ₃ | 5.13% | 3.29% | 15.21% |
| Fe ₂ O ₃ | 5.13% | 2.39% | 6.05% |
| CaO | 60.61% | 76.40% | 2.66% |
| MgO | 2.39% | 2.09% | 2.21% |
| P ₂ O ₅ | 0.14% | - | 0.28% |
| K ₂ O | 0.86% | 0.76% | 4.14% |
| Na ₂ O | 0.43% | 0.34% | 3.34% |
| SO ₃ | 3.01% | 0.50% | - |
| Blaine [m ² /kg] | 382 | 361 | 85.6 |
| D ₅₀ [µm] | 13.3 | 17.9 | 52.8 |
| Specific weight [g/cm ³] | 3.15 | 2.75 | 2.68 |

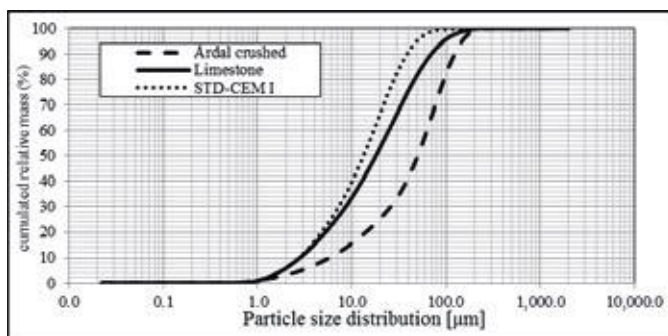


Figure 1 - The particle size distributions of the cement and filler powders.

Table 2 - The main characteristics of the water reducers.

| Properties | PCE | LS |
|---|-------------|-------------|
| Viscosity* (mPa·s) | Low, < 30 | Low, < 30 |
| Solid content | 30.0 ± 1.5 | 39.0 ± 2.0 |
| Specific gravity (g/cm ³) | 1.09 ± 0.02 | 1.20 ± 0.03 |
| pH-value | 6.5 ± 1 | 8.0 ± 1 |
| Chloride content (%) | < 0.01 | ≤ 0.1 |
| Alkali (Na ₂ O equivalent) (%) | < 2.5 | ≤ 6 |

*Viscosity is measured by Brookfield Viscometer, DV-1, LV1, 100 rpm, 20 ± 2°C

Three liters of cement pastes or matrixes with filler addition were prepared for both *HYSPT* and bleeding measurements. The mixtures were made using a Hobart mixer with the following mixing procedure: the dry powder was mixed at low speed (591 rpm) for 1 min; water and *SP* were added simultaneously and mixed for 2 min at lower speed; then continued mixing at

middle speed (1485 rpm) for 1 min; waited for 5 min while using spatula and hand to check the dispersing status and reduced the agglomerates; finally mixed at middle speed for 1 min. All experiments started about 10 min after water addition.

2.2 Experiments

a) HYSPT

HYSPT was used to investigate the sedimentation of the matrices. Figures 2 and 3 show HYSPT system setup with two stationary positions for $p(t, h)$ at the depths $h_b = 200$ mm and $h_m = 110$ mm. The pressure sensors (Endress&Hauser) have an accuracy of 0.75 Pa. They automatically correct for atmospheric pressure variations giving only the hydrostatic pressure contribution. More details about the measurement method can be found in our previous papers [16, 17].

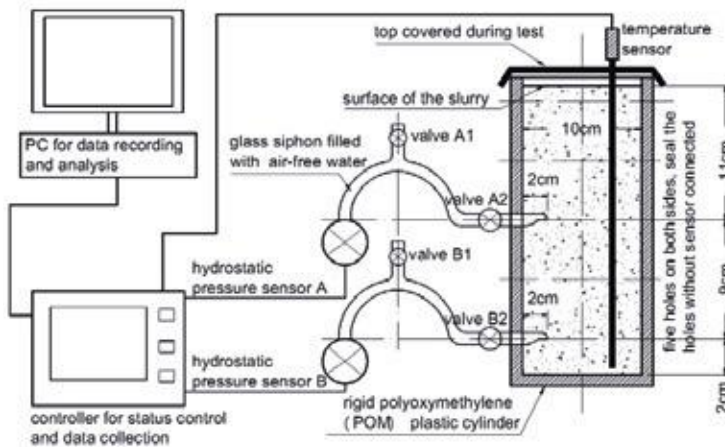


Figure 2 - HYSPT diagram for sedimentation measurements [16].



Figure 3 - HYSPT measuring system setup [16].

The recipes for the HYSPT measurements are shown in Table 3. The proportioning of cementitious materials for industry use is normally done on a mass basis. Therefore, the proportioning in this research was also done by keeping w/c constant at 0.50 and 0.70 and replacing cement with filler on a mass basis. However, from Eq. (1) and R-Z Equation it can be seen that the volume based fraction is an important factor for investigating the particle sedimentation and bleeding. Two different fillers, crushed Årdal and limestone, were applied either as additions to reduce w/p or as replacement for the cements (approximately constant w/p whereas w/c increased). The small variation in w/p ratio at the same volume-based filler addition was due to the density difference between Årdal and limestone. So the main variables at similar or constant solid fraction were the type of filler and/or admixture.

Table 3 - The recipes of all the cement matrices for HYSPT and visual bleeding measurements.

| Matrix code | Mass based fractions | | Filler types | Add.f./c mass based | Av. powder density (ρ , kg/m ³) | Volume based fraction | | Water reducer | |
|-------------------------|----------------------|-------|--------------|---------------------|---|-----------------------|-------|---------------|---------|
| | w/c | w/p | | | | Φ | Vf/Vp | type* | dosage* |
| wc0.5wp0.5 | 0.50 | 0.500 | | | 3150 | 0.388 | | | |
| wc0.7wp0.7 | 0.70 | 0.700 | | | 3150 | 0.312 | | | |
| wc0.5wp0.5PCE0.18 | 0.50 | 0.500 | | | 3150 | 0.388 | | PCE | 0.18% |
| ård-wc0.7wp0.585PCE0.18 | 0.70 | 0.585 | Årdal | 20% | 3063 | 0.358 | 18.5% | PCE | 0.18% |
| ård-wc0.7wp0.5 | 0.70 | 0.503 | Årdal | 40% | 3003 | 0.397 | 31.2% | | |
| ård-wc0.7wp0.5PCE0.18 | 0.70 | 0.503 | Årdal | 40% | 3003 | 0.397 | 31.2% | PCE | 0.18% |
| ård-wc0.7wp0.5LS0.18 | 0.70 | 0.503 | Årdal | 40% | 3003 | 0.397 | 31.2% | LS | 0.18% |
| lim-wc0.7wp0.5 | 0.70 | 0.500 | limestone | 40% | 3025 | 0.397 | 31.2% | | |
| lim-wc0.7wp0.5PCE0.18 | 0.70 | 0.500 | limestone | 40% | 3025 | 0.397 | 31.2% | PCE | 0.18% |
| lim-wc0.7wp0.5LS0.18 | 0.70 | 0.500 | limestone | 40% | 3025 | 0.397 | 31.2% | LS | 0.18% |

*Notes:
1. PCE means polycarboxylate water reducer, LS means lignosulfonate.
2. The water reducers were added with solid by the weight of the powder (sbwp);

b) Bleeding

The bleeding of all HYSPT samples was measured visually, as shown in Figure 4. The experiments were done by filling samples from the same batch of mixtures as for HYSPT into a graduated glass cylinder with 65 mm diameter and measuring the depth of the visible bleeding water after 4 h. The filling height of samples for the bleeding measurements was the same as for the HYSPT. The cylinder was kept covered with sealing tape during the test to avoid evaporation.

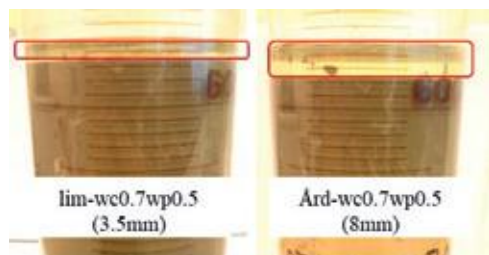


Figure 4 - The visual bleeding of the matrices with fillers (left with limestone; right with Årdal), see the water layer shown in red box.

c) *Zeta-potential*

The zeta-potential of the above two different filler particles, limestone and Årdal, were quantified by the electroacoustic method [18], applying a model *DT1200* Electroacoustic Spectrometer from Dispersion Technology Inc. (Bedford Hills, NY/USA). The principle of this method was based on ultrasound propagation through the medium, resulting in an electroacoustic phenomenon called colloid vibration current, from which the zeta-potential is then calculated. The electroacoustic technique characterized the dynamic mobility of particles in suspension. Usually, this technique was used to measure stable homogeneous suspensions with spherical particles (1 nm to 10 µm). An electric field with frequency around 106 Hz was applied to the samples, causing charged particles to oscillate, and to produce a sound wave at the same frequency. The oscillation (dynamic mobility) of the particles was described by its magnitude and phase angle (how far the particle motion lags behind the field applied). The sound wave was detected and analyzed to determine the motion of the particles. The main advantage of this technique over “traditional” electrophoretic apparatus is its ability to measure zeta-potential in slurries of greater than 10% wt. solids concentration, up to 60% wt. (= 33% vol. for a relative solid powder density of 3000 kg/m³ suspended in water) depending on the sample.

Table 4 - The mixtures for zeta-potential measurements.

| No. | group | Recipes* ¹ | Cement | Filler | | Water reducer* ³ | | | w/c | Apparent w/p* ⁴ | Medium |
|-------|--|-----------------------|--------|--------|------------|-----------------------------|------------|------------------|-------------------|----------------------------|--------|
| | | | [g] | type | amount [g] | type | amount [g] | amount [sbwp, %] | | | |
| 1 | group I | Cem+water | 50 | - | - | - | - | - | 0.5 | 0.5 | water |
| 2 | | Cem+LS | 50 | - | - | LS | 0.3 | 0.24 | 0.5 | 0.5 | water |
| 3 | | Cem+PCE | 50 | - | - | PCE | 0.3 | 0.18 | 0.5 | 0.5 | water |
| 4 | group II | Lim+water | - | Lim | 50 | - | - | - | - | 0.57 | water |
| 5 | | Lim+(Cem-PS) | - | Lim | 16.8 | - | - | - | 0.67 | 0.5 | Cem-PS |
| 6 | | Lim+LS (Cem-PS) | - | Lim | 50 | LS | 0.3 | 0.24 | 0.5 ⁺² | 0.57 | Cem-PS |
| 7 | | Lim+PCE (Cem-PS) | - | Lim | 50 | PCE | 0.3 | 0.18 | 0.5 ⁺² | 0.57 | Cem-PS |
| 8 | | Ård+water | - | Ård | 50 | - | - | - | - | 0.57 | water |
| 9 | | Ård+(Cem-PS) | - | Ård | 16.8 | - | - | - | 0.67 | 0.5 | Cem-PS |
| 10 | | Ård+LS (Cem-PS) | - | Ård | 50 | LS | 0.3 | 0.24 | 0.5 ⁺² | 0.57 | Cem-PS |
| 11 | | Ård+PCE (Cem-PS) | - | Ård | 50 | PCE | 0.3 | 0.18 | 0.5 ⁺² | 0.57 | Cem-PS |
| 12 | group III | Lim+Cem+LS | 33.2 | Lim | 16.8 | - | - | - | 0.67 | 0.5 | water |
| 13 | | Lim+Cem+PCE | 33.2 | Lim | 16.8 | 0.3 | 0.3 | 0.18 | 0.67 | 0.5 | water |
| 14 | | Ård+Cem+LS | 33.2 | Ård | 16.8 | - | - | - | 0.67 | 0.5 | water |
| 15 | | Ård+Cem+PCE | 33.2 | Ård | 16.8 | 0.3 | 0.3 | 0.18 | 0.67 | 0.5 | water |
| Notes | *1: Cem-cement, Lim-limestone, Ård-Årdal; | | | | | | | | | | |
| | *2: the w/c with *2 means the w/c ratio only used for the pore solution medium. | | | | | | | | | | |
| | *3: the dosage of all the water reducer refer to solid by the weight of the powder. | | | | | | | | | | |
| | *4: Because the cement was used to prepare the pore solution while the filler and water reducer were added | | | | | | | | | | |

The zeta-potential for the samples containing only cement was measured on samples prepared with deionised water. For the samples containing filler without water reducer, cement pore solution was used. The cement pore solution was obtained by filtering (1) standard cement slurries, (2) filler slurries or (3) cement + filler slurries using a Büchner funnel with cellulose filter paper and connected to a water pump setup. The w/c of the suspensions was kept at 0.5 when preparing the cement pore solution. For each batch of pore solution, 400 g of dry powder was employed to minimize any systematic error which could arise as a result of differences in suction force on samples based on differences in their weight. The yield of pore solution per batch of suction filtration was less than 100 g. The pore solutions were used almost immediately

and stored under vacuum to reduce the risk of carbonation. Prior to the zeta-potential measurements, all dry powders (cement and fillers when applicable) were weighed out in a 50 ml PE tube. The total amount of dry powder for each preparation was kept at a constant amount of 50 g. Water or pore solution at the desired water to filler ratio (w/f) was added to the dry powder and the sample was mixed in a vortex for 15 s. The homogenized mixture was subsequently poured into a 15 mL beaker, where the zeta-potential values were measured within 3 min after wetting. Where required, the water reducers were mixed into the solution before adding it to the dry powder. The amount of materials and the type of medium (water or pore solution) employed for each measurement can be found in Table 4. High concentrations of filler were not used in this study to avoid excessive sedimentation of particles that could affect the zeta-potential measurements.

3. RESULTS AND DISCUSSION

3.1 Bleeding

Table 5 enables comparison of the bleeding depths of the suspensions shown in Table 3 at 4 h after mixing. The paste with higher w/c ratio (i.e. low solid fraction) without water reducer showed much higher bleeding. No clear bleeding could be observed for the paste or matrices with 0.18% PCE. The top of these matrices contain a diluted muddy layer (see Figure 5), instead of the transparent bleeding water that could be seen with the same dosage of LS (Figure 6). This could be due to the different dispersing efficiency between LS and PCE. When the particles are better dispersed in matrices with PCE, the particles sink slower or even remain suspended.

Table 5 - The visible bleeding depth of the matrices for HYSPT at 4 h after mixing.

| No. | matrix code | visible bleeding [mm] |
|-----|-------------------------|-----------------------|
| 1 | wc0.5wp0.5 | 2.5 |
| 2 | wc0.7wp0.7 | 28.0 |
| 3 | wc0.5wp0.5PCE0.18 | / |
| 4 | ård-wc0.7wp0.585PCE0.18 | / |
| 5 | ård-wc0.7wp0.5 | 8.0 |
| 6 | ård-wc0.7wp0.5PCE0.18 | / |
| 7 | ård-wc0.7wp0.5LS0.18 | 12.0 |
| 8 | lim-wc0.7wp0.5 | 3.5 |
| 9 | lim-wc0.7wp0.5PCE0.18 | / |
| 10 | lim-wc0.7wp0.5LS0.18 | 6.5 |

The matrix with Årdal filler, displays higher bleeding depth than the matrix with limestone, both with and without admixture, compare No. 5 with No. 8 and No. 7 with No. 10 (all with the same initial solid fraction), see also Figure 6. The higher bleeding depth is to be expected because the coarser particle size and lower specific surface area of Årdal filler induces a higher particle sinking velocity and therefore more water flowing upwards. The change of bleeding with water reducer is in line with earlier observations [17] and is presumably due to the smaller effective particle size in a de-flocculated suspension.

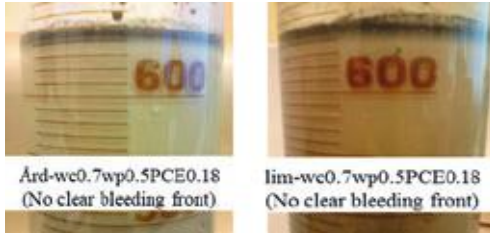


Figure 5 - No clear bleeding was observed for the matrices with filler and 0.18% PCE.



Figure 6 – Visible bleeding was observed for the matrices with filler and 0.18% LS.

3.2 Sedimentation of matrices

a) Reference pastes with and without water reducer

Figure 7 shows the pressure changes at bottom (left plot) and middle (right plot) for pastes of varying w/p ratio without water reducer. The differences between the starting points for the two materials in each plot show the different initial pressure due to different densities and heights of the suspensions in the container (shown in Figure 2). The paste with higher Φ ($w/p = 0.5$) shows a slightly larger dp/dt and thus a higher sedimentation rate. This does not coincide with the $R-Z$ Eq. [8], which predicts that a higher initial solid fraction Φ_0 induces lower particle sinking velocity. The most probable reason is that more flocculation occurred in the pastes with higher Φ_0 , which induces larger “effective” particle sizes and higher particle sinking velocity. At around 2 h, both pastes reach the plateau with a clear inflection point. At the plateau the solid particles above the sensor tip have settled and the pressure detected is the liquid pressure. Fig. 7 shows that both pressure curves reach the plateau pressures close to the pure water pressures of 1100 Pa in the middle and 2000 Pa at the bottom. This confirms that the pressure detected is governed by particle sedimentation.

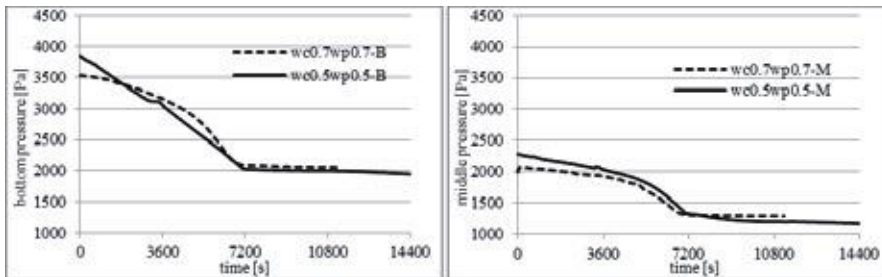


Figure 7 - Pressure curves of the pastes with different w/c ratio without water reducer.

Figure 8 shows the pressure results of the pastes with PCE water reducer. In the first 0.5 h, the matrix with lower Φ_0 ($wc0.7wp0.7PCE0.18$) shows a larger dp/dt and a higher sedimentation rate. This coincides with the *R-Z Eq.* However, the matrix with higher Φ_0 ($wc0.5wp0.5PCE0.18$) presents a higher sedimentation rate after this period and thus does not obey the *R-Z Eq.* any longer. This alteration indicates two possible phenomena: either 0.18% *PCE SP* is not enough to disperse all the particles for the paste with $w/p = 0.5$; or particle flocculation may be delayed by water reducer until after a period of measurement.

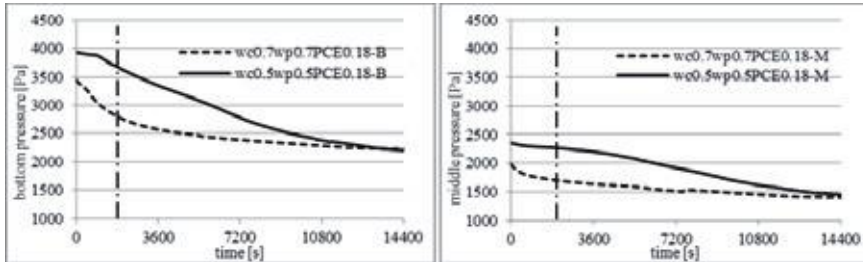


Figure 8 - Pressure curves of the pastes with $w/c = 0.5$ and 0.7 and 0.18% PCE.

b) Filler replacement/addition effect for matrices without water reducer

The matrices with constant $w/p = 0.5$ without water reducer were investigated to check the filler replacement effect, as shown in Figure 9. Note that the matrices with fillers have a bit higher Φ_0 (0.397) than that of the paste with $\Phi_0 = 0.388$ due to differences in powder density. The 40% limestone replacement by mass leads to higher sedimentation rate and takes less time to reach the plateau than the reference cement paste $wc0.5wp0.5$, while the coarser Årdal replacement induces the opposite effect. This indicates that the finer limestone induced higher sedimentation rates, which does not coincide with Stokes law [15]. It is believed that this was caused by more flocculation of the matrix with limestone, see the separate zeta-potential investigation below. Compared with $wc0.7wp0.7$, the additions of the different fillers result in quite different effects. Figure 9 shows that the average dp/dt is slightly higher for the limestone matrix than for the pure paste with $w/c = 0.7$. However, comparing dp/dt of $wc0.7wp0.7$ with $\text{ard-}wc0.7wp0.5$, the Årdal matrix shows slightly lower dp/dt and takes a longer time to reach the plateau. This indicates that the Årdal modified matrix had the slowest sedimentation rate.

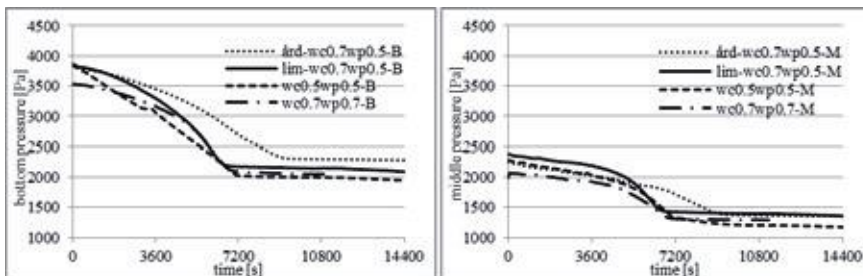


Figure 9 - Pressure curves of the matrices with $w/p = 0.7$ or 0.5 by adding various fillers, no water reducer.

c) *Filler effect for matrices with SP*

• **Filler replacement (constant w/p)**

It has previously been observed [17] that water reducer helps stabilizing the cement paste by dispersing the particles, which reduces the effective particle size and delays the early hydration of cement. Figure 10 shows the sedimentation behavior of matrices with limestone or Årdal filler and with 0.18% solid dosage of *PCE* water reducer ($\Phi_0 = 0.397$) compared with the paste with the same SP ($\Phi_0 = 0.388$). Compared to Figure 9, dp/dt is lower and the inflection point less sharp in Figure 10 as more small particles settled. Figure 11 shows that with *LS* water reducer, there is no longer any difference in the sedimentation behavior of the matrices at the same Φ_0 as opposed to Figure 9. It seems that the dosage applied is sufficient to disperse the limestone particles so that the different particles behave in a similar way at $\Phi = 0.397$. Compared with the matrices without water reducer shown in Figure 9, it can also be seen that the time periods to reach the plateau were all delayed and a less sharp inflection points appeared for all matrices in Figure 10. Again, the dispersing effect of 0.18% of *PCE*, i.e. the normal dosage of this water reducer overshadowed the influence of various fillers on the sedimentation process compared to the matrices without water reducer. Similarly, the two matrices with *LS* (see Figure 11) show identical dp/dt . According to Table 5, the *LS* addition at 0.18% seems to increase the bleeding though only the visual bleeding was taken into account. The matrices with coarser particles, either with or without water reducer, caused higher bleeding as expected from *K-C Eq. [10, 11]*. This is why fillers with different particle sizes showed an opposite effect on sedimentation and visual bleeding. It is reasonable because visual bleeding tests did not include the soft turbid bleeding and the solid fraction differences at the zones below bleeding, while HYSPT measurements take solid fraction changes of more zones into account at both levels. This phenomenon will be explained further in Figure 15 below.

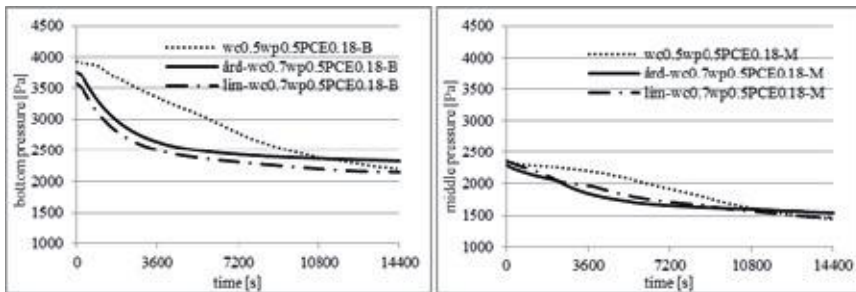


Figure 10 - Pressure curves of paste ($\Phi_0 = 0.388$) and two matrices with the same dosage of *PCE* but with different types of filler ($\Phi_0 = 0.397$).

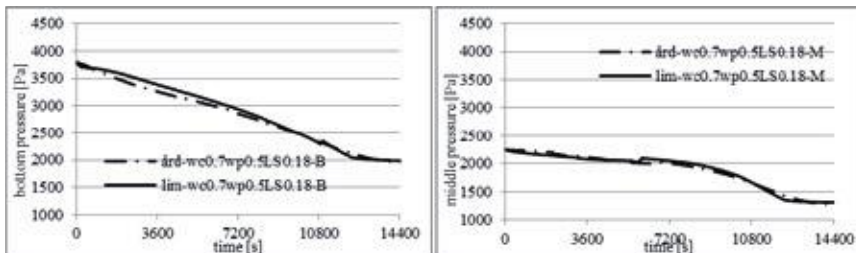


Figure 11 - Pressure curves of two matrices with the same dosage of *LS* but with different types of filler ($\Phi_0 = 0.397$).

• **Filler addition (constant $w/c = 0.7$)**

Figure 12 shows the HYSPT results for cement paste ($\Phi = 0.312$) and matrices with two different filler dosages ($\Phi_0 = 0.358$ and 0.397), all with the same water reducer. There is very little difference in the sedimentation curves. The variation is probably within the expected variation of the test method itself [16, 17]. This is surprising but indicates that at this Φ_0 , this dosage of *PCE* leads to equal states of dispersion. This is a very important factor and could describe the critical dosage of this *SP* for matrix at this Φ_0 , with which all the particles get totally dispersed. Visual bleeding tests show that there were no clear bleeding fronts but turbid bleeding zones for both matrices, see Figure 15.

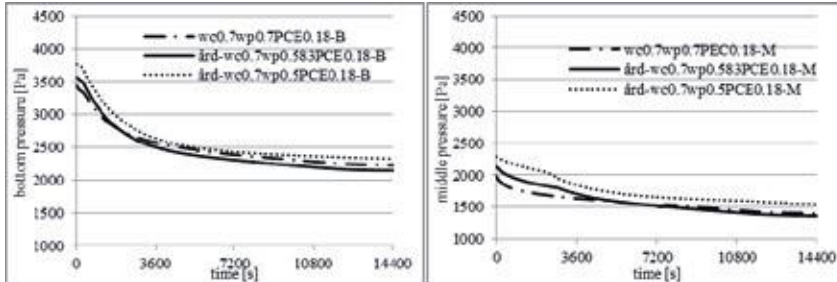


Figure 12 - Pressure curves of paste ($\Phi_0=0.312$) and two matrices with different percentage of Årdal filler ($\Phi_0=0.358$ and 0.397) but the same dosage of *PCE*.

d) *The effect of different water reducer*

Figure 13 shows the effects of no water reducer, *LS* and *PCE* on the sedimentation of the matrices with limestone filler. Compared with the matrix without water reducer, the matrices with *PCE* and *LS* take much longer time to reach a plateau or did not reach it within 4 h. The matrix with *PCE* displays a very low sedimentation rate during most parts of the sedimentation process. The matrix with *LS* also takes longer time and has less clear inflection point. This indicates that with the same filler addition, *PCE* has more effect on slowing down sedimentation due to the better dispersing effect. Previously, these two types of water reducers have been investigated in a plain cement paste with $w/c = 0.5$ ($\Phi_0 = 0.388$) [17] without noticing any particular effect of changing the type of water reducer.

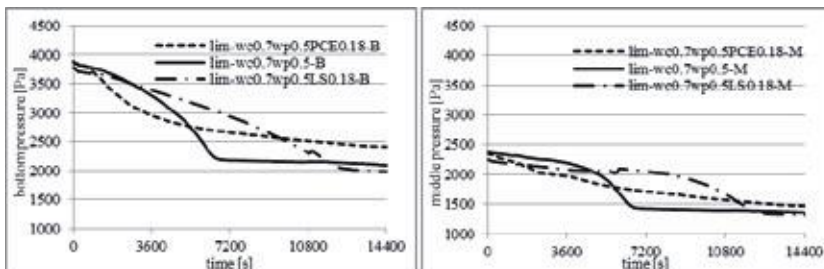


Figure 13 - Pressure curves of matrices with the same limestone addition without and with 2 different water reducers at 0.18%.

A conceptual model for sedimentation and bleeding of cement paste was proposed in the previous paper [16]. It describes the process to be variation of zones including supernatant (bleeding), homogeneous zone, variable concentration and sediment cake, as shown in Figure 14. The bleeding observations accentuates the importance of the volume fraction curve (Φ -

curve), which indicates that in stage 1 the transition between bleeding and paste is not a sharp front shown as the various gray scales. According to the photo with high resolution shown in Figure 15, the phenomena observed during experiments seem to coincide qualitatively with the conceptual model.

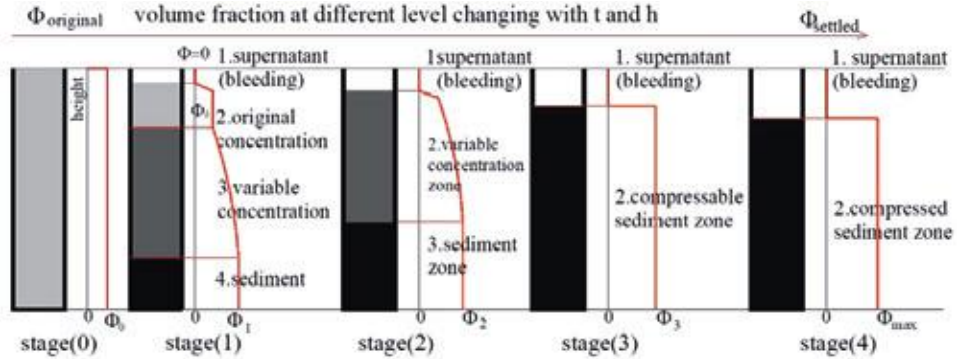


Figure 14 - The conceptual model for stability of cement paste [4, 16].



Figure 15 - Zones transformation for $lim-wc0.7wp0.5PCE0.18$ at 2 h sedimentation after mixing.

The effect of different water reducers is also compared for the matrices with the Årdal filler, as shown in Figure 16. The features of the curves are similar to those in Figure 13, but the rank of sedimentation differs from the reference. With regard to dp/dt and the time to reach the plateau, Figure 16 shows that the matrix with *PCE* presents faster sedimentation than that with *LS*. So *LS* seems to stabilize the Årdal matrix better than *PCE* water reducer. The reason for the faster sedimentation with *PCE* could be the different influence of these two water reducers on the inter- the middle level. There could be two reasons for this. Firstly, there are probably particle forces, which will be discussed in section 3.3 below. Moreover, these results only show the sedimentation process within the first 4 h. Figure 16 also shows that the pressure after 4 h is more than 2000 Pa at the bottom level and more than 1100 Pa at tiny particles which settled at a very low velocity or could not sink at all. Secondly, the compression of the sediment cake continues. Our previous research [4, 16, 17] also found that cement paste with the same *PCE* showed a gradual pressure reduction after reaching the plateau. The combined effect of *SP* and filler on compressibility was earlier discussed in terms of paragenesis [17].

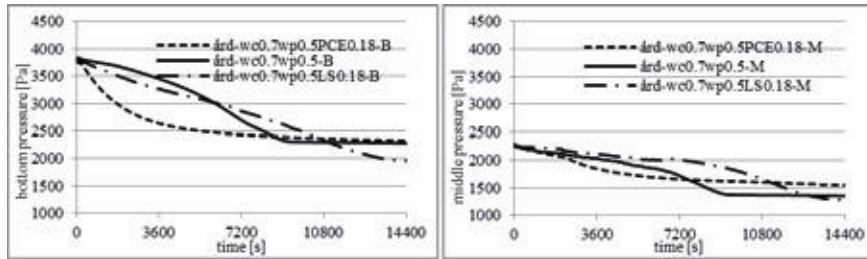


Figure 16 - Pressure curves of the matrices with the same Årdal addition and different water reducers.

3.2 Combined effect of filler and water reducer on zeta-potential

a) Effect of water reducer on cement

The zeta-potential results are shown in Figures 17 to 19 in the three different groups as presented in Table 4: (1) cement only, (2) filler only and (3) filler mixed with cement. The zeta-potentials of the first group are shown in Figure 17. There are at least two possible explanations for the positive zeta-potential (+2.2 mV in the pure cement paste with $w/c = 0.5$): (1) the heterogeneous cement particles is represented by more positively charged clinker phases on the surfaces; (2) the rapid hydration of $\sim 7\%$ C_3A happened in presence of gypsum. Hydration of the aluminate phase leads to the formation of CAH compounds, which carry a positive zeta-potential [19]. Possibly, it could be a combination of with high Ca^{2+} concentrations in the pore solution which shields the negatively charged surfaces and potentially “recharge” them.

When water reducer was added, the zeta-potential increased slightly to become more positive, which is in line with better dispersion effect by adding water reducer and thus a lowered sedimentation rate as observed by the *HYSPT*. A possible hypothesis for this observation could be linked to the negative nature of the water reducer and abundant cations such as Ca^{2+} released in cement pore solutions [20]. The presence of negative water reducer on the cement particles masks their positive surfaces, turns them negative and promoted adsorption of cations onto the polymer to form a double layer. This hypothesis is supported by the fact that the cement pastes with the more anionic *LS* water reducer show a lower zeta-potential value than that with *PCE*.

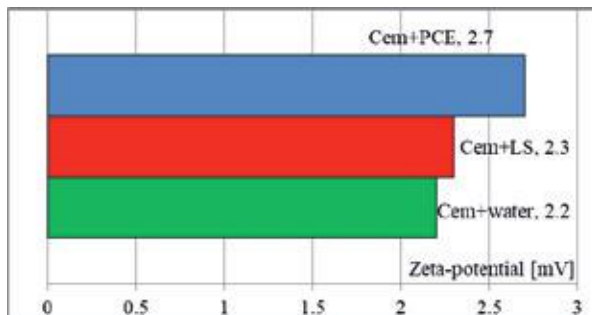


Figure 17 - zeta-potential of group 1 samples - cement paste with and without LS or PCE water reducer, respectively.

b) *Effect of water reducer on fillers*

The fillers were first tested in deionized water to determine the innate surface of the particles. Figure 18 shows that both fillers had a zeta-potential value close to zero: limestone gave a positive value of +0.8 mV, whereas Årdal was negative at -0.5 mV. This renders them less stable than the cement particles, thus the fillers may be more susceptible to flocculation in deionized water, but not in the same environment, i.e. pH and ionic strength as Cem-PS. When added to cement pore solution, the zeta potentials are rapidly reversed, indicating a quick adsorption of ions, Ca^{2+} and SO_4^{2-} most likely onto the charged surfaces of the fillers.

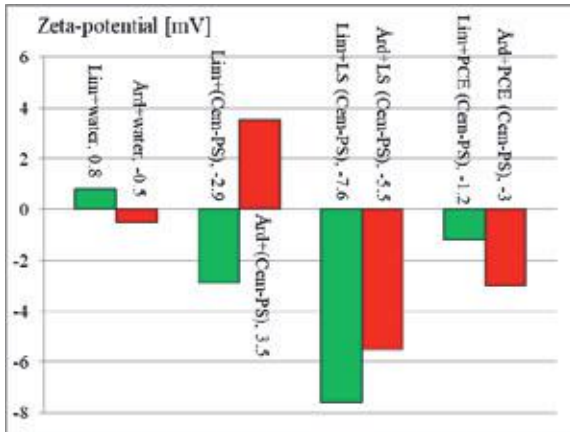


Figure 18 - Zeta-potential of cement paste, limestone and Årdal in water or pore solution with either presence or absence of water reducer.

Due to the rapid uptake of ions, the addition of both fillers does not intensify the flocculation of the matrices *lim-wc0.7wp0.5* and *ard-wc0.7wp0.5*. Figure 18 also shows that both fillers display negative zeta-potentials when adding water reducer, whereby the zeta-potentials of the suspensions with LS are more negative than that with PCE. This can be accounted for the steric bulk or the higher charge density of LS, which enhances the stability of the suspension and thus lower the sedimentation rate as shown in Figure 13. Similar phenomenon can also be seen in the filler modified matrices that will be discussed later.

The two water reducers exert various interesting effects on the fillers. In the presence of LS, limestone suspensions display a more negative zeta-potential value (-7.6 mV) than Årdal suspensions (-5.5 mV). This can be attributed to the initial zeta-potentials of the fillers, whereby an overall less negative zeta-potential in Årdal than by limestone occurs after adsorption. However, ΔZ (9 mV) between *Ard+(Cem-PS)* / *Ard+LS(Cem-PS)* ($\Delta Z = 9$ mV) is greater than that between *Lim+(Cem-PS)* / *Lim+LS(Cem-PS)* ($\Delta Z = 4.7$ mV). This suggests that a higher amount of LS is adsorbed by Årdal than by limestone, which could lead to LS having a better dispersing effect on Årdal. In general, the higher the zeta-potential value (+/-), the more stable fillers in the polyelectrolyte rich medium would be, due to the better dispersion of the particles. This could be the reason for the lower sedimentation rates of matrices with LS than those of matrices with PCE, as shown in Figure 13 and 16.

c) *Cement mixed with filler in presence of water reducers*

Figure 19 shows zeta-potential results of suspension group III (see Table 4) for the combination of filler and cement in a water reducer dispersed suspension. Based on their polarity, both the cement and fillers are potential docking sites for the adsorption of the water reducer, which in turn effectively varies the zeta-potential of the suspension. The zeta-potential values of the

matrices with LS are lower than for pure filler suspensions due to the inherent positive nature of the cement suspension. Such negative zeta-potential also indicates that LS adsorbed onto the filler equally rapidly as on to cement particles, which allows the zeta-potential of the matrices with both types of fillers to be negative. However, the change of filler from limestone to Årdal in the matrices with *PCE* made the zeta-potential vary from +0.2 to -1.8 mV. This indicates that *PCE* may preferentially adsorb onto cement particles for the matrices with limestone, while competitive adsorption of *PCE* between cement and Årdal may happen due to the highly positive surface charge of Årdal filler after *SP*-adsorption (see Figure 18). In group III of Table 4, the suspensions with *LS* shows similar negative zeta-potential values, which match with the similar sedimentation rate between matrices with *LS* and various fillers, as shown in Figure 11.

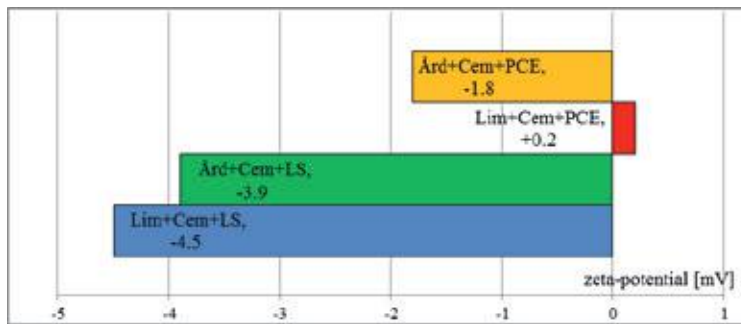


Figure 19 - zeta-potential of the combined filler and cement particles in pore solutions with presence of *LS* or *PCE*.

Considering the various zeta-potential values of the matrices with *PCE*, the addition of Årdal or limestone filler should present very different effects on particle dispersion and therefore the sedimentation process. However, both Figures 10 and 12 show that the addition of various fillers brings about a similar effect on sedimentation when combined with same *PCE*. This seemingly contradictory effect can be related to the following three facts. Firstly, the steric effect needs to be taken into account for the matrices with *PCE*-based water reducer. It can greatly alter the dispersion and reduce flocculation in the matrices which appears to have low stability in zeta-potential measurements. Moreover, the preferential adsorption of *PCE* onto cement particles for the matrices with limestone may further increase the overall dispersivity of the suspensions. Finally, the w/c ratios of the samples in group III are higher than those for *HYSPT*, which might partially explain the contradictory effect of the filler on sedimentation and zeta-potential. In general, the matrices with *LS* displayed a larger absolute value of the zeta-potential than those with *PCE*. This again indicates lower tendency to particle flocculation in the samples with *LS* and resulted in lower sedimentation rates, as can be seen in Figure 13 and 16. After the initial few minutes, the results are relatively stable for all samples in the zeta-potential measurements. Small changes are observed in measurements up to 10 min. This indicates two points: firstly the overall variation of the filler surfaces is minimal after the initial change; secondly the adsorption of water reducer on the particle surfaces is rapid and stable as long as no external factor presents to influence this attraction.

3.3 Final discussion

The bleeding results show that the solid fraction and specific surface of the particles could be the main parameters in line with the *K-C Eq.* [10]: the highest and lowest bleeding (28 mm and 2.5 mm as shown in Table 5) are for the pure pastes with large difference in solid fraction and equal particle fineness. However, the two reference pastes show similar sedimentation processes. This indicates that the total bleeding- and sedimentation measurements might not separately demonstrate the same stabilizing effect. This is in line with the findings [21] on fundamental differences between total bleeding- and hydrostatic pressure measurements and how bleeding rates and dp/dt close to the surface relate. It should also be noted that only the transparent bleeding could be observed in the visual bleeding tests. For the cases with *PCE*, a long compressing process which did not reach a plateau was observed. A turbid bleeding layer existed but there were still zones transformation in the matrix. However, a clear bleeding layer can be observed in the visual bleeding test for the matrices with the same volume addition of fillers and 0.18% *sbwp LS*, see Figure 6. This indicates differing dispersing effects on particles with the different water reducers.

Table 6 - The average dp/dt [Pa/s] of the mixtures at bottom and middle level after 2 h.

| No. | matrix code | average dp/dt in 2 h (bot.) | average dp/dt in 2 h (mid.) |
|-----|-------------------------|-------------------------------|-------------------------------|
| 1 | wc0.5wp0.5 | 0.250 | 0.116 |
| 2 | wc0.7wp0.7 | 0.205 | 0.100 |
| 3 | wc0.5wp0.5PCE0.18 | 0.168 | 0.068 |
| 4 | ård-wc0.7wp0.585PCE0.18 | 0.151 | 0.077 |
| 5 | ård-wc0.7wp0.5 | 0.152 | 0.066 |
| 6 | ård-wc0.7wp0.5PCE0.18 | 0.164 | 0.091 |
| 7 | ård-wc0.7wp0.5LS0.18 | 0.124 | 0.039 |
| 8 | lim-wc0.7wp0.5 | 0.256 | 0.132 |
| 9 | lim-wc0.7wp0.5PCE0.18 | 0.177 | 0.088 |
| 10 | lim-wc0.7wp0.5LS0.18 | 0.115 | 0.024 |

In Table 6, dp/dt by *HYPST* measurements for all samples are compared, which indicates the combined effects of filler and water reducer on sedimentation. When the filler is applied as an additional powder, it generally stabilizes the cement paste due to the increased solid fraction and presumably also higher inter-particle forces, but the different fillers have different behaviour. The addition of the coarser Årdal filler prolongs the sedimentation period but gives a similar sedimentation rate, while the addition of the finer limestone may cause more flocculation and therefore induces a higher sedimentation rate. However, the additional limestone filler probably reduces the bleeding because the suspensions became more homogeneous and the sediment cake less compact. When the filler is applied as a replacement of cement to increase the *w/c* ratio, e.g. *Årdal-wc0.7wp0.5*, *lim-wc0.7wp0.5* and *wc0.5wp0.5*, the replacement with coarse Årdal filler lowered the sedimentation rate more visibly than the limestone filler did. This is possibly due to the greater zeta-potential change which Årdal filler induces for the particles in the matrix than limestone filler does. It is also likely that the flocculation state affected the bleeding. However, limestone filler decreases the total clear bleeding depth either with or without presence of water reducer. For the matrices with the addition of water reducer at a dosage of 0.18%, the stabilizing effect of water reducer overshadows the effect from both types of fillers even at 40% addition or replacement. Both *PCE* and *LS* reduce the difference of the sedimentation performance shown for cement matrices without water reducer. The matrix with combined application of *LS* and Årdal shows the lowest sedimentation rate in *HYSPT* measurements, which is probably due to the greatest zeta-potential change compared with that of the matrix without *LS*.

Finally, it should be figured out that the particle interaction may vary with time and depth. The flocculation state of the particles would change with time and also be various at different zones of the mixtures. *HYSPT* experiments that carried out in 4 h take the effect of the particle flocculation on the sedimentation into account while zeta-potentials were measurement shortly after mixing. Therefore, the sedimentation rate may have varied at different levels in the mixtures, which may have induced different rates of expulsion of bleeding water. The matrix with fine limestone addition may therefore have had a lower sedimentation rate and bleeding rate at the bleeding front. However, as sedimentation continues, more serious flocculation could take place for finer particles than for the coarser ones with the same solid fraction, which results in a higher sedimentation rate.

4. CONCLUSION

The sedimentation and bleeding of cement matrices have been studied using *HYSPT* and bleeding measurements to investigate the effect of various combinations of fillers and water reducers on stability. To study how the interactions of the particles influence particle sinking, the zeta-potentials of cement and filler powder were measured electro-acoustically. It is found that the matrices show zones transformation, which coincides with the conceptual model previously proposed. To sum up:

1. The stability of a cement matrix with filler and water reducer cannot be characterized from final bleeding alone, because of turbid bleeding layers, particularly for *PCE* and filler.
2. Filler modifies the sedimentation and bleeding by varying the solid fraction, specific surface and inter-particle's forces.
3. Without water reducer, the addition of the coarser Årdal filler prolongs the sedimentation period but gives similar sedimentation rate, while the addition of the finer limestone filler induces higher sedimentation rate possibly due to the occurrence of more flocculation.
4. Filler can be used as either replacement or addition to cement. A finer filler does not always stabilize the matrix more than the coarser one. The replacement of coarse Årdal filler lowers the sedimentation rate more visibly than limestone, especially when combined with LS, probably due to the higher zeta-potential change it induces.
5. For the matrices with water reducer added at a solid dosage of 0.18%, the stabilizing effect of water reducer overshadows the effect from both types of fillers even at 40% addition or replacement.

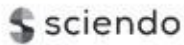
For further research, it is suggested to investigate the sedimentation, bleeding rate and bleeding of matrices with more types of fillers combined with water reducer and the effect of particle size, mineralogy and adsorption of admixtures on the stability of cement matrices.

ACKNOWLEDGEMENT

This research was part of research work of the COIN Centre led by SINTEF. Thanks to Espen Rudberg, previously at Mapei, for providing admixtures; to Norcem and Norstone for supplying cement, fillers and all PSD measurements as COIN partners; to G. Zirgulis for photographing and to the NTNU Concrete lab for their support with experiments.

REFERENCES

1. E. Mørtzell, M. Maage, S. Smepllass: “A Particle-Matrix Model for Prediction of Workability of Concrete”, *Proceedings*, International Conference on Production Methods and Workability of Fresh Concrete”, Glasgow, Scotland 1995, 11 pp.
2. Josserand L, Coussy O and de Larrard F: “Bleeding of concrete as an ageing consolidation process”, *Cement Concr. Res.*, V.36, 2006, pp.1603–1608.
3. Martius-Hammer T.A., Smepllass S., De Weerd K., Peng Y.: “Stability of SCC-robustness for changes in water content and sand grading”, *COIN Report*, Trondheim, Norway, 2013, 27p
4. Peng Y., Jacobsen S.: “Influence of water cement ratio, admixtures and filler on sedimentation and bleeding of cement paste”, *Cem. Conc. Res.*, V.54, 2013, pp. 133-142
5. Pedersen B.: “Alkali-reactive and inert fillers in concrete – Rheology of fresh mixtures and expansive reactions”, Doctoral thesis, NTNU, Trondheim, Norway, 2004, 292 pp.
6. Rhodes M., “Introduction to Particle Technology”, 2nd Edition, 2008, John Wiley & Sons, Ltd, UK, ISBN 978-0-470-01428-8, 474 pp.
7. Stokes G.G., *Math. Phys. Papers*, 1901, Vol. 3
8. Richardson J F; Zaki W N.: “The sedimentation of a suspension of uniform spheres under conditions of viscous flow”, *Chem. Eng. Sci.*, V.3, 1954, pp. 65-73
9. Kynch G. J.: “A theory of sedimentation”, *Trans. Faraday Soc.*, V.48, 1952, pp.166-176
10. Powers T.C., “The Properties of Fresh Concrete”, Wiley & Sons, London, 1968, 664 pp.
11. Steinour H. H.: “Further studies of the bleeding of Portland cement paste”, *Research Bulletin* No. 4, Portland Cement Association, Skokie, USA, 1945
12. Zingg A., Winnefeld F., Holzer L., Pakusch J., Becker S., Gauckler L.: “Adsorption of polyelectrolytes and its influence on the rheology, zeta-potential, and microstructure of various cement and hydrate phases”, *Journal of Coll. Inter. Sci.*, V.323, 2008, pp. 301-312
13. Zingg A., Winnefeld F., Holzer L., Pakusch J., Becker S., Figi R., Gauckler L.: “Interaction of polycarboxylate-based superwater reducers with cements containing different C3A amounts”, *Cem. Conc. Comp.*, V.31, 2009, pp. 153-162
14. Hunter R.J.: “Zeta-potential in Colloid Science”. England: Academic Press, 1981
15. Williams R.A., Xie C.G., Bragg R., Amarasinghe W.P.K.: “Experimental techniques for monitoring sedimentation in optically opaque suspensions”, *Coll. Surf.*, V.43, 1990, pp.1-32
16. Peng Y., Jacobsen S., De Weerd K., Pedersen B.: “Model and test methods for stability of fresh cement paste”, *ASTM-Adv. Civ. Engi. Mat.*, V.3, 2014, pp. 1-24, doi:10.1520 / ACEM20130097
17. Peng Y., “Sedimentation and bleeding of fresh cement paste”: *Doctoral thesis*, Norwegian University of Science and Technology, Trondheim, Norway, 2014:89 ISBN 978-82-326-0102-8 (printed), 2014:89 ISBN 978-82-326-0103-5 (electronic), 2014, NTNU, Norway
18. O'Brien R.W., Cannon D.W., Rowlands W.N.: “Electroacoustic Determination of Particle Size and Zeta-potential”, *Journal of Coll. Inter. Sci.*, V.173, 1995, pp. 406-418
19. Lank J., C. Hirsch: “Impact of zeta-potential of early cement hydration phases on superwater reducer adsorption”, *Cem. Conc. Res.*, Vol. 37, 2007, pp. 537-542
20. Lesti M., Ng S., Plank J.: "Ca²⁺ Ion – Mediated Interaction between Microsilica and Polycarboxylate Comb Polymers in Model Cement Pore Solution", *Journal of the Ame. Cer. Soc.*, V.93, 2010, pp. 3493 – 3498
21. Peng Y., Lauten R.A., Reknes K., Jacobsen S. “Bleeding and sedimentation of cement paste measured by hydrostatic pressure and Turbiscan”, *Cem. Conc. Com.*, V.76, 2017, pp. 25-38.



DOI: 10.2478/ncr-2018-0008

ISSN online 2545-2819

ISSN print 0800-6377

© Article authors. This is an open access article distributed under the Creative Commons Attribution-NonCommercial-NoDerivs licens. (<http://creativecommons.org/licenses/by-nc-nd/3.0/>).

Received: March 22, 2018

Revision received: May 29, 2018

Accepted: May 29, 2018

Continuous Preventive Bridge Maintenance of Swedish Municipalities – A Survey on Common Practice



Louise Andersson,
MSc, PhD student
RISE Swedish Cement and Concrete Research Institute
Drottning Kristinas väg 26
SE- 100 44, Stockholm
E-mail: louise.andersson@ri.se



Johan Silfwerbrand,
PhD, Professor
KTH Royal Institute of Technology
Dept. of Civil & Architectural Engineering
Brinellvägen 23
SE-100 44 Stockholm
E-mail: jsilfwer@kth.se



Anders Selander,
MSc, PhD
CEMENTA
Cementa AB, Heidelberg Cement Group
Marieviksgatan 25
SE-100 74 Stockholm
E-mail: anders.selander@cementa.se



Jan Trägårdh,
MSc, Lic. Of Phil
RISE CBI Swedish Cement and Concrete Research Institute
Drottning Kristinas väg 26
SE- 100 44, Stockholm
E-mail: jan.tragardh@ri.se

ABSTRACT

As part of a report [1] on continuous preventive bridge maintenance, a survey was conducted with Swedish municipalities. The survey's focus was on bridges and preventive maintenance, as well as the demands and performance control stated by the municipalities. The preventive maintenance the survey focused on was the annual maintenance concerning washing, cleaning of drainage system and removal of vegetation. The survey showed both similarities and differences within the municipalities but also in comparison with Swedish Transport Agency (STA).

Key words: bridge maintenance, preventive maintenance, survey.

1. INTRODUCTION

In Sweden, the primary owner of the country's over 30 000 bridges is the state, through the Swedish Transport Administration (STA) [2]. This of course means that the vast majority of knowledge and experience exists within this organization. But a few thousand of bridges belong to Swedish municipalities. As part of a pre-study [1] on the preventive bridge maintenance in Sweden, the STA's experience and requirements [3]-[10] were examined. The question about possible similarities and differences between municipalities arose. Therefore a survey was conducted with the goal of examining the municipalities' bridge maintenance. The results from the survey and pre-study are the base used in further research that will examine the effect of washing on concrete bridge elements.

2. BACKGROUND

The majority of Swedish bridges were constructed during the three decades between 1950 and 1980. They have now reached an age of 40-70 years and many of these bridges are in need of repair if they have not already been repaired. The knowledge on durability was less during this period which means that the deterioration processes go faster than what will be anticipated for modern bridges which are constructed for a service life of 120 years. However, both old and new bridges need some kind of maintenance in order to reach the intended service life and fulfil the performance criteria. From a sustainability point of view, every year of prolonged use leads to less use of new virgin construction materials and, thus, less environmental footprint.

The maintenance is traditionally divided into preventive and corrective maintenance, but the wording and definitions may vary. In Sweden, STA has made the definitions and developed the requirements as stated above. The preventive bridge maintenance consists of simple measures, e.g., water washing, cleaning, vegetation removal, crack repair, material refill, and stretching of bridge railings. The Swedish preventive bridge maintenance has been analysed and criticized [11-12] and research needs has been identified. A hypothesis is that improved preventive bridge

maintenance will be a cost-effective measure to prolong the bridge's service life and improve its performance. Current research project is a result of these efforts.

As a minor part of a pre-study on the continuous preventive maintenance of Swedish bridges [1], a survey was sent out to municipalities. 17 replies were sent back of over a 100 contacted municipalities. In total there are 290 municipalities in Sweden. Over 210 of these municipalities use the database designed for bridge and tunnel management (BaTMan), created and managed by the STA. In total there are over 30 000 bridges in Sweden and the vast majority of them belongs to the STA [2]. Due to this, the STA and its predecessors are the leading source for requirements of bridge maintenance in Sweden. BaTMan contains a lot of structural information on bridges, results from inspections and measures but nothing concerning the washing or cleaning is registered in the database. The procedures and controls contracts used by the STA are based on information from BaTMan, such as information about length of edge beams, length of bridge joints and number of drainages. Several municipalities use and adapt the requirements and procedures used by the STA [5], [8] & [10]. But due to the information gathered in the survey, there are some factors the municipalities do differently and have a different view on than the STA. Noteworthy is that for a lot of municipalities, there has been unwanted neglect of bridge maintenance or prioritizing due to lack of funds. For several municipalities in the survey, and even information from non-participants, there has been an increase in funds and prioritizing of infrastructure in recent years. This has resulted in an increased standard of bridges enabling "catch up" maintenance and repairs. Most municipalities in the survey are still in the phase of catching up and some are just starting. From a maintenance point of view it is positive to increase funds for maintenance in order to avoid or delay major repairs.

As mentioned, this survey was considered to constitute a minor part of a pre-study. However, there are a lot of interesting answers from the responders that presented a good indication of the situation. The survey's goal was to examine similarities and differences between the STA and municipalities and between the municipalities. The lack of variation in geographical location resulted in that its influence could not be examined.

3. METHOD

A survey was sent out to representatives or responsible persons of bridge maintenance in the municipalities. Depending on the size of the municipalities and the amount of bridges the maintenance responsibility could include a small side task for one person to divided responsibility between many people. All surveys that were filled in, except one, generally answered all the questions completely.

The responders either filled out the questions on their own or over the phone with the first author. A translated version of these questions can be seen in the appendix as the original is in Swedish.

3.1 The responders

The responses are from representatives of 17 municipalities in Sweden. All except one are located in the middle and south of Sweden. Nine municipalities are located along the coast sides (five on the west coast and four on the east coast). An additional three are located near the capital, Stockholm. The last five municipalities are all located near one of the three biggest lakes in Sweden.

Despite few responses, observed differences and similarities in answers have given a good initial indication of the situation between municipalities themselves and in comparison with the STA. In the questionnaire the municipalities could choose between allowing the name of person and municipalities to be published in the report and total anonymity with steps in-between. As some choose total anonymity, no municipalities will be referenced by name in this article for consistency. The 17 participating municipalities generally gave thorough answers and additional interesting information beyond what the questions required. Some of these answers will be presented as examples by those that gave their permission.

The contacted municipalities were chosen from a process where municipalities with a population under 15 000 and those that had fewer than five bridges in BaTMan were eliminated. Of the over 100 municipalities contacted, more than half didn't respond at all. Several responded that they were quitting or just started and therefore could not answer as they were themselves trying to get to grips with the matter. A few also referred to their contractors, which was not the group of interest for this survey, as the goal was to examine the municipalities, but could be of further interest when comparing and examining contractors.

3.2 The survey

The survey consisted of 31 questions where 16 were multiple choice questions and the rest generally required short answers. For each question there was an option for comment, which mostly was used to explain, give examples or provide additional information that would be of interest. A translated version can be seen in full in the appendix.

4. RESULT

Initially there was a wish for diversity and many replies, but the end result was few but satisfactory. The initial goal of the survey was to detect similarities and differences between municipalities and the STA. Some of the municipalities were under change in several aspects, from economically, contracts, investments, personnel, etc. In that case the municipality reported both the current situation and the future one. For future changes, it could mean from weeks to years depending on nature, extension, and degree of the change.

4.1 General facts

While there wasn't a satisfactory diversity in geographical location, there was a good diversity in number of bridges in each municipality, see Figure 1. The number of bridges owned by a municipality ranged from 22 to over 200. The municipality with the highest number of structures had over 800 bridges registered in the database BaTMan. The municipality commented however that the number was a bit misleading. This is because other types of structures are registered as bridges in the database. For example traffic decks were registered as bridges, and continuous bridges could be registered as one single bridge or as several bridges. The exact number of bridges was thereby uncertain.

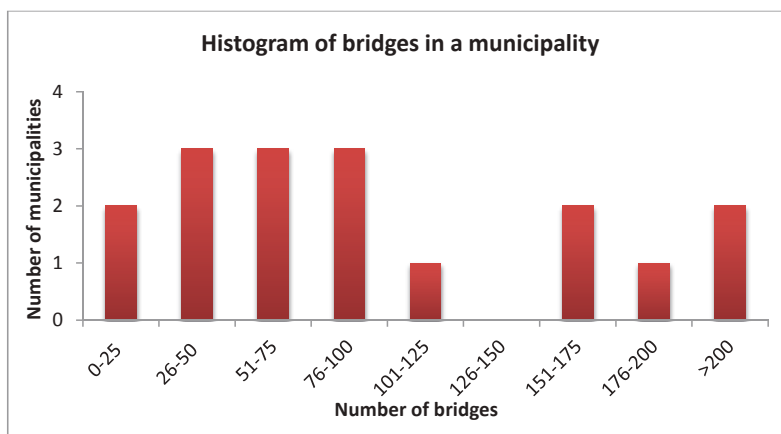


Figure 1 – Histogram over the number of bridges of the participating municipalities.

For the majority of the municipalities the main construction material of their bridges was reinforced concrete or a combination of steel and concrete. A few municipalities had smaller timber bridges, usually only for pedestrians. In most municipalities there was around the same number of pedestrian bridges as road bridges. Otherwise road bridges were more common. Only for one municipality were pedestrian bridges more common than road bridges. Five of the responders had movable bridges, in range from 1 to 18.

The municipalities' budgets for bridge maintenance varied between them, with no clear relation, except maybe incitements from the politicians. Some had very large budgets and others smaller ones. No direct correlation between the budget and the number of bridges or population could be seen. Simple tests with the least square method (R^2) showed around almost no correlation between municipalities' budgets with the number of bridges, population or area. The R^2 values for a trend lines was between 0.07 and 0.12, as one example shows in Figure 2. Even if the municipality with the most eccentric result in Figure 2 is removed the R^2 value only increases a bit on the second decimal. This indicates that there is no distinct correlation with the maintenance budget and these individual factors. The only factors that had high R^2 (0.73) value were unsurprisingly between the population and the number of bridges. Some municipalities

had large budgets in order to catch up on required maintenance and repairs. Some were doing repairs after several decades of only acute maintenance and repairs. These investments were both short and long term. Some municipalities were going to start and some were in the middle or end of their catch up repairs. Generally, there seems to be an effect of political decisions to invest in infrastructure. To the frustration of the people working with bridge maintenance there is always a shortage of means in comparison to required maintenance. Thereby there is always a choice on what needs to be prioritized.

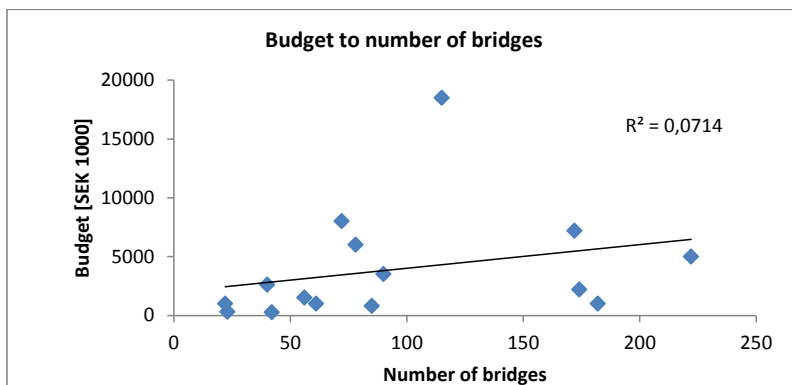


Figure 2 – Diagram with the number of bridges in a municipality plotted against the budget.

The STA uses something they call “integrated bridge maintenance” [13]. It is simplified a way to improve the efficiency of bridge maintenance. By having contractors working in determined geographical areas as to conduct maintenance for bridges in geographical closeness to one-another to increase time efficiency and reduce costs. The integrated bridge maintenance contract also includes minor repairs on selected bridges during the contract period. The STA’s experience with the integrated bridge maintenance have had positive with better efficiency and reduction in costs.

For the participating municipalities, four responded that they use integrated bridge maintenance. Another two responded that they were planning to implement it in the future. Some of the municipalities that didn’t use integrated maintenance motivated this by the fact that their geographical area was too small.

Two thirds of the municipalities use annual scheduling for their continuous preventive bridge maintenance. Most scheduled activities are inspections, washing and cleaning of drainage in correlation with when the gritting sand from the winter season is collected.

The municipalities were asked the question of who’s responsible for the maintenance of a bridge when the ownership is shared. Shared bridges are not common and usually exist when the bridge is geographically located at the border between municipalities. Another possibility is that one part of the bridge belongs to the STA and another part belongs to a municipality, this is usually when roads belonging to each part meet or are connected to each other by ramps for example.

The responses can be seen in Figure 3, where the left circle shows how many of the municipalities share bridges (65 %) and those that don't share or didn't respond to the question (35 %). In that case it has been assumed that the municipality don't share any, as it was an extended question. The right circle shows the answers for those municipalities that answered "yes" to shared bridges. The majority answered how they share responsibility and cooperated. The municipalities often specified or gave examples of what each part did. Usually it was different types of maintenance. For example, one municipality answered that they were responsible for the electronics on the bridge and removal of graffiti. Otherwise the answers were evenly split between doing all of it themselves or it was depending on the bridge concerning responsibility.

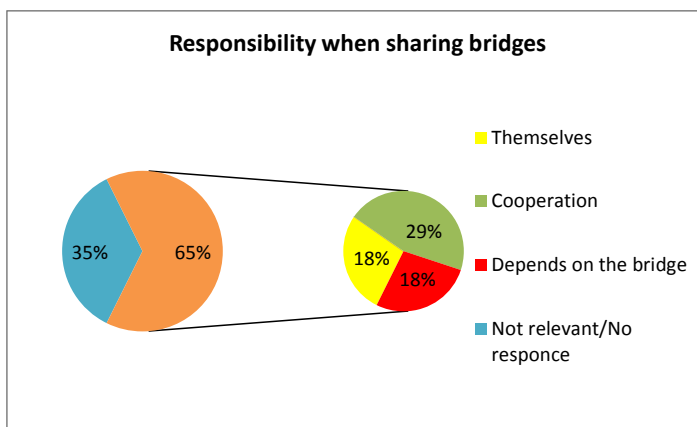


Figure 3 – Diagrams over who is responsible for maintenance of a bridge when the ownership is divided. The left circle shows the percentage of those that share and don't share or didn't answer. The right diagram shows the responsible part when sharing bridges.

4.2 Contracts for bridge maintenance

The STA has been using contractors for the practical aspects of the maintenance for the last decades. The assumption that municipalities also did was examined.

All of the municipalities have contracts with consultant firms for the inspection of the bridges, similar to the STA. Two municipalities did this partly, where some small and simple bridges were inspected by their own personnel. One municipality stated that they inspected the small timber bridges in the forest on their own. These bridges were not in BaTMan and the municipality specified that only those registered in BaTMan were inspected by consultants.

The washing of bridges was generally done by contractors (10 municipalities). The rest either had contractors doing some of it or the municipalities did everything themselves. For removal of vegetation the municipalities were almost evenly split between using only contractors, partly contractors and or by the municipalities themselves. One municipality couldn't answer who was

responsible for the washing and removal of vegetation as this was the responsibility of another division and considered a part of the road maintenance.

Cleaning of drainage systems was either fully or partly done by contractors. Only two municipalities didn't use any contractors for cleaning the drainage system. For both small repair and controls the operation was usually done by contractors. A few municipalities didn't use contractors at all.

Five municipalities used contractors for everything, two municipalities partly used contractors for everything, excluding inspection. One municipality didn't use contractors at all except for inspections. The rest had varied or mixed usage of contractors.

4.3 Inspection

In Sweden there are different types of bridge inspections that have different levels of thoroughness and have different recommended frequencies[14]. There are three major inspection types with corresponding frequency of 1, 3 and 6 years. The lower the frequency of the inspection, the more detailed and thorough inspection. The municipalities used one or more of these types. Some municipalities also made one or several of their own minor inspections. It is common that maintenance contractors perform continuous supervision and should report if they find any damage or something not functioning. There were some exceptions to the normal frequency of inspections. One municipality reported that they inspected their movable bridges every fortnight during sailing season.

The inspectors from the consultancy firms get a certain period or dates where they can do their inspections. Usually this is done during the warmer season but can happen at any time during the year. There was a great range between the consultancy firms used by the municipalities, where almost every municipality used a different firm.

4.4 Maintenance

Due to the winter conditions in Sweden, the use of de-icing salts is common practice. The use of it in the municipalities is therefore an important aspect to consider, especially because de-icing salt contributes to corrosion of steel and of the rebars in concrete. A special focus in Sweden is on the edge beams, which constitute a continuous problem. The participants were asked when the salting occurred and how many of their bridges that were directly exposed to de-icing salts. Almost all of the participants used de-icing salts on their bridges to some degree, see Figure 4. Some municipalities only use de-icing salts on their road bridges or, as one municipality commented, only on the roads used by public transport. The geographical location of the municipalities didn't indicate any influence on the amount of bridges exposed to de-icing salts.

For municipals located next to each other or very close, one municipality usually had a high number and the neighbour a low one.

The period for using de-icing salts was quite consistent for the 15 municipalities that used de-icing salts. Unsurprisingly, the main period is during the winter months but as all the municipalities commented on, it depends on the weather conditions and prognosis. All had December to February with most also including March (87 %) and November (73 %). A few also said April and/or October. This could of course be because the question was interpreted differently with some only stating all of the possible months and others only stating the most common ones.

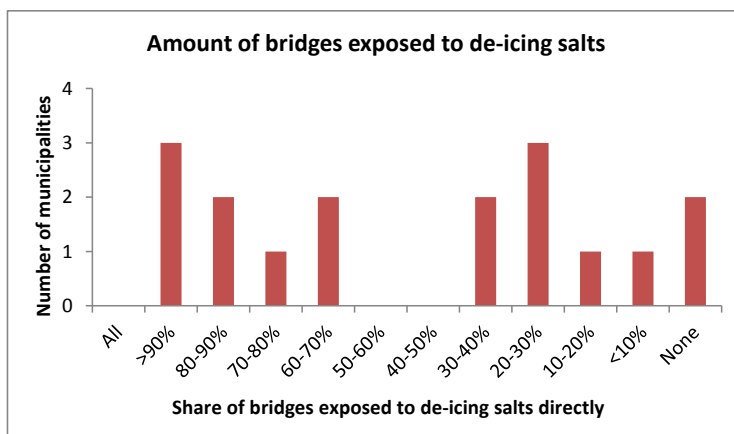


Figure 4 – Histogram showing what percentage of a bridges within a municipality are directly exposed to de-icing salts

Washing of bridges occur when the winter season is over and after the collection of grit sand used for ice prevention during the winter. The main period of washing is late spring and/or early summer, but could also be done later, see Figure 5. The municipalities usually have a period or a date of when the washing of bridges should be done. Some also have a specified starting date when work can start, which is usually in April or May. The municipals that answered August to November also had washing done in May and/or July, indicating two washing periods. The STA states in their contracts for integrated bridge maintenance [15] that the period for washing is generally from the middle of May to the middle of July. The geographical location indicated no influence on the period of washing.

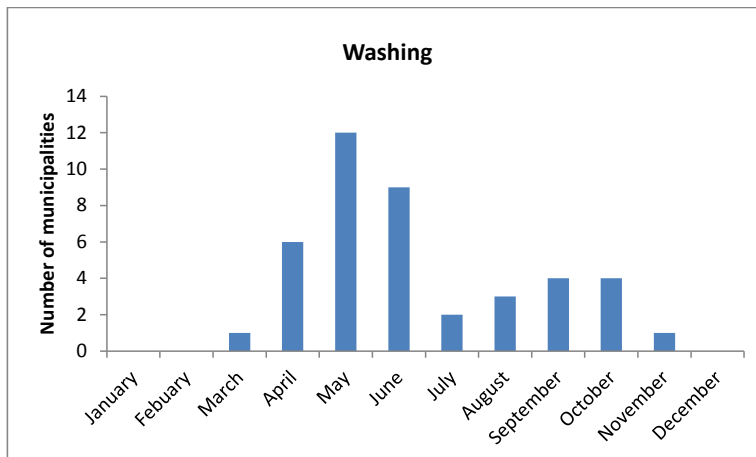


Figure 5 – The period of a bridge washing in the municipalities.

4.5 Demands

The majority of the municipalities reported that they used the STA's current demands (TDOK 2013:0415) [4] and advice (TDOK 2013:0416) [7] for bridge maintenance. Of these 17 municipalities only two had additional demands than those based on the STA's. Another two municipalities had occasionally more demands. But the majority didn't have more requirements than those the STA has for bridge maintenance. Some comments from the municipalities indicated, however, the usage of older versions' demands. Certain comments were made on demands on washing that were the same as in the STA's older versions [9], [10] but not the newer one. This can be the result of preferences or lack of knowledge of updates. When asked for their demands on washing, the municipalities either referred to STA's or answered edge beam, bridge bearing & pillars, railings, drainage systems etc. The majority of the municipalities felt that their demands were being fulfilled. Only a quarter of the municipalities felt that the demands had been fulfilled partly while the rest felt that it had been fulfilled completely. One municipality commented that it had shown flaws during checks and another commented that their subsidiary didn't have the right equipment, making it hard to reach and perform the maintenance correctly.

4.6 Problems and actions

The most common problems for bridge maintenance in municipalities were quite different depending on the municipality and interpretation of the question. The answers touched upon railings, joints, edge beams, accumulations, different surface damages, economy etc. and no municipality answered the same. Many municipalities responded with a few different answers.

This also reflects the different and many issues that exist with the bridges. Some problems could be solved with washing and cleaning while other requires minor or major repairs.

There is a consensus amongst the participants that the actions taken on their bridges have had a positive effect on the standard of the bridges.

4.7 Control

The people that performed the controls of maintenance were generally different consultants, contractors or someone from the municipalities' own staff. The way to make sure the maintenance has been performed correctly and the demands have been met is mainly by self-monitoring and/or sampling controls from the municipalities. In the case of shortcomings it is usually solved by the contractors having to redo it on their own expense or by form of a penalty. During the year of the survey, the controls had been positive for most of the municipalities. A few had larger faults that needed to be corrected. One municipality that for a long time had to neglect maintenance has in recent years received a larger budget to deal with their problems. The municipalities have noticed an improvement in recent years, which shows that investments in infrastructure have positive effects.

Noteworthy is how much maintenance and repairs that can be done depends heavily on the municipality's budget where they have to prioritize, which for a long time meant doing few things on the bridges that are in the greatest need and neglect other bridges which resulted in more problems on the other bridges and higher repair costs.

4.8 Definition of preventive bridge maintenance

The participants were finally asked how they would define preventive bridge maintenance. The answers could be divided into four categories where the municipalities only gave one answer or a combination of two or several ones. The categories are:

- Cleaning- washing, removal etc. (60%).
- Impregnation and small repairs (60%).
- Continuous supervisions and/or actions done on time (40%).
- Improve or preserve the bridge standard or value (33%).

According the standard for maintenance terminology EN 13306:20 [16] the definition for preventive maintenance is:

“maintenance carried out at predetermined intervals or according to prescribed criteria and intended to reduce the probability of failure or the degradation of the functioning of an item “

This definition can be in agreement to the responses from the participants, with their answers fitting within the definition.

5. CONCLUDING REMARKS

The survey showed both differences and similarities between municipalities. The actual maintenance, demands and controls of the bridges are generally the same, but when and by whom it is done differentiate greatly, which could have an effect on the efficiency of the washing. This is probably connected to the way that the municipalities use and adopt the demands and recommendations previously used by the STA as well as their own previous experiences. The survey also showed that each municipality often had a separate issue or solution that was a result of their bridge stock or the budget. An unspoken consensus among the answers seemed to be that having to prioritize and neglect certain maintenance only increases the problems later on. There is always more to be done than can be met with available means.

The survey shows that the washing of the bridges often starts late. This means that the chlorides from the de-icing have all the time during winter and most of the spring to migrate into the concrete before the washing. This may affect both frost attack and corrosion of rebars. Research on the effect by washing is therefore of interest.

REFERENCES

1. Andersson L: "Det kontinuerliga förebyggande underhållet av broar – en förstudie" ("The continuous preventive maintenance of bridges – a pilot study"), *Report*, RISE CBI Betonginstitutet, Stockholm, Sweden, 2018. (In Swedish).
2. Swedish Transport Agency: "BaTMan Bridge and Tunnel Management, Swedish Transport Agency, 2018. [Online]. Available: <https://batman.trafikverket.se/externportal>. [Visited October 2017]. (Database in Swedish).
3. Swedish Transport Agency: "TDOK 2013:0415, Version 1, Demands Bridge maintenance," Swedish Transport Agency, Borlänge, Sweden, 2013. (In Swedish).
4. Swedish Transport Agency: "TDOK 2013:0415, Version 2, Demands Bridge maintenance," Swedish Transport Agency, Borlänge, Sweden, 2015. (In Swedish).
5. Swedish Transport Agency: "TDOK 2013:0415, Version 3, Demands Bridge maintenance," Swedish Transport Agency, Borlänge, Sweden, 2017. (In Swedish).
6. Swedish Transport Agency: "TDOK 2013:0416, Version 1, Bridge maintenance Advise," Swedish Transport Agency, Borlänge, Sweden, 2013. (In Swedish).
7. Swedish Transport Agency: "TDOK 2013:0416, Version 2, Bridge maintenance Advise," Swedish Transport Agency, Borlänge, Sweden, 2015. (In Swedish).
8. Swedish Transport Agency: "TDOK 2013:0416, Version 3, Bridge maintenance Advise," Swedish Transport Agency, Borlänge, Sweden, 2017. (In Swedish).

9. Swedish National Road Administration: "Bridge maintenance 2006, Publication 2006:146" Swedish National Road Administration , Borlänge, Sweden, 2006. (In Swedish).
10. Swedish National Road Administration: "VVK Bridge maintenance 2010-03," Swedish National Road Administration , Borlänge, Sweden, 2010. (In Swedish).
11. Silfwerbrand J: "Technical Demands for Preventive Bridge Maintenance- A Critical review," *Proceedings, fib Symposium "Concrete Structures- Stimulators od Development"* pp.871-880, Dubrovnic, Croatia, 2007.
12. Silfwerbrand J: "Improving Preventive Maintenance," *ACI Special Publication No. SP-277CD ("Recent Advances in MAintenance and Repair of Concrete Bridges")*, pp. 67-78, American Concrete Institute, Farmington Hills, Michigan, USA, 2011.
13. Swedish Transport Agency: "Bridge maintenance," 14 December 2017. [Online]. Available: <https://www.trafikverket.se/for-dig-i-branschen/vag/underhall-vag/Bro-och-tunnel/brounderhall/>. [Used 10 March 2018]. (In Swedish).
14. Swedish National Road Administration: "BRO Manual for bridge inspection," Swedish National Road Administration, division of road & trafic, Borlänge, Sweden, 1993. (In Swedish).
15. Swedish Transport Agency: "Contract document- Integrated bridge maintenance- Time controlled maintenance-Jönköping- Technical description," Swedish Transport Agency, Sweden, 2014. (In Swedish).
16. SIS Swedish Standards Institute, "SS-EN 13306:2010 Maintenance- Terminology," SIS Swedish Standards Institute, Stockholm, Sweden, 2010. (In Swedish).

APPENDIX SURVEY QUESTIONS

(This is an English translation of the Swedish original)

Preventive bridge maintenance – A survey for municipalities

Generally about bridges

1. How many bridges are you responsible for?

(In this case bridges is defined as having a theoretical span of more than 2.0 meters)

| | |
|---------------------|--|
| Total | |
| Road bridges* | |
| Pedestrian bridges* | |
| Other* | |
| Movable | |
| Fixed | |

*Not necessary but would be helpful

Comment:

2. How many bridges are there with the following construction material?

| | |
|------------------|--|
| Concrete | |
| Steel | |
| Concrete & steel | |
| Wood | |
| Stone | |
| Other | |

Comment:

3. How much money in the municipality is spent on maintenance each year?

Answer:

4. How much is in a preventive purpose? (for example washing, removal of vegetation and minor repairs)

Answer:

5. Do you use integrated bridge maintenance?

(Bridge maintenance contracts on STA's bridges are divided based on geographical location, called integrated bridge maintenance package. These packages include both time-controlled (preventive) and state-controlled (remedial) bridge maintenance. In this case, bridges located within a geographic area are maintained within a period of time. You "perform maintenance on several bridges while in the area")

- Yes
- No

Comment:

6. For which services do you use contractors?

| | Completely | Partly | Not |
|-----------------------|--------------------------|--------------------------|--------------------------|
| Inspections | <input type="checkbox"/> | <input type="checkbox"/> | <input type="checkbox"/> |
| Washing of bridges | <input type="checkbox"/> | <input type="checkbox"/> | <input type="checkbox"/> |
| Removal of vegetation | <input type="checkbox"/> | <input type="checkbox"/> | <input type="checkbox"/> |
| Cleaning of drainage | <input type="checkbox"/> | <input type="checkbox"/> | <input type="checkbox"/> |
| Small repairs | <input type="checkbox"/> | <input type="checkbox"/> | <input type="checkbox"/> |
| Control/ Checks | <input type="checkbox"/> | <input type="checkbox"/> | <input type="checkbox"/> |

Comment:

7. Is there a time schedule for the year?

- Yes
- No

Comment:

8. If you share responsibility of bridges with the STA and/or other municipals. Who is responsible for maintenance?

| | |
|--------------------------|-----------------------|
| <input type="checkbox"/> | Yourself |
| <input type="checkbox"/> | STA/Other municipals |
| <input type="checkbox"/> | Cooperation |
| <input type="checkbox"/> | Depends on the bridge |

Comment:

Inspection

9. Do you do the inspection yourself or does a consultant?

- Ourselves
- Consultant
- Combination

Name of consultant*:

Comment:

10. Is it the same person(s) that inspects the same bridges or does it vary?

- Same
- Different
- Combination/depends
- Don't know

Comment:

11. Choose a) and/or b)

a) How many times a year is a bridge generally inspected?

- 1
- 2
- 3
- 4
- >4
- Don't know

Comment:

b) If the bridges are inspected less than 1 time per year, how large gaps are there between inspections?

- 2 years
- 3 years
- 4 years
- 5 years
- >5 years
- Don't know

Comment:

12. When are the bridges inspected?

- January
- February
- March
- April
- May
- June
- July
- August
- September
- October
- November
- December
- Don't know

Comment:

Maintenance

13. How large part of the bridges is salted with de-icing salts each year?

(This means on the roads both on and under the bridge)

- All
- >90%
- 80-90%
- 70-80%
- 60-70%
- 50-60%
- 40-50%
- 30-40%
- 20-30%
- 10-20%
- <10%
- None

Comment:

14. During which months are de-icing salts used?

(This means on the roads both on and under the bridge)

- January
- February
- March

- April
- May
- June
- July
- August
- September
- October
- November
- December
- Don't know

Comment:

15. When are the bridges washed?

- January
- February
- March
- April
- May
- June
- July
- August
- September
- October
- November
- December
- Don't know

Comment:

Demands

16. Do you base your demands on the STA's documents on demands and advice?

- Yes, current
- Yes, previous version
- Even older
- No, other document(s)

If other, the document's name:

Comment:

17. Which instruction or demands do you have on washing?

(If a reference is used, please name it)

Answer:

18. What is the most common problem? (not counting accidents)

Answer:

19. What is the most common measure? (in regards to the previous question)

Answer:

20. Are the measures considered to have had a positive effect on the bridge standard?

Answer:

21. Are the demands you have fulfilled?

- Yes
- No
- Partly

Comment:

22. Out of the demands you have on bridge maintenance, is it something you wish would be further investigated?

Answer:

23. If the following documents are used, TDOK Krav (2013:0415) and Råd (2013:0416), are additional demands included in the contracts?

- Yes
- No
- Sometime

Comment:

Control/Checks

24. Who performs the check/control?

Answer:

25. How do you verify that the maintenance and demands have been fulfilled?

Answer:

26. Do you have any controls or investigations that you wish to be furthered investigated?

Answer:

27. What happens if the control shows shortcomings in the preventive bridge maintenance?

Answer:

28. Do you use BaTMan?

- Yes
- No
- Have own system

Comment:

29. What is the outcome of the latest checks/controls?

Answer:

Other

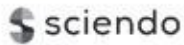
30. How would you define preventive maintenance? What does it include?

Answer:

31. Would it be possible to get in contact with you again concerning additional questions/developments?

- Yes
- No
- Maybe

Comment:



DOI: 10.2478/ncr-2018-0009

ISSN online 2545-2819

ISSN print 0800-6377

© Article authors. This is an open access article distributed under the Creative Commons Attribution-NonCommercial-NoDerivs licens. (<http://creativecommons.org/licenses/by-nc-nd/3.0/>).

Received: March 15, 2018

Revision received: May 29, 2018

Accepted: May 29, 2018

Towards the Understanding of the pH Dependency of the Chloride Binding of Portland Cement Pastes



Alisa Machner
Researcher, NTNU
Department of Structural Engineering
Richard Birkelandsvei 1A
7491 Trondheim
alisa.machner@ntnu.no



Petter Hemstad
MSc Student, NTNU
Department of Materials Science and Engineering
Alfred Getz vei 2
7491 Trondheim
petter@hemstad.net



Klaartje De Weerd
Førsteamanuensis, NTNU
Department of Structural Engineering
Richard Birkelandsvei 1A
7491 Trondheim
klaartje.d.weerd@ntnu.no

ABSTRACT

Hydrated Portland cement paste exposed to a NaCl solution was acidified by adding HCl in small steps, gradually lowering the pH. The chloride binding of the cement paste changed as a function of the pH. For the range of pH from 13.2 to 12.2, decreasing pH resulted in a considerable increase in the chloride binding. At a pH of 11, the cement paste showed almost no chloride binding. In order to explain the changes in chloride binding upon lowering the pH, the phase assemblage was investigated with SEM-EDS, TGA and XRD and compared to a thermodynamic modelling.

Key words: chloride binding, pH, C-S-H, thermodynamic modelling, leaching

1. INTRODUCTION

One of the major deterioration mechanisms of reinforced concrete structures, which can limit their service life, is chloride induced corrosion of the reinforcement steel. As chlorides diffuse into the concrete structure from external sources such as sea water or de-icing salts, the chloride concentration at the reinforcement will eventually increase. When a critical chloride concentration is reached in the proximity of the reinforcement, pitting corrosion of the steel may be initiated. The time until the critical concentration at the steel surface is reached is therefore generally used as a limit state for the service life of a reinforced concrete structure.

Service life prediction models commonly predict the chloride ingress profiles using Fick's law [1,2], which describes diffusion caused by a concentration gradient [3]. Ions, such as chlorides, dissolved in the pore solution, will always move from a high concentration to a lower concentration in the pore solution unless opposed by other forces. Figure 1 shows experimentally obtained chloride profiles (solid lines) of Portland cement mortar samples exposed to sea water, and fitted curves using the error function solution of Fick's law (dashed lines) [4]. With increasing distance from the surface, the chloride content in the mortar decreases according to Fick's law. However, with increasing exposure time, the outermost sections show a lower chloride content than the fitted solution of Fick's law, and show a peak before decreasing with increasing depth from the surface.

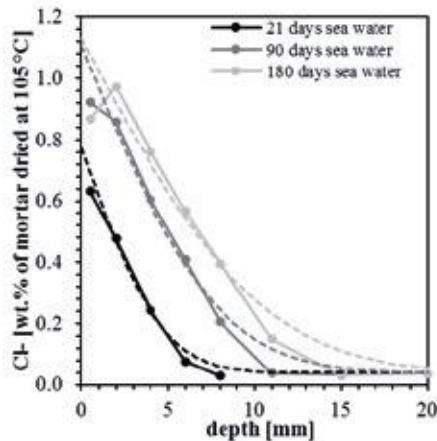


Figure 1 - Chloride profiles experimentally obtained on Portland cement mortars submerged in sea water for 21, 90, and 180 days (solid lines) and fitted to the error function solution of Fick's law (dashed lines) (adapted from [4]).

Similar peaking behaviour in chloride profiles have also been reported elsewhere [5–8]. Current service life models ignore the outer sections and only use the parts of the chloride profile that fits the mathematical model [2]. Our hypothesis is that we can capture this peaking behaviour if we are able to take into account leaching in the models.

When concrete is exposed to sea water there are several phase changes that occur with varying depths of penetration [5]. Due to the presence of $\text{Ca}(\text{OH})_2$ and the alkali metal content in hydrated cement paste, the pore solution is highly alkaline, with a pH of 13 or even higher [9]. Constant exposure to sea water of near neutral pH will reduce the pH of the pore solution. The phase assemblage in the cement paste will change both because the pH is lowered, and because of ingress of ions from the sea water.

In the cement paste, chlorides are bound either chemically, by the formation of chloride-containing AFm phases, such as Friedel's salt ($3\text{CaO}\cdot\text{Al}_2\text{O}_3\cdot\text{CaCl}_2\cdot 10\text{H}_2\text{O}$), or physically, by their accumulation in the diffuse layer of the C-S-H phase [10]. Consequently, changes in the phase assemblage of the cement paste with regards to Friedel's salt or the C-S-H phase caused by the exposure of concrete structures to sea water might be the reason for the deviation of the chloride profiles experimentally obtained from Fick's law.

Changing pH influences both the chemical and physical binding of chlorides. Roberts [11] showed that lowering the pH would slightly increase the stability of Friedel's salt, thus increasing the chemical chloride binding of the cement. Lowering the pH too far would however decrease its stability and lead to reduced binding [12,13]. Since OH^- and Cl^- both accumulate in the diffuse layer of the C-S-H, they can be considered as competitively adsorbing ions. Reducing the pH would reduce the competition from OH^- , thereby increasing the apparent adsorption of Cl^- in the diffuse layer [14]. Small decreases in the pH were reported to increase the chloride binding of the cement paste [14,15]. However, this was done by introducing chlorides in the mixing water, which will affect the microstructure of hydrated concrete. Because of this effect, studies using admixed chlorides might not be representative for external chloride ingress and binding in concrete. The exposure of cement pastes to CaCl_2 solutions has also been reported to be accompanied by a decrease in the pH of the pore solution and an increase in chloride binding [14,16–19]. However, no previous studies have systematically investigated how pH affects chloride binding for chlorides introduced after hydration.

The focus of this study was therefore to develop a method for studying chloride binding for hydrated cement pastes exposed to chlorides and systematically lowering the pH. Well-hydrated cement pastes of ordinary Portland cement (OPC) were exposed to a NaCl-solution. HCl was then added to lower pH without adding other types of ions not already present in the system. First, a relationship between volumes of added acid and pH in the pore solution was established. This relationship was used to determine how much acid is required to reach specific pH-levels. The combination of changes in the phase assemblage and lowering of the pH in the pore solution upon acid addition is referred to as leaching in this study. The second part of this study consists of acidifying five cement paste samples to targeted levels of pH and determine how the acidification affects the chloride binding. The effects of artificial leaching with HCl on the phase assemblage were studied, to explain the mechanisms causing changes in chloride binding.

2. MATERIALS AND METHODS

2.1 Materials and sample preparation

In this study, Portland cement pastes were investigated, prepared with an ordinary Portland cement (OPC) supplied by Norcem AS, to which only natural gypsum was added during grinding. Table 1 shows the chemical composition of the Portland cement used determined with

X-ray fluorescence (XRF). The Portland cement used had a Blaine specific surface of 416 m²/kg.

Table 1 - Chemical composition of the Portland cement (OPC) used determined with XRF [wt. %].

| | SiO ₂ | Al ₂ O ₃ | TiO ₂ | MnO | Fe ₂ O ₃ | CaO | MgO | K ₂ O | Na ₂ O | SO ₃ | P ₂ O ₅ |
|-----|------------------|--------------------------------|------------------|------|--------------------------------|-------|------|------------------|-------------------|-----------------|-------------------------------|
| OPC | 19.91 | 5.15 | 0.28 | 0.06 | 3.42 | 62.73 | 2.34 | 1.09 | 0.48 | 3.16 | 0.11 |

The cement paste was prepared in 4 batches of 540 g with a w/b ratio of 0.5 in a high-shear mixer (Braun MR5550CA). The pastes were mixed for 30 s, left to rest for 5 min and mixed again for 60 s. The paste was cast in several plastic bottles (125 mL) and sealed with a lid and parafilm. The tubes were stored up to their bottle necks in water in sealed boxes at 60°C. To maximize hydration and thus minimize any continued hydration during exposure, the samples were ground and rehydrated after 3 months of curing. They were crushed in a jaw crusher and sieved through a 1 mm sieve. Remaining particles were crushed further in a rotating disc mill until they also passed the sieve. After crushing, the samples were put in 1 L polypropylene bottles with additional 30wt% of water. The bottles were then sealed with lids and parafilm, and stored for another 4 months at 60°C. After this final curing at 60°C, the bottles were stored at 20°C for 13 months before chloride exposure. The exposure was also performed at 20°C.

2.2 Exposure of the samples to NaCl and HCl

For the exposure, 15 g of the well-hydrated cement paste, which had a homogenous moist-sand appearance, was weighed into 50 mL centrifuge tubes, to which 20 mL of NaCl solution (1.5 mol/L) was added using a volumetric pipette. The 1.5 mol/L NaCl solution was prepared with deionized water and laboratory-grade NaCl (supplied by Merck). The tubes were then closed with lids and parafilm, and thoroughly shaken to mix the liquid and the solid. They were then left for two weeks at 20 °C to reach equilibrium, while being shaken once per week to ensure full exposure.

After reaching equilibrium with the NaCl solution, one sample (OPC-22.5, see Table 2) was used to establish the relationship between the volume of added acid and the resulting pH of the pore solution. For this 4 mol/L HCl was added in steps until the sample tube was filled. The acid was added in small steps to avoid uneven dissolution of the hydrated cement paste. In addition, the samples were centrifuged and the acid was added to the supernatant to avoid direct contact between the acid and the solids. The acid was first added in 10 steps of 0.25 mL, then 4 steps of 0.5 mL, 3 steps of 1 mL, then in 8 steps of 2 mL until the sample tube was filled. The final volume of acid added was 22.5 mL. The pH of the sample was measured after 10-15 minutes and after 1-3 days of each addition step (“instant pH” and “pH at EQ” respectively in Figure 3).

To one sample tube no HCl was added (OPC-0, see Table 2). This sample was used as a reference. To the other tubes of the prepared and equilibrated samples, various amounts of 4 mol/L HCl (0.5, 2.5, 5, and 17 mL) were added in small steps (12 steps of 0.25 mL, then 2 steps of 0.5 mL, then 1 step of 1 mL, then 6 steps of 2 mL) to reach the target pH in the pore solution (see Table 2). The additions were stopped after the target acid volume was reached in the various samples. After each addition, the samples were shaken and left to rest until the next acid addition. Acid was added each workday, leading to a minimum resting time of 1 day and a maximum of 3 days. After having the full amount of acid added, the samples were stored at 20°C for two weeks, while they were all shaken once per week.

Table 2: Overview of the various exposed samples in this study.

| Sample name | Cement paste | 1.5 mol/L NaCl | 4 mol/L HCl |
|---------------------------|--------------|----------------|-------------|
| | [g] | [mL] | [mL] |
| OPC-0 (Reference) | 15.00 ± 0.01 | 20 | - |
| OPC-0.5 | 15.00 ± 0.01 | 20 | 0.5 |
| OPC-2.5 | 15.00 ± 0.01 | 20 | 2.5 |
| OPC-5 | 15.00 ± 0.01 | 20 | 5 |
| OPC-17 | 15.00 ± 0.01 | 20 | 17 |
| OPC-22.5 (pH development) | 15.00 ± 0.01 | 20 | 22.5 |

2.3 Analyses after exposure

Analyses of the liquid

The liquid phase of the samples was investigated 2 weeks after exposure to the NaCl solution (OPC-0) or 2 weeks after the full amount of acid had been added (OPC-0.5 – OPC-17).

The chloride concentration in the liquid phase was determined by potentiometric titration with a Titrand 905 titrator from Metrohm using 0.1 mol/L AgNO₃ solution (Titrisol, supplied by Merck). A known volume (0.2–1 mL, depending on the chloride concentration of the exposure solution) of the supernatant was pipetted into a measurement beaker with 1 mL of HNO₃ (65% supplied by Merck, and diluted 1:10), 2.5 mL of 0.2% polyvinyl alcohol (supplied by Merck, 2 g was dissolved in 1 L deionized water), and approx. 20 mL of deionized water.

The actual concentration of free chlorides present before binding ($C_{Cl,free}$) was calculated using Eq. (1) according to [20]:

$$C_{Cl,free} = \frac{(C_{NaCl} \cdot V_{NaCl}) + (C_{HCl} \cdot V_{HCl})}{V_{H_2O} + V_{NaCl} + V_{HCl}} \quad (1)$$

where C_{NaCl} is the concentration of chlorides in the NaCl solution, which was measured with potentiometric titration prior to exposure; C_{HCl} is the concentration of the acid used (4 mol/L); V_{NaCl} is the volume of NaCl solution added to the samples (20 mL); V_{HCl} is the volume of acid added to the various samples (0, 0.5, 2.5, 5, 17 mL); V_{H_2O} is the volume of free water (in g) per 15 g of the well-hydrated hydrated cement paste before exposure, and was assumed to be equal to m_{H_2O} (4.6 g per 15 g of well-hydrated cement paste), which was determined by the weight loss of the unexposed well-hydrated cement pastes after drying at 40°C in a TGA until constant weight.

During the exposure of cement pastes, chlorides from the solution are bound by the hydrates of the cement paste. The chloride concentration in the solution will therefore decrease until equilibrium between the solid and the liquid phase is established. The amount of bound chlorides ($N_{Cl,bound}$) can be calculated as mg/g cement paste dried at 40°C using Eq. (2), according to [20]:

$$N_{Cl,bound} = \frac{M_{Cl} \cdot (C_{Cl,free} - C_{Cl,eq}) \cdot (V_{H_2O} + V_{NaCl} + V_{HCl})}{m_{sample} - m_{H_2O}} \quad (2)$$

where $C_{Cl,free}$ is the actual concentration of free chlorides present at the beginning of the exposure (in mol/L), which can be calculated using Eq. (1); $C_{Cl,eq}$ is the chloride concentration of the supernatant measured at equilibrium (in mol/L); M_{Cl} is the molar mass of chlorine (35.453 g/mol); m_{sample} is the mass of the sample added to the centrifuge tube (15 g); and m_{H_2O} is the mass of free water (in g) per 15 g of hydrated cement paste.

After determining the amount of free chlorides, the pH of the liquid phase was measured using a 6.0255.100 Profitrode from Metrohm in the laboratory at 20°C. Before measuring the pH, the sample was centrifuged at 4000 rpm for 2 minutes and 30 seconds. 2 mL of the supernatant was pipetted into 15 mL centrifuge tubes, in which the pH was measured. The electrode was calibrated each day before the measurements using buffer solutions of pH 7, 10 and 13. After each measurement, the remaining supernatant was poured back into the sample.

The concentrations of Ca, Cl, K, Na and S and in the solution were determined by a Thermo Scientific Element 2 ICP-MS. 150 µl of the supernatant was acidified with 104 µl 65 % HNO₃. This mixture was then diluted to 15 ml with deionized water, to reach a HNO₃-concentration of 0.1 mol/L in the samples.

Analyses of the solid

After concluding the investigations of the liquid phase, the phase assemblage in the Portland cement pastes was investigated. For that approximately 3-5 g of cement pastes was taken out from the centrifuge tubes and was placed in 125 mL plastic bottles with 100 mL isopropanol. The bottles were shaken for 30 seconds before resting for 5 minutes. After resting, the liquid was decanted and another 100 mL isopropanol was added. The bottles were again shaken for 30 seconds and left to rest for 5 minutes, before the contents were poured into a vacuum filtration unit. The isopropanol was filtrated off, and 20 mL petroleum ether was added. The petroleum ether and solids were stirred with a glass rod for 30 seconds before resting for 5 minutes. Afterwards, the petroleum ether was filtrated off using a vacuum filtration unit, and the samples were dried in a desiccator overnight under a slight vacuum (-0.2 bar) applied using a water pump. A part of the dried samples were ground to a particle size <63 µm and then analysed with TGA or XRD. The rest of each of the dried samples was not ground and used for SEM-EDS investigations.

Thermogravimetric analysis (TGA) was used to determine the free water content in the well-hydrated samples before exposure to a NaCl solution, and to investigate the phase assemblage in the samples, which were exposed to only NaCl or NaCl and various amounts of HCl. For all TG analyses, approximately 150 mg of the solids were placed in 600 µl alumina crucibles and analysed in a Mettler Toledo TGA/DSC3+ device. To determine the free water content of the cement paste prior exposure, non-solvent exchanged paste was dried at 40°C until constant weight (10 hours) while purging with N₂ at 50 mL/min. The weight loss was normalized to the initial sample mass, giving the free water content of the cement paste. The solvent exchanged, dried, and ground samples were heated from 40 to 900°C with a heating rate of 10°C/min while purging with N₂ at 50 mL/min. The decomposition of specific phases can be detected as a weight loss in specific temperature intervals. This was used to identify various hydration phases as suggested by Lothenbach et al. [21]. The first weight loss peak at around 100°C is related to the ettringite (Et) decomposition and the beginning of the dehydroxylation of the C-S-H phase. C-S-H decomposes gradually between 40°C and 600°C and appears as a polynomial baseline

under the other peaks. AFm phases such as monosulphate (Ms), monocarbonate (Mc), and Friedel's salt (Fs) shows typically two mass loss events, the first one between 150 and 200°C and the second between 250 and 400°C. Hydrotalcite (Ht) typically also causes a decomposition peak in the DTG signal around 350°C. The subsequent sharp peak between approx. 400°C and 550°C is related to the decomposition of portlandite (CH). Above 550°C, carbonates decompose and emit CO₂.

The dried powders were also analysed using X-ray diffraction (XRD) to confirm phase changes. Approximately 0.5 g of the powders were placed in the sample holders by front loading. We used a Bruker AXS D8 Focus with a Lynxeye detector, operating at 40 kV and 40 mA with a CuK α radiation source (wavelength 1.54 Å). The samples were measured between 5° 2 θ to 55° 2 θ , with a step size of 0.01° 2 θ , and a sampling time per step of 0.5 s.

The samples to be investigated with scanning electron microscopy (SEM) were cast in epoxy, polished and carbon-coated. A Hitachi S-3400N electron microscope equipped with an energy dispersive spectrometer (EDS) from Oxford Instruments was used. BSE images and EDS-maps of all samples were captured, in addition to 100 EDS point-scans of the cement paste matrix per sample. The SEM was operated at an accelerating voltage of 15 keV and a probe current of 70 μ A, a working distance of 5 mm for taking the BSE images, and a working distance of 10 mm for operating the EDS.

Thermodynamic modelling

The Gibbs free energy minimization software for Geochemical Modelling [22–24], was used to model the phase assemblage, the pH, and the composition of the liquid phase at equilibrium with increasing amounts of HCl (4 mol/L) added at 20°C. The thermodynamic data from the PSI-GEMS database were supplemented with a cement-specific database (CEMDATA14 database) [25], which includes solubility products of the solids relevant for cementitious materials. For the C-S-H phase, the CSHQ model proposed by Kulik was used [26]. For the model, TiO₂, MnO, MgO, and P₂O₅ and C₄AF were assumed to be inert. Therefore, the amounts of TiO₂, MnO, P₂O₅ and MgO in the cement clinker determined with XRF (see Table 1) were subtracted from the composition. The amount of C₄AF was calculated with the Bogue calculation, and then subtracted from the composition. The remaining oxide composition (approx. 85%) was then normalized to 100 %. A reaction degree of 50% was assumed in the modelling. Taking into account that only 85% of the oxide composition was used as input in the model, this resulted in a total assumed reaction degree of the cement of approx. 70%. During the modelling the following phases were prevented from forming: gibbsite, kaolinite, siliceous hydrogarnet, thaumasite, hematite, magnetite, brucite and quartz. Further details on the model are provided in [27]. In the model, Friedel's salt is the only phase that is assumed to bind chlorides. The chloride binding predicted by the model was therefore calculated using the amount of Friedel's salt predicted by the model (for more details on the calculations see [27]).

3. RESULTS AND GENERAL DISCUSSION

3.1 Development of the pH with increasing amounts of acid added

First, we needed to determine the acid additions that would yield a relevant change in the pH and the phase assemblage for further investigation. As hydrated cement paste is a complex system with several pH-buffering phases, we used the thermodynamic model to predict the changes in the pH of the exposure solution and the phase assemblage upon the addition of increasing volumes of acid (HCl). The system initially consisted of 15 g moist hydrated cement paste and 20 mL of 1.5 mol/L NaCl solution. One of the limitations was the volume of exposure solution, as high volumes of exposure solution would increase the error on the determination of the bound chlorides. Preliminary simulations pointed out that HCl with a concentration of 4 mol/L would allow us to reach sufficiently low pH for a limited volume of acid added (50 mL exposure tubes).

Figure 2 shows the volume of the phases in the samples as a function of the volume of HCl (4 mol/L) added, as predicted by the thermodynamic model. The amount of portlandite is predicted to decrease linearly with increasing acid addition until it has completely dissolved at 10 mL of acid added. Once the portlandite completely dissolved, the C-S-H is predicted to start dissolving as well. The volume of ettringite remained stable until 19 mL of acid was added, after which the volume decreased steadily until it was fully removed at 21 mL acid. The amount of Friedel's salt remained nearly constant up to 15 mL acid, for higher volumes it starts dissolving until nothing is left at 17.5 mL acid. At high volumes of acid and low pH, the model predicted the formation of natrolite ($\text{Na}_2\text{O}\cdot\text{Al}_2\text{O}_3\cdot 3\text{SiO}_2\cdot 2\text{H}_2\text{O}$), gypsum ($\text{CaSO}_4\cdot 2\text{H}_2\text{O}$) and amorphous silica (SiO_2).

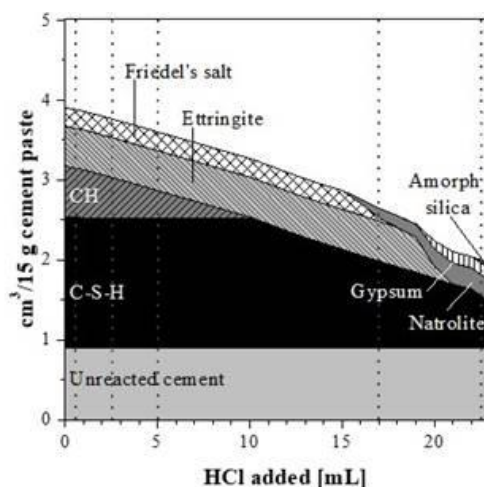


Figure 2 - The predicted changes in phase assemblage (in $\text{cm}^3 / 15 \text{ g cement paste}$) upon the addition of increasing volumes of 4 mol/L HCl (in mL). The sample contained initially 15 g moist hydrated cement paste and 20 mL of 1.5 mol/L NaCl solution. The acid additions (0.5, 2.5, 5, 17, and 22.5 mL) which were used in this study are indicated by the dotted lines.

Figure 3 shows the predicted development of the pH of the exposure solution for increasing amounts of HCl added (pH GEMS - solid line) which corresponds to the modelling of the solid phase assemblage shown in Figure 2. The pH decreases steadily upon HCl addition, with a small plateau between approx. 5 and 10 mL acid added. This is due to the presence of portlandite which buffers the pH. When portlandite is predicted to have dissolved, at around 10 mL HCl added, the pH drops further. In order to verify the predicted pH development experimentally, one sample was acidified (OPC 22.5) in steps of 0.25, 1 and 2 mL HCl until the sample tube was filled. The pH-values were measured both directly after adding acid (instant pH - triangles) and after 1-3 days of equilibration (pH at EQ - spheres). The experimentally obtained pH-development curves are also included in Figure 3. The measured pH and the modelled pH agree well.

The fact that there was hardly any difference in pH directly after adding acid and one day later when less than 7 mL acid was added in steps of 0.25 mL indicates that for these small additions the system rapidly reaches equilibrium, meaning there is no severe instantaneous drop in the pH of the solution. The risk of locally dissolving phases other than portlandite is therefore low. However, the difference between pH immediately after acid addition and after 1-3 days increased for higher additions, likely because of larger amounts acid were added per step combined with the lower buffer capacity of the system.

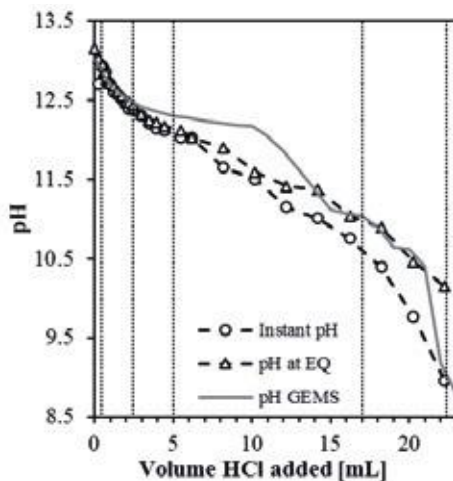


Figure 3 - Development of the pH of the exposure solution upon stepwise addition of HCl (4 mol/L). The sample contained initially 15 g moist hydrated cement paste and 20 mL of 1.5 mol/L NaCl solution. The values experimentally determined 10 min after acid addition, i.e. instant pH (spheres), the pH after 1-3 days of equilibration (triangles) and the pH predicted by thermodynamic modelling with GEMS (solid line) are compared. The acid additions (0.5, 2.5, 5, 17, and 22.5 mL) which were used in this study are indicated by the dotted lines.

Based on the measured pH and the predicted phase assemblage, four levels of acid addition were selected for further investigation: 0, 0.5, 2.5, 5 and 17 mL HCl. The levels are indicated in Figure 2 and Figure 3 with dotted lines. The sample without acid (OPC-0) is considered as a reference. At these acid additions, separate samples were prepared to investigate the chloride binding and the phase assemblage. The results of these investigations are reported in the

following sections. The 0.5, 2.5 and 5 mL additions were aimed to reflect different levels of moderate leaching as the system was predicted to still contain portlandite. The level of 17 mL would reflect advanced leaching as portlandite was nearly depleted and the main hydration phase C-S-H would start to decompose.

3.2 Chloride binding

Figure 4 a) and b) show the experimentally determined amount of bound chlorides for the samples as a function of the pH or the free chloride concentration in the liquid phase respectively. With increasing amounts of acid added (indicated by the arrows in both figures), the pH decreases and the free chloride concentration increases. When the pH drops from 13.2 to about 12.2 (≤ 5 mL of acid added), the amount of bound chlorides increased with decreasing pH and increasing free chloride concentration. At a pH of 11 (sample OPC-17) the cement paste showed close to no chloride binding. Figure 4 also shows the amount of bound chlorides as predicted by the thermodynamic model (dotted line). Friedel's salt is the only phase that is assumed to bind chlorides in the thermodynamic model, thus the model also predicts constant chloride binding in the range of 0-15 mL acid added (pH 13.2-11.1). At higher acid addition, Friedel's salt was predicted to decompose (see Figure 2) and consequently the amount of bound chlorides is predicted to drop to zero. Hence, the model can potentially account for the loss of binding capacity at a pH of 11, but not for the observed increase of chloride binding upon lowering the pH from 13.2 to about 12.2.

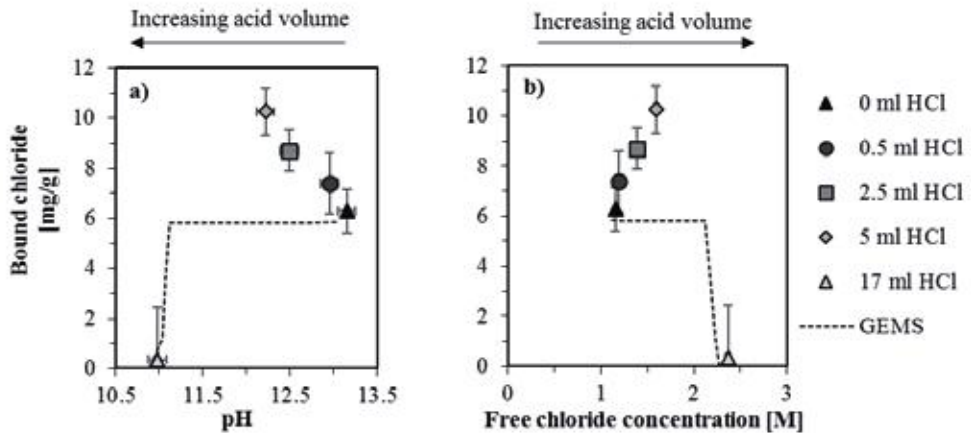


Figure 4 - Amount of bound chlorides in the ordinary Portland cement paste samples exposed to 1.5 mol/L NaCl solution to which varying amounts of HCl was added (0, 0.5, 2.5, 5 and 17 mL) as a function of a) the pH, and b) the free chloride concentration in the liquid phase at equilibrium. The symbols represent the experimentally determined bound chlorides and the dotted line the one predicted by the model. The error bars for the amount of bound chloride and the free chloride concentration were calculated with a Gaussian error propagation. The error of the pH determination was estimated to ± 0.1 .

3.3 Phase assemblage

To elucidate the mechanisms that cause the changes in chloride binding described above, this section presents the investigation of the phase assemblage of the Portland cement paste samples

exposed to 1.5 mol/L NaCl solution to which 0, 0.5, 2.5, 5, 17 and 22.5 mL of HCl was added. The results are discussed and compared to the results of the thermodynamic modelling in the following.

Figure 5 presents the TGA-curves for all the chloride exposed samples and for OPC that has not been exposed to any chloride solutions (OPC-No Cl), as well as the derivative of the TGA-curves of these sample, the DTG curves. The typical weight loss peaks for ettringite (Et), C-S-H, monosulphate (Ms), monocarbonate (Mc), Friedel's salt (Fs), hydrotalcite (Ht), portlandite (CH) and carbonates are indicated.

Figure 6 shows the XRD-spectra of all samples in this study, including the reference, to which no HCl was added (OPC-0) in the range between $8.5\text{-}12^\circ 2\theta$ and $31\text{-}35^\circ 2\theta$. The peak positions of ettringite (Et), Friedel's salt (Fs), portlandite (CH) and NaCl are indicated. Clear peaks of NaCl were observed in all samples exposed to a chloride solution. This indicates that the sample preparation for XRD was not able to remove the pore solution completely, which resulted in the precipitation of e.g. NaCl upon drying.

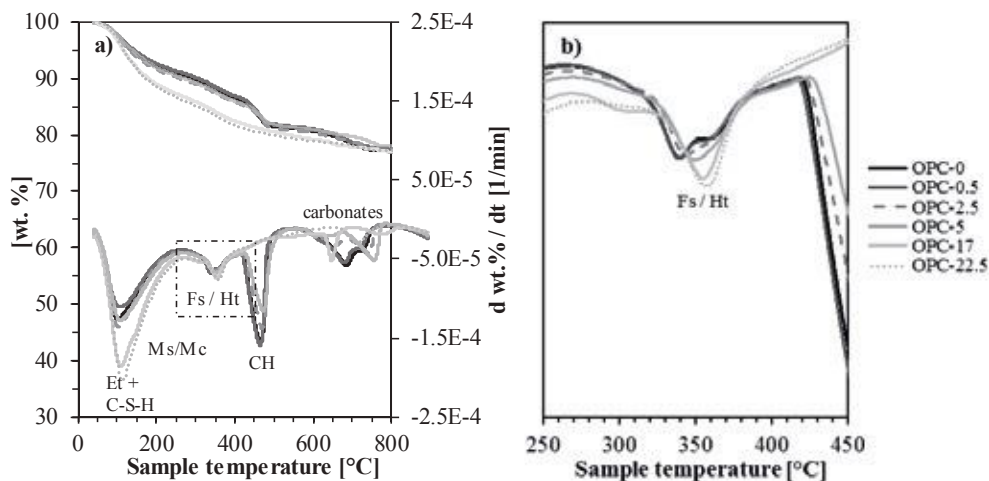


Figure 5 – a) TG (in wt. % of initial mass) and DTG (in wt. %/min) curves of the ordinary Portland cement (OPC) paste samples exposed to 1.5 mol/L NaCl solution to which varying amounts of HCl (4 mol/L) was added (0, 0.5, 2.5, 5, 17, and 22.5 mL). The typical weight loss peaks for ettringite (Et), C-S-H, monosulphate (Ms), monocarbonate (Mc), Friedel's salt (Fs), hydrotalcite (Ht), portlandite (CH) and carbonates are indicated. Figure 5 b) shows the DTG curves of all samples zoomed into the temperature range between 250 and 450°C as indicated by the rectangle in a).

Portlandite

A clear decrease in the portlandite weight loss peak near 450°C was observed with increasing acid additions (Figure 5). Moreover, the XRD peak for portlandite also appears to decrease with increasing additions of acid (Figure 6). The experimental results from TGA and XRD agree well with the thermodynamic model. The amount of portlandite in the samples for the various additions of acid predicted by the thermodynamic modelling (OPC-0: 19 wt%, OPC-5:

10wt%/10, OPC-17: 0 wt%) agree well with the experimentally obtained values with TGA (OPC-0: 15 wt%, OPC-5: 10 wt%, OPC-17: 0 wt%).

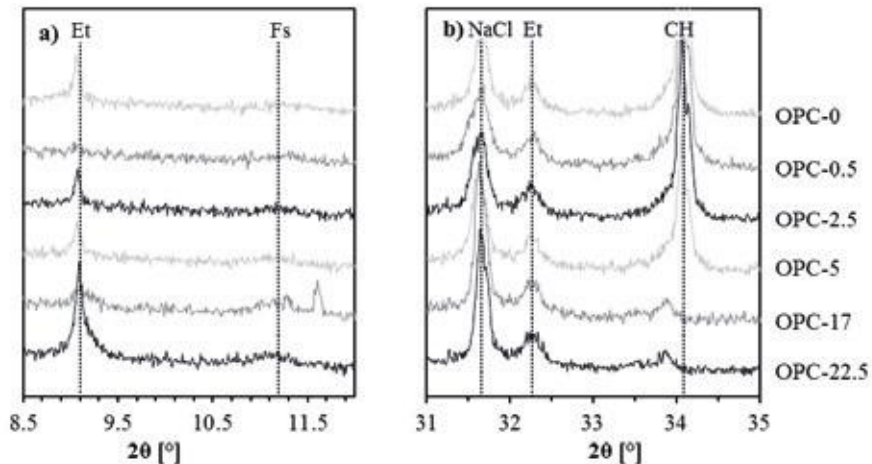


Figure 6 - XRD spectra of the ordinary Portland cement (OPC) paste samples exposed to 1.5 mol/L NaCl solution to which varying amounts of HCl was added (0, 0.5, 2.5, 5, 17 and 22.5 mL in the range between a) 8.5-12° 2 θ and b) 31-35° 2 θ . The peak positions of ettringite (Et), Friedel's salt (Fs), portlandite (CH) and NaCl are indicated.

AFm/AFt

The weight loss peak near 350°C showed a double peak for the samples to which no or only small amounts of acid were added (≤ 2.5 mL), which might indicate the formation of Friedel's salt in these samples [21]. As acid was added, the peak shape changed back to a single peak, as in samples to which no chlorides (NaCl) were added (not shown here). Neither the presence nor the decomposition of Friedel's salt could be verified by XRD as no characteristic reflection peaks for Friedel's salt were observed in any of the XRD spectra (Figure 6). There is a small hump in the spectra near 11.19° 2 θ , which might indicate that the phase is present but is poorly crystalline. SEM-EDS did also not allow the detection of Friedel's salt, indicating that if it is present it is finely intermixed with the other hydrates.

The model predicts the presence of Friedel's salt in the chloride containing samples, and its decomposition for acid additions above 15 mL (Figure 2). Even though the model does not predict any changes in the amount of Friedel's salt for acid additions up to 15 mL, there are some slight changes in the DTG peaks related to the AFm phases upon acid addition up to 5 mL (Figure 5b). However, without clear XRD peaks of these phases their identification is not possible.

The absence of typical diffraction peaks for AFm phases such as Friedel's salt ($3\text{CaO}\cdot\text{Al}_2\text{O}_3\cdot\text{CaCl}_2\cdot 10\text{H}_2\text{O}$, 11.19° 2 θ), monocarbonate ($3\text{CaO}\cdot\text{Al}_2\text{O}_3\cdot\text{CaCO}_3\cdot 11\text{H}_2\text{O}$, 11.7° 2 θ) or monosulphate ($3\text{CaO}\cdot\text{Al}_2\text{O}_3\cdot\text{CaSO}_4\cdot 11\text{H}_2\text{O}$, 10.3° 2 θ) in the XRD-spectra is most likely related to the high curing temperature applied [28]. The paste was cured for 7 months at 60°C, before being stored at 20°C for more than 13 months. Ettringite is not stable at 60°C [28]. Lowering of the curing temperature afterwards might have caused delayed ettringite formation

[29]. The occurrence of delayed ettringite formation in the current study is supported by the distinct reflections for ettringite in the samples investigated (Figure 6). The only sample that did not show a clear reflection of ettringite is OPC-0.5. The reason for this is unknown. The presence of ettringite for HCl additions up to 19 mL was predicted by the thermodynamic model (Figure 2).

C-S-H

According to the thermodynamic model (Figure 2), C-S-H remains stable as long as there is portlandite present in the cement paste. The TGA results (Figure 5) might give the impression that more C-S-H is present in the heavily leached samples (OPC-17 and OPC-22.5), however this is not the case. This is due to the dissolution of portlandite, which is causing the weight loss peaks of all other non-dissolving phases to increase, as the results are expressed relative to the initial mass of the sample.

SEM-EDS was used to investigate changes in the C-S-H composition with increasing amounts of HCl added. SEM-EDS point analyses were taken in the matrix of the various samples. The results of these point analyses were plotted as the Al/Ca over the Si/Ca ratio. The Si/Ca ratio (and thereby the Ca/Si ratio) of the C-S-H was determined as described by Taylor [9]. Figure 7 shows the Ca/Si-ratio of the C-S-H as determined by EDS, and the predicted Ca/Si-ratio and volume of C-S-H in the GEMS model as a function of the pH of the exposure solution.

Figure 7 shows that there are changes in the Ca/Si ratio of the C-S-H even though its volume remains constant. The EDS data and the model both show that the Ca/Si ratio of the C-S-H slightly increased with decreasing pH (acid additions ≤ 5 mL). For acid additions larger than 5 mL ($\text{pH} \leq 11$) the Ca/Si ratio decreased again. The sample OPC-22.5 showed with 1.2 a considerably lower Ca/Si ratio as the sample OPC-0 (Ca/Si = 1.4). According to the model, the decomposition of C-S-H starts at a pH of 12.6, at which point the Ca/Si-ratio also rapidly declines as the pH decreases. This indicates that for sample OPC-17 and OPC-22.5, it is possible that decomposition of the C-S-H has occurred.

The results from the EDS should be interpreted with care, as sample preparation might have caused an artificial increase in the calcium content due to precipitation from the exposure solution. However, similar trends of changed Ca/Si-ratio have been observed by De Weerd and Justnes [30], who showed that in cement paste leached by sea water, C-S-H was decalcified from a Ca/Si-ratio of 1.8 down to 1.

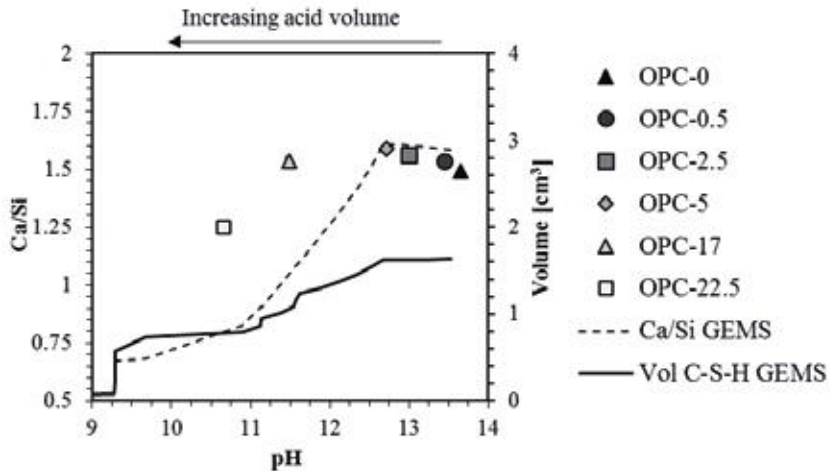


Figure 7 - Development of the Ca/Si ratio of the C-S-H as a function of the pH in the pore solution determined experimentally (symbols) and predicted by the thermodynamic modelling (dashed line). In addition, the predicted volume of C-S-H upon increasing amounts of acid as predicted by the thermodynamic modelling is shown.

Composition of the liquid phase

The symbols in Figure 8 show the concentrations of Ca, Cl, Na, K and S experimentally obtained with ICP-MS in the solution of the samples over a) the amount of acid added and b) the pH in the samples. The lines represent the concentration of the various elements in the pore solution as predicted by GEMS. There is a relatively good agreement between the measured and modelled results. The concentrations of Ca and Cl increase as acid is added, whilst the concentrations of Na and K decrease. The increase in Cl concentration is due to the addition of 4 mol/L HCl. The increase in the Ca-content is caused by the dissolution of portlandite and the decreased Ca/Si-ratio of the C-S-H. The gradual decrease in the Na and K concentrations are due to the dilution with acid. The concentration of S decreases initially, before increasing for the 17 ml acid sample and decreasing slightly from 17 to 22.5 ml. For S the initial decrease in concentration is likely due to dilution, whilst the eventual increase is caused by the dissolution of ettringite.

4. DISCUSSION ON THE ALTERED CHLORIDE BINDING DUE TO THE ARTIFICIAL LEACHING

4.1 Increase in chloride binding for acid additions ≤ 5 mL

Figure 9 combines the chloride binding results from this study (Figure 4b) with the chloride binding isotherms determined by Machner et al. [31] on samples with the same composition cured as well at 60°C and exposed at 20°C to either NaCl or CaCl₂ solutions. In the case of NaCl, the slope of the binding isotherm at free chloride concentrations above 1 mol/L increases only marginally and develops towards a plateau [31]. This means that increasing the chloride concentration above 1 mol/L should not contribute to considerably increased chloride binding.

However, upon the addition of HCl, the chloride binding increases more than could be explained by the increase in free chloride concentration.

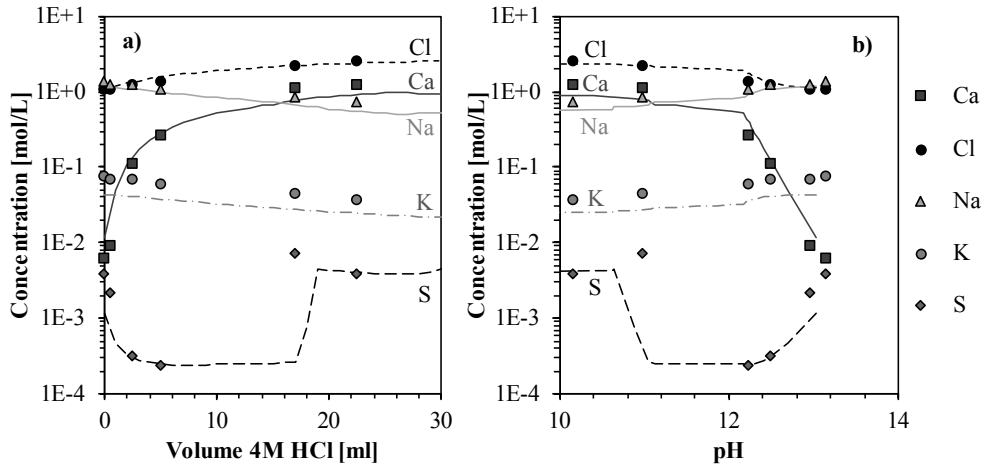


Figure 8: The measured (symbols) and modelled (lines) elemental concentrations in the solution of the samples as a function of a) the amount of acid added to each sample and b) the pH of the solutions.

The values of the bound chloride with HCl additions develop rather towards the values of the chloride-binding isotherm for CaCl_2 exposure reported previously [31]. Significantly greater chloride binding has been reported previously when samples were exposed to solutions of CaCl_2 rather than NaCl [13,16–20,32]. HCl has a similar effect on the system as CaCl_2 , as both lower the pH and increase the calcium concentration, the former by dissolving portlandite and the latter by supplying additional calcium during its dissolution. The difference between the chloride-binding capacity of samples exposed to NaCl and CaCl_2 has been largely attributed to two different mechanisms.

Role of the Friedel's salt

Shi et al. [16] observed the formation of a larger amount of Friedel's salt in composite cement paste samples containing metakaolin exposed to CaCl_2 than in samples exposed to NaCl . He explained this by the additional calcium that is available in the case of CaCl_2 exposure. With the formation of larger amounts of Friedel's salt, more chloride ions are bound chemically and the chloride-binding capacity of the cement paste increased. However, no increase in the amount of Friedel's salt formed was observed for Portland cement pastes [16].

Whether the additional calcium in the pore solution due to the dissolution of the portlandite upon HCl addition lead to the formation of additional Friedel's salt could not be elucidated in this study. The high curing temperature (60°C) of the samples before exposure caused the AFm phases to be poorly crystalline, which made their identification with XRD impossible. For acid additions up to 5 mL, the thermodynamic modelling predicts the dissolution of portlandite and the changes in the Ca/Si ratio of the C-S-H fairly well. Therefore, the thermodynamic model should be able to predict additional Friedel's salt formation due to an increased calcium concentration in the pore solution. However, the model predicts a constant amount of Friedel's

salt to be present in samples to which less than 15 mL of HCl was added, which is within the range of acid additions that showed an increased chloride binding. This indicates that the increased chloride-binding capacity of the samples is probably not due to the formation of additional Friedel's salt.

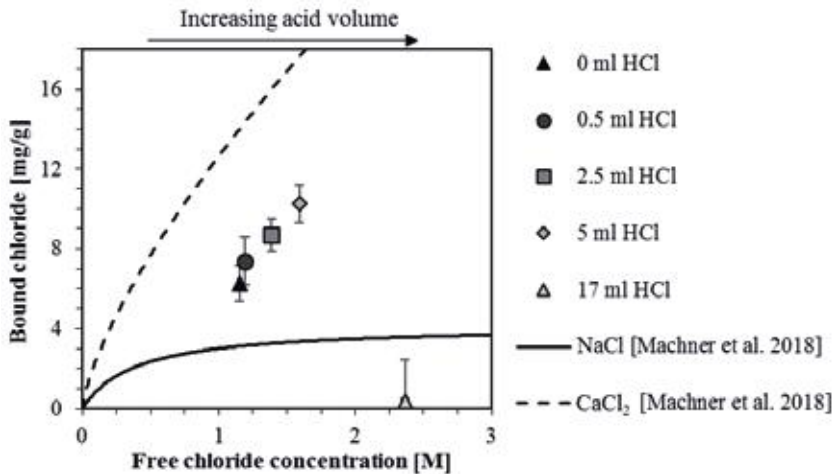


Figure 9 - Development of the amount of bound chlorides with increasing free chloride concentrations in the liquid phase of this study compared to previous results from Machner et al. [31].

Role of the C-S-H

The increased chloride-binding capacity of cement paste samples exposed to CaCl_2 compared to NaCl has also been explained by an increased amount of chlorides that can be accumulated in the diffuse layer of the C-S-H in the case of CaCl_2 exposure. This has previously been explained by the overcompensation of the originally negative surface charge of the C-S-H by the adsorption of divalent calcium ions in the Stern layer of the C-S-H [33]. This overcompensation reverses the surface charge and turns it positive [33], which means negatively charged chloride ions can accumulate in the diffuse layer of the C-S-H [19,34]. Such a reversal in the surface charge leading to the accumulation of chlorides in the diffuse layer has not been observed with monovalent ions, like Na^+ [19]. The exposure of cement pastes to CaCl_2 solutions has also been reported to be accompanied by a decrease in the pH of the pore solution and an increase in chloride binding [14,16–19].

The C-S-H in this study changed its Ca/Si ratio upon HCl addition (Figure 7). The changes in chloride binding could therefore be due to changes in accumulation of ions in the diffuse layer of C-S-H. As shown in Figure 4 the amount of bound chlorides increased with increasing amount of acid added up to 5 mL and consequently with decreasing pH from 13.2 to 12.2. With decreasing pH, more silanol groups are deprotonated (as schematically shown in Eq. (4), where > indicates the connection of the silanol group to the calcium layer), which leads to an increase in the negative surface charge density [35]. Consequently, more calcium ions from the pore solution can be adsorbed on the C-S-H in the Stern layer leading to a larger overcompensation of the surface charge [35]. This is visible in the increased Ca/Si ratio of the C-S-H for acid

additions ≤ 5 mL (Figure 7). This might consequently lead to a larger amount of chloride ions accumulated in the diffuse layer of the C-S-H. The dissolution of portlandite upon acid addition ensured sufficient calcium ions in the pore solution (Figure 8) to overcompensate the negative surface charge of the C-S-H.



Moreover, a decrease in the pH of the pore solution leads to a reduction of competing accumulation by hydroxyl ions, which might increase the accumulation of chloride ions in the diffuse layer additionally [14].

4.2 Decrease in the chloride-binding capacity for higher acid additions

The results of the chloride binding in this study also showed that when 17 mL of HCl was added the cement paste shows almost no chloride-binding capacity. This indicates that after a certain amount of acid has been added, the reduced pH in the pore solution caused the dissolution of chloride-binding phases or prevents them in other ways from binding chlorides.

When more than 5 mL of HCl has been added the C-S-H starts to decalcify, as shown by the Ca/Si ratio in Figure 7. This potentially renders the phase less positively charged, and reduces the accumulation of chloride in the diffuse layer. Additionally, the amount of C-S-H is predicted to decrease for pH values lower than 12.6 (less than 5 mL acid added). Both mechanisms are probably responsible for the decrease in the chloride-binding capacity of the paste samples at HCl additions of more than 5-10 mL. The loss of chloride binding in the outermost section of concrete due to extensive leaching has also been reported for field samples exposed to sea water [7,8] and exposed to NaCl solution [4].

4.3 Further work

The current study was performed as a proof of concept for an experimental setup that can be used to study the impact of the pH of the pore solution on the chloride binding of hydrated cement paste. For further work, the following remarks will be taken into account.

Due to the limited availability of cement paste and therefore the number of samples in the current study, the exact point at which the chloride binding decreases is unknown. If it continues to increase until it drops to zero or gradually declines will be investigated in a follow-up study.

Because the cement paste samples were cured at 60°C before they were exposed to NaCl solutions and HCl, the Friedel's salt in the paste was not crystalline and its contribution to the chloride binding could not be conclusively determined. In a follow-up study, cement paste samples cured at 20°C will be prepared and investigated using the methods developed here. This should lead to samples containing crystalline AFm phases and should make it possible to distinguish between the effects of AFm phase and C-S-H to the chloride binding of the cement paste.

Improvements should be made to the sample preparation for analysis of the solids. The current method of double solvent exchange and filtration appears to cause the precipitation of NaCl and potentially calcium from the pore solution, probably due to the inability of the used solvents

(isopropanol and petroleum ether) to penetrate the gel porosity of the C-S-H phase during the solvent exchange and replace the pore solution between the C-S-H sheets. This was explained by the big molecular size of alcohols compared to water, which inhibits the replacement of the water in very small pores [36]. This makes the solids analyses by XRD, SEM and TGA less representative. A possible solution could be “washing” the solids with a known amount of deionized water over a specified amount of time, similarly to the method described by Plusquellec et al. [37]. This would help to remove precipitates like NaCl before solvent exchange.

5. CONCLUSIONS

A method for lowering the pH of the pore solution in a hydrated cement paste in a closed system was developed.

Chloride binding of a hydrated cement paste was observed to be closely linked to the pH in the pore solution. Lowering the pH from 13.2 to 12.2 increases chloride binding. If the pH drops to 11, the chloride binding of the cement paste is greatly reduced.

The applied thermodynamic model indicates that the pH dependency of the chloride binding is connected to pH-dependent changes in the Ca/Si ratio of the C-S-H. The low crystallinity of the Friedel’s salt in the investigated samples did not allow us the experimentally verify its role in the pH-dependent chloride binding.

These findings might explain why in concrete structures, harsh leaching at the surface will reduce the chloride binding, while moderate leaching further into the concrete leads to increased chloride binding and therefore an increased maximum in the chloride profile. In order to obtain more accurate chloride ingress predictions, service life prediction models for concrete structures exposed to chlorides should incorporate the effect of lowered pH due to leaching on chloride binding.

ACKNOWLEDGMENTS

The authors would like to thank Kjell Wiik (NTNU) for the cooperation within the Master Thesis project of Petter Hemstad, which resulted in this study. The authors would also like to thank Norcem AS for providing the cement used in this study. We are also very grateful for the helpful discussions on the chloride exposure and the C-S-H with Tone Østnor (SINTEF) and Gilles Plusquellec (RISE).

REFERENCES

1. Galan I & Glasser F P: “Chloride in cement,” *Advances in Cement Research*, Vol. 27, 2015, pp. 63–97.
2. International Federation for Structural concrete, *fib*, Model Code for Service Life Design: Model code prepared by Task group 5.6, fib, Lausanne, 2006.
3. Fick A, “Über Diffusion,” *Annalen der Physik*, Vol. 170, 1855, pp. 59–86.

4. De Weerd K, Lothenbach B & Geiker M R: “Comparing chloride ingress from sea water and NaCl solution in Portland cement mortar,” Submitted for publication to *Cement and Concrete Research*, April, 2018.
5. De Weerd K, Justnes H, Geiker M R: “Changes in the phase assemblage of concrete exposed to sea water,” *Cement and Concrete Composites*, Vol. 47, 2014, pp. 53–63.
6. Geiker M R: “Fly ash in concrete, Danish experience,” 2015. *Report No. 370*, Norwegian Public Roads Administration, Oslo, Norway.
7. Jakobsen U H, De Weerd K & Geiker M R: “Elemental zonation in marine concrete,” *Cement and Concrete Research*, Vol. 85, 2016, pp. 12–27.
8. De Weerd K, Orsáková D, Muller A C A, Larsen C K, Pedersen B, Geiker M R: “Towards the understanding of chloride profiles in marine exposed concrete, impact of leaching and moisture content,” *Construction and Building Materials*, Vol. 120, 2016, pp. 418–431.
9. Taylor H F W: *Cement Chemistry*, 2nd ed., Telford, London, UK, 1997.
10. Justnes H: “A Review of Chloride Binding in Cementitious Systems,” *Nordic Concrete Research*, Vol. 21, 199, pp. 48-63.
11. Roberts M H: “Effect of calcium chloride on the durability of pre-tensioned wire in prestressed concrete,” *Magazine of Concrete Research*, Vol. 14, 1962, pp. 143–154.
12. Suryavanshi A K, Narayan Swamy R: “Stability of Friedel’s salt in carbonated concrete structural elements,” *Cement Concrete Research*, Vol. 26, 1996, pp. 729–741.
13. Arya C, Buenfeld N R, Newman J: “Factors influencing chloride-binding in concrete,” *Cement Concrete Research*, Vol. 20, 1990, pp. 291–300.
14. Tritthart J: “Chloride binding in cement - II. The influence of the hydroxide concentration in the pore solution of hardened cement paste on chloride binding,” *Cement Concrete Research*, Vol. 19, 1989, pp. 683–691.
15. Hansson C M, Frølund T, Markussen JB: “The effect of chloride cation type on the corrosion of steel in concrete by chloride salts,” *Cement Concrete Research*, Vol. 15, 1985, pp. 65–73.
16. Shi Z, Geiker MR, De Weerd K, Østnor TA, Lothenbach B, Winnefeld F & Skibsted J: “Role of calcium on chloride binding in hydrated Portland cement–metakaolin–limestone blends,” *Cement Concrete Research*, Vol. 95, 2017, pp. 205–216.
17. Zhu Q, Jiang L, Chen Y, Xu J, Mo L: “Effect of chloride salt type on chloride binding behavior of concrete,” *Construction Building Materials*, Vol. 37, 2012, pp. 512–517.
18. De Weerd K, Colombo A, Coppola L, Justnes H, Geiker MR: “Impact of the associated cation on chloride binding of Portland cement paste,” *Cement Concrete Research*, Vol. 68, 2015, pp. 196–202.
19. Wowra O, Setzer MJ: “Sorption of chlorides on hydrated cement and C₃S pastes,” in: M.J. Setzer, R. Aberg - Eds., *Frost Resistance of Concrete*, E & FN Spon, London, UK, 1997, pp. 147–153.
20. De Weerd K, Orsáková D, Geiker M: “The impact of sulphate and magnesium on chloride binding in Portland cement paste,” *Cement Concrete Research*, Vol. 65, 2014, pp. 30–40.
21. Lothenbach B, Durdzinski P, De Weerd K: “Thermogravimetric Analysis,” in: Scrivener K, Snellings R, Lothenbach B- Eds., *A Practical Guide to Microstructural Analysis of Cementitious Materials*, CRC Press Taylor & Francis Group, Raton, 2015, pp. 177–211.
22. Kulik D: GEM-Selektor v.3.3, available at: <http://gems.web.psi.ch/>.

23. Kulik D, Wagner T, Dmytrieva S, Kosakowski G, Hingerl FF, Chudnenko KV, Berner UR: GEM-Selektor geochemical modeling package: Revised algorithm and GEMS3K numerical kernel for coupled simulation codes, *Computer and Geoscience*, Vol. 17, 2013, pp. 1–24.
24. Wagner T, Kulik D, Hingerl F, Dmytrieva SV: “GEM-Selektor geochemical modeling package: TSolMod library and data interface for multicomponent phase models,” *The Canadian Mineralogist*, Vol. 50, 2012, pp. 1173–1195.
25. Thermodynamic database, provided by EMPA, available at: <https://www.empa.ch/web/s308/thermodynamic-data>.
26. Kulik D: “Improving the structural consistency of C-S-H solid solution thermodynamic models,” *Cement Concrete Research*, Vol. 41, 2011, pp. 477–495.
27. Hemstad P: “pH-dependency of chloride binding in ordinary Portland cement.” Master Thesis, Trondheim, Norway, 2018.
28. Lothenbach B, Winnefeld F, Alder C, Wieland E, Lunk P: “Effect of temperature on the pore solution, microstructure and hydration products of Portland cement pastes,” *Cement Concrete Research*, Vol. 37, 2007, pp. 483–491.
29. Scrivener K, Taylor HFW: “Delayed ettringite formation: a microstructural and microanalytical study,” *Advances in Cement Research*, Vol. 5, 1993, pp. 139–146.
30. De Weerd K, Justnes H: “The effect of sea water on the phase assemblage of hydrated cement paste,” *Cement and Concrete Composites*, Vol. 55, 2015, pp. 215–222.
31. Machner A, Zajac M, Ben Haha M, Kjellsen KO, Geiker MR, De Weerd K: “Chloride-binding capacity of hydrotalcite in cement pastes containing dolomite and metakaolin,” *Cement Concrete Research*, Vol. 107, 2018, pp. 163–181.
32. Delagrave A, Marchand J, Ollivier J-P, Julien S, Hazrati K: “Chloride Binding Capacity of Various Hydrated Cement Paste Systems,” *Advanced Cement Based Materials*, Vol. 6, 1997, pp. 28–35.
33. Labbez C, Nonat A, Pochard I, Jönsson B, “Experimental and theoretical evidence of overcharging of calcium silicate hydrate,” *Journal of Colloid and Interface Science*, Vol. 309, 2007, pp. 303–307.
34. Plusquellec G, Nonat A: “Interactions between calcium silicate hydrate, C-S-H, and calcium chloride, bromide and nitrate,” *Cement Concrete Research*, Vol. 90, 2016, pp. 89–96.
35. Haas J, “Etude expérimentale et modélisation thermodynamique du système CaO-SiO₂-(Al₂O₃)-H₂O,” *PhD thesis*, Université de Bourgogne, Dijon, France, 2012.
36. Zhang J, Scherer GW: “Comparison of methods for arresting hydration of cement,” *Cement Concrete Research*, Vol. 41, 2011, pp. 1024–1036.
37. Plusquellec G, Geiker M, Lindgård J, Duchesne J, Fournier B, De Weerd K: “Determination of the pH and the free alkali metal content in the pore solution of concrete,” *Cement Concrete Research*, Vol. 96, 2017, pp. 13–26.



DOI: 10.2478/ncr-2018-0010

ISSN online 2545-2819

ISSN print 0800-6377

© Article authors. This is an open access article distributed under the Creative Commons Attribution-NonCommercial-NoDerivs licens. (<http://creativecommons.org/licenses/by-nc-nd/3.0/>).

Received: March 29, 2018

Revision received: May 31, 2018

Accepted: May 31, 2018

Prediction Models for Thermal Conductivity of Cement-based Composites



Mohammad H. Baghban
Associate Professor
Department of Manufacturing and Civil Engineering, Norwegian University of Sciences and Technology (NTNU)
Teknologivegen 22, 2815 Gjøvik
mohammad.baghban@ntnu.no



Mahdi Kioumars
Associate Professor
Department of Civil Engineering and Energy Technology, Oslo Metropolitan University (OsloMet)
Pilestredet 35, Oslo
mahdi.kioumars@oslomet.no



Sotirios Grammatikos
Professor
Department of Manufacturing and Civil Engineering, Norwegian University of Sciences and Technology (NTNU)
Teknologivegen 22, 2815 Gjøvik
sotirios.grammatikos@ntnu.no

ABSTRACT

Cement-based materials are the most consumed materials in the construction industry. Low or high thermal conductive cement-based materials are of interest in applications such as

embedded floor heating systems, building envelopes or structural elements. This paper describes prediction models for thermal conductivity of cementitious composites by considering different variables such as constituent materials, porosity and moisture content. The presented prediction models may be used for thermal conductivity based mix design of cementitious materials. Based on the desired accuracy, different solutions are proposed.

Key words: Mix Design, Model, Thermal Conductivity, Cement-based Materials.

1. INTRODUCTION

Thermal conductivity is an important material property in the energy design process of buildings. While cement-based materials are the most consumed materials in the construction industry, case-tailored thermal conductivity is desirable for these materials depending on the application area. Indoor surfaces such as embedded floor heating systems or cementitious materials mixed with phase change materials, may demand high thermal conductivity. On the other hand, materials with low thermal conductivity may be of interest as a part of heat insulation or for thermal bridge calculations as well as structural elements.

Moisture content, porosity and constituent materials are the main parameters affecting thermal conductivity of cement-based materials. The thermal conductivity of water >20 times higher than thermal conductivity of the stagnant air and replacement of air by water can make a significant change in the thermal conductivity of porous materials. While changes in constituent materials and porosity may be neglected after concrete curing for thermal conductivity determination, the moisture content is expected to have considerable changes during the lifetime of most cementitious materials. This indicates that considering one certain value for thermal conductivity of such types of composites, may provide low accuracy when considering the material performance during the service life of the material. Calculating thermal conductivity as a function of main effective variables such as moisture content, porosity and constituent materials using simplified prediction models, can be a practical solution to this challenge. The thermal conductivity of dry material may be adjusted in the mix design, using the knowledge from concrete technology with regards to porosity and constituent materials. Variations in such material property due to moisture content can be estimated based on the saturation degree. Moreover, the water sorption can be controlled by modifying the pore structure as well as internal or surface hydrophobation [1, 2]. The prediction model can for example be introduced to building physics tools, where the thermal conductivity can be adjusted based on the existing climate conditions.

2. PREDICTION MODELS FOR CEMENTITIOUS COMPOSITES

2.1 Particle-matrix model based on multiphase semi-empirical equation

Determination of the thermal conductivity of the particle and the matrix phases individually, makes it possible to determine the thermal conductivity of the cementitious composites using the following two-phase model [3].

$$\lambda_{\text{composite}}^n = V_{\text{matrix}} \lambda_{\text{matrix}}^n + V_{\text{particle}} \lambda_{\text{particle}}^n \quad (1)$$

where $\lambda_{\text{composite}}$, λ_{matrix} and $\lambda_{\text{particle}}$ are the thermal conductivity of the composite, the matrix and the particles, respectively. V_{matrix} and V_{particle} are the volume fractions of the matrix and the

particles, respectively, and n is a constant value determined by experimental investigation. The upper and lower limits of n factor are 1 and -1 which are identical to parallel and series models, respectively.

The accuracy of the model can be modulated based on the accuracy in predicting the thermal conductivity of individual phases, which will be discussed further in this study. The expected porosity and moisture content of the cement-based materials may also be estimated and tuned by using the knowledge of concrete technology and building physics. Consequently, by introducing appropriate constituent materials, a particle-matrix model can be used for thermal conductivity based mix design of cementitious materials with desirable accuracy.

2.2 Particle-matrix model based on Hirsch model

Hirsch [4] proposed a model which may be used for predicting thermal conductivity of cement-based composites by considering the two particle and matrix phases. This model combines parallel and series models by giving them a share based on the x factor.

$$\frac{1}{\lambda_{\text{composite}}} = x \left[\frac{1}{V_{\text{particle}} \lambda_{\text{particle}} + V_{\text{matrix}} \lambda_{\text{matrix}}} \right] + (1-x) \left[\frac{V_{\text{matrix}}}{\lambda_{\text{matrix}}} + \frac{V_{\text{particle}}}{\lambda_{\text{particle}}} \right] \quad (2)$$

where x is a constant value determined by experimental investigation. In addition to the x factor, the accuracy of this model is also dependent on accurate estimation of the thermal conductivity of individual phases.

2.3 Simplified estimation using Parallel-Series bounds

While the above mentioned semi-empirical models can be used for thermal conductivity based mix design as well as estimation of thermal conductivity of cement-based composites with a reasonable accuracy, a simplified method may be used for predicting the range of this material property. These models are especially appropriated for cases where the upper or lower limits of thermal conductivity are required. Such cases could for example be the maximum heat loss through a building envelope due to moisture condensation in the pore structure of the materials or the estimating upper limit of the thermal resistance property of the cementitious materials in an embedded floor heating system due to drying. The upper limit is given by the parallel model:

$$\lambda_{\text{composite}} = V_{\text{matrix}} \lambda_{\text{matrix}} + V_{\text{particle}} \lambda_{\text{particle}} \quad (3)$$

and the series model gives the lower limit:

$$\frac{1}{\lambda_{\text{composite}}} = \frac{V_{\text{matrix}}}{\lambda_{\text{matrix}}} + \frac{V_{\text{particle}}}{\lambda_{\text{particle}}} \quad (4)$$

Thermal conductivity of particle and matrix phases can also be extracted from the literature to avoid experimental investigations.

2.4 Simplified estimation using Hashin-Shtrikman bounds

The Hashin-Shtrikman (H-S) model gives tighter bounds compared to parallel and series models. H-S lower (λ_l) and upper (λ_u) bounds for two material phases with $\lambda_1 \geq \lambda_2$, are given by [5]:

$$\lambda_l = \lambda_1 + \frac{V_2}{\frac{1}{\lambda_2 - \lambda_1} + \frac{V_1}{3\lambda_1}} \quad (5)$$

$$\lambda_u = \lambda_2 + \frac{V_1}{\frac{1}{\lambda_1 - \lambda_2} + \frac{V_2}{3\lambda_2}} \quad (6)$$

When the difference between thermal conductivity of matrix and particle phases becomes lower, the two-phase H-S bounds become tighter and a reasonable estimation of thermal conductivity of cement-based composites is readily available without experimentally investigating the composite. The same procedure may be adopted to predict the thermal conductivity of matrix or particle phases separately. For example, in the case of water-submerged hardened cement pastes (HCPs) where most of the air (low thermal conductivity), is replaced by water (thermal conductivity closer to that of solid structure of the plain HCP), the H-S bounds become tight enough to allow for a reasonable estimation of the material property (Figure 1).

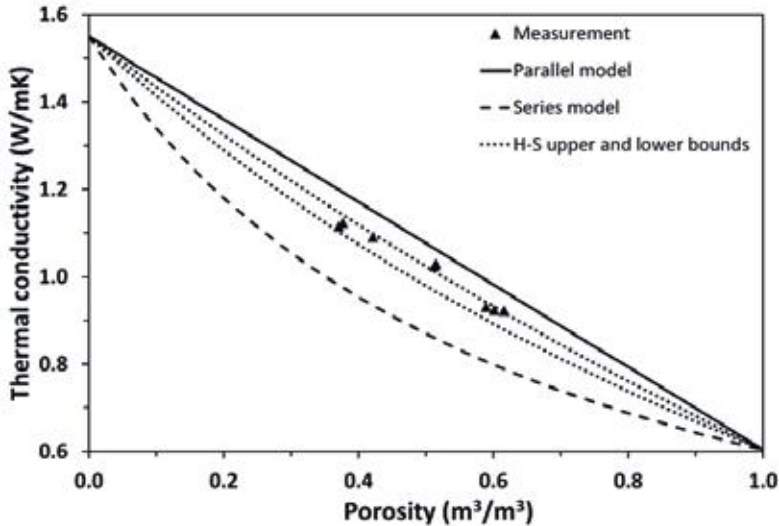


Figure 1– Measured thermal conductivity of plain HCPs submerged in water and analytical bounds [3].

2.5 Response surface method (RSM)

The Response Surface Method (RSM) method, which was developed by Box et al. [6-8] is a collection of statistical and mathematical methodologies, useful for predicting material

properties considering different variables and for developing, improving, and optimizing processes. It also finds applications in the design, development, and formulation of new products, improvement of existing product designs [8], and more recently in reliability analysis. The thermal conductivity can for example be approximated with a second-order polynomial function, which for k random variables is expressed as:

$$\lambda = \beta_0 + \sum_{i=1}^k \beta_i X_i + \sum_{i=1}^k \beta_{ii} X_i^2 + \sum \sum_{i<j}^k \beta_{ij} X_i X_j \quad (7)$$

where, λ is the predicted thermal conductivity, X_i is the coded level of a design variable i , k is the total number of variables present in the problem, coefficient β_0 is a constant and β_i , β_{ii} and β_{ij} are the regression coefficients for the linear, quadratic and interaction effects, respectively.

2.6 Multi-scale model

Liu et al. [9] presented a multi-scale micromechanical model based on Mori-Tanaka scheme [10].

$$\lambda_{MT} = \frac{V_M \lambda_M + \sum_{s=1}^n V_s \lambda_s A_s}{V_M + \sum_{s=1}^n V_s A_s} \quad (8)$$

Where V_s and V_M are the volume fraction of the inclusions (can be particles) and the matrix, respectively, and λ_{MT} , λ_s and λ_M are the thermal conductivity values of the composite, inclusions and the matrix, respectively. By setting $A_s=1$, this model will function as a parallel model and considering $A_s = \lambda_M / \lambda_s$ it will be equivalent to a series model.

This model can be deployed for considering the influences of HCP as well as fine and course aggregates in different scales. Multi-scale modelling can be an appropriate solution for high accuracy results. However, the above mentioned model has large errors in some cases such as predicting thermal conductivity of saturated materials. Further study is needed for developing this multi-scale model to increase the accuracy.

3. PREDICTING THERMAL CONDUCTIVITY OF INDIVIDUAL PHASES IN PARTICLE-MATRIX MODEL

3.1 Matrix

The main factors affecting thermal conductivity of the matrix can be considered as variables in a multiphase composite model. Baghban et al. [3] presented a three-phase model for predicting thermal conductivity of HCPs:

$$\lambda_{hcp}^n = m \lambda_w^n + (\varepsilon_{tot} - m) \lambda_a^n + (1 - \varepsilon_{tot}) \lambda_s^n \quad (9)$$

where λ_{hcp} , λ_w , λ_a and λ_s are the thermal conductivity of the HCP, water, air, and solid structure of the HCP, respectively. ε_{tot} is the total porosity, m is the saturation degree showing volumetric moisture content and n is a constant value. While λ_w and λ_a are known, a proper estimation needs to be done for λ_s and n based on experimental investigation.

The graph in Figure 2 illustrates the thermal conductivity of plain HCPs at different total porosities (ϵ_{tot}) and saturation degree (m) based on Eq. 9. λ_s is estimated as 1.55 W/mK and n is found to be 0.55 for plain hcps. Note that these two values are obtained by minimizing the calculation error of Eq. 9 to match the experimental data at different moisture states, which is in agreement with the results obtained from the laboratory (see Figure 3). λ_w and λ_a are known parameters which are considered as 0.026, 0.604 W/mK, respectively. Since thermal conductivity of solid structure of the matrix, λ_s , may vary due to changes in constituent materials such as presence of pozzolanic materials, fibres or changes in the cement chemistry, λ_s can be determined as a function of these variables by laboratory research. Furthermore, changes in the thermal conductivity of the fluid phase due to variations in the pore structure or different fluid chemistries can also be investigated by the same procedure. Other models described in previous sections can also be used for predicting thermal conductivity of each phase.

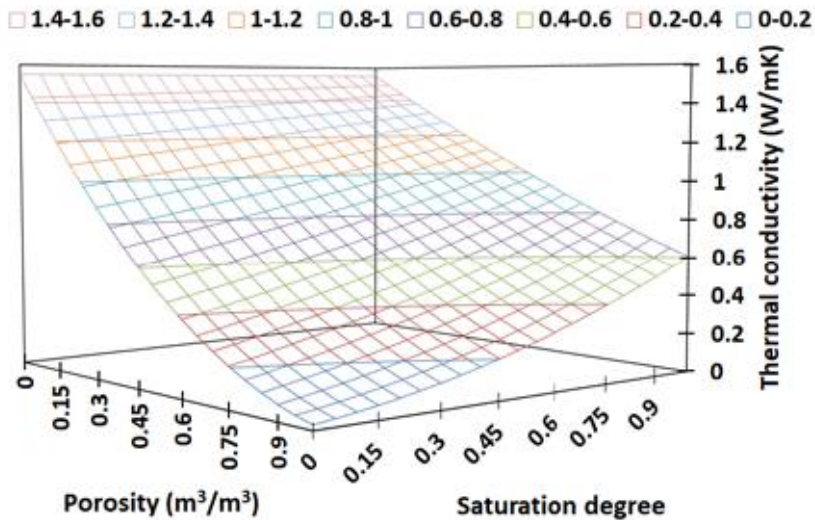


Figure 2 – Thermal conductivity of plain HCPs at different total porosities and saturation degrees calculated from Eq. 9 [3].

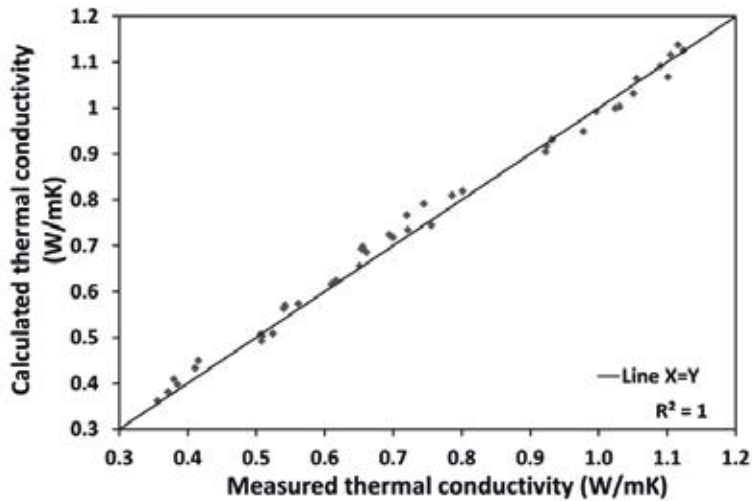


Figure 3 – Comparison of the measured and calculated thermal conductivities [3].

3.2 Particle

Stone aggregates are the most commonly used particle types in cementitious composites. These aggregates have usually a low porosity and the effect of moisture sorption may be neglected for many practical applications. On the other hand, multiphase prediction models can also be presented for the particles in case of using aggregates with considerable porosity, such as using light weight aggregates.

Fine particles in the size range of the matrix particles can be considered as a part of the matrix. Moreover, the coupling effects such as effect of interfacial transition zone can also be defined as a function of the surface area of the particles in the mix.

4. DISCUSSION

Depending on the application and intended accuracy of thermal conductivity prediction, the appropriate prediction model may be chosen. Theoretical bounds are appropriate tools to approximate the highest and lowest values. When the maximum heat loss through a building envelope due to moisture condensation in the pore structure of the material needs to be estimated or highest thermal resistivity of the cementitious materials in an embedded floor heating system due to drying is under investigation, the theoretical bounds can help to provide with the solution eliminating experiments. In this case, providing the data for thermal conductivity of individual phases in the composite is sufficient, which can usually be extracted from the existing literature with a reasonable accuracy. While parallel and series models provide the absolute upper and lower limits, H-S model can present tighter bounds. When the thermal conductivity of the phases are not so far from each other (See Figure 1), H-S bounds can even be used for estimating the thermal conductivity of the composite. Figure 4 illustrates a comparison of different prediction models for dried HCPs considering two phases of air (porosity) and solid

structure, based on experimental results from Baghban et al. [3]. Since the thermal conductivity of air is more than 20 times lower than the thermal conductivity of water, the difference between H-S bounds are much higher in Figure 4 compared to Figure 1. However, the experimental data is close to the upper H-S bound for this case which can be used for predicting thermal conductivity of the composites with some over estimation. The parallel model is still farther than upper H-S bound and gives considerable difference with the experimental results.

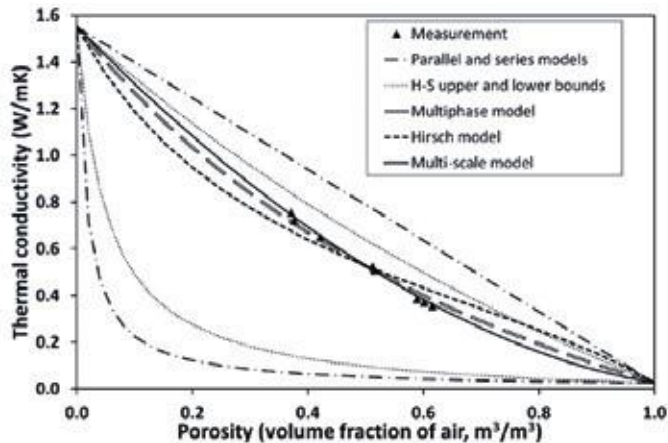


Figure 4 – Comparison of different models with the experimental results of HCPs with two phases of air and solid structure.

Multiphase semi-empirical model has shown the best fit to the experimental data in Figure 4. The three-phase model in Figure 2 generated from Eq. 9 is also based on this model which has been in alignment with the experimental results. The multi-scale model also matches for this example and has the potential for accurate prediction. However, increasing accuracy may bring up complications in the modelling, which can make this method difficult to use. On the other hand, the Hirsch model gives some error and makes this model less suitable for this case. Since RSM is an interpolation technique and not a predefined composite model, which uses statistical approaches, it is able to calculate a regression model to predict the response (in this example, thermal conductivity of the composite). The result of RSM is a polynomial of existing variables, which can easily be fitted to the experimental results in figure 4 and specially multiple variables like surfaces such as the one shown in Figure 2. Since this method is not based on a predefined composite model, providing properly distributed experimental data in the actual boundaries of the composite model can facilitate more accurate estimation of the thermal conductivity pattern. Predefined composite models are less sensitive to distribution of the experimental data.

Changes in the mix composition such as incorporating fibres, additives, different types of aggregates or moisture changes, may change the thermal conductivity pattern and prediction models should be investigated for these cases as well. In general, above-mentioned models are expected to have the potential for predicting the thermal conductivity of cementitious composites with intended accuracy.

5. CONCLUSION

In the framework of this study, different solutions for predicting thermal conductivity of cement-based composites were described. Theoretical bounds such as H-S bounds are appropriate tools to approximate the highest and lowest values. Semi-empirical models based on particle-matrix model can simply approximate this material property with a reasonable accuracy. Further investigation is needed for approximating the thermal conductivity of the individual phases under different conditions such as moisture changes and incorporation of different materials to the composite. Multi-scale modelling has the potential for accurate prediction, however, increasing accuracy may result into complications, which can render adoption of this method difficult. RSM as an interpolation technique can provide a reasonable prediction if properly distributed experimental data are available.

REFERENCES

1. Baghban M H, Hovde P J, Jacobsen S: “Effect of internal hydrophobation, silica fume and w/c on water sorption of hardened cement pastes,” *Proceedings*, International Conference on Durability of Building Materials and Components (XII DBMC), Porto, Portugal, April 12-15, 2011, pp 1495-1502.
2. Justnes H, “Low water permeability through hydrophobicity,” *Report*, SINTEF Building and Infrastructure, Oslo, Norway, 2008.
3. Baghban M H, Hovde P J, Jacobsen S, “Analytical and experimental study on thermal conductivity of hardened cement pastes”, *Materials and Structures*, Vol. 46, No. 9, 2013, pp. 1537-1546.
4. Monteiro P J M, “A note on the Hirsch model,” *Cement and Concrete Research*, Vol. 21, 1991, pp. 947-950.
5. Hashin Z, Shtrikman S, “A Variational Approach to the Theory of the Effective Magnetic Permeability of Multiphase Materials,” *Journal of Applied Physics*, Vol. 33, No. 10, 1962, pp. 3125-3131.
6. Bezerra M A, Santelli R E, Oliveira E P, Villar L S, Escalera L A, “Response surface methodology (RSM) as a tool for optimization in analytical chemistry,” *Talanta*, Vol. 76, 2008, pp. 965–977.
7. Hooshmandi S, Kioumarsi M, Kioumarsi B, Baghban M H, “Application of response surface method (RSM) on sensitivity analysis of reinforced concrete bridge pier wall,” *Proceedings*, XXIII Nordic Concrete Research Symposium, Aalborg, Denmark, 2017, pp. 303-306.
8. Kioumarsi M M, Hendriks M A N, Geiker M R, “Quantification of the interference of localised corrosion on adjacent reinforcement bars in a concrete beam in bending”. *Nordic Concrete Research (NCR)*, Vol. 49, 2014, pp. 39–57.
9. Liu J, Xu S, Zeng Q, “A multi-scale micromechanical investigation on thermal conductivity of cement-based composites,” *IOP Conf. Series: Materials Science and Engineering* 167 012069, 2017.
10. Mori T, Tanaka K, “Average stress in matrix and average elastic energy of materials with misfitting inclusions,” *Acta metallurgica*, Vol. 21, No. 5, 1973, pp. 571-574.

Research Council & Editorial Board of Nordic Concrete Research

| Dr. Terje F. Rønning, Chairman of the Research Council | | |
|--|---|---|
| Danish Concrete Association | Dr. Marianne Tange Hasholt Associate professor Technical University of Denmark Department of Civil Engineering Tel: +45 25 17 02 matah@byg.dtu.dk | Mrs. Gitte Normann Munch-Petersen Teknologisk Institut Kongsvang Allé 29 DK - 8000 Aarhus Mobile: +45 72 20 32 45 gnmp@teknologisk.dk |
| Finnish Concrete Association | Professor Jouni Punkki Aalto University, Dept of Civil Engineering P.O.Box 12100 FI-00076 Aalto, Finland tel. +358 50 322 4155 jouni.punkki@aalto.fi | Prof. Dr. Jukka Lahdensivu Tampere University of Technology P.O.Box 527 FI-33101 Tampere Mobile: +358 40 0733852 jukka.lahdensivu@tut.fi |
| Icelandic Concrete Association | Dr. Jón E. Wallevik Innovation Center Iceland IS - 112 Keldnaholti Tel: +354 522 9362 Mobile: +354 Fax: +354 522 9111 jon.w@nmi.is | Prof. Dr. Olafur H. Wallevik Innovation Center Iceland IS - 112 Keldnaholti Tel: +354 522 9000 Mobile: +354 860 7650 wallevik@ru.is |
| Norwegian Concrete Association | Dr. Terje F. Rønning Heidelberg Cement NE / Cement Product development & Implementation P.O.Box 38 N - 3991 Brevik Tel.: +47 3557 2000 Mobile: +47 915 76 046 terje.ronning@heidelbergcement.com | Prof. Dr. Mette R. Geiker Department of Engineering NTNU N - 7034 Trondheim Tel: +47 7359 4529 Mobile: +47 4045 1218 mette.geiker@ntnu.no |
| Swedish Concrete Association | Tekn. Dr. Peter Utgenannt CBI Swedish Cement and Concrete Research Institute P.O. Box 857 SE - 501 15 Borås Tel: +46 105 166 870 Mobile: +46 706 452 008 Peter.utgenannt@cbi.se | Tekn. Dr. Mårten Janz ÅF, International Division Hallenborgs gata Box 585 SE-201 25 Malmö Tel: +46 10 505 7334 Mobile: + 46 70 293 6338 marten.janz@afconsult.com |
| Editor | Prof. Johan Silfwerbrand KTH Royal Institute of Technology Dept. of Civil & Architectural Engrg. Brinellvägen 23 SE-100 44 Stockholm Tel: +46 8 790 8033 Mobile: +46 70 726 4005 jsilfwer@kth.se | <i>June 1st, 2018</i> |

ISBN 978-82-8208-061-3 ISSN PRINT 0800-6377 ISSN ONLINE 2545-2819
www.nordicconcrete.net